Characterization and correction of multilayer X-ray optics

Universität Hamburg
DER FORSCHUNG | DER LEHRE | DER BILDUNG

Dissertation
zur Erlangung des Doktorgrades
an der Fakultät für Mathematik, Informatik und Naturwissenschaften
Fachbereich Physik
der Universität Hamburg

vorgelegt von

Jan Lukas Dresselhaus

Hamburg

2024

Gutachter/innen der Dissertation: Dr. Saša Bajt
Prof. Dr. Henry N. Chapman

Zusammensetzung der Prüfungskommission: Dr. Saša Bajt
Prof. Dr. Henry N. Chapman
Prof. Dr. Franz X. Kärtner
Prof. Dr. Robin Santra
Prof. Dr. Arwen Pearson

Vorsitzende/r der Prüfungskommission: Prof. Dr. Robin Santra

Datum der Disputation: 27.01.2025

Vorsitzender des Fach-Promotionsausschusses PHYSIK: Prof. Dr. Markus Drescher

Leiter des Fachbereichs PHYSIK: Prof. Dr. Wolfgang J. Parak

Dekan der Fakultät MIN: Prof. Dr.-Ing. Norbert Ritter

Acknowledgement

This work would not have been possible without the invaluable assistance and encouragement of many individuals, to whom I am profoundly grateful. I would like to express my heartfelt gratitude to all those who have supported me throughout the process of writing this thesis.

First of all, I would like to thank Saša Bajt, my supervisor, who made it possible for me to work on the frontiers of scientific research. Her contagious ambition and encouragement continuously pushed me forward to achieve what is presented in this thesis, and she was always there to help me when I needed guidance. Next, I want to thank Henry Chapman, whose courageous ideas allowed me to participate in exciting experiments and whose knowledge was always valuable. I would also like to thank Franz Kärtner who helped me to reflect on my achievements and to convey my work clearly to a broader audience. In this context I would also like to thank the Hamburg Centre for Ultrafast Imaging for the opportunity to work in a collaborative cluster together with many excellent scientists with which I shared both, great scientific exchange and fun experiences.

I want to thank my colleagues Margarita Zakharova, Jia Chyi Wong and Mauro Prasciolu for their unconditional support during my time as a PhD student and the plentiful invigorating moments we shared together. Without them, my results and fun would have been much sparser. Thanks also to Holger Fleckenstein, who imparted a lot of useful knowledge to me, from instrumentation to the German language. Many thanks to Nikolay Ivanov for his support in programming and simulations and Kevin Murray for introducing me to multilayer optics and their experimental characterization.

Thanks to Wenhui Zhang and Chufeng Li as well as all other group members of Henry's group who were always supportive and helped me to expand my knowledge in various fields. I am thankful to Tang Li for assisting me at the beginning of my journey as a graduate student and to Naufal Ismail Kreshnaviyanto for taking some of the workload off my shoulders at the end, allowing me to focus on writing the thesis.

Without the support of many individuals, none of the experiments would have been possible. Thanks go out to our laboratory technicians Sabrina Schneider and Harumi Nakatsutsumi, the engineers Marcel Görlitz, Tjark Delmas, Julia Maracke and Lars Gumprecht as well as to our IT support Martin Domaracký, Jerome Carnis, Ivan De Gennaro Aquino, Philipp Middendorf and Dmitry Egorov. Many thanks also to the beamline staff at PETRA III P11 and P07 as well as at MID and SPB/SFX at the EuXFEL for making these experiments possible.

Not only the time spent at the university during the PhD period is important but also the time spent outside of it. I am grateful for my friends with whom I have been able to keep in touch and share an ever-growing amount of fond memories. I want to express my gratitude to my sister and brother, who share my enthusiasm for science while keeping me grounded. I would like to thank my father for always encouraging me to try out new things and set ambitious goals. I want to thank my mother for always supporting me in whatever unusual ideas I came up with without judgment. Finally, I would like to thank my girlfriend Julia, who has supported me throughout most of my academic career and has always had my back. Her faith in me has kept me going through difficult times.

Abstract

Highest resolution X-ray microscopy requires high numerical aperture (NA) optics of excellent quality which allow to focus X-ray beams to small focal points. Multilayer Laue lenses (MLLs) are a new type of diffractive optic with the capability to focus hard X-rays with high efficiency to nanometer spots. However, they are currently limited by wavefront aberrations caused by layer misplacements during their fabrication process. The determination and correction of wavefront aberration are therefore crucial aspects for the development and improvement of MLLs designed to achieve the highest possible resolutions. Wavefront characterization for lens development cannot rely solely on access to synchrotrons, as beamtime must be applied for and is therefore only available to a limited extent. For that reason, the aim of this thesis was to determine the requirements that have to be met in order to enable fast and precise wavefront characterization of MLLs using a laboratory-based setup. This requires a dedicated table top X-ray system and a suitable software.

To determine the optimal structure for MLLs, periodic multilayer gratings with different layer thicknesses on the scale of a few nanometers were studied. It was found that high quality and high efficiency ($>$ 60 % at 17.5 keV and $>$ 80 % at 60 keV) periodic multilayers can be fabricated, which are mainly limited by the interdiffusion of the layers. The interdiffusion depth was found to be around 0.4 nm for WC/SiC multilayer-based optics, the material pair our MLLs are typically made of. Based on these findings, high NA ($>$ 0.01) MLLs were produced for highest resolution microscopy. To determine the wavefront aberrations of the MLLs in a laboratory setup, a phase retrieval algorithm with low requirements on coherence and monochromaticity was needed. Ptychographic X-ray speckle tracking (PXST) is an in-house developed phase gradient reconstruction algorithm that was found to fulfill these requirements and was recently augmented to incorporate machine learning techniques, which allow accurate phase retrieval even in noisy and low intensity environments. It is based on the X-ray speckle tracking approach and can be understood as a generalized Hartmann sensor that tracks sample features between overlapping images to determine local phase gradients. It was found that due to the robustness of the algorithm, wavefront reconstructions are largely accurate regardless of the measurement conditions, as long as the lens and a suitable sample are aligned with respect to each other. This has reduced the time required for the

characterization of MLLs from $>$ 10 hours to a few minutes, allowing feedback on a lens' performance on the same day it is manufactured.

The wavefront error of an MLL is a map of the relative deviation from the wavefront of an ideal lens, which can be related to the misplacements of its layers, allowing subsequent fabrication cycles to be improved based on previous lens characterizations. However, residual aberrations remain that have to be corrected externally. As it becomes increasingly difficult to produce high NA MLLs with the required precision, they tend to have larger aberrations. To correct these, a compound refractive corrector consisting of an array of individual refractive elements had been proposed. For the first time, such a design was realized based on nano-scale 3D printing to correct an MLL pair for hard X-ray high-resolution imaging, resulting in a record focusing of 2.9 nm × 2.8 nm at 17.5 keV.

The well characterized and aberration corrected MLLs were then used in a series of imaging schemes at the PETRA III synchrotron and the European X-ray free electron laser. There, imaging techniques such as projection holography and near-field ptychography, which benefit from the strong focusing of the lenses, were used with improved MLLs to achieve resolutions well below 10 nm. Novel imaging techniques that are now possible due to high NA MLLs such as convergent beam crystallography have been successfully implemented. At high photon energies, where MLLs become more efficient in contrast to other optics, the dark-field imaging method of scanning Compton X-ray microscopy was successfully used, allowing high-resolution imaging of biological samples with minimal radiation dose. This method in particular will benefit significantly from fourth generation synchrotrons, as their higher brightness and larger coherence in combination with better X-ray optics allows for both higher resolution and faster data acquisition times. This should enable 3D imaging of microscopic samples at high resolutions and low radiation doses.

Zusammenfassung

Hochauflösende Röntgenmikroskopie erfordert exzellente Optiken mit hoher numerischer Apertur (NA), die es ermöglichen, Röntgenstrahlen auf kleine Punkte zu fokussieren. Multischicht-Laue-Linsen (MLL) sind eine neue Art diffraktiver Optiken, welche harte Röntgenstrahlen mit hoher Effizienz auf nanometer-große Punkte fokussieren können. Derzeit sind sie allerdings durch Wellenfrontaberrationen beschränkt, die während des Herstellungsprozesses durch Positionierungsfehler der Schichten entstehen. Wellenfrontbestimmung und Aberrationskorrektur sind daher entscheidende Faktoren für die Entwicklung und Verbesserung von MLL, mit denen die höchstmögliche Auflösung erreicht werden soll. Die notwendige Wellenfrontcharakterisierung für die Linsenentwicklung sollte nicht allein von einem Synchrotonzugang abhängig sein, da dieser unter anderem durch das Beantragen von Strahlzeiten nur sehr begrenzt verfügbar ist. Ziel dieser Arbeit war es daher herauszufinden, welche Voraussetzungen erfüllt sein müssen, um eine schnelle und präzise Wellenfrontcharakterisierung von MLL in einem Laboraufbau zu ermöglichen. Dies erfordert ein spezielles kompaktes Röntgensystem und eine geeignete Software.

Um die optimale Struktur für MLL zu bestimmen, wurden periodische Multischicht-Gitter mit verschiedenen Schichtdicken in der Größenordnung von wenigen Nanometern untersucht. Es wurde festgestellt, dass periodische Multischichten von hoher Qualität und mit hoher Effizienz (> 60 % bei 17.5 keV und > 80 % bei 60 keV) hergestellt werden können, deren Leistung hauptsächlich durch die Durchmischung der Schichten begrenzt ist. Bei WC/SiC-Multischicht-Optiken, der Materialpaarung, aus der unsere MLL typischerweise hergestellt werden, beträgt die Tiefe dieser Durchmischung etwa 0.4 nm. Auf der Grundlage dieser Ergebnisse wurden MLL mit hoher NA (> 0.01) für die Mikroskopie mit höchster Auflösung hergestellt. Um die Wellenfrontaberrationen der MLL in einem Laboraufbau zu bestimmen, benötigte es einen Phasenrekonstruktionsalgorithmus mit geringen Anforderungen an Kohärenz und Monochromatizität. *Ptychographic X-ray Speckle Tracking* (PXST) ist ein intern entwickelter Algorithmus zur Rekonstruktion von Phasengradienten, der diese Anforderungen erfüllt. Vor kurzem wurde dieser um maschinelle Lerntechniken erweitert, was auch in verrauschten Umgebungen mit geringer Intensität eine genaue Phasenbestimmung ermöglicht. Er basiert auf dem *X-ray-Speckle-Tracking*-Ansatz und kann als verallgemeinerter Hartmann-Sensor verstanden werden, der Proben-

merkmale zwischen überlappenden Bildern verfolgt, um lokale Phasengradienten zu bestimmen. Es wurde festgestellt, dass aufgrund der Robustheit des Algorithmus die Wellenfrontrekonstruktionen unabhängig von den Messbedingungen weitestgehend genau sind, solange die Linse und eine geeignete Probe korrekt zueinander ausgerichtet sind. Dadurch konnte die für die Charakterisierung von MLL benötigte Zeit von > 10 Stunden auf wenige Minuten reduziert werden, was eine Aussage über die Qualität einer Linse noch am Tag ihrer Herstellung ermöglicht.

Der Wellenfrontfehler einer MLL ist eine Abbildung der relativen Abweichung von der Wellenfront einer idealen Linse, welche mit den Fehlstellungen der Linsenschichten in Verbindung gebracht werden kann, sodass nachfolgende Herstellungszyklen auf der Grundlage früherer Linsencharakterisierungen verbessert werden können. Es verbleiben jedoch Restaberrationen, die extern korrigiert werden müssen. Da es immer schwieriger wird, MLL mit hoher numerischer Apertur mit der erforderlichen Präzision herzustellen, weisen sie tendenziell größere Aberrationen auf. Um diese zu korrigieren, wurde ein refraktiver Komposit-Korrektor vorgeschlagen, der aus einer Anordnung einzelner refraktiver Elemente besteht. Zum ersten Mal wurde ein solches Design auf der Basis von 3D-Druck im Nanomaßstab realisiert, um ein MLL-Paar für hochauflösende Abbildungen mit harten Röntgenstrahlen zu korrigieren, was zu einer Rekordfokussierung von 2.9 nm × 2.8 nm bei 17.5 keV führte.

Die gut charakterisierten und aberrationskorrigierten MLL wurden in einer Reihe von Bildgebungsverfahren am PETRA III-Synchrotron und am Europäischen XFEL eingesetzt. Dort wurden bestehende Abbildungsverfahren wie die Projektionsholographie und die Nahfeld-Ptychographie, die von der starken Fokussierung der Linsen profitieren, in Kombination mit verbesserten Linsen eingesetzt um so Auflösungen von deutlich unter 10 nm zu erreichen. Neuartige Abbildungsverfahren, die nur aufgrund der hohen NA der MLL möglich sind, wie z. B. die Konvergenzstrahlkristallographie, ließen sich erfolgreich umsetzen. Bei hohen Photonenenergien, bei denen MLL im Gegensatz zu anderen Optiken an Effizienz gewinnen, wurde die Dunkelfeld-Abbildungsmethode der Raster-Compton-Röntgenmikroskopie erfolgreich eingesetzt, die eine hochauflösende Abbildung biologischer Proben bei minimaler Strahlendosis ermöglicht. Insbesondere diese Methode wird von Synchrotrons der vierten Generation erheblich profitieren, da die höhere Brillanz und größere Kohärenz in Kombination mit besseren Röntgenoptiken sowohl eine höhere Auflösung als auch schnellere Datenerfassungszeiten ermöglicht. So könnte die 3D-Abbildung mikroskopischer Proben mit hoher Auflösung bei geringer Strahlendosis ermöglicht werden.

Contents

Introduction

1

Contemporary advancements in scientific research are frequently conducted at large-scale facilities, such as synchrotrons and free electron lasers. Their beam properties allow precise manipulation of light over a wide range of energies from the soft- to the hard X-ray regime. High flux, small foci and short pulses probe matter with previously unprecedented precision. The understanding of processes at the atomic and molecular level advances scientific research fields from material science to biology and quantum systems. Currently, fourth generation synchrotrons utilizing multi-bend achromats are already in operation [1–3], being upgraded [4–6] and planned [7, 8]. Their ultralow emittance increases the coherent flux by multiple orders of magnitude, allowing a much larger fraction of the beam to be focused to the diffraction limit [7]. This opens up the possibility to probe samples at resolutions approaching the single digit nm scale. In order to fully capitalize on the provided beam properties, efficient and high-quality X-ray optics are indispensable [9]. X-ray optics for focusing rely on either refraction, reflection or diffraction. The most prominent example of refractive optics which are routinely used at synchrotrons are compound refractive lenses (CRLs), which consist of a series of individual refractive lenses [10, 11] and are typically used for X-rays in the range from 5 keV to 100 keV. Since the refractive index n of all materials is close to unity for hard X-rays, CRLs rely on the combined focusing of many individual elements to achieve small foci and reasonable focal length. The resolution that CRLs of constant radius can achieve is limited by the critical angle of reflection, which is equal to $\sqrt{2\delta}$ for a material of refractive index $n = 1 - \delta + i\beta$ [12]. This limitation can be overcome through the use of adiabatically focusing lenses (AFLs), in which the lens shape of individual elements is adapted to the beam size [13]. While this type of lenses can in principle focus X-rays to below 10 nm [12], they are currently limited by the required manufacture precision, rather than the fundamental physical limitations, which is why focusing of hard X-rays with AFLs to 18 nm has only recently been demonstrated [13].

The critical angle of reflection restrains reflective optics in a similar fashion, limiting the theoretical highest resolution of (uncoated) reflective focusing mirrors to 7 nm [14, 15]. The most common example of reflective optics are Kirkpatrick–Baez mirrors (or short KB mirrors), which form a 2D focus using a pair of concave reflective mirrors [14]. They are placed at small grazing angles such that total external reflection occurs. Due to the required incident angle for sub 10 nm focusing being higher than the critical angle, they are limited to focusing to about 10 nm [16]. To overcome this limitation and break the 10 nm barrier, reflective optics can be coated with a multilayer, increasing the acceptance angle. Using this approach, first one dimensional [17] and later two dimensional [18, 19] focusing to 7 nm was realized. Extreme precision in the manufacture of the required mirrors and phase correction were required to achieve this record. In contrast to CRLs which absorb a significant amount of the incident beam, KB mirrors can focus with minimal intensity losses. Due to the small reflection angles however, they are typically required to be large (centimeter - meter) which amplifies the requirement for precise surface control.

Diffractive optics are not limited by the critical angle of reflection as the angle a ray can be bent by diffraction depends on Bragg's law and thereby only on the highest spatial frequency in the optic. In Fresnel zone plates (FZPs), the most known type of diffractive optic, concentric rings of width decreasing with distance to the optical axis focus X-rays through constructive interference. The largest diffraction angle and therefore also the resolution depend on the ring of smallest width present in the structure. These optics found great success in the extreme ultraviolet (EUV) and soft X-ray regime, focusing beams to spot sizes down to 12 nm [20]. The achievable resolution of these optics is limited by e-beam lithography. Higher resolution requires finer structures which are challenging to produce with the needed precision. Additionally, they have to be extended along the beam direction in order to achieve high efficiency, which requires not only fine structures but large aspect ratios (the ratio between the optical thickness and width of a zone/layer). They are predominantly utilized in the soft X-ray regime since this requirement is less stringent at lower X-ray energies. By combining two interlaced FZPs, which enables effective zone doubling, focusing to around 8 nm was realized at a photon energy of 9 keV [21]. However, the fine zones are limited in their manufacture to small aspect ratios which limits the efficiency of the optic, in this case to < 1 % [21].

Multilayer Laue lenses (MLLs), also referred to as volume zone plates, have emerged over the past two decades as a promising new type of diffractive optic [22–29], which can in principle focus hard X-rays to a few nm and below [30–32] with high efficiency (> 60 %) [27, 28]. As the name suggests, they consist of many individual layers of at least two different materials, which are deposited individually with thicknesses following the zone plate law (see fig. 1.1), as to achieve constructive interference in a single point, the focus. This is typically done using magnetron sputtering [24, 33–35] or pulsed laser deposition [36]. In contrast to FZPs, the individual zones can have almost arbitrary aspect ratios and have to be tilted as to obey Bragg's law locally, which allows high diffraction (focusing) efficiency. As diffractive optics, they do not suffer from the small refractive index decrement δ of their material, which limits the focusing angle (and thus numerical aperture (NA)) of refractive and reflective optics.

If they have such superior focusing properties, why are they not used at a variety of nano-probe beamlines and routinely focus hard X-ray beams to 1 nm? Similar to

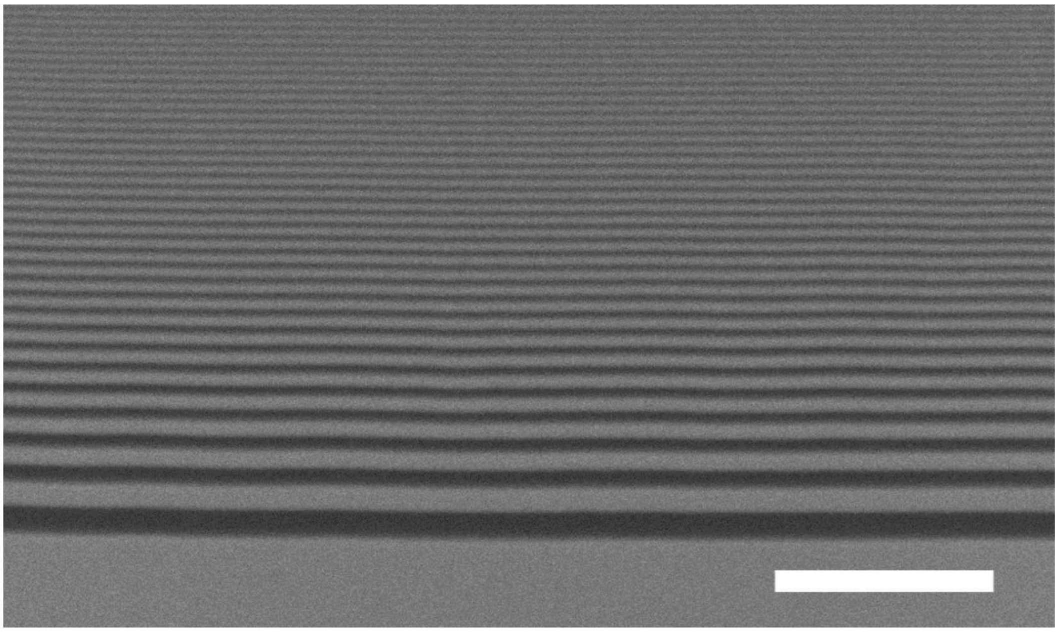

Fig. 1.1: Scanning electron microscopy (SEM) image of a multilayer Laue lens part showing layers of decreasing thickness from the optical axis (bottom) following the zone plate law. The scale bar is 1 μm. Reproduced by courtesy of M. Prasciolu.

other X-ray optics for nm focusing, their manufacture requires extreme precision and in the case of MLLs, control of the layer placements. A high NA MLL requires tens of thousands of layers. Since each layer is deposited individually, the manufacture is a lengthy process which can take up to a week. For an ideal lens, the required relative layer position precision is sub-Å [32], which becomes increasingly more difficult to achieve over long time periods using current manufacture techniques. Drifts of the sputter rates and instabilities cause layers to be misplaced with respect to the design, resulting in an aberration of the lens wavefront, degrading the resolution and peak intensity the lens can achieve (see fig. 1.2). Wavefront aberrations are present in other X-ray optics as well, induced by a misplaced zone in FZPs or a surface shape deviating from the design in refractive and reflective optics. It is therefore crucial to precisely determine the quality of X-ray optics by characterizing their wavefront (aberrations). This is no different for MLLs where the metrology of the lens wavefront and hence aberrations become a crucial part in MLL development, as the wavefront or phase of the lens, in combination of its scattering amplitude, fully determines the focusing performance of the lens.

While the wavefront of a beam, focused or not, cannot be measured directly like the intensity, there are many approaches to solve this so called "phase problem", including interferometric and non-interferometric methods [37–54]. In order to enable fast wavefront determination of MLLs, the phase retrieval method of choice should be compatible with laboratory-based X-ray sources. Since access to synchrotrons requires to apply for beamtime and is therefore sparse, rapid feedback and improvement to lens development benefit from an laboratory X-ray setup where

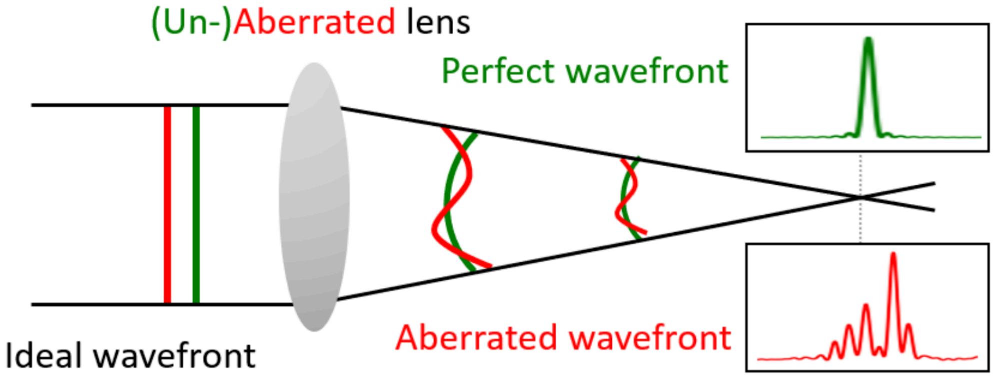

Fig. 1.2: Effect of an aberrated lens. The layer misplacements of the lens lead to an aberrated wavefront which results in sidelobes in the focal plane and a less intense focal point. Green shows an ideal lens and red an aberrated one. The inlets show the 1D point spread functions (PSFs) in the focal plane.

X-ray optics can be characterized. Commercially available X-ray sources provide sufficient flux for precise wavefront reconstruction on reasonable timescales but cannot offer comparable levels of coherence or monochromaticity as synchrotrons. Wavefront metrology with laboratory sources therefore requires methodology that can accurately retrieve wavefront aberrations under such circumstances. A phase gradient retrieval method with low requirements regarding coherence introduced in 2012, called X-ray speckle tracking (XST) [55, 56], traces the displacement of random features (referred to as "speckles") in samples to determine the local phase gradients of the illuminating beam [57]. Ptychographic X-ray speckle tracking (PXST) is a phase gradient retrieval method based on the speckle tracking approach [58–60]. It does not require coherence or high monochromaticity, making it an excellent candidate to be used in laboratory setups. A more robust version of the algorithm called robust ptychographic X-ray speckle tracking (R-PXST or RST for robust speckle tracking) was recently introduced, which utilizes machine learning for accurate reconstructions also in noisy environments. Laboratory lens characterization allows fast feedback for lens development but is only useful if the wavefront can be reconstructed with sufficient accuracy and precision.

This thesis aims at determining the optimum working conditions of high NA MLLs for highest resolution imaging. This includes the optimal lens properties as well as characterization and correction of wavefront aberrations utilizing a laboratory setup. Since MLLs are optically thick diffractive elements, their diffraction properties have to be described by the dynamical theory of diffraction (DTD) [61]. In order to determine the optimum working conditions for MLLs such as the thickness of highest efficiency, a simpler multilayer optic is studied first, a periodic multilayer grating. Gratings of various periods allow to precisely study the optimum thickness and diffraction efficiency over the range of periods present in MLLs. While the optimum thickness of MLLs can be calculated and the diffractive properties of sectioned multilayers in transmission (Laue) geometry were tested before [62], no extensive study on multilayers of varying periods (as are present in an MLL) has been performed. Imperfections in multilayer structures and their impact on the performance of multilayer optics are investigated in this thesis. The knowledge gained from multilayer gratings can then be used to manufacture lenses with optimum shape and thickness. To enable fast feedback on lens quality, a study is carried out which aims at determining the requirements for laboratory-based wavefront characterization of MLLs using the robust PXST approach. By characterizing the aberrations of the lenses shortly after their manufacturing, the gained knowledge can be incorporated into the fabrication of the subsequent multilayer deposition, greatly accelerating the improvement of lens fabrication. This allows to fully utilize sparse beamtime access for novel and improved imaging schemes by employing only the best and well pre-characterized lenses. Knowledge of lens aberrations is also necessary for the fabrication of refractive phase correctors. Such correctors aim to add a phase term to the wavefront of equal shape and amplitude but opposite sign of the lens aberration, as to cancel them out [63–69] (see fig. 1.3). For strongest focusing, lenses of high NA are required. This further increases the demands on their production and makes the lenses more susceptible to larger aberrations, which in turn are more difficult to compensate for. Since a (thin) phase corrector can only compensate a limited amount of wavefront aberrations, it cannot be employed to correct the aberrations of high NA MLLs. In this thesis, the fabrication of a compound corrector approach is explored, where many individual elements are positioned in a row to have their - individually small - contributions add up to a strong correction effect, similar to CRLs. Such a compound refractive corrector (CRC) was proposed [67] but not realized for 2D imaging. In this work, a CRC correcting an MLL lens pair is realized for the first time using state-of-the-art nano-scale 3D printing, which enabled record X-ray focusing below 3 nm [70]. Well characterized and aberration corrected high NA MLLs were then utilized at large scale facilities to enable and improve novel

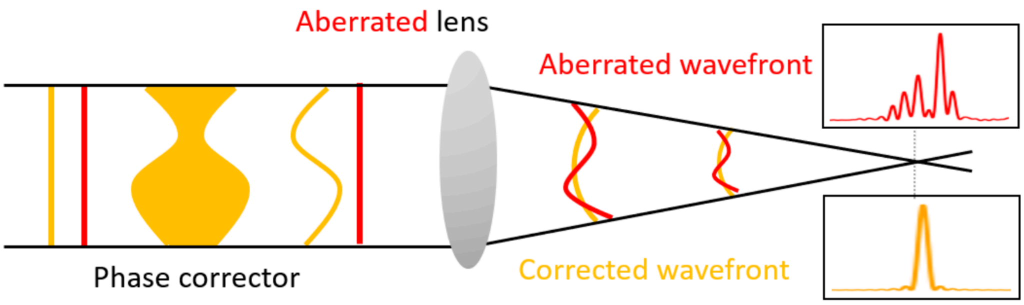

Fig. 1.3: Aberration correction. A phase corrector adds a phase term opposite of the lens aberration to the beam. The wavefronts of the corrector and lens add to zero, leading to an un-aberrated focus. Red shows the aberrated lens without corrector present and orange the case with corrector. The inlets show the 1D PSFs in the focal plane.

imaging methods such as projection holography, convergent beam crystallography and scanning Compton X-ray microscopy.

1.1 Structure of the thesis

The following chapter 2 introduces the fundamental topics required to understand the methods and results of this thesis. These include a short overview of wavefront metrology with focus on the method used here and a brief introduction to dynamical diffraction theory. It also presents the laboratory setup at which a majority of the work is conducted with descriptions on how measurements are carried out.
Chapter 3 follows up on the dynamical diffraction of multilayers and presents the characterization and exploration of multilayer based gratings. They are fabricated by equal means to MLLs but exhibit an easier structure, which provides a great test-bed for the determination of their diffraction properties.
In chapter 4, a thorough study on requirements for quantitative lens characterization using a laboratory source is presented. The goal is to understand the necessary and sufficient criteria that allow fast feedback on lens quality without compromising accuracy. Wavefront metrology methods introduced in chapter 2 are utilized in combination with the laboratory setup.
Once the lenses are well characterized, aberration correctors can be designed and fabricated, which is the topic of chapter 5. Compound refractive correctors are prepared using high precision 3D printing. This method allows fast and precise fabrication, is inexpensive and tunable to a large range of desired parameters.
Chapter 6 focuses on the applications of high NA, well characterized and corrected MLLs. The high NA leads to small focusing spots which increase the resolution of scanning imaging techniques. Additionally, the beam produced by high NA MLLs is highly convergent. This allows the exploration of novel imaging techniques which utilize the large range of angles present or require high magnifications.
The thesis concludes with chapter 7 where a brief summary of the achieved results with respect to the scientific field is given and an outlook on future work which can be build upon the knowledge gained in this thesis is drawn.

2

Fundamentals

This chapter gives an overview of the topics required to follow the content of the thesis. It introduces the concepts and methods which this work builds upon without deriving basic equations which can be found in literature. This includes a brief discussion on dynamical diffraction theory, which describes multiple scattering inside thick diffractive elements, followed by a description of MLLs. After the means to design and the fabrication of MLLs are introduced, attention is given to wavefront metrology with the focus on the speckle tracking based methods used in this work. Since a majority of this work was carried out by use of a laboratory setup, this setup is described with examples on how typical measurements are conducted.

2.1 Dynamical theory of diffraction

When a plane wave diffracts off a slit, for example, a single diffraction event occurs. The so-called kinematic theory of diffraction then predicts the position of the Bragg peaks of said diffraction event. When a periodic structure like a crystal or multilayer is intersected by an X-ray beam at Bragg angle, diffraction can occur at each plane. Described by kinematic diffraction theory, the reflected beam from such a multilayer is the sum of all beams reflected from different planes. An example can be seen in figure 2.1 (a). Multiple scattering effects which can occur are neglected here.

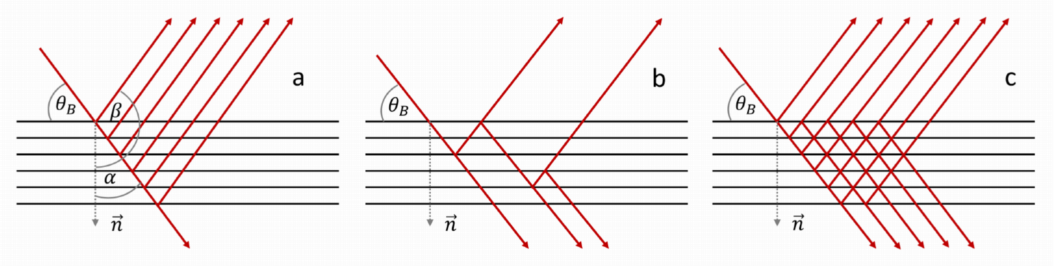

Fig. 2.1: Reflections inside a multilayer in Bragg geometry. Kinematic description of scattering inside a multilayer (a). The reflected beam is the sum of the reflection from each layer. An example of multiple scattering that can occur (b). Dynamical description of a reflection from a multilayer (c). The refracted and reflected beams are the sums of all possible path resulting from multiple scattering events.

An X-ray beam obeying Bragg's law reflected from a layer inside the material also obeys Bragg's law after being reflected and intersecting with another layer. It can therefore be reflected again. An example of such a multiscattered beam can be seen

in figure 2.1 (b). Both, the refracted and reflected beams are therefore the sums of all beams that exit the periodic structure on their respective side. The dynamical theory of diffraction takes such effects into consideration and also accounts for refraction inside the material. This leads to the case shown in figure 2.1 (c), where the transmitted and reflected beams are the sum of all scattered beams. The depth until which scattered beams meaningfully contribute to either beam is called the extinction length, beyond which the contribution from additional scattered signals becomes negligible, as photons are largely absorbed.
Bragg and Laue geometries can be distinguished by the asymmetry parameter b, equal to [71]

$$b = \frac{\cos\alpha}{\cos\beta}, \tag{2.1}$$

where α and β are the angles between the surface normal $\vec{n}$ and the incident and reflected beams, respectively. In Bragg geometry, $b < 0$ while $b > 0$ indicates Laue geometry. Values of $b = -1$ and $b = 1$ correspond to symmetric Bragg- and symmetric Laue geometry, respectively. For a structure in Bragg geometry, that is, the reflected beam leaving the structure on the same side it entered, there exists a range of angles within which total reflection occurs for a non-absorbing structure. This is due to the dispersion relation in the material leading to a gap in the electronic band structure within which no traveling waves are allowed. This leads to a plateau around the Bragg angle, the so-called Darwin plateau, whose width depends on the crystal properties. In Laue geometry, that is, the reflected beam leaving the structure on the opposite side from where it entered, intensity is initially transported from the incident beam to the diffracted beam. Since the diffracted beam is in diffraction condition, intensity is then shuffled back into the initial direction. This oscillatory behavior is called *Pendellösung* and the period of one oscillation is given as the *Pendellösung* period Λ_s [71]

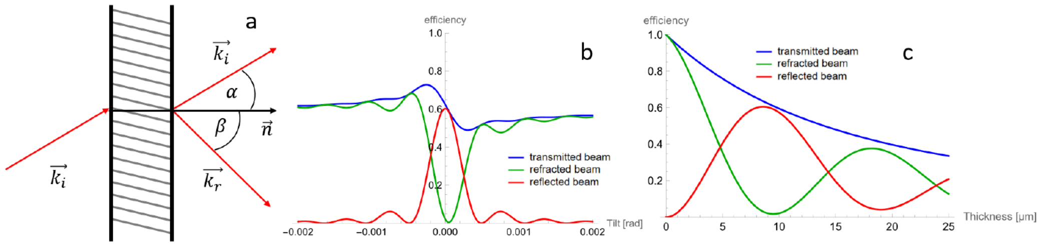

Fig. 2.2: A multilayer in Laue geometry (a). Diffraction efficiency of a periodic multilayer in Laue geometry based on tilt angle around the Bragg condition (b). The reflected beam is $\vec{k}_r$ and the refracted beam $\vec{k}_i$. The total transmitted beam is their sum. Diffraction efficiency in Laue geometry based on the optical thickness at the Bragg angle (c). The *Pendellösung* effect can be seen.

$$\Lambda_s = \frac{\lambda|\gamma_m|}{\delta_s \sin 2\theta_B} \tag{2.2}$$

Here, λ is the wavelength and θ_B is the Bragg angle. γ_m is the direction cosine of the reflected beam equal to $\cos\beta$. $\Re(2\delta_s)$ is equal to the Darwin width and δ_s can be expressed as

$$\delta_s = \frac{C\sqrt{\chi_m \chi_{\overline{m}}}}{\sqrt{|b|}\sin 2\theta_B}, \tag{2.3}$$

with the polarization factor C and the susceptibility modulation $\sqrt{\chi_m \chi_{\overline{m}}}$. Further details can be found in [71]. Due to absorption, the oscillation of the *Pendellösung* is damped (see fig. 2.2 (c)). Maximum diffraction efficiency in Laue geometry is therefore achieved with a structure of thickness equal to half the *Pendellösung* period Λ_s. This optimum thickness τ_{opt}, equal to half the *Pendellösung* period Λ_s, is then given by [72]

$$\tau_{opt} = \frac{\pi\lambda\cos(\theta_B)}{4\Delta n \sin \pi\Gamma}, \tag{2.4}$$

where Δn is the difference in refractive index decrement of the two materials and Γ is the ratio of the layer thickness of the material of higher atomic number Z to the bilayer thickness [72]. For multilayers with Γ equal- or close to 0.5, equation 2.4 simplifies to [73]

$$\tau_{opt} = \frac{\pi\lambda\cos(\theta_B)}{4\Delta n}. \tag{2.5}$$

If θ_B is small, equation 2.5 can be further simplified to

$$\tau_{opt} \approx \frac{\pi\lambda}{4\Delta n}. \tag{2.6}$$

For a more in depth description, the reader is referred to [71, 73, 74]. Close to the Bragg angle, anomalous transmission takes place, i.e. the total transmission is higher (or lower) than far from Bragg angle (see fig. 2.2 (b)). The reason for that is a standing wave, which is present due to the two wavefields inside the material. If the anti-nodes of the standing wave overlap with the positions of the absorbing atoms, absorption is increased. If they are in between atomic planes, absorption is reduced. Each case is present once, on either side of the Bragg angle, leading to an asymmetric signal. Both, multilayer gratings and lenses that are subject of this work are operated in Laue geometry.

2.2 Multislice simulations

In order to simulate the diffractive behavior of arbitrary nano-focusing X-ray optics, numerical simulations can be conducted. The approach of using multislice scalar wave propagation allows to simulate the propagation of a complex wavefield through any structure of complex X-ray refractive index. This method is well suited for the calculation of the performance of periodic multilayer structures and MLLs. Imperfections and defects are straight forward to simulate without the need for a sophisticated analytical description. The principle behind this method is quite simple and its description here follows Li et al. [75]. An object is discretized into voxels along each direction. At each position (x, y, z), it is described by its complex refractive index

$$n(x, y, z) = 1 - \delta(x, y, z) - i\beta(x, y, z). \tag{2.7}$$

An incoming wavefront $\Phi_j(x, y)$ interacting with a single slice of the object of optical thickness Δz is then modulated by the optical response of the slice, resulting in a modified wave $\Phi'_j(x, y)$ given as

$$\Phi'_j(x, y) = \Phi_j(x, y)\exp\left[i\frac{2\pi\Delta z}{\lambda}(\delta(x, y, z_j) + i\beta(x, y, z_j))\right]. \tag{2.8}$$

Here, z_j represents the j^{th} slice of the object. The resulting wave $\Phi'_j(x, y)$ is then propagated a distance Δz to the next slice of the object using free space propagation. The resulting wave $\Phi_{j+1}(x, y)$ at the next slice a distance Δz from $\Phi_j(x, y)$ is then given by

$$\Phi_{j+1}(x, y) = \mathcal{F}^{-1}\left[\mathcal{F}[\Phi'_j(x, y)] \cdot \exp\left(-i\frac{2\pi\Delta z}{\lambda}\sqrt{1 - \lambda^2(u_x^2 + u_y^2)}\right)\right]. \tag{2.9}$$

Here, $\mathcal{F}$ represents the Fourier transform and $\mathcal{F}^{-1}$ its inverse while u_x and u_y are the spatial frequencies. This wave can then interact with the $(j + 1)^{th}$ slice of the object and afterwards be propagated to the $(j + 2)^{th}$ slice which continuous throughout the whole object. Note here that vacuum can also be treated as an object and the propagation through it can be conducted in the same way. If, however, the propagation step along z exceeds $N_t(\Delta x)^2/\lambda$ with N_t being the number of transverse pixels and Δx their size, a different propagation approach has to be adopted [75]. For all simulations shown in this work, the propagation step along z was chosen as to stay below this limit. Since multilayer gratings and MLLs change in structure only along one of the two transverse direction x and y, they can be simulated in 2D, instead of 3D. This can speed up the simulations and allows larger structures to be probed, as much fewer voxels have to be considered.

An advantage of the multislice method is that any arbitrary structure can be simulated, by simply describing it in terms of $\delta(x, y, z)$ and $\beta(x, y, z)$. This allows to explore structural changes such as a slight change of period in a multilayer grating throughout its height. Additionally, many structures (or free spaces) can be simulated in series by choosing the exit wave of the last slice of one object as the incident wave on the first slice of the next one.

2.3 Multilayer Laue lenses

Before describing multilayer Laue lenses in more detail, it is advisory to discuss FZPs, as MLLs can be seen as volume zone plates which solve some of the difficulties that FZPs face. FZPs are diffractive optics consisting of concentric rings with width decreasing with distance from the optical axis [76]. For constructive interference in a single point, the optical path difference between adjacent zones (with each zone being one structure and a gap) has to be one wavelength. This is readily satisfied if the positions of the rings x_n follow

$$x_n^2 = n\lambda f + n^2\lambda^2/4, \tag{2.10}$$

the zone plate law [77], where f is the focal length. If the focal length is much bigger than the size of the lens, equation 2.10 can be approximated as

$$x_n^2 \approx n\lambda f. \tag{2.11}$$

This causes the periods $d(r)$ to reduce approximately inversely with the distance to the optical axis

$$d(r) = \frac{\lambda}{2d\sin(\theta(r))} \approx \frac{\lambda f}{r}. \tag{2.12}$$

An example of a zone plate schematic is given in figure 2.3 (a). Such FZPs have found great success in high-resolution imaging in the soft X-ray regime [78, 79]. While FZPs have found their way into the hard X-ray regime [80, 81], there are still two aspects that limit what can be achieved with this optic. The first is the thinnest structure that can be fabricated, which limits the maximum diffraction angle and hence NA and thereby sets the resolution limit. In fact, the resolution D is directly proportional to the smallest (outermost) zone $\Delta x_{min} = x_N - x_{N-1}$ that can be fabricated as $D \approx 1.22\Delta x_{min}$ [82]. Nanometer resolution hence requires nanometer structures, which are difficult to fabricate with conventional techniques such as electron beam lithography [83] and ion beam lithography [84]. The second limiting factor is the achievable optical thickness, which limits the efficiency. Highly efficient diffractive elements require optically thick structures as given by τ_{opt} described in the previous section, which is typically in the micron range [26]. Thin structures and large optical depth both increase the required aspect ratio of the zones. While techniques like zone doubling [85–87] or interlacing [88] can be employed to improve on creating higher aspect ratios and thinner periods, the aspect ratio still stays limited. While some groups have achieved aspect ratios of 66:1 [89], highest diffraction efficiency still requires aspect ratios of 1000:1 and comparable, which is not feasible. This causes the diffraction efficiency to be limited to a maximum of a few percent [88, 90, 91].

MLLs can solve both of these limitations, offering nanometer structures with almost

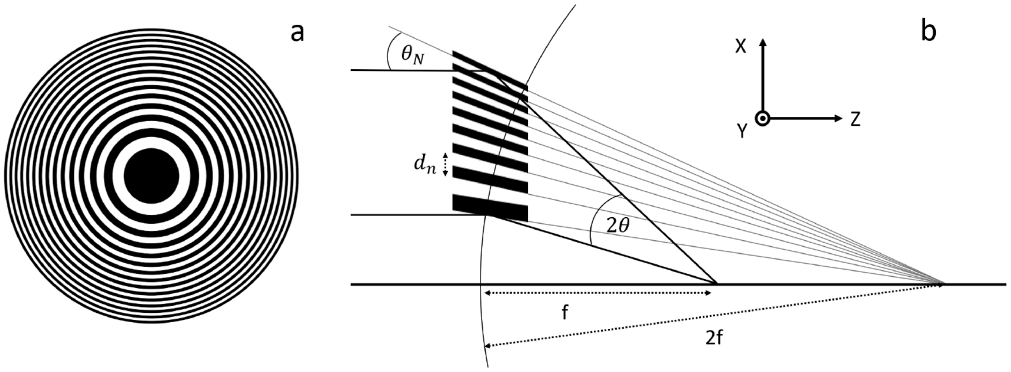

Fig. 2.3: Schematic of a Fresnel zone plate (a). Concentric rings of decreasing thickness from the optical axis following the zone plate law lead to constructive interference in the focus. Schematic of the principle of a wedged MLL (b). The layer period reduces with distance from the optical axis following the zone plate law. For high efficiency over the full range of diffracting angles 2θ, the layer tilts have to lay normal to a circle of radius 2f with origin on the optical axis, where f is the focal length.

arbitrary aspect ratios. They consist of many individual layers of at least two different materials, which are individually deposited onto a substrate. Every other zone is made from a dense, absorbing material with spacing layers in between of less dense material. By depositing nm sized layers onto a substrate, they can reach large aspect ratios, routinely exceeding 1000:1 [34]. After the multilayer stack has been deposited, it can be cut to the desired optical thickness. In contrast to FZP, stability in large aspect ratio structures is given due to the spacing layer. Such a multilayer lens can be understood as a volume zone plate. To fabricate a circular volume zone plate,

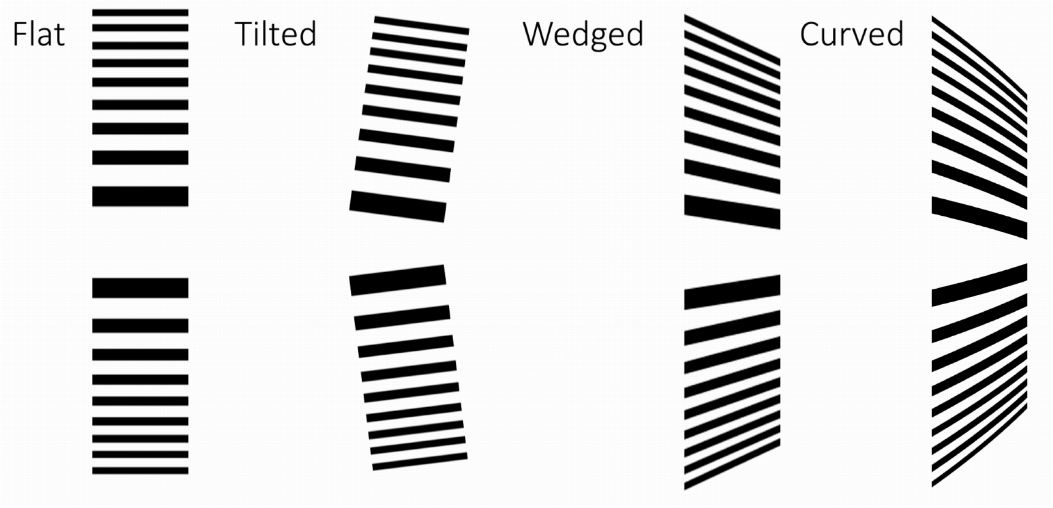

Fig. 2.4: Types of MLLs. Flat, tilted, wedged, curved. The optical axis is in the center between the thickest layers. Typically, only the part on one side of the optical axis is fabricated and does not extend all the way to the optical axis. This results in an off-axis geometry as shown in figure 2.3 (b) and does not require the deposition of very thick layers.

layers have to be deposited onto a round wire. Since layer precision requirements are so stringent, ultra-round wires with extreme surface smoothness are required. It is therefore much more convenient to deposit layers onto a flat surface, as smooth substrates with low surface roughness (< 0.2 nm) are readily available. A layer deposited onto a flat substrate additionally has a more homogeneous thickness than one deposited onto a wire, though both methods require extreme deposition control. Deposition onto a flat substrate results in a lens with layer thicknesses changing only along one direction and the lens therefore focuses only in one dimension. Two crossed lenses are then required for 2D focusing. Depositing layers onto a flat substrate has another advantage. Since the resolution D is proportional to the thinnest layers Δx_{min} present in the structure and their efficiency depends on the layer quality, they should be fabricated with the highest degree of control, regarding roughness and position. During the course of the deposition, the layer roughness on the surface increases. Only the first layers experience the low surface roughness of the substrate while the last deposited layers exhibit increased roughness due to the buildup of roughness throughout the deposition. In a volume zone plate deposited onto a wire, the layer thickness has to decrease with distance from the wire. The thick, less sensitive layers hence experience low roughness while the more sensitive thin layers experience a higher degree of roughness. In a 1D lens, it is possible to start the deposition from the thin layers and build the multilayer up towards the optical axis, allowing the thinnest layers to be fabricated with the lowest roughness, potentially increasing their quality and efficiency.

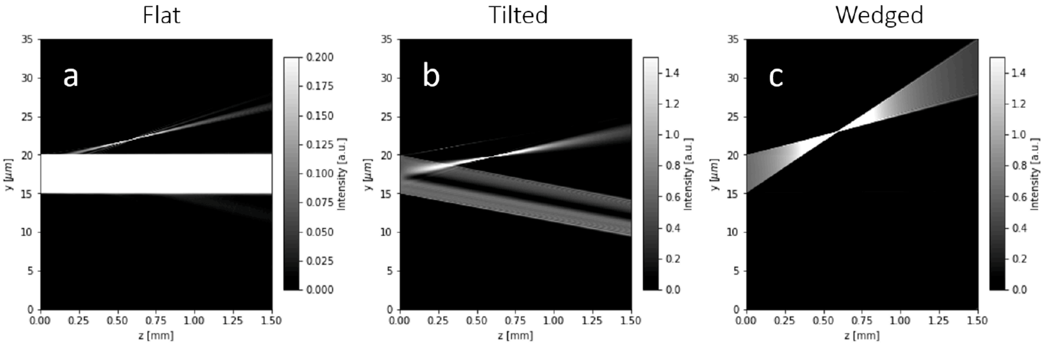

Fig. 2.5: Multislice simulations for different types of MLLs. A flat lens shows low diffraction efficiency where only the layers closest to the optical axis contribute to the focused beam (a). A tilted lens shows high efficiency for the range of layers within the Darwin width where the refracted beam is strongly suppressed (b). Outside of the central region, layers do not contribute significantly to the focused beam. In a wedged lens, all layers obey Bragg's law and therefore have high diffraction efficiency (c). The simulation were done following [75] as described in chapter 2.2.

Such a volume zone plate, may it be deposited onto a wire or flat surface (off-axis or not) has all its layers parallel to the optical axis. This is referred to as a "flat" MLL, as can be seen in figure 2.4. The diffraction efficiency is high for layers close to the optical axis and decreases with distance from the optical axis, as can be seen in figure 2.5 (a). This limits the effective NA, such that higher multilayer stacks do not increase the resolution as the outermost layers do not contribute to the focusing. The efficiency and usable NA can be enhanced by tilting the lens (or lens half) such that part of the layers are at the Bragg condition. Such a "tilted" MLL has high efficiency in the middle between the inner- and outermost layers with decreasing efficiency in either direction (see fig. 2.5 (b)). Tilted MLLs have shown success in focusing hard X-ray to spot sizes below 50 nm [23, 92]. However, they are still limited in their NA by the acceptance width of the Bragg condition given by the Darwin width [29]. Increasing the physical aperture of the lens beyond the range within which rays are reflected from the layers within the Darwin width does again not increase the focusing performance of the lens [93]. To achieve high diffraction efficiency over the full aperture of the lens, all layers have to be tilted to obey Bragg's law. This requires them to follow a modified zone plate formula, where the positions and thicknesses vary with the depth z in the lens, which changes equation 2.10 to

$$x_n^2 = n\lambda(f - z) + n^2\lambda^2/4. \tag{2.13}$$

Layers that follow this formula are curved, as can be seen in figure 2.4. For NAs below 0.1, where $f >> z$, equation 2.13 can be approximated as

$$x_n^2 = \left(n\lambda f + \frac{n^2\lambda^2}{4}\right) a(z)^2,\ a(z) = 1 - \frac{z}{2f}, \tag{2.14}$$

resulting in straight layers along beam propagation direction with tilt angle increasing with distance from the optical axis. A lens obeying this formula is referred to as a "wedged" MLL (see fig. 2.4) and shows high efficiency over the full range of diffraction angles, as can be seen in figure 2.5 (c). The working principle of a wedged (off-axis) MLL is shown in detail in figure 2.3 (b). All layers satisfy Bragg's law locally, resulting in high diffraction efficiency along the full multilayer height. This condition is satisfied if the layer tilts θ_n change as

$$\theta_n = \tan^{-1}\left(\frac{x_n}{2f}\right) \approx \frac{x_n}{2f}. \tag{2.15}$$

This is equivalent to all layers being normal to a circle of radius $2f$ centered on the optical axis a distance of $2f$ from the lens. Wedged MLLs have been fabricated [33, 35, 94, 95] with large apertures [96] and high efficiency [29, 97]. They can be fabricated by using a mask during deposition [30, 33, 35, 94] or by adding a stress layer to a flat lens [95]. In addition, there have been attempts to approximate a wedged MLL with a structure not exactly following eq. 2.14 by either stacking multiple flat MLLs with relative tilts between flat segments [98] or by assuming a linear gradient of layer tilts [99]. However, these designs have only been discussed theoretically. While the structure in such designs is simplified from an ideal wedged lens, they do not appear simpler to fabricate than an actual wedged MLL, since the latter can be fabricated simply by employing a straight edge mask as will be discussed in the next section [33, 35].

2.3.1 Fabrication of wedged MLLs

The lenses that are subject of this work are wedged MLLs which are all fabricated with our in-house deposition system. It is a magnetron sputter deposition system which can mount up to four targets at the same time. Typically, only two are used for the fabrication of an MLL. The lenses in this work are made from WC/SiC or Mo_2C/SiC bi-layers with 1000s to 10000s of layers. At an earlier stage, lenses were also made from W/SiC but it turned out that a phase transition from amorphous to crystalline happens in W layers at a thickness of around 3 nm [27], which is not the case for WC in the range of periods typically used in our designs. They are fabricated by having a substrate alternatingly move inside the plasmas of the two sputter targets. The thickness of the layers depends on the time the substrate spends inside the plasma of each target. The deposition usually starts from the thinnest layers and builds up towards the optical axis but does not extend all the way to the optical axis, as to create an off-axis lens. This eases the separation of the focused and unfocused beams. To achieve a wedging of the structure, a straight edge mask is placed between the sputter target and the substrate which moves with the substrate (see fig. 2.6). This creates a penumbra region below the mask, resulting in a gradient in the multilayer height along the substrate [33]. This gradient leads to the desired wedging of the layers. By varying the height of the mask, the width of the penumbra can be modified which changes the steepness of the layers [35]. This

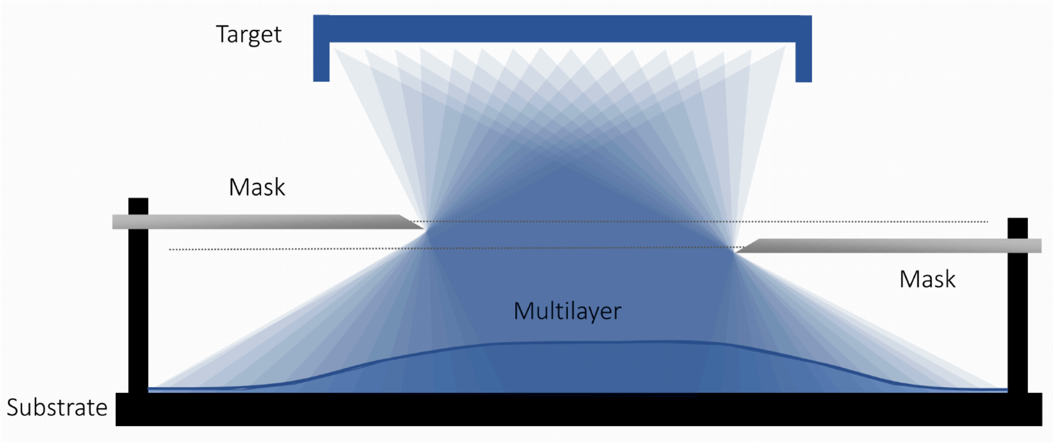

Fig. 2.6: Masked deposition of a multilayer. To fabricate MLLs with wedged layers, a straight edge mask is placed above the substrate which moves together with it. The resulting penumbra region leads to a gradient from which wedged lenses can be cut. The position along this gradient determines the focal length and optimum energy of the lens. Placing two masks at opposite ends allows to cut two lenses for the same energy and with the same NA but with different focal length to form a pair.

can be used to fabricate a lens with a desired focal length which is optimized for a chosen wavelength.

After a multilayer has been deposited, a lens can be sliced from it. The slice has to be cut such, that the design optical thickness is along the direction of the thickness gradient of the multilayer, resulting in the height of the lens being constant along its width. This is done using a dual beam focused ion beam (FIB), which allows imaging of the cut in parallel using an SEM. We recently upgraded from a Ga FIB to a Xe+ Plasma FIB (PFIB), which allows cutting a structure up to 40 times faster. Additionally, the heavier Xe ions cause less damage to the surface of the sample and the implantation of them into the sample is negligible compared to a Ga FIB. The position of the cut along the height profile of the multilayer determines the working energy of the lens. The lens is then placed on a 100 μm thick silicon chip glued to a metallic L-shaped holder. This allows the easy exchange of lenses and enables two lenses to be placed close to each other. Figure 2.7 shows an example of an MLL on a silicon chip. Since wedged MLLs require each layer to be tilted to its Bragg angle, ideal wedging along the full height can only be achieved for a single wavelength. A slight mismatch in energy can be tolerated, as long as the required tilts along all layers lay inside the Darwin width. The larger the NA, the smaller the energy acceptance range. How the optimal working energy of a lens can be determined will be described later in the laboratory setup section 2.5.1.

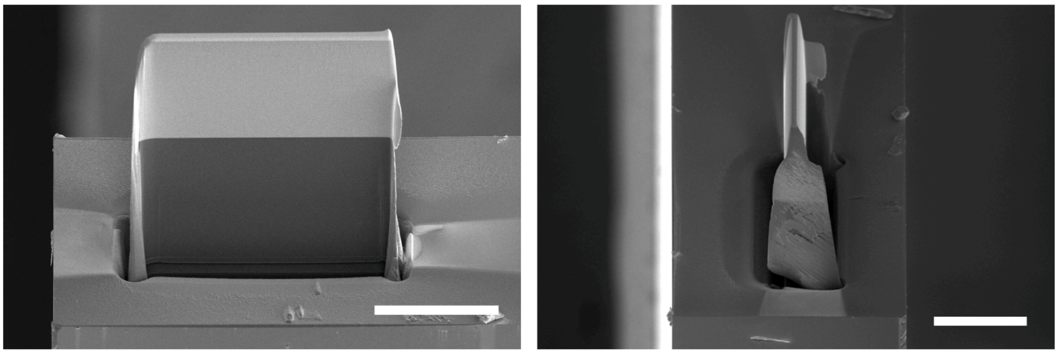

Fig. 2.7: SEM images showing the front (left) and side (right) view of an MLL placed on a 100 μm thick silicon chip. The light gray area at the top is the multilayer and the dark gray part below the substrate. The scale bars are 50 μm. Reproduced by courtesy of M. Prasciolu.

MLLs fabricated by layer deposition onto a flat substrate focus only in one dimension. For 2D focusing, two lenses have to be aligned orthogonal such that one lens focuses along the vertical- and one along the horizontal direction. Since they are supposed to focus to the same plane, that have to have different focal length. A change of focal length requires a lens to be cut from a different position along the gradient, which also changes the optimum working energy. However, a minimum working energy exists at the steepest point along the profile. Therefore, two lenses, optimized for the same energy but with different focal length can be cut from the same penumbra region. Their physical height and NAs, however, are different. To fabricate a matching lens to form a pair with similar NA and optimum energy but different focal length, two masks with different distances to the substrate can be placed at both ends of the substrate. A pair can then be formed by using a lens from either side.

The quality of the lens depends on how closely the layer placements follow the zone plate law, as well as how well defined each layer is. For the layer placement, four different types of errors and their impact were investigated [100]. A single layer of incorrect thickness as could be produced by a single sudden malfunction of the deposition system (for example due to a power glitch) leads to a local fringy intensity change in the whitefield far downstream of the focus but does not change the shape of the beam in the focal plane and its intensity much. Such an error can be tolerated. If a random change of layer thickness is present for all layers (following a Gaussian distribution), individual layers can be misplaced by much larger distances. This leads to a reduction of peak intensity in the focal plane and strong side lobes. In this case, the whitefield becomes very noisy. The third type of error is a systematic error of layer thicknesses. This leads to a build-up of the misplacement of layers which causes large wavefront aberrations and leads to weak foci with many side lobes. Interestingly, this error causes almost no changes in the whitefield, it hence requires wavefront reconstruction to be detected. This type of error causes the largest loss in lens performance and is hence the most crucial to avoid. Unfortunately, the lens is also quite sensitive to this error, requiring a relative layer position precision of 10^{-4} [32]. The fourth error type is a change of layer thickness along the beam propagation direction. This causes a loss of peak intensity in the focal plane and an inhomogeneous illumination of the whitefield but does not change the overall shape of the beam in the focal plane. Similar finding were reported by other groups as well [101, 102].

Systematic errors in the layer thickness were also found to lead to the most severe aberrations in our experience. Such can arise from a change in deposited layer thickness due to a change in sputter rate. As the sputter target is consumed over the course of a multilayer deposition, the sputter rate changes systematically. If left uncorrected, this leads to a systematic change of deposited layer thickness which causes the most severe aberrations in the lens, coma in the case of a linear change. To counteract this effect, the change of sputter rate can be calibrated. By measuring the systematic layer misplacements from a multilayer deposition by measuring the wavefront of a lens cut from it, the predicted change of sputter rate can be build into the next deposition to reduce errors caused by this drift. Such a prediction can never perfectly counteract the actual change but can still lead to a significant reduction of wavefront aberrations. It was found that such a drift in sputter rate was the main cause of wavefront aberrations in our lenses [67]. For the improvement of lens development, it is therefore crucial to characterize said aberrations in a timely manner, such that the estimate of the sputter rate drift can be updated for subsequent depositions. This requires two things, a readily available setup (such as a laboratory X-ray setup) and a methodology and software to quantitatively measure and calculate the aberrations. These are the subjects of the next few sections of this chapter.

2.4 Wavefront metrology

In the previous section it was noted that MLLs are limited in their fabrication process, where a change of sputter rate leads to misplaced layers, even in specialized deposition systems with excellent software control. Such misplacements manifest as an aberration in the wavefront arising from a mismatch in optical path difference between zones and thus, a phase error which broadens the focus and induces strong side maxima. This worsens the resolution and imaging performance of the lens. For lens development, it is therefore crucial to characterize these misplacements and correct for them. Layer misplacements caused by layers of incorrect thickness manifest as a change in phase gradient [29], therefore retrieving the phase gradient and thereby phase allows to quantitatively characterize the layer misplacements. The wavefront or phase aberrations here are the difference between the retrieved wavefront and an ideal aberration free spherical reference. Since the complex wavefield in the lens plane is sufficient to determine the beam propagation and shape in the focal plane and beyond, the focusing performance of a lens can be calculated from its wavefront and intensity distribution, the latter being called the whitefield. This includes the size of the point spread function (PSF) in the focal plane and the Strehl ratio, which is a measure of the peak intensity of a point source [103, 104], more about that later. The knowledge about the wavefront of a lens also allows to adjust the deposition recipe for subsequent multilayers and the fabrication of refractive phase correctors, which will be discussed in detail in chapter 5. In this section, the phase retrieval method used for the majority of the work presented will be introduced. To allow fast feedback for lens development, the method has to be compatible with laboratory setups. The laboratory setup used in combination with the phase retrieval method will be introduced afterwards.

2.4.1 From Hartmann mask to speckle tracking

An optical wave E is a complex valued function, with an amplitude A and phase ϕ, where $E = Ae^{i\phi}$. A detector measures the intensity which is the absolute square of the wave, $I = |E|^2 = A^2$. It thereby retrieves only the amplitude information, while the phase information is lost. This is known as the "phase-problem" [105–108]. In order to retrieve the phase information, the phase has to be converted into a measurable signal or be detected through the effect it has on the wave propagation. Using interferometers, two (or more) beams are overlapped as to interfere, resulting in a modulation of the amplitude based on the phase difference between the two beams [109]. A different approach is the use of a Hartmann sensor. Since the phase gradient determines the propagation direction of the wavefront at each point, measuring this propagation direction of the wavefront allows the reconstruction of the phase gradient and thereby phase. To determine the propagation direction of the wave, a Hartmann mask can be employed. A Hartmann mask consists of an array of holes (or lenses/lenslets, which is then referred to as a Shack-Hartmann sensor) of well-known positions and sizes, which probes the local propagation direction at many points of a wavefront [110, 111]. To characterize the wavefront, the Hartmann mask is placed in the beam and its transmission pattern is recorded on a screen downstream. In case of a perfect flat wavefront, the screen will show an image of the mask with spots which are at the same (usually equidistant) positions with respect to each other (see fig. 2.8 (a) and (b)). For an aberrated wavefront however, the positions (or even shapes, in extreme cases) of the transmitted beams will vary from the positions of the holes. The direction and strength of this shift can be determined by comparison with a reference. Such a reference could either be the mask itself, the pattern obtained from an un-aberrated beam or the same pattern recorded at a different distance between the mask and screen. The propagation direction, proportional to the phase gradient, can then be reconstructed from the geometry and the shift. By reconstructing the phase gradient, the phase can be retrieved in an integration step. This method is straightforward, but limited by the density of the pattern, which limits at how many points the wavefront can be probed. High sensitivity requires a dense pattern of many holes or lenses. However, if the phase gradient is large, it is no longer unambiguous which spot on the screen belongs

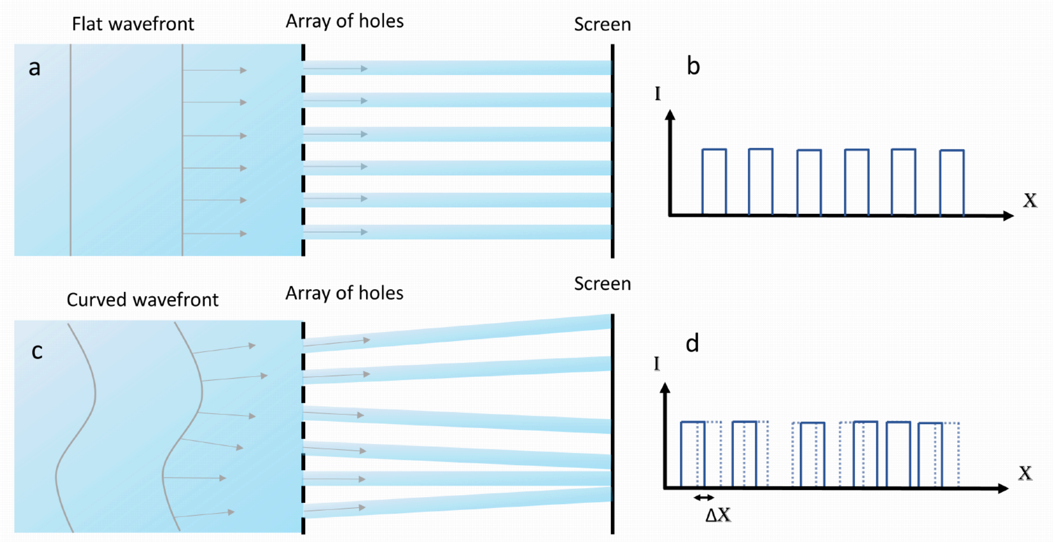

Fig. 2.8: Principle of a Hartmann mask. A regular hole array (mask) is placed between the incoming wave and a detector (a),(c). The corresponding intensity distribution on the screen is shown in (b),(d), respectively. In the case of a flat wavefront ((a),(b)), the illuminated spots have the same position and relative distances as in the mask. An aberrated wavefront ((c),(d)) leads to shifts which are proportional to the local propagation direction and hence the phase gradient and thereby phase.

to which point in the pattern, that is, the shift of a beam might be larger than the distance between holes or lenses. This limits the mask density and thereby sensitivity. In case of a focused (defocused) beam as produced by a lens, the pattern on the screen will be magnified.

Since Hartmann masks are limited in resolution, a more general phase retrieval method is needed for highest precision lens characterization. Morgan et al. developed an iterative phase retrieval method based on a generalized Hartmann sensor, which combines the means of speckle tracking and ptychography called Ptychographic X-ray speckle tracking (PXST) [58–60]. It's a phase gradient retrieval approach where features of a speckly sample (with sufficient features) are traced along the aperture of the lens by obtaining images of the sample while it is moved through the beam in steps smaller than the field of view. The relative shift of all sample features with respect to their position along the lens pupil provides insights about the local phase gradient. This is sketched in figure 2.9. In the case of an ideal wavefront, the shift of sample features is equal everywhere and equal to the shift of the sample. In case of a divergent beam, the features are shifted by the magnified sample shift $\Delta X = M\Delta Y$, where M is the magnification. In the case of a non-ideal wavefront, the shift depends on the position along the lens aperture. To probe the local shifts, a sample is moved along the lens aperture with steps smaller than the field of view while (magnified) projection holograms are recorded on a detector. These images are overlaid based on the magnified shift between images to form an

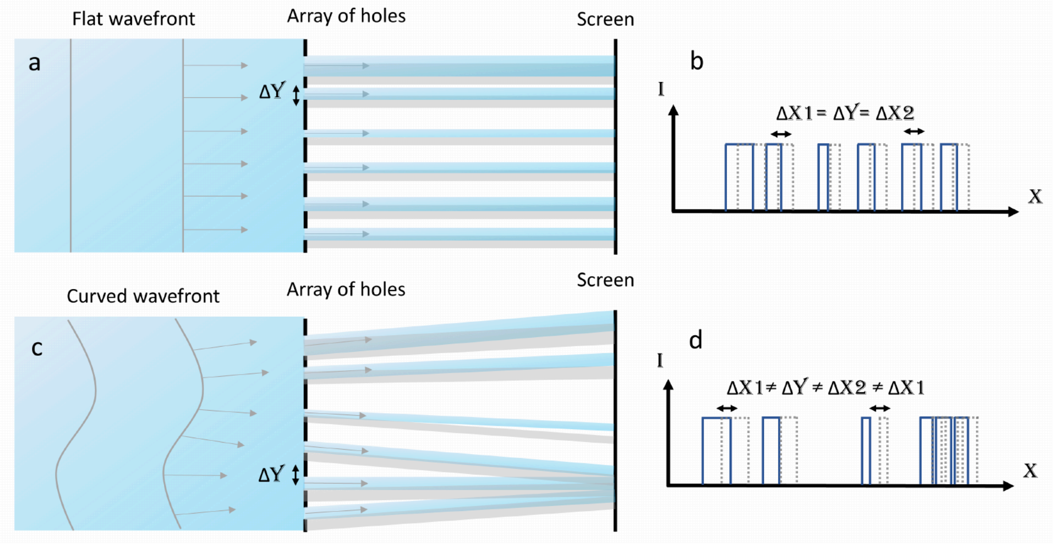

Fig. 2.9: Principle of PXST. An arbitrary sample (here an aperiodic array of holes) is moved transverse to the beam direction in steps smaller than the field of view ((a),(c)). The corresponding intensity distribution on the screen is shown in (b),(d), respectively. In the case of an ideal wavefront ((a),(b)), the shift of each feature is identical and equal to the step size of the sample (or magnified step size in case of a divergent beam). In the case of an aberrated wavefront ((c),(d)), the shift of each feature is different as it is probing a different part of the wavefronts local phase gradient.

initial reference image of the sample. In the presence of aberrations, this image will be blurred but the aberrations cancel each other out. Each individual image is then compared to this reference image. The required shift of sample features at each position along the lens aperture to match the reference image forms a displacement map, which is proportional to the phase gradient. Based on this displacement map, each image is corrected and overlaid again, to form an improved estimate of the reference image. This reference image is then again compared to each individual frame. This iterative procedure of updating the best estimate reference image and the displacement map continues until convergence. This is usually achieved after a few ($\sim 10s$ of) iterations which takes seconds in 1D and minutes in 2D. After convergence, an aberration free reference image of the sample is obtained, as it would be recorded with an aberration free beam. To increase the contrast, individual frames can be normalized by the whitefield, which is the intensity distribution without a sample present. Instead of capturing such an empty frame, the whitefield can be approximated by summing up all recorded frames. The sample features approximately cancel each other out in this case. Since the displacement map is proportional to the phase gradient of the lens along its aperture, the phase can be retrieved by a simple integration step. The main loop is shown in figure 2.10. It should be noted here that the reference image that each frame is compared to is reconstructed from the overlapped images and is not required to be prior known nor are exposures at different detector distances required. In contrast to a Hartmann mask, the sample can have arbitrary patterns and feature densities and does not have to be characterized beforehand. This method has low requirements on the beam quality, it does not require high coherence or strict monochromaticity. It is

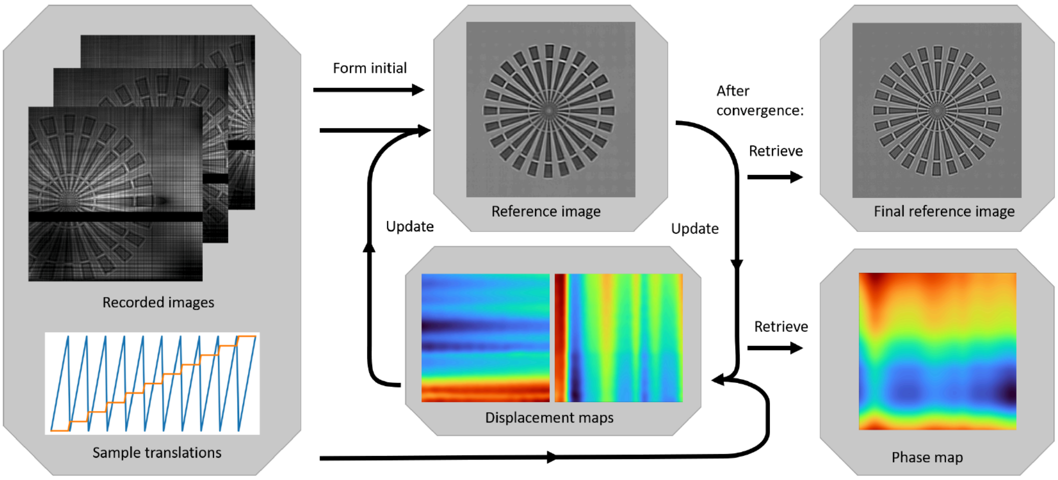

Fig. 2.10: Flow chart of the main PXST loop. Based on the recorded frames and their relative positions, a reference image estimate is formed. Comparing individual frames to the reference image results in a displacement map. By correcting individual frames based on this displacement map, an updated reference image can be formed. This loop is repeated until convergence. Afterwards, an aberration free reference image and the phase (wavefront aberration) is retrieved.

therefore an excellent method to be used for the characterization of lenses using a laboratory source. It can be applied to characterize a single 1D MLL, focusing only in one direction by using a 1D sample such as a barcode-like structure or to retrieve the 2D wavefront of a lens pair. Due to its nature of requiring many overlapping frames and the retrieval being iterative, acquiring a dataset takes longer and the retrieval is computationally more expensive.

2.4.2 Robust speckle tracking

Ptychographic X-ray speckle tracking works well for most applications but is limited in performance when the intensity or signal to noise ratio is low or when the sample is probed sparsely. The latter is the case when the field of view is small, such as at positions close to focus. Since the reconstructed phase sensitivity scales with the magnification and is hence larger close to focus, it is advantageous to operate in this regime, if possible. Due to the nature of laboratory sources, counts are much lower and noise is higher than at synchrotrons. Since our lenses are mostly characterized with a laboratory source, but fast and precise phase reconstruction is required, it is important to achieve quantitative characterizations also in this environment. To achieve reliable reconstructions with such a setup, a more robust version of PXST was developed, called robust speckle tracking (RST) or robust ptychographic X-ray speckle tracking (R-PXST) [112]. To be less prone to outliers in the data and noisy signals, it divides the data into outliers and inliers and supresses the outliers. It then applies a smoothing kernel to the data and employs machine learning techniques like Huber regression and non-parametric regression to update its size at each iteration, allowing greatly enhanced reconstructions even under harsh conditions.

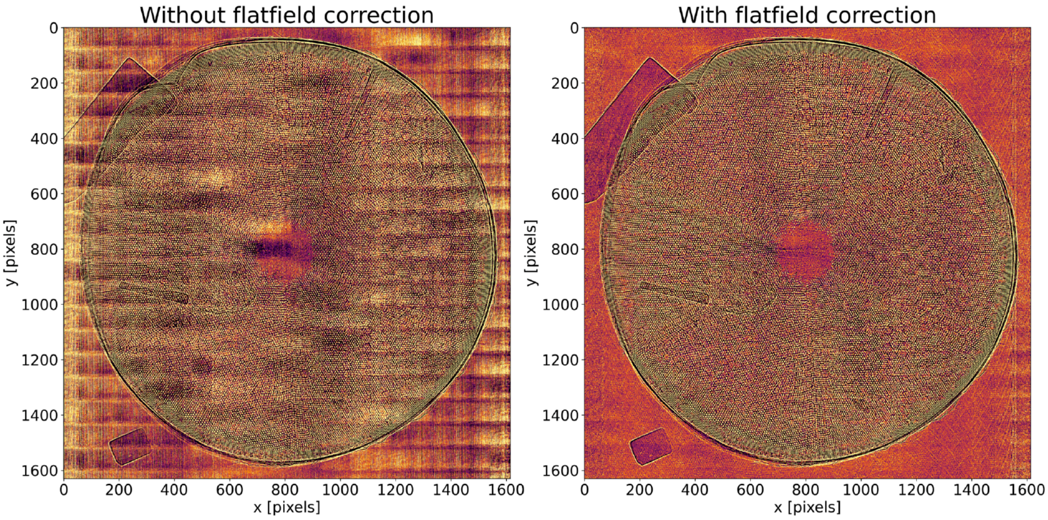

Fig. 2.11: Reference image of a diatom sample obtained from RST without (left) and with (right) flatfield correction. Periodic artifacts and stripes are suppressed by the flatfield correction.

Intensity fluctuations of the source can lead to a speckly background, increasing the difficulty to distinguish between sample and background. Further, grid artifacts can be present from the scan pattern. RST uses a dynamical whitefield correction, which suppresses such fluctuations, resulting in higher quality reconstructions. A better reconstructed reference image leads to a better reconstructed phase. Furthermore, since the whitefield is reconstructed from the average of all frames, inhomogeneities in the whitefield may arise, for example from the edges of the sample. Figure 2.11 shows how such a dynamical correction can enhance the image quality, reducing scan- and whitefield artifacts. A more detailed description can be found elsewhere [112, 113].
Wavefront reconstructions shown in this thesis were done with this method and software. It is publicly available as python module under the name "pyrost" available under version 3 or later of the GNU General Public License. The next section describes in more detail, how this method is used to retrieve the wavefront of a lens, using the laboratory setup presented there. In chapter 6, results of 2D imaging at a synchrotron using speckle tracking are presented as well.

2.5 Laboratory setup

This chapter follows the publication *Precise wavefront characterization of X-ray optical elements using a laboratory source* [114]. The laboratory setup was not built by myself but thoroughly tested, studied and improved. Measurements shown in this chapter were done by myself using this setup unless stated otherwise.

The phase retrieval algorithm based on speckle tracking introduced in the previous section can work well with laboratory environments due to its low requirements on coherence and monochromaticity. In order to capitalize on that and enable fast feedback on lens quality for accelerated development, a testing station was set-up, which allows quantification of lens aberrations without the need for synchrotron access. Since synchrotron access is sparse, available time should be optimized, therefore, pre-characterization and selection of only the highest quality lenses increases the available time for experiments building on high NA MLLs. A schematic of the laboratory setup is shown in figure 2.12. It contains a source, mounts for optics and motors for positioning, and detectors for data acquisition. The whole setup is positioned on top of a 5 m long optical table with air damped feet and encapsulated by radiation protection enclosure walls. The enclosure features two lead glass windows, one which allows viewing downstream towards the detectors and a second one on the side. At the setups heart is a commercially available X-ray micro-source (Sigray XCITE, Sigray, Inc., USA). It can produce X-rays with energies of 8 keV (Cu Kα), 17.5 keV (Mo Kα), 20.2 keV (Rh Kα) and 8.4 keV (W Lα). Change

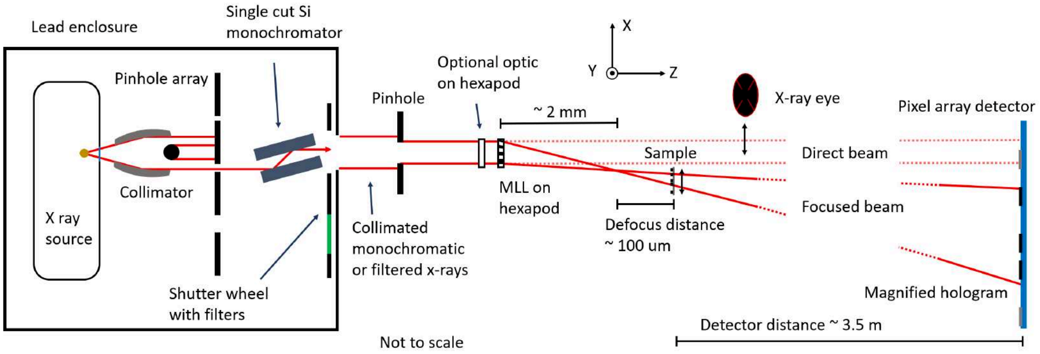

Fig. 2.12: Sketch of the laboratory setup. The X-ray beam can be shaped and manipulated by a collimator, pinholes, a monochromator and filters. Optics to test are positioned on hexapods and samples are placed downstream of the optics. Two detectors, a scintillator based "X-ray eye" and a photon counting pixel array detector can be positioned up to 3.5 m downstream. The "X-ray eye" is typically used for alignment and the photon counting detector for data acquisition.

of desired energy is done in the associated software with only a few clicks and within a few minutes. The source size is around 15 μm × 12 μm in the horizontal and vertical directions, respectively, estimated from a knife edge scan, with a brightness of about 1.7×10^{10} photons s^{-1} mm^{-2} mrad^{-2} (for the Mo target), according to the manufacturer. The produced X-rays are collected by a Pt-coated paraboloid mirror collimator with a working distance of 44 mm. It is 25 mm long and has a 0.56 mm opening- and 0.7 mm exiting diameter. A central beamstop blocks uncollimated light. The resulting beam has the footprint of an annulus. Since the optics are small compared to the full beam, a fraction of the beam can be selected by use of a pinhole. The size of the pinhole can be chosen from a set with sizes between 45 μm and 150 μm, depending on the required beam size. This selected beam can then either, depending on intended usage, be monochrommatized using a Si(111) channel-cut

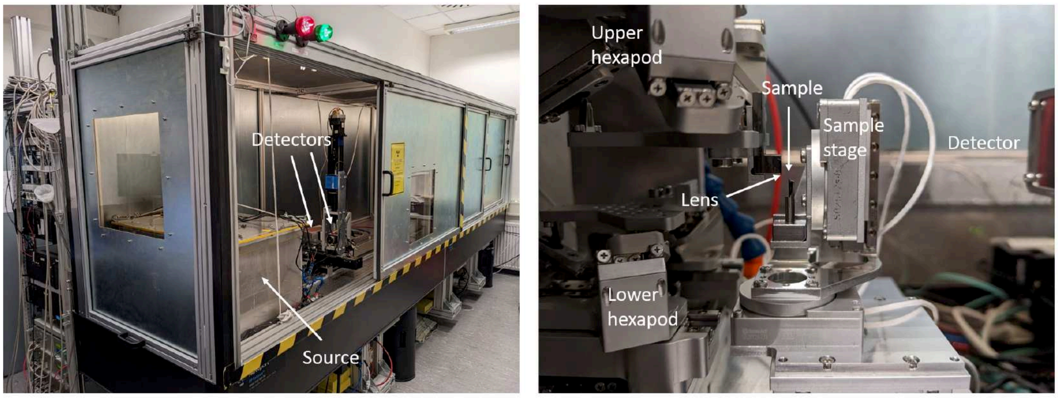

Fig. 2.13: The laboratory setup. Left: The whole setup on the optical table with protective enclosure. Through the open door the small enclosure containing the source and the detector stage can be seen. Right: The hexapods and stages for optics and samples just behind the source box. The X-rays travel from the left to the right, where the LAMBDA detector can be seen.

monochromator, or filtered by a material with an absorption edge between the Kα and Kβ lines of the target material. The monochromator is placed about 17 cm from the source and can accept photons with energies ranging from 7 keV to 21 keV, covering both Cu (8.05 keV Kα) and Rh (20.22 keV Kα) well. Using it greatly reduces the bandwidth at the cost of flux. When using a filter, the flux is higher by about a factor of 5 compared to the monochromator, while still suppressing most of the intensity of the $K\beta$ radiation. For Mo, for example, the Kα and Kβ lines are at 17.5 keV and 19.6 keV, respectively. Employing a 50 μm thick Nb filter with an absorption edge at 18.4 keV suppresses the Kβ line of the source. A 25 μm Ni filter is used when operating the system with Cu as the source material and a 25 μm Cu filter can be used to suppress the Lβ line of the W anode. The filters are placed on a wheel which allows quick changing between them and also acts as a beamstop in positions between two filters. All components mentioned above are positioned inside a second, smaller enclosure with aluminum sandwiched lead plates for radiation protection. Closing the shutter by rotating the wheel of filters allows human access to the rest of the setup to exchange optics without the need to turn off the source. Downstream of the filter wheel, a 1 mm pinhole is used to block any scattered light and let only the filtered (or monochromatized) and collimated beam through.

The beam coming through the 1 mm pinhole is then used to test the optics. For that, two SmarAct hexapods are used which are above (hanging, upside down) and below the beam. They can be used to place up to two optics in the beam at the same time, like two lenses, a lens and a corrector, a grating and another pinhole etc. They allow motion along six degrees of freedom, three translational and three rotational, with a resolution length of about 1 nm in translation, and 1 μrad in rotation. The rotational range is about 16°. To mount optics on them, magnetic receptacles are placed on top of the hexapods and optics are placed on metal holders, which can slide into the receptacles. The pivot point of the hexapods can be adjusted such that the optics are at the center of rotation. This is followed by a set of stages for sample alignment, with movement in X,Y,Z directions as well as rotation around the optical axis Z (called "Roll") and the Y axis (called "Yaw", rotation around the X axis is called "Pitch"). A coordinate system is shown in figure 2.12. The translational movement precision is about 10 nm and the rotational 0.4 μrad. The sample is usually placed on a metal pin which can be placed on a magnetic metal base, similar to the optics on the hexapods. Downstream of the sample stage are two detectors, placed on a joint and motorized stage which allows movement in X and Y. One detector consists of a scintillator being imaged with a 10× objective onto a PCO 4.2LT CCD camera, which we refer to as an X-ray eye. The effective resolution is about 2 μm. This detector is used to image the beam shape and align optics. The second detector is a LAMBDA 750k (X-Spectrum GmbH, Germany) photon counting pixel array detector [115]. Initially, this detector had a Si sensor with 516×1556 pixels with a side length of 55 μm and was later replaced by one with a GaAs sensor of equal dimensions, owing to its higher quantum efficiency at the energies probed here (factor of ~ 2 at 17.5 keV).

This detector is used to record images for the quantitative optics characterization. The two detectors can be manually moved along the z-direction sliding on metallic rails. This allows to adjust the distance between the optics and the detector(s) from about 10 cm to 3.6 m. Two pictures of the whole setup and the optics stages are shown in figure 2.13.

All motorized stages can be controlled by Kamzik3 [116], an in-house developed software control system based on Python3. It allows the precise control, logging and visualization of all motor positions through a user interface. All motors can be scanned in 1D or 2D, while acquiring detector frames at each position if wanted, through a custom scan macro. The software is available under the GNU General public license. Since all components and movements are motorized, except the detector z-motion, the whole setup can be operated remotely (except for changing optics such as MLLs or multilayer gratings). To allow safe operation also with the optics and samples in close proximity to each other, four miniature cameras (Watec WAT-240E) are placed such that the sample (stage) and optics (hexapods) can be viewed at various magnifications and from a set of directions. Further details of the setup can be found at [67, 114].

2.5.1 Lens energy determination

The next few sections give an overview of the measurements which are typically conducted with the laboratory setup, including a few examples. Results presented later follow the process being described here unless stated otherwise.

As mentioned earlier, MLLs need to follow the zone plate law in the positioning of layers, in order to achieve focusing. The period of the n-th layer can be approximated as $d_n \approx \lambda f / r_n$ for small NAs. Since this is wavelength dependent, an MLL works efficient only at a single wavelength (with a bandwidth equal to the inverse of the number of layers). For a change in energy, a new MLL has to be fabricated (which can typically be cut from the same multilayer stack). For which energy a lens is optimized can be determined from the intensity distribution of its diffraction signal. Since the lens focuses in one direction, the beam downstream of the focus diverges along one direction. The resulting signal on the detector is a line, in addition to the direct, transmitted beam. If the lens is produced as an off-axis lens, a gap remains between this direct beam and the diffraction line. If the ideal operating energy of the lens E_m of wavelength λ_m is the same as the probing energy E_p of wavelength λ_p, high efficiency over the full multilayer stack and thereby angular range is observed if the lens is tilted to its diffracting condition. If the energies differ, the working energy of a lens can be determined by tracing which angular range along the opening angle 2θ efficiently scatter X-rays based on the tilt angle of the lens ω [35]

$$\omega = \frac{1}{2}\left(1 - \frac{\lambda_m}{\lambda_p}\right) 2\theta. \tag{2.16}$$

Since the period changes throughout the multilayer stack, the angles 2θ trace out the scattering efficiency along the height of the lens. When the two energies match, $\omega(2\theta)$ becomes a constant, resulting in high scattering efficiency at a single lens tilt. A mismatch of energies produces a linear slope in the ω - 2θ plot. Two examples of such plots can be seen in figure 2.14. They are obtained by capturing a detector image on the LAMBDA detector at each lens tilt ω and integrating the image along the orthogonal direction with respect to the scattering direction of the lens, with subsequent stacking of the resulting 1D images. In (a), the probing wavelength λ_p and the operating wavelength of the lens λ_m are close to identical, resulting in a vanishing slope. In (b), the operating wavelength λ_m is much lower than that of the probe, resulting is a steep slope. In the convention used here, an increasing 2θ with increasing ω relates to the optimum working energy being higher than the probe. Note that the probing energy does not have to be close to the optimum working energy of the lens for a precise determination of it. In addition to the optimum

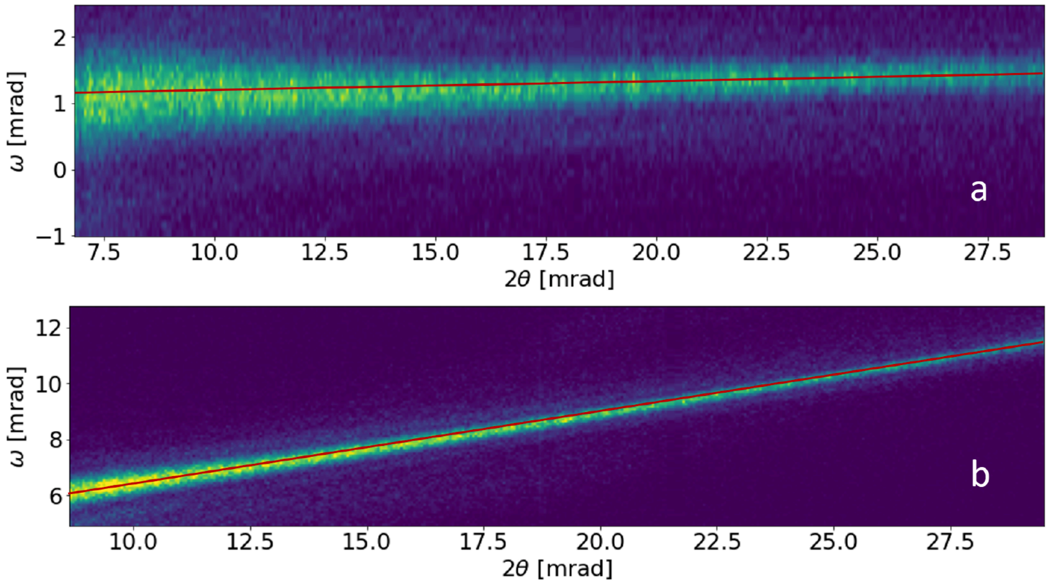

Fig. 2.14: Examples of the lens diffraction efficiency along 2θ based on the lens tilt ω. Both lenses are measured at 17.5 keV. A lens optimized for 17.9 keV, close to the photon energy of 17.5 keV (a). Here the diffraction line is almost horizontal and high efficiency along the full 2θ range can be obtained at a single tilt ω. A lens optimized for 35.8 keV (b). The diffraction line shows a steep slope where only a fraction of the 2θ range efficiently diffracts X-rays and said fraction varies with ω. The red lines indicate the linear slope between ω and 2θ.

working energy, the focal length of the lens can also be determined from the plots shown above. It can be calculated as

$$f = \frac{D \cdot h}{h + N \cdot pix}, \tag{2.17}$$

where D is the detector distance, h the physical height of the lens, N the number of pixels spanned by 2θ on the detector and pix the pixel size. Typical values for MLLs range from 0.5 mm to 15 mm, depending on the design energy and experimental requirements.

2.5.2 Lens wavefront determination

To determine the wavefront (aberrations) of a lens, the probing- and design energies have to match. Only then is the diffraction efficiency high along the full multilayer stack and the wavefront can be retrieved over the full range of angles 2θ. Once such a lens is fabricated, the phase is determined using the robust version of PXST, described earlier. It requires a speckly sample to be placed in the divergent beam downstream of the lenses focus and stepped through the beam with steps smaller than the field of view, while projection holograms are recorded on the LAMBDA detector. As samples, aperiodic multilayers of absorbing and spacing materials with pseudo random thicknesses are used. They are fabricated in the same multilayer deposition system as the lenses but with layer thicknesses between 100 nm and 1500 nm instead. This is much thicker than the layers in the MLLs and is required to resolve individual layers with high contrast using a laboratory source, which has a large source size. Cutting a slice from such a stack results in a barcode-like structure. Since a single lens only focuses along one direction, the sample requires features to change only along one direction as well, which is the case for such a barcode. An aperiodic structure is useful to suppress artifacts from periodicity's and prevent ambiguities. An example of such a barcode structure is shown in figure 2.15 (b).

To measure the wavefront of a lens, it is placed on one of the hexapods. It is rotated in the x-y plane such that the line on the detector emerging from the divergent beam is parallel to the pixel arrays. The barcode-like sample is then placed downstream of the focus such that its layers align with the line focus of the lens. It is stepped in equidistant steps through the beam with large overlaps between adjacent field of views. Note that equidistant steps are not necessary, as long as the actual motor positions are well recorded. In fact, a more random scan pattern can help to reduce grid pattern artifacts but reduces the homogeneity of the reconstruction, as some parts are probed more often than others. At each step, a frame is recorded on the LAMBDA detector. Since the signal is only one dimensional, the frames can be integrated along the direction orthogonal to the diffracted line. Doing so at each point and stacking them allows to show the full 1D scan in a single 2D image, similar to the energy measurement. We call such an image a ptychograph and an example is shown in figure 2.15 (a). The sample features (lines in this example) can be seen crossing the field of view. The first step in the reconstruction is to mask bad pixels as

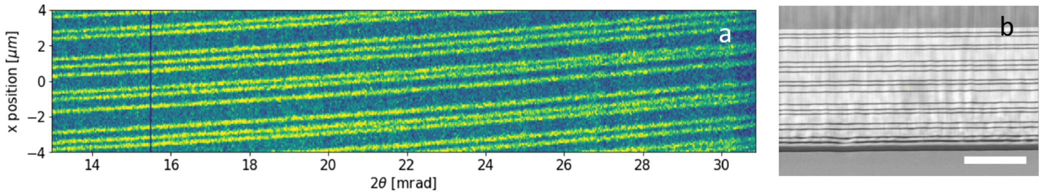

Fig. 2.15: Example of a ptychograph (a). The lines of the barcode-like multilayer structure move through the field of view. An un-aberrated lens would result in perfectly straight lines, any deviation from such is evidence that wavefront aberrations are present. A barcode like multilayer structure (b). The dark lines are SiC and the bright lines W. The scale bar is 5 μm.

they can throw off the algorithm. Then, the defocus distance of the sample has to be determined. At a constant detector distance, the defocus changes the magnification and hence the magnified step size of the sample. The smaller the defocus, the bigger the change in 2θ per change in sample position x. The defocus can therefore be estimated from the slope of the lines in the ptychograph. The shallower the slope, the smaller the defocus. To estimate the defocus of the sample, the ptychograph is integrated along various slopes and the contrast of the obtained images is compared. When the contrast is high, the slope matches the magnified sample step size. The effect of a non-zero phase gradient is directly visible in the ptychograph. Since equidistant steps are employed, each feature of the sample is expected to trace out a straight line. Any deviation from such is a result of the wavefront and proportional to the phase gradient. After the defocus is retrieved, the phase retrieval loop of RST can be applied to the data, resulting in the wavefront of the lens and an aberration free image of the 1D sample. Applying RST to the ptychograph shown in figure 2.15, results in the reconstructed sample, displacement map (equal to phase gradient) and phase shown in figure 2.16. For an ideal lens, the displacement map and wavefront

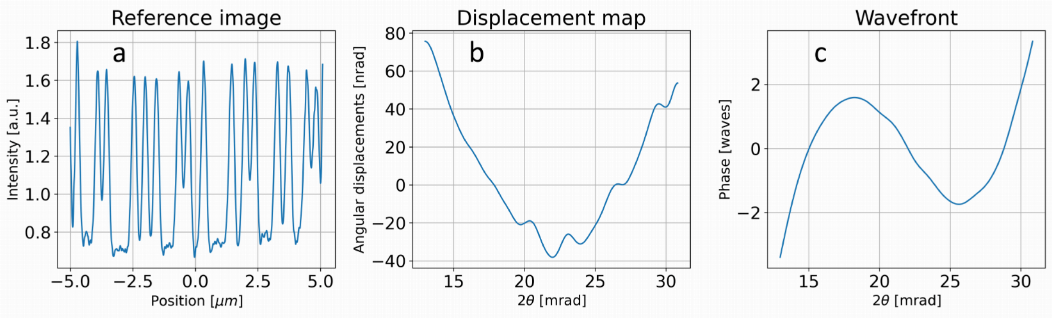

Fig. 2.16: The reference image (a), displacement map (b) and wavefront (c) reconstructed from the ptychograph shown in figure 2.15 using the robust speckle tracking algorithm.

would be 0. A linear change in sputter rate during multilayer deposition would result in a quadratic change of the phase gradient and a wavefront errors that scales with the pupil coordinate to the power of 3. This is the case in this example, indicating that the wavefront aberrations of this lens are a result from such a drift. Based on these results and the shape of the displacement map, a correction can be fed back into the deposition system for subsequent multilayer depositions.

3

Multilayer gratings

Measurements shown in this chapter were carried out by myself unless specifically stated otherwise. Images and figures shown were made by myself unless stated otherwise in the figure caption. Multilayer structures were deposited and cut into shape by colleagues. Measurements done at PETRA III involved a group of people aiding in the setup and operation of the experiment. The evaluation of the data presented and simulations were done by myself.

The motivation for the fabrication and study of multilayer gratings is twofold. First, gratings are relevant optical elements with dispersive and phase shifting properties which can be exploited for the precise manipulation of light. They therefore have a variety of applications over a wide range of wavelengths ranging from imaging [117–121] over pulse compressors [122–124] to spectroscopy in astronomy [125–127], to name a few. One of the better-known forms of gratings are blazed gratings [128] where the surface is shaped like a sawtooth with a certain periodicity and angle. The period is also known as the grating pitch and often given in grating lines per mm. These gratings can operate in transmission or reflection geometry. Blazed gratings are optimized for high efficiency for a single diffraction order while suppressing other orders and they can be manufactured in several ways [129], including mechanical ruling [130–133], electron beam lithography (EBL) [134, 135] and etching [136–138]. Aside from blazed gratings there are also non-angled laminar gratings [139–142] which are often fabricated in a similar fashion like EBL [143], and volume phase holographic gratings (VPHGs) [144–146] which utilize volume diffraction in either reflection or transmission geometry. The reflectivity of gratings can be increased by coating them with a multilayer [139, 141, 147]. Gratings based on multilayers can be classified as different types [148], including multilayer-coated blazed gratings (MBGs) [149–152], sliced multilayer gratings (SMGs) [71, 153–156], lamellar multilayer gratings (LMGs) [157, 158] and blazed lamellar multilayer gratings (BLMGs), the latter being a combination of an SMG and an LMG. An overview of different grating types (of solid structures) is given in figure 3.1. Bajt et al. showed that the reflection from (f) and (g) is identical, since the multilayer structure is the same [71, 159]. This enables the fabrication of nm period (10^{5-6} lines/mm) volume gratings, by simply depositing a multilayer and slicing it at a certain angle. These gratings all operate in reflection geometry i.e. the beam exits the (multilayer-) structure on the same surface it entered. Methods

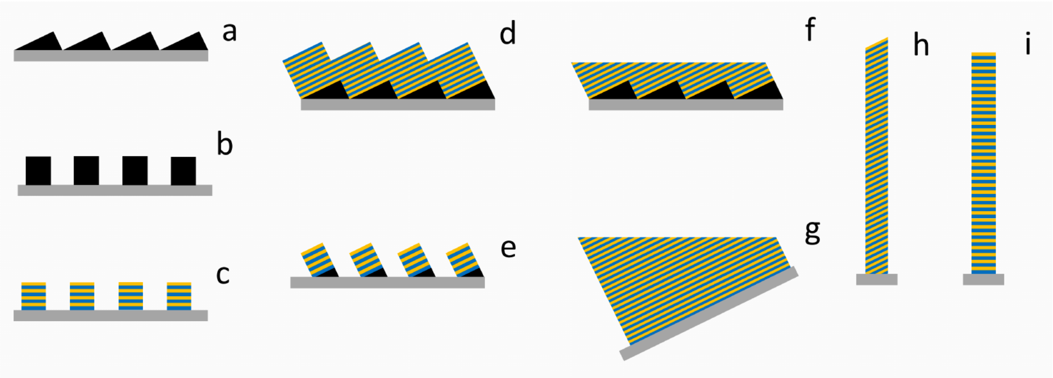

Fig. 3.1: Types of solid optical gratings. A blazed- (a) and a lamellar grating (b). Multilayer based gratings (c) to (i). Lamellar multilayer grating (c), multilayer coated blazed grating (d), blazed lamellar multilayer grating (e), extended asymmetric cut multilayer grating (f), asymmetric cut multilayer (g), volume holographic multilayer grating (VHMG) (h) and the special case of a symmetric VHMG (i). The reflection from the structure in (f) is identical to the one in (g) due to the identical multilayer structure. Gratings (a) to (g) operate in reflection while (h) and (i) are used in transmission.

such as Talbot interferometry [118, 120] require grating structures that operate in transmission geometry. The same is true for gratings used as beamsplitters. Such can be manufactured from multilayers as well, by slicing a multilayer stack to a thin (μm sized) slice as shown in figure 3.1 (h) if sliced at an angle or figure 3.1 (i) if sliced straight. Volume gratings as are shown in (i) are of interest here as the nm sized layers lead to large diffraction angles even in the hard X-ray regime while the optically thick structure allows high diffraction efficiency. By slicing the multilayer to a specific thickness, the ratio between the refracted and reflected beams can be tuned.

Volume holographic multilayer gratings are diffractive optics in Laue (transmission) geometry, which leads to the second motivation for their study, their similarity to MLLs. Locally, each part of an MLL can be understood as a grating with close to constant period. Their description by the dynamical theory of diffraction is thus similar. Dynamical diffraction theory states that for an optically thick diffractive optic in Laue geometry, there exists an optimum thickness τ_{opt} equal to half the *Pendellösung* period, at which the reflected beam intensity is highest [71, 73]. An MLL and a multilayer grating therefore have highest diffraction efficiency, if they are cut in thickness equal to τ_{opt}. Since in contrast to the grating the period changes throughout the stack of a multilayer in an MLL, and the efficiency is period dependent, measuring the efficiency of an MLL only results in an average value of the range of periods present. To quantitatively probe the dependency of the maximum diffraction efficiency and τ_{opt} on the period, multilayer gratings with various periods can be probed. This results in better insights of the ideal shape and expected performance of MLLs. To quantize the properties of thick diffractive optics in Laue geometry, multilayer gratings over a range of periods were fabricated from different materials

and tested at multiple photon energies to determine their quality, optimum thickness τ_{opt} and maximum diffraction efficiency. While other optics typically suffer from decreasing efficiency at increasing photon energies, diffractive optics do not. Far from absorption edges, absorption reduces as λ^2. Therefore, Δn in equation 2.4 is proportional to λ^2 as well, leading to a linear increase of τ_{opt} with increasing photon energy. Since τ_{opt} is only required to increase linearly while absorption reduces quadratically, the maximum efficiency increases with increasing photon energy.
This chapter reports on the characterization of multilayer gratings at the aforementioned laboratory setup at an energy of 17.5 keV as well as at the beamline P07 at the synchrotron PETRA III, Germany at 60 keV. Imperfections in the structure lead to a change in diffracting behavior and a reduction of maximum efficiency. Multislice simulations are carried out to simulate the effect such imperfections could have on the performance of the lens which are then compared to the presented results.

3.1 Fabrication

In similar fashion to multilayer based lenses, multilayer gratings are fabricated by magnetron sputter deposition, where layers are deposited one after another. To form a periodic structure, layers of two alternating materials are deposited. SiC is used as the less dense, spacing material and either W or WC as the absorbing material. The substrate on which the gratings are deposited on are moved between the plasmas of the two targets and the time it spends below each determines the thickness of the layers. This can be used to tune the Γ ratio, which is the fraction of the absorptive layer thickness to the bi-layer thickness. Once a multilayer is deposited, structures of various thicknesses can be cut from it. This is done with a microPREP^{TM} Pro laser cutter [160] which uses high repetition rate picosecond pulses for fast and precise cutting with minimal damage to the surface, resulting in a series of multilayer posts (referred to here as "comb") which are subsequently thinned to a range of varying thicknesses using a FIB. An example can be seen in figure 3.2. In the shown example, 12 structures can be seen as individual posts of different thicknesses with gaps in between. This geometry allows to characterize the structures of each thickness individually without interference from neighboring structures by reducing the incident beam to an area of size comparable to the front surface of a structure (or smaller). A series of grating structures with periods between 1.5 nm and 10 nm made from either WC/SiC or W/SiC was prepared. Table 3.1 summarizes the key features of each multilayer grating. Grating G11 is special in the sense that active feedback was used during its deposition. For gratings G0 to G10, the sputter rates and target consumption were calibrated in order to keep the period constant throughout the deposition. This greatly reduces a drift in period though some error remains, resulting in a change of period throughout the multilayer height.

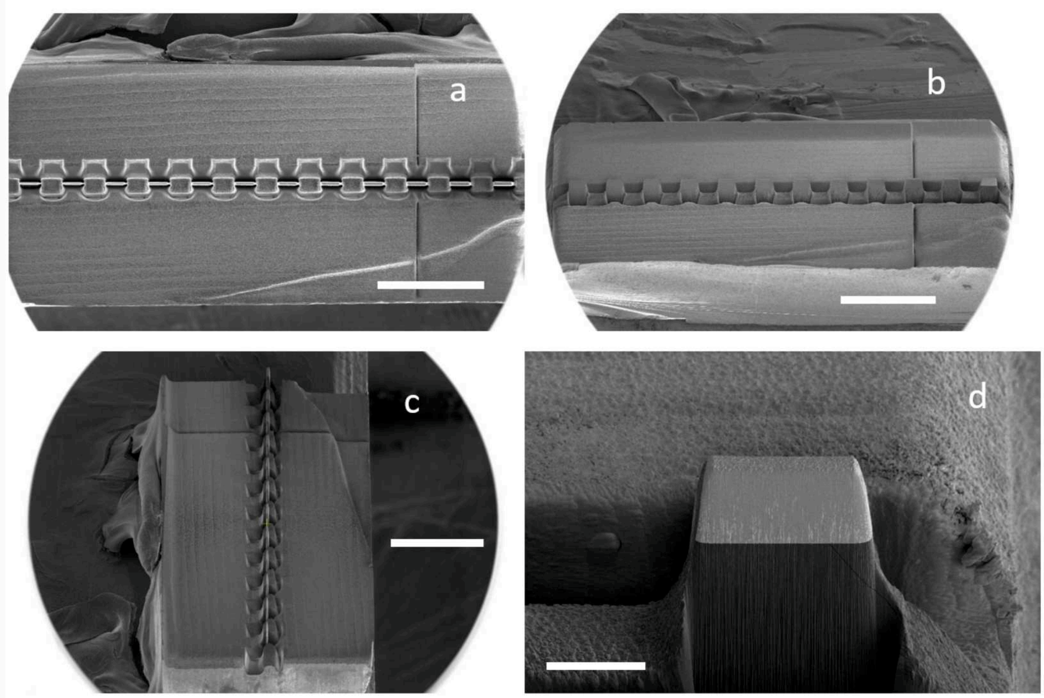

Fig. 3.2: Example of a grating comb. Top (a) front (b) and side (c) view of a structure containing 12 gratings of different thicknesses. A single structure is shown in (d). The bright part is the multilayer and the dark part beneath is Silicon. The scale bars are 500 μm in (a), (b) and (c) and 50 μm in (d). Reproduced by courtesy of M. Prasciolu.

Tab. 3.1: Key parameters of the prepared multilayers. W/SiC gratings are marked by a gray background.

Grating	Material	Period [nm]	Energy tested [keV]	Thicknesses [μm]
G0	WC/SiC	10	17.5	5-37
G1	WC/SiC	10	17.5	5-37
G2	WC/SiC	5	17.5	4-26
G3	WC/SiC	2.5	17.5	4-15
G4	WC/SiC	1.5	17.5	3-14
G5	W/SiC	5	17.5	3-10
G6	WC/SiC	10	60	25-75
G7	WC/SiC	5	60	10-75
G8	WC/SiC	2.5	60	12-75
G9	WC/SiC	1.5	60	12-75
G10	W/SiC	5	60	12-75
G11	WC/SiC	9	17.5	4-15

The period may vary from 10.0 to 10.2 nm throughout the grating, resulting in an error of $(10.2 - 10.0)/10 = 0.02$ or 2 %. For grating G11, a new active feedback system was used, which measures the drift of sputter rate *in situ* and can therefore correct for it during the deposition. With this feedback system, the error for G11 was reduced to $0.003 = 0.3\%$.

3.2 Characterization

In order to measure the efficiency of a grating structure, it is placed in the X-ray beam and tilted to its respective Bragg angle, using a hexapod. This can be observed on the X-ray eye camera as a reduction of intensity in the refracted beam and an increase in intensity in the reflected beam. To measure the absolute efficiency, the beam is reduced in size to be smaller than the front surface of the multilayer. At the laboratory setup this is done using a 17 μm round pinhole in 100 μm thick Pt, placed on a second hexapod upstream of the grating. At the beamline P07, this is achieved by a slit pair. Figure 3.3 shows a schematic of the experimental setup. The structure is then rocked around the Bragg angle while the intensity of the refracted and reflected beams are recorded on a photon counting pixel detector. For a normalization intensity I_0, the grating is removed from the beam. This is repeated for all thicknesses of a multilayer.

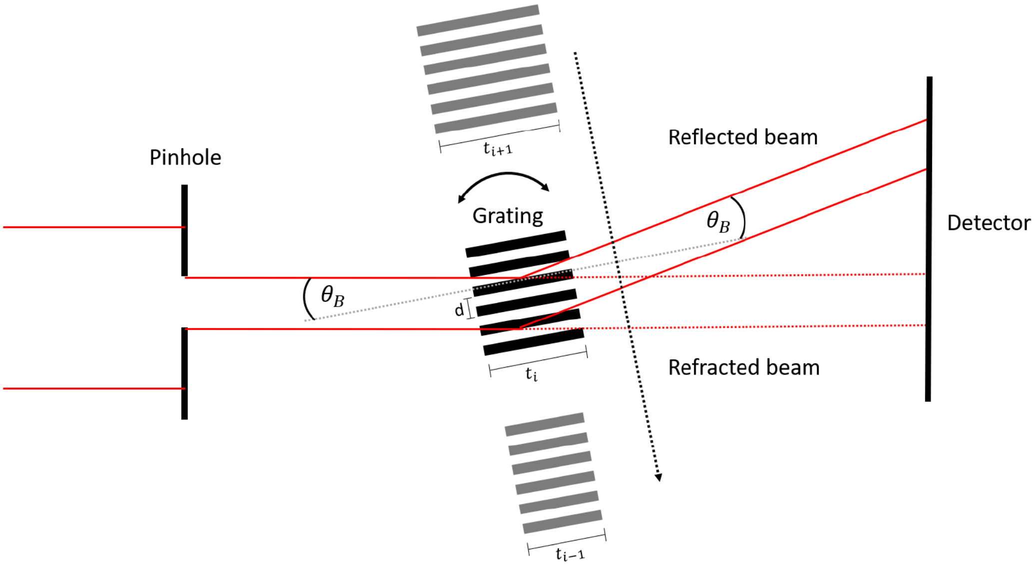

Fig. 3.3: Schematic of the experimental geometry. The beam is reduced in size using a pinhole or slits and the structure is tilted to Bragg angle while the refracted and reflected beams are recorded on a detector. Each structure of different thickness is probed individually.

3.2.1 17.5 keV

Gratings G0 to G5 and G11 were tested at the laboratory setup with a photon energy of 17.5 keV. The X-ray beam was monochromatized with the Si monochromator as described in the laboratory section. Acquiring the efficiency based on the tilt angle is called a rocking curve scan and is used to precisely determine the position of the Bragg condition and the maximum efficiency of a given structure thickness. Figure

3.4 shows two rocking curves of gratings G1 and G5 at thicknesses of 8.8 μm and 6.6 μm, respectively. The uncertainty of the thickness is around 0.3 μm. The measured values shown as dots are compared to the prediction by dynamical diffraction theory shown as lines. The dynamical diffraction calculations are based on the formulas given in [71] assuming ideal structures (constant period, no layer mixing, constant optical thickness throughout the multilayer height etc.), a Γ of 0.5 as designed and material densities as obtained from X-ray diffraction (XRD) measurements of the multilayer surface using a Panalytical X'pert [161]. For the WC/SiC structures, the retrieved densities are 13.87 g/cm^3 for WC and 2.67 g/cm^3 for SiC. In the case of W/SiC, they were 18 g/cm^3 for W and 2.8 g/cm^3 for SiC. Note that these are lower than the respective bulk densities of 19.25 g/cm^3 for W, 15.63 g/cm^3 for WC and 3.21 g/cm^3 for SiC. The density of the sputtered materials depend on the sputter conditions and lower than bulk densities are expected based on the sputtering gas pressure of 1.5 mTorr used here.

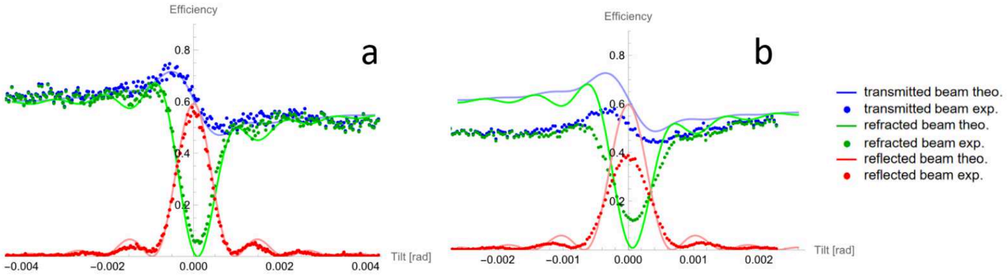

Fig. 3.4: Rocking curves of G1 (a) and G5 (b) at thicknesses of 8.8 μm and 6.6 μm, respectively. Dots are measurements and lines predictions by dynamical diffraction theory assuming a perfect two-layer structure with $\Gamma = 0.5$ and densities as retrieved by XRD. Shown are the reflected beam (red), refracted beam (green) and their sum (blue).

The maximum diffraction efficiency is then obtained in the center of the rocking curve and the central peak is well defined with second order side lobes being visible. Asymmetric anomalous transmission can be seen as expected from dynamical diffraction theory. At Bragg angle, the refracted beam almost vanishes and almost all of the transmitted intensity is in the reflected beam. While the measurement of G1 matches well with the theory, the measured intensity for G5 is lower than expected. This is likely due to a difference between the assumed and actual Γ ratio in that multilayer, more about that later in section 3.3 on imperfections. Such a rocking curve scan was repeated for the different thicknesses of the gratings as listed in table 3.1. By collecting the efficiencies at the Bragg angle (in the center of the rocking curve) and plotting them against the optical thickness of the multilayer, the *Pendellösung* curve is obtained. The expected shape of the reflected beam efficiency is a damped oscillation while the total transmitted beam should decrease exponentially due to absorption. The *Pendellösung* curves for gratings G0 to G5 and G11 can be seen in figure 3.5. A few interesting things can be observed here.

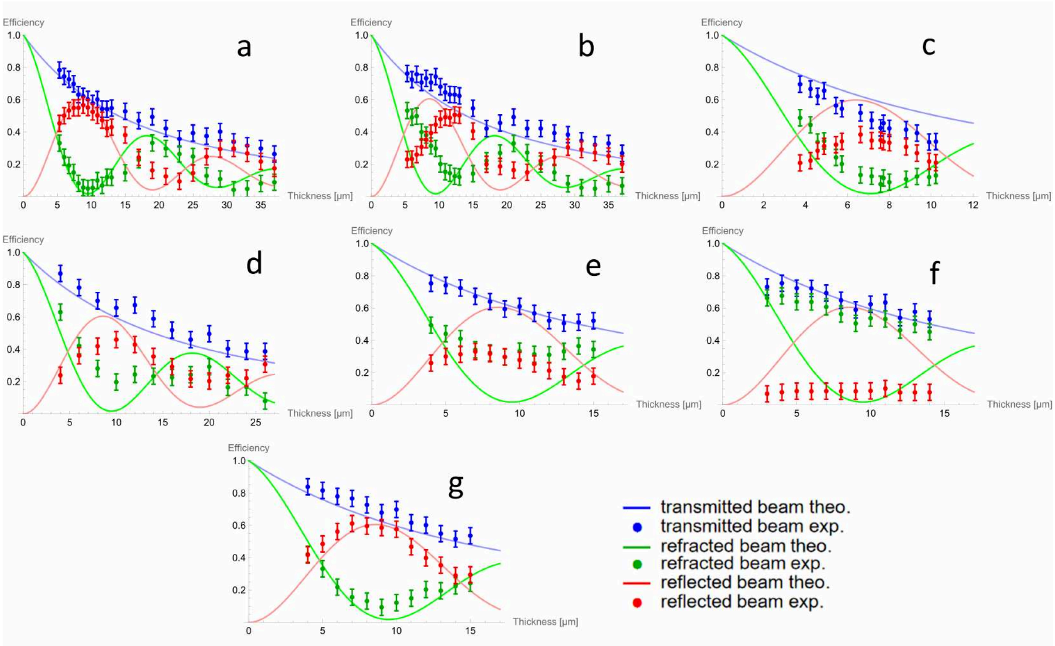

Fig. 3.5: *Pendellösung* curves for G1 (a), G0 (b), G5 (c), G2 (d), G3 (e), G4 (f) and G11 (g). Dots are measurements and lines predictions by dynamical diffraction theory assuming a perfect two-layer structure with $\Gamma = 0.5$ and densities as retrieved by XRD. Shown are the reflected beam (red), refracted beam (green) and their sum (blue).

Good agreement with the theory can be seen at thicker periods while lower than expected intensities are present at thin periods. This is likely due to imperfection which affect thin structure stronger. The transmitted beam (blue) is expected to exponentially reduce with optical thickness. For WC/SiC gratings, it follows the expected transmission values, independent of the distribution between the reflected and refracted beams. This indicates that material properties like the densities in the material match the assumed values. The W/SiC multilayer shows an overall lower transmission than predicted while the overall shape of the *Pendellösung* curve matches, which is consistent with the rocking curve scan shown in figure 3.4 (b), indicating a difference between assumed and actual grating properties. A summary of the optimum thicknesses τ_{opt} and maximum efficiency of the reflected beam at that thickness is given in table 3.2. The highest efficiency is seen for grating G11 which is 61 % at a thickness of 7 μm.

Tab. 3.2: Optimum thickness τ_{opt} and maximum efficiency at τ_{opt} for gratings G0 to G5 and G11 at 17.5 keV. The error of the optimum thickness is around 0.3 μm and about 5 % on the efficiency.

Grating	G0	G1	G2	G3	G4	G5	G11
Period [nm]	10	10	5	2.5	1.5	5	9
τ_{opt} [μm]	12.3	8.8	10.0	7.0	11.0	6.6	7.0
max efficiency [%]	51	57	46	33	10	38	61

3.2.2 60 keV

As mentioned previously, the maximum achievable efficiency increases with increasing photon energy. At 60 keV, efficiencies as high as 90 % should be possible. Not only is this energy interesting for the increased efficiency that can be achieved for diffractive optics such as gratings or MLLs, it is also where the Compton signal per absorbed energy in biological samples is the highest. A new imaging scheme based on Compton scattering at high energies using MLLs is explored in chapter 6.6. In order to fabricate efficient lenses for high energies, the optimum thickness has to be determined there as well. The optimum thickness τ_{opt} shifts towards larger values at higher photon energies.

To be able to determine the optimum thickness for gratings G6 to G10, they had to be characterized at the beamline P07 at PETRA III, Germany. The energy was fixed at 60 keV and a collimated beam was incident on the grating structures. In a similar fashion as at the laboratory setup, the structures were positioned in the X-ray beam and tilted around the Bragg angle individually. Rocking curves were again obtained for each structure. An example of a rocking curve of grating G7 at a thickness of 35 μm is shown in linear and log scale in figure 3.6 (a) and (b), respectively. Due to the higher photon flux at the synchrotron, sidelobes up to the ninth order can be seen. The minima of the rocking curve are asymmetric, being closer to 0 on one side compared to the other. As expected due to the reduced absorption, the reflection efficiency is higher than at 17.5 keV, in good agreement with the prediction. Such a rocking curve scan was repeated for each thickness of gratings G6 to G10. The efficiency at the Bragg angle as a function of thickness again results in the *Pendellösung* curves which are shown in figure 3.7. Similar to measurements at 17.5 keV, the transmitted beam decays exponentially with the grating thickness and matches the predicted decay, even if the distribution between reflected and refracted beams differ. The highest efficiency of 82 % was reached with grating G7 at a thickness of 35 μm. A summary of the optimum thickness and the maximum reflected beam efficiency for the various gratings tested can be found in table 3.3. Note that here in similar fashion to the measurements done at 17.5

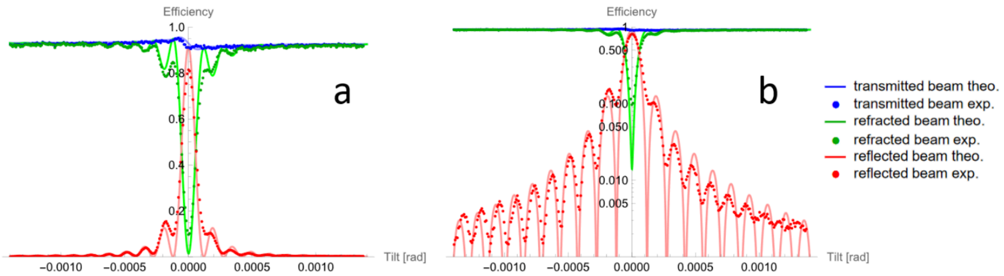

Fig. 3.6: Rocking curve of grating G7 at an optical thickness of 35 μm on a linear (a) and logarithmic (b) scale. Colors and lines/dots as in figure 3.4.

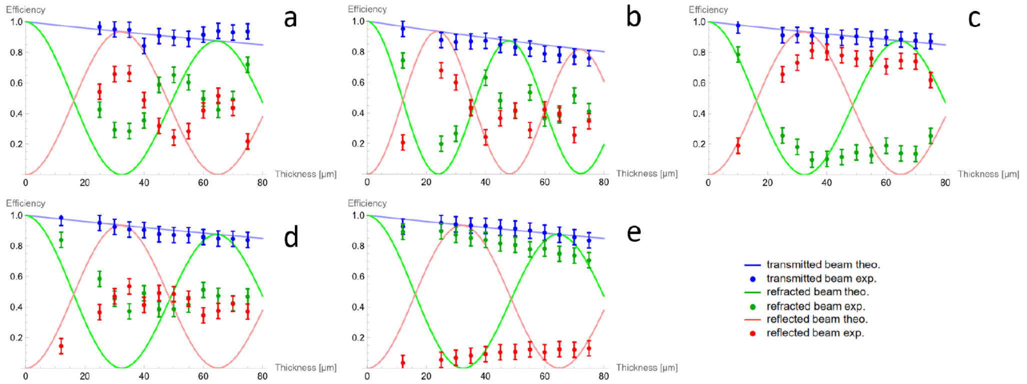

Fig. 3.7: *Pendellösung* curves for G6 (a), G10 (b), G7 (c), G8 (d) and G9 (e). Colors and lines/dots as in figure 3.5.

Tab. 3.3: Optimum thickness τ_{opt} and maximum efficiency at τ_{opt} for gratings G6 to G10 at 60 keV. The error of the optimum thickness is around 0.3 μm and about 5 % on the efficiency.

Grating	G6	G7	G8	G9	G10
Period [nm]	10	5	2.5	1.5	5
τ_{opt} [μm]	35	35	35	75	25
max efficiency [%]	66	81	54	13	68

keV, the small period of 1.5 nm shows the lowest efficiency. While high efficiencies up to above 80 % were reached, none of the reflected beam efficiencies follows the predicted *Pendellösung* curve. Since the range of thicknesses tested at 60 keV covers much thicker structures, the gratings exhibit a larger optical thickness and volume within which imperfections can impact and deteriorate the performance. The main contributors to imperfections in the structures are discussed in the following section.

3.3 Imperfections

The simulated or predicted efficiencies based on the dynamical theory of diffraction assume ideal structures without any imperfections. In reality, no structure is perfect. In the case of multilayer gratings, there are several deviations from the ideal which a structure might suffer from. The question arises which ones are present, how they change the grating performance and if their impact is significant or can be neglected. Multislice simulations as well as dynamical diffraction theory calculations were carried out in order to understand these imperfections.

The first imperfection of interest is a change of period throughout the multilayer height. The accumulated thickness difference results in an elongated (or contracted) structure which can be described in a similar fashion as a structural deformation due to strain. Such an error can be a result of sputter rate drift of the magnetron deposition system, which also leads to wavefront aberrations in MLLs. When this error is present, only a fraction of the structure can be exactly at Bragg angle. The parts of the structure not exactly at Bragg angle due to their difference in local period essentially diffract with an efficiency off center of the rocking curve, leading to an overall reduction of diffraction efficiency. Since the position of side lobes depends on the period, such an error leads to the superposition of multiple rocking curves which washes out the contrast of the side lobes. Figure 3.8 (a) to (c) shows multislice simulations of the change of the rocking curve under the presence of a change in period. Shown is an example of a 10 nm period WC/SiC grating at an optical thickness of 7 μm probed at 17.5 keV. (a) shows a typical example, where the period changes from 10.0 to 10.2 nm. In this case, the difference from the ideal case in terms of diffraction efficiency is negligible. (b) and (c) show an example where the period changes from 10.0 to 12.0 nm. In this case, a reduction of peak efficiency can be observed, together with a shift- and reduction of contrast of side lobes. Note that the reduction in side lobe contrast is asymmetric, in agreement with the rocking curve scan of grating G7 shown in figure 3.6. Presence of a period change can easily be observed by reducing the beam in size significantly smaller than the grating and measuring the reflection angle at various positions along the structure height. If the period is not constant, the diffraction angle changes. This also leads to slight focusing or de-focusing of the beam. Placing an X-ray eye detector downstream of the grating allows to record the size and shape of the refracted and reflected beams. Figure 3.9 (a) and (c) show a few grating structures diffracting downwards and

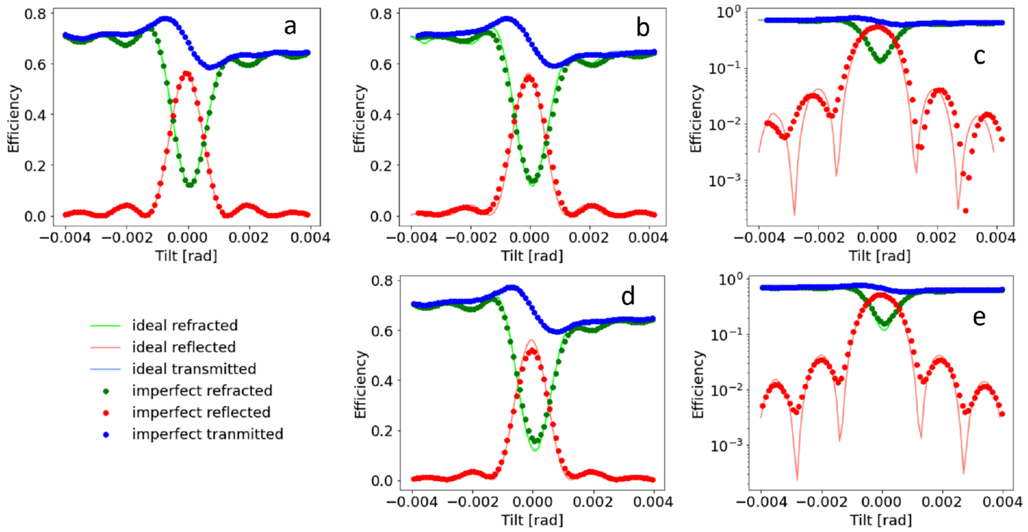

Fig. 3.8: Multislice simulations of a period change and wedge in a WC/SiC grating with 10 nm period and 7 μm optical thickness at 17.5 keV. A typical change of period from 10.0 to 10.2 nm (a). A much larger change of period from 10.0 to 12.0 nm (b). A logarithmic plot (c) of (b). A wedged structure where the layer tilt changes by 1 mrad from the bottom to the top (d). A logarithmic plot (e) of (d).

upwards, respectively, as captured on an X-ray eye detector at the beamline P07 at PETRA III. The structures appear dark since they are tilted to Bragg angle, largely

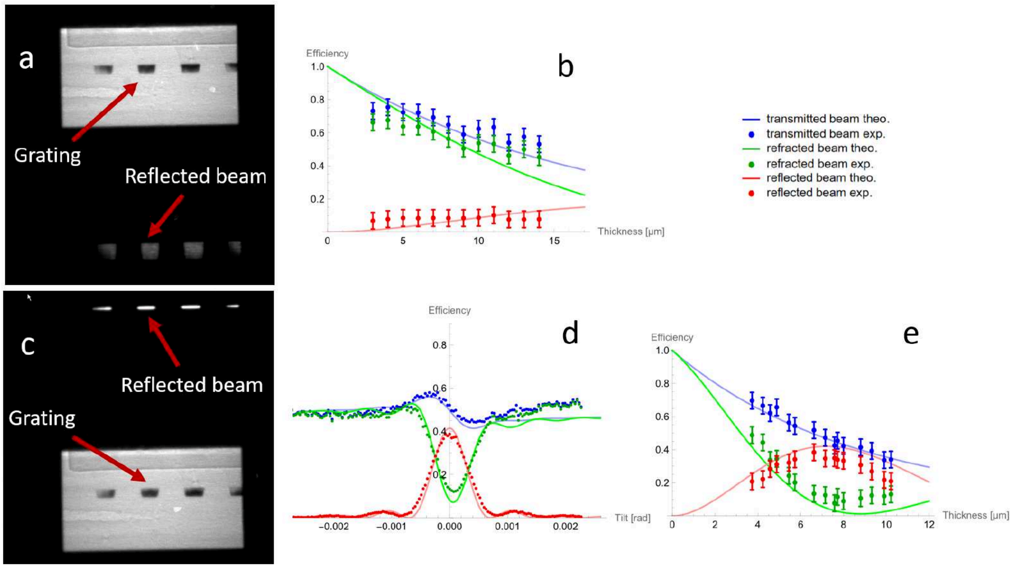

Fig. 3.9: A grating with a change in periods diffracting in downwards (a) and upwards (c) directions, showing de-focusing and focusing effects, respectively. The *Pendellösung* curve of grating G4 compared to the prediction assuming a layer intermixing of $\sigma = 0.4$ nm (b). The measured rocking- (d) and *Pendellösung* curves (e) of grating G5 could be matched to the theoretical curves if a Γ of 0.7 instead of 0.5 was used.

extinguishing the refracted beam. One can clearly see a de-focusing effect in (a) and a focusing effect in (c), indicating a change of period in the structure.

An effect similar to this is wedging. In a wedged grating, the layers at the top are tilted with respect to the layers at the bottom. The height of the multilayer stack therefore varies between the front and back surface. This could be caused by stress induced during the deposition or the fabrication process. When a structure is thinned to a specific thickness, one side is cut before the other, which could induce such stress induced wedging. The reason this effect is similar to a change in period is because a wedge causes parts of the multilayer to be slightly off Bragg angle, this time not due to a different period requiring a different angle but because the angle of the layers changes throughout the stack. This again reduces the maximum efficiency but does not cause a change in reflection angle or focusing. Multislice simulations reveal (see fig. 3.8 (d), (e)), that the effect on contrast reduction side lobes is symmetric this time, on the contrary to the previous error. In the gratings, no wedging which could be distinguished from a change in period could be found, if there is a wedge of the structures, it is negligible.

The next main contributor to imperfections could be layer surface roughness and interdiffusion [162, 163]. H. Yan simulated that these would have the same effect on the diffracted wave field inside the structure [164]. Therefore, they are referred to here only as layer interdiffusion. Interdiffusion leads to a reduced electron density between the two layers and therefore the maximum efficiency drops. The grating structure is assumed to be composed of two different layers with a mixing region in which the refractive index follows an error function along the layer stacking direction. Here, no difference between a WC-SiC (or W-SiC) layer interface and a SiC-WC (or SiC-W) layer interface is assumed. If the depth of the interdiffusion is equal to the layer thickness, no grating structure would be left. The depth of this effect σ is assumed to be independent of the period, it should therefore affect thinner periods stronger, as a larger fraction of the layer is intermixed, as can be seen in figure 3.10 (b) and (c). XRD measurements indicate that σ is expected to be around 0.4 nm. A comparison between the measurement of G4 (1.5 nm period) with the dynamical diffraction theory prediction assuming such layer mixing is shown in figure 3.9 (b), where good agreement can be observed, confirming the magnitude of this effect. Layer mixing reduces the efficiency and causes the optimum efficiency to shift to larger values. For this grating especially, the effect is strong since the individual layer thickness is 0.75 nm, comparable to the mixing of 0.4 nm. This is a ratio of $0.5\overline{3}$ which is significantly larger than 0.1 which is found to be the limit below which such layer interdiffusion can be neglected [164]. For a multilayer of varying period such as an MLL, the ideal shape for highest possible diffraction efficiency would be a structure which is optically thinnest at the thickest layers and increases in optical thickness as the layer period decreases.

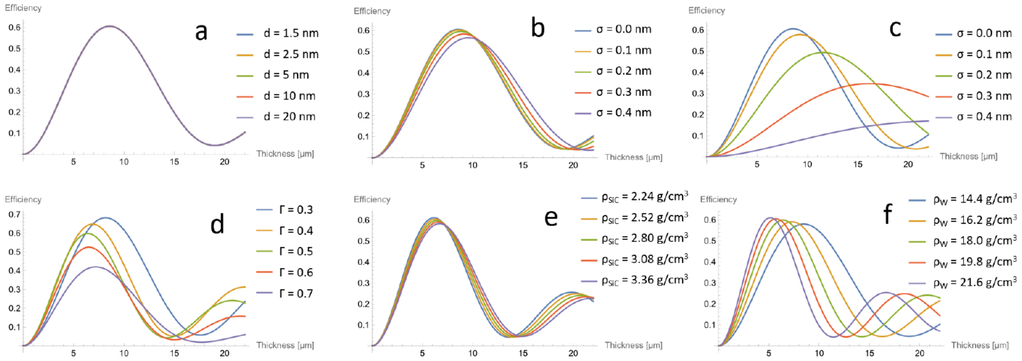

Fig. 3.10: *Pendellösung* curve dependency based on layer intermixing σ, material density and Γ for a W/SiC grating at 17.5 keV. Only one parameter is varied while the rest is kept constant. Shape dependent on the grating period (a). Change caused by a layer intermixing σ for a 5 nm period grating (b) and a 1.5 nm period grating (c). *Pendellösung* curve change based on Γ (d). A change of the density of SiC (e) and W (f) by up to $\pm 20\%$.

Aside from imperfections, there are material parameters that are hard to access and to determine precisely which can lead to a mismatch between theory and experiment. The period of a multilayer structure can easily be determined with high accuracy from the diffraction angle. Other parameters which determine the shape of the rocking- and *Pendellösung* curves are harder to access. These include the density of the materials and the Γ ratio of a bilayer. Γ can be estimated from XRD measurements as well but not with an accuracy as high as for the period. Additionally, the structure is assumed to be a two-layer system with a symmetric layer interdiffusion at both interfaces. The real system might have an asymmetric depth or shape of interdiffusion. According to the dynamical theory of diffraction, a change in Γ from 0.5 in either direction shifts the optimum thickness τ_{opt} towards larger values (see eq. 2.4), as can be seen in figure 3.10 (d). If the larger fraction of the bilayer is of the denser material, the efficiency reduces as more photons are absorbed. On the contrary, thicker layers of the less dense material can lead to an increase in efficiency. While increasing the efficiency this way is possible, one has to note that since one layer will be thinner, layer intermixing could again be more severe, which could limit the increase in efficiency one can achieve. An increased τ_{opt} also requires thicker structures which are again more prone to other imperfections. The difference between the prediction and measurement of the rocking curve scan of G5 shown in figure 3.4 (b) and the *Pendellösung* curve shown in figure 3.5 (c) is mostly a reduced intensity. Assuming a Γ of 0.7 instead of 0.5 shows good agreement between prediction and measurements, as can be seen in figure 3.9 (d) and (e). It is unlikely that the Γ value deviates that much from 0.5, instead it is more likely that the grating with a likely more complex structure than assumed here can be approximated with a simple two-layer system that has a Γ of 0.7. Different densities can cause a shift of the optimum thickness in either direction and also increase or decrease the efficiency (see fig. 3.10 (e) and (f)). Since two densities determine four non-independent parameters (δ and β for each material), deviations of the densities are hard to trace back, especially since their effects are small for reasonable deviations.

Optically thicker grating structures appear to deviate more from theory. This could be because imperfections in the structure accumulate throughout the grating, leading to a larger effect. It could also be that the gratings undergo structural changes at large thicknesses. For example, the reflected beam efficiency of G7 increases as expected up to a thickness of about 40 μm (see Fig. 3.7 (c)). At larger thicknesses, the reflected beam efficiency remains high instead of decreasing. An explanation for this could be that the grating undergoes a sudden change in structure around this thickness, which causes the reflected beam to no longer be at the Bragg angle and therefore just transmit through the remaining structure.

The last part discussed here which can cause deviations between the simulations and measurements is the geometry and shape of the grating structures. Since the cut with a FIB does not result in a perfectly vertical surface, the shape of a grating is a trapezoid, thicker at the bottom and thinner at the top. This leads to an uncertainty of the thickness, depending on where the beam intersects the surface. It also reduces the maximum efficiency slightly, as parts of the grating are not of the optimal thickness. In connection to that, the FIB might also damage the multilayer structure [165]. If the cut is done incorrectly, the region of the multilayer close to the surface could become amorphous, resulting in part of the structure thickness contributing to absorption but not reflection. This could be the case for grating G0 shown the figure 3.5 (b), where the *Pendellösung* shape is as expected, but shifted towards higher thickness. This structure was prepared using a Ga FIB instead of a Xe PFIB as was done for the other structures.

Despite many factors which can deteriorate the performance of such multilayer based gratings, high and close to expected efficiencies of 61 % at 17.5 keV and 81 % at 60 keV are realized. In order to fabricate more efficient gratings also for thinner layers, the biggest contributors to imperfections have to be addressed. For thin layers, this is the layer mixing. This might require a different way of depositing the layers or a different pair of materials. The latter can also be used to tune the optimum thickness and/or increase the optimum efficiency. Using active feedback to control and correct for sputter rate drifts, the change in period can be reduced.

For the fabrication of MLLs, a few things can be learned. While the optimum thickness is almost independent of the period for an ideal structure, layer intermixing causes τ_{opt} to shift to larger values for thinner periods. The ideal structure of an MLL is hence a trapezoid, thicker at the thin layer part. Since the FIB does not produce straight walls as mentioned before and multilayer depositions usually start with the thin layers, the MLL shape has already the right trend, being more optically thick at the thin layers. Increasing the size of the lens by starting with thinner layers further off axis only increases the effective NA by a limited amount. If the layer periods are close to- or below the layer interdiffusion value σ, they are expected to not contribute to the overall diffraction of the lens as their efficiency reduces to 0. Furthermore, the achievable efficiency can be increased by allowing Γ to change to lower values. Since this requires the layers of the denser material to reduce in size, it might be suited best for lower NA lenses, where the thinnest layers are considerably thicker than the layer interdiffusion σ. Fabricating MLLs from lower Z materials with less absorption could also be a path for higher efficiencies [72]. One should not neglect here that the layers in the multilayer are still required to form smooth interfaces, stay amorphous over the full range of periods present and that the stress in the multilayer is required to stay small enough to not cause delamination [72].

3.4 Hard X-ray interferometer

While determining the thickness of maximum reflection efficiency of multilayer gratings is relevant in order to fabricate high efficiency MLLs, they also have many independent applications. Their dispersive properties can be used as spectrum analyzers or they can be used as beamsplitters, for example. A useful beamsplitter is required to have good efficiency and a sufficiently large splitting angle, as to create two (or more) beams which separate on reasonable length scales. Since multilayer gratings with nm periods produce large angular deviations with high efficiency, they are excellent candidates for beamsplitters in the hard X-ray regime. Below is a design example of a hard X-ray interferometer based on a skewed Mach-Zehnder geometry with multilayer gratings as beamsplitters.

Interferometers for light around the visible spectrum typically use optics rotated 45 degree with respect to the beam, as to create reflections at 90 degree angles. Such large angles are not possible for hard X-rays, instead, a Mach-Zehnder interferometer skewed from a rectangle to a parallelogram can be adopted. A sketch of such a skewed interferometer is shown in figure 3.11. In order to realize a geometry in which movement of a single motor induces a path difference between the two beams, a setup in which each of the two beams is reflected twice instead of once is proposed. A schematic is shown in figure 3.12. The incident beam intersects the first multilayer grating at the Bragg angle θ, resulting in a reflected beam at 2θ and a refracted beam along the initial direction. For a $50 : 50$ split, the optical thickness of the multilayer has to be below τ_{opt}, where the intensity distribution of the two beams is equal. Each beam is then reflected twice at half the angle, which can be realized with multilayer coated mirrors in Bragg geometry, with half the period of the grating. They are then recombined on a second, identical multilayer beamsplitter and the interference signal can be recorded on a photon counting pixel detector, like the

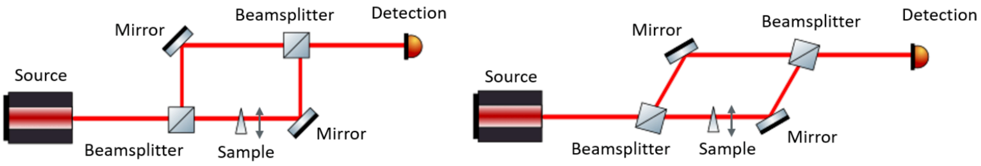

Fig. 3.11: Classical (a) and skewed (b) Mach-Zehnder interferometer [166, 167]. The skewed geometry allows shallower angles.

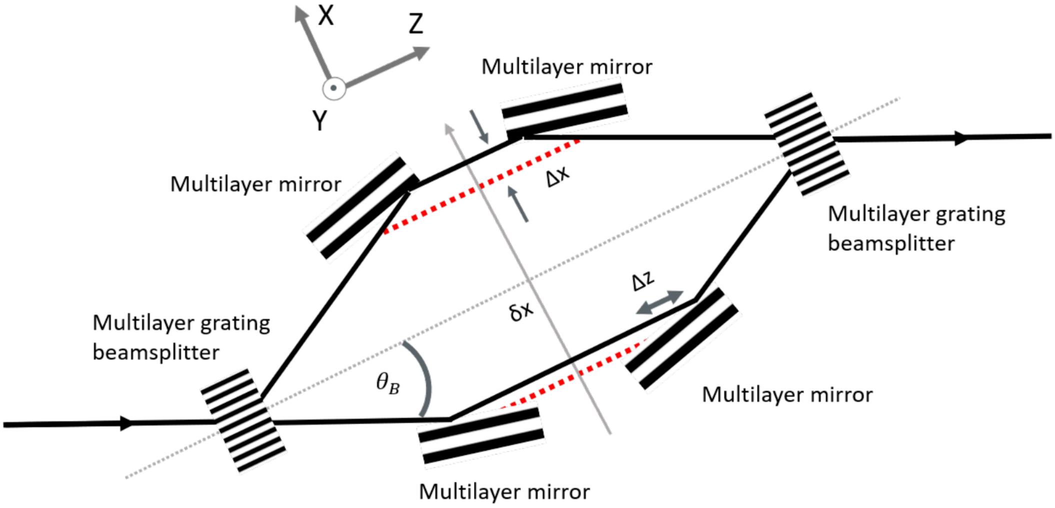

Fig. 3.12: Hard X-ray interferometer schematic based on a skewed Mach Zehnder interferometer using multilayer optics. Translation of the four mirrors along X on a joint stage induces a path difference between the two beams. Multilayer gratings in Laue geometry are utilized as beamsplitters and multilayer coated mirrors as mirrors.

LAMBDA detector, for example. The four mirrors have to be placed on a joint stage allowing movement along X (note that X is not orthogonal to the beam direction but offset by θ instead). A movement of the four mirrors on a joint stage of δx along X results in an optical path difference (OPD) of

$$OPD = 4\sin(\theta)\delta x \approx 4\theta\delta x. \tag{3.1}$$

A large path difference therefore requires a large deviation angle θ, which is why structures with nanometer periods are required. One has to note here that a change in X also causes the position on the mirror of which the beam reflects to shift along Z. This shift is given by

$$\Delta z = \frac{\sin(\theta)}{\tan(\theta)\cdot\tan(\theta/2)}\delta x \approx 2\frac{\delta x}{\theta}. \tag{3.2}$$

Even for thin periods, this distance is large, compared to the OPD, as it scales inversely with θ. The multilayer mirrors therefore need to be significantly extended along Z. This requires the surface to be ultra-flat (radius of curvature $\geq$ 1 km), such that the angle does not change under a lateral movement of the beam. The multilayer mirrors have to be coated onto a thick enough substrate as to not induce bending. To ease the alignment of the beams along the Y direction, the surface should be sufficiently large. Figure 3.13 shows a realistic design for such an interferometer, with multilayer mirror substrates being about 5 cm $\times$ 3 cm $\times$ 1 cm (Z $\times$ Y $\times$ X) in size and θ_B on the scale of 1°, requiring a period of 4.4 nm at an energy of 8.05 keV (Cu Kα), for example. To allow precise angular positioning of the mirrors, they are required to rotate around the Y axis and at least one has to be able to rotate around the Z axis, to ensure spacial overlap of the two beams at the position of the second grating. The grating beamsplitters have to be placed close to the setup. To allow optimal alignment, they require controllability in all translational and rotational directions of motion, which can be ensured by use of hexapods. To allow all stages to be in close proximity they could be placed hanging upside down. Such a setup can

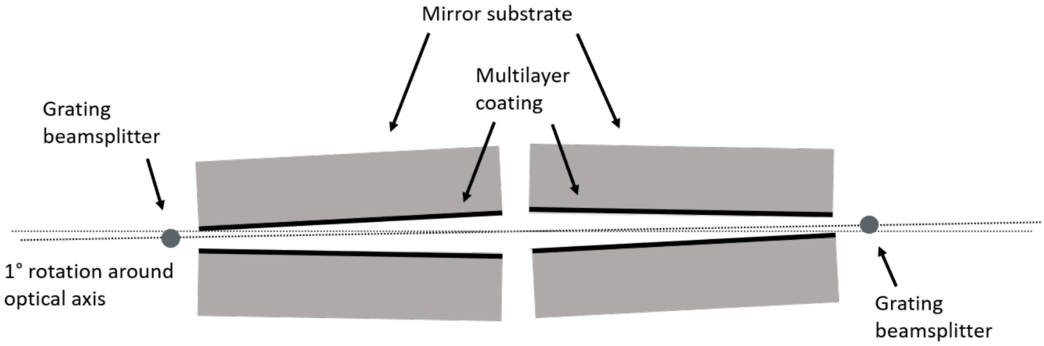

Fig. 3.13: Interferometer design with realistic angles and relative sizes. The tilt around the optical axis is equal to θ_B at 1°. The grating beamsplitters have to be close to the large mirrors.

for example be used to determine the spectrum of the source (or samples), through Fourier transform spectroscopy.

4

Multilayer Laue lens characterization

All measurements shown in this chapter were carried out and evaluated by myself, unless specifically stated otherwise. All images and plots in this chapter are made by myself, unless stated otherwise in the figure caption. The multilayers were deposited and the lenses were cut and mounted by colleagues.

The importance of wavefront metrology and the limitation of MLL performance through systematic layer misplacements during the deposition process are both emphasized throughout this work. In order to not rely on sparse beamtime access for lens characterization, the laboratory testing station described in chapter 2.5 was set-up, which allows fast feedback on multilayer depositions. It is a powerful tool to complement experiments at large-scale facilities. However, this tool is only relevant, if the results acquired are precise and accurate. This chapter therefore present a thorough analysis of what requirements have to be met in order to fully and quantitatively characterize an MLL using the laboratory setup. The wavefront reconstructions are done using the robust speckle tracking software suite introduced in chapter 2.4.2. The study on characterization parameters includes requirements on the lenses themselves, what kind of samples can be utilized and how the measurement has to be conducted, in order to correctly determine the lens properties.

4.1 Energy determination

For a lens's wavefront to be characterized, sufficient intensity is required over the full range of angles (full NA). Since an MLL is optimized for a specific energy, this is only the case if this optimum working energy of the lens coincides with (or is close enough to) the probing energy of the source. For accurate wavefront determination, a lens matching the energy of the source has to be cut. It is obvious, when the energy matches, as the full range of angles will show high efficiency at a single lens tilt. However, if it is not matching, the difference has to be measured based on which a new position along the multilayer profile can be determined, from which the correct energy can be cut. In addition, when a lens for a specific energy is to be prepared which does not match any of the available targets in the source, a verification of the energy is required. The wavefront of a such a lens can be measured by first preparing an MLL with an optimum working energy which matches one of the available energies of the laboratory X-ray source and subsequently cutting a lens for the required energy. Since the wavefront aberrations are encoded in the multilayer structure, such two lenses have the same aberration. The first step of the lens characterization procedure is therefore determining the optimum working energy of a lens. It will become apparent that the probing energy and optimum lens energy do not have to be close to each other for high determination accuracy.

The first section of this chapter presents on the determination of the ideal operating lens wavelength λ_m. As introduced in chapter 2.5.1, λ_m can be determined from a $\omega - 2\theta$ plot - showing which parts of the lens efficiently diffract based on the lens tilt. Figure 4.1 shows a few examples of such plots for the energy determination of three lenses, one where $\lambda_m > \lambda_p$ and therefore $E_m < E_p$ (a), one where $E_m = E_p$ (b) and one where $E_m > E_p$ (c), measured at a photon energy E_p of 17.5 keV. One can see that only for (b), high efficiency can be achieved for the full 2θ range at a single tilt ω. The optimum energy of the lenses in cases (a) and (c) can be determined from the linear fit indicated by the red line using equation 2.16. Such result in E_m = 15.2 keV in (a) and E_m = 36.9 keV in (c). The easiest way to make a linear fit

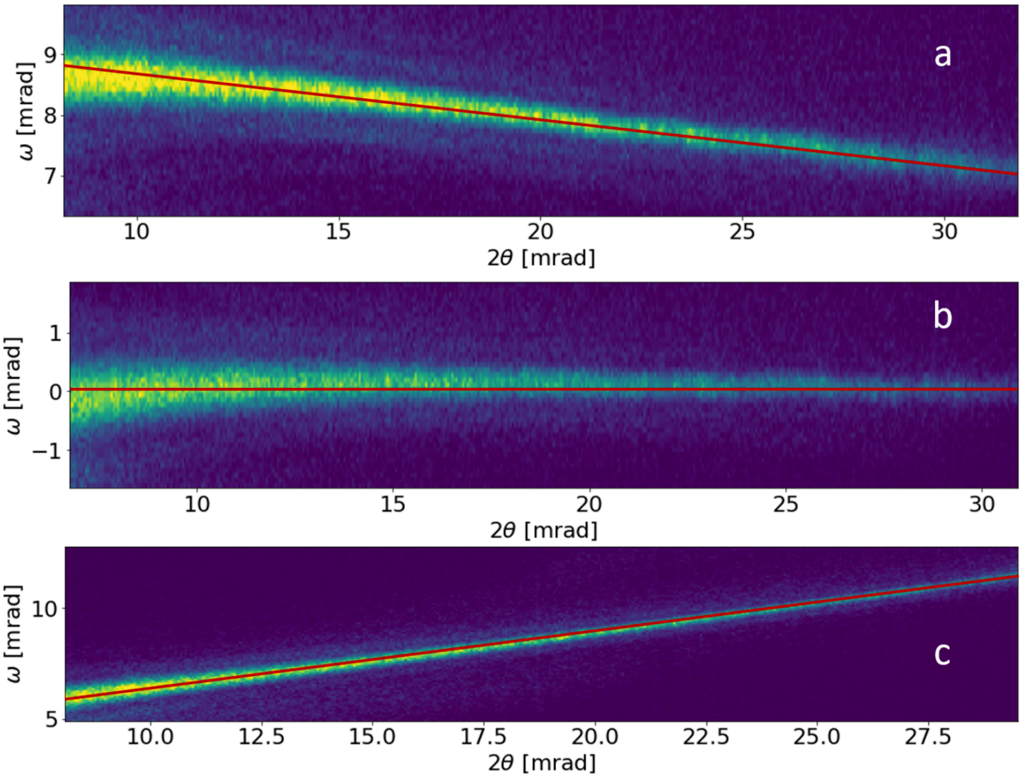

Fig. 4.1: $\omega - 2\theta$ plots for energy determination of lenses. The probing energy E_p is 17.5 keV in all three cases. A case there $E_m < E_p$ (a), $E_m = E_p$ (b) and $E_m > E_p$ (c). The red lines indicate linear fits from which the optimum energy E_m can be determined. These are 15.2 keV (a), 17.5 keV (b) and 36.9 keV (c).

to the diffraction line is to determine where along ω the intensity is highest at any given point along 2θ. However, if a lens is prepared to be used at an energy different from the probe, it is also required to have a different thickness τ_{opt}. This causes a broadening of the line when probed at the incorrect energy, which, together with fluctuations, can cause the fit to not accurately represent the optimal energy. Instead, additionally fitting a Gaussian along ω at each point along 2θ allows to smooth the diffraction line center and more accurately represent the trend that determines the optimum energy. Figure 4.2 shows an example of a lens optimized for about 70 keV, measured at 17.5 keV. Since the lens is much thicker than optimal for 17.5 keV, the diffraction line is wide which causes large deviations of the brightest part from the center at some points along 2θ. The smoothing step results in a line more accurately representing the trend of the $\omega - 2\theta$ plot. In principle, only two lens tilts are required for a linear fit. However, more points allow robustness against noise and intensity fluctuations of the source. While the diffraction line is supposed to be a straight line, effects such as stress can cause it to bend. A higher sampling rate is therefore also beneficial to determine the quality, diffraction efficiency along the lens height and straightness of the line. For such a measurement, three parameters are of highest importance. The tilting step size, which determines the resolution $\delta\omega$. The detector distance, which, based on the NA of the lens and at a given pixel size, sets the resolution $\delta 2\theta$, and the exposure time, which determines the signal to noise ratio (SNR). The number of scan steps and the scanned range are determined by the step size and the trivial goal, that the full signal range should be covered.

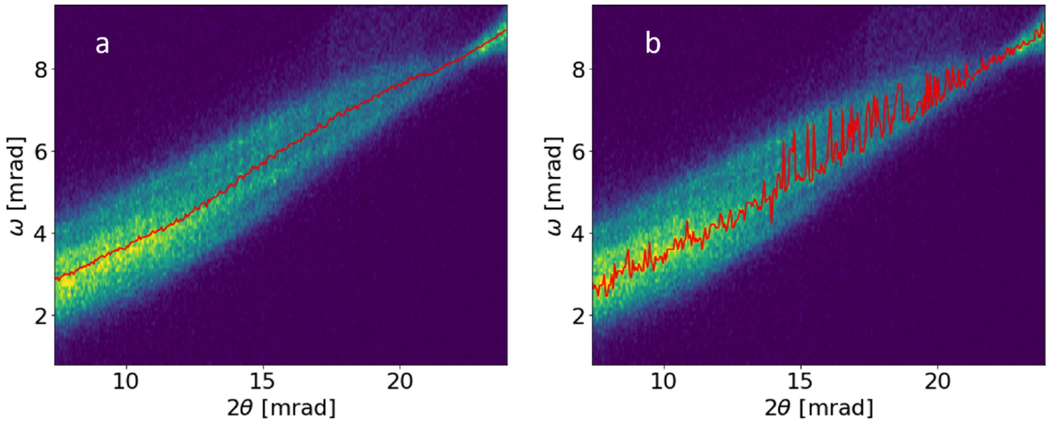

Fig. 4.2: Energy scan with (a) and without (b) smoothing of a lens optimized for an energy of about 70 keV with a thickness of 35 μm, which is higher than optimal for the probe energy of 17.5 keV. The red line indicates the positions of highest intensity in (b) and the center of the smoothing Gaussian in (a). The energy is determined from a linear fit to the red lines.

To test which parameters are most crucial to accurately determine the optimum energy, a series of scans was conducted, varying $\delta\omega$, $\delta 2\theta$ (by changing the detector distance) and the exposure time t, for a lens with $E_m = E_p$ (here referred to as lens 1) and a second lens with $E_m > E_p$ (here referred to as lens 2). The starting values of the parameters are $\delta\omega = 5$ mdeg for lens 1 and $\delta\omega = 10$ mdeg for lens 2, $\delta 2\theta =$ 3.15 mdeg, resulting from a pixel size of 55 μm at a detector distance D_{det} of 1 m and $t = 10$ s, from where one parameter was varied each time. It had previously been shown that these parameters can be used to accurately determine the optimum energy, both for lenses with energies matching and deviating from the probe [114]. The scan range is 200 mdeg for lens 1 and 500 mdeg for lens 2. At each parameter combination, a measurement was conducted and a $\omega - 2\theta$ plot obtained. The lens energy E_m was then retrieved from a linear fit to the Gaussian smoothed center of the diffraction line. A summary of the results are given in tables 4.1 to 4.5.

Tab. 4.1: Optimum energy E_m depending on $\delta\omega$ for lens 1 at a constant $\delta 2\theta$ of 3.15 mdeg and an exposure time t of 10 s.

$\delta\omega$ Lens 1 [mdeg]	2.5	5	10	20	40
number of steps	80	40	20	10	5
Lens 1 energy [keV]	17.45	17.45	17.47	17.35	17.45

Tab. 4.2: Optimum energy E_m depending on $\delta\omega$ for lens 2 at a constant $\delta 2\theta$ of 3.15 mdeg and an exposure time t of 10 s.

$\delta\omega$ Lens 2 [mdeg]	10	20	41.7	83.3
number of steps	50	25	12	6
Lens 2 energy [keV]	52.9	53.1	56.2	67.7

Tab. 4.3: Optimum energy E_m depending on $\delta 2\theta$ with a fixed exposure time t of 10 s and a constant $\delta\omega$ of 5 mdeg for lens 1 and 10 mdeg for lens 2.

$\delta 2\theta$ [mdeg]	1.58	3.15	6.30	12.60	31.5
D_{det} [m]	2	1	0.5	0.25	0.1
Lens 1 energy [keV]	17.47	17.45	17.43	17.43	17.43
Lens 2 energy [keV]	53.3	52.9	53.0	53.3	54.4

Tab. 4.4: Optimum energy E_m depending on $\delta 2\theta$ where t/D_{det} is kept constant at 10 [s/m] and $\delta\omega$ constant at 5 mdeg for lens 1 and 10 mdeg for lens 2.

$\delta 2\theta$ [mdeg]	1.58	3.15	6.30	12.60	31.5
D_{det} [m]	2	1	0.5	0.25	0.1
t [s]	20	10	5	2.5	1
Lens 1 energy [keV]	17.46	17.45	17.43	17.44	17.45
Lens 2 energy [keV]	53.1	52.9	53.1	53.4	54.1

Tab. 4.5: Optimum energy E_m depending on the exposure time t at a constant $\delta 2\theta$ of 3.15 mdeg and $\delta\omega$ constant at 5 mdeg for lens 1 and 10 mdeg for lens 2.

t [s]	20	10	5	2.5	1
Lens 1 energy [keV]	17.44	17.45	17.46	17.47	17.37
Lens 2 energy [keV]	52.8	52.9	53.0	52.9	53.2

With only one exception (lens 2 measured with $\delta\omega = 83.3$ mdeg, see table 4.2), all values are close to each other within a few percent. It might initially be surprising, that accurate energy determination does not depend much on either $\delta 2\theta$, D_{det}, $\delta\omega$ or t. However, it was mentioned earlier, that only a minimum of two points is in principal required for a linear fit. With the default parameters, many more points are available (40 for lens 1 and 50 for lens 2), which results in stable energy determinations, even if the number of points is reduced by, for example, increasing $\delta\omega$. One should note here that due to the nature of equation 2.16, even a large change of energy does not lead to a big change in the slope if $E_m \gg E_p$ (and therefore $\frac{\lambda_m}{\lambda_p} \ll 1$). Considering that the energy of lens 2 is about three times as large as the probe energy, the energy determination precision is impressive. Since the lenses have high diffraction efficiency, the signal to noise (SNR) ratio is sufficiently high even for short exposure times.

4.1.1 Variable energy lens

While a regular MLL as the ones mentioned before can only be optimized for a single energy, a lens can be fabricated where the working energy can be quickly changed over a range of multiple keV, by means of a simple translation [168]. It should be noted here, that this lens does not have an increased bandwidth, instead, individual energies can be chosen based on the section of the lens that is utilized. When preparing two lenses with different energies from the same multilayer, they have to be cut at different positions along the gradient profile [35]. By cutting a long lens not orthogonal to this profile but under an angle (25° to 30°, for example), the height of the lens and thereby also the layer wedge and the optimum energy E_m changes along the width of the lens. An example of such a lens can be seen in figure 4.3 which is 500 μm wide. The height of the multilayer and thereby the optimal energy E_m changes along the horizontal direction. Since two lenses have to be combined for 2D imaging, only a fraction of the lens width, equal roughly to its height (more precisely, the multilayer height of the second lens) is exposed to X-rays and contributes to the 2D focusing. Within this range, E_m only varies slightly which allows efficient diffraction at a single probing energy E_p as long as all layers within this range lie within the Darwin width. To determine the range of energies for which this lens can be utilized, a 75 μm pinhole was employed to illuminate only a fraction

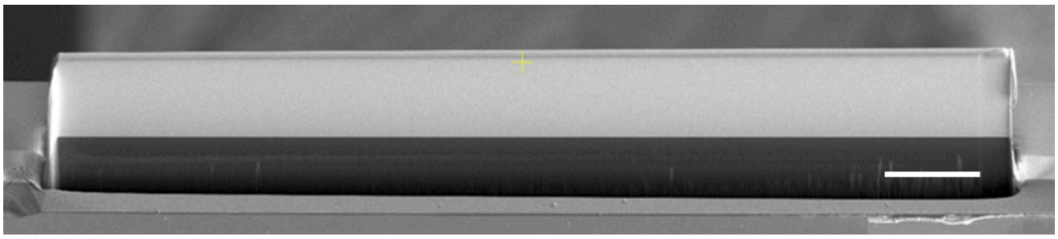

Fig. 4.3: SEM image of a long lens for a range of energies. The lens is slightly higher at one end, due to the gradient of the multilayer deposition. The scale bar is 50 μm. Reproduced by courtesy of M. Prasciolu.

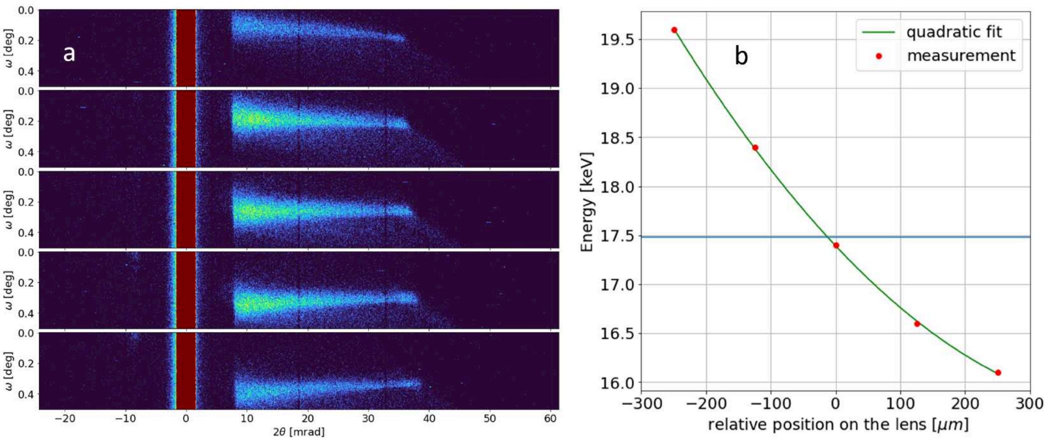

Fig. 4.4: An example of the range of energies present in a long lens. Energy scans at five positions along the lens width (a) and the corresponding energies E_m (b). The blue line in (b) shows the probing energy E_p, which matches E_m close to the center. The change of energy can, in this case, be roughly followed by a parabola.

of the lens. Five energy scans with the pinhole positioned at five different positions along the lens width were conducted. The resulting $\omega - 2\theta$ plots are shown in figure 4.4 (a). A clear trend of a change in the slope can be seen, where one end of the lens has $E_m > E_p$ and the other $E_m < E_p$. The corresponding energies E_m are given in (b). The change in energy can be approximated by a parabola in this case, as indicated by the fit. This lens covers a range of energies from about 16.1 keV to 19.6 keV. The energy of the probe E_p matches E_m roughly in the center of the lens.

One has to note here that since the lens is cut under an angle, it should be placed under that angle in the beam as well, as to keep the direction of the gradient parallel to the beam direction. When a change of operating energy is desired, the overlap region of the lenses has to be translated to the corresponding lens parts and the distances to the sample has to be adjusted, since the focal length scales with the energy. Such a setup could be interesting for beamlines offering nanofocusing optics over a range of energies. Once the positions for various energies are aligned, a user may swap between them with only a few clicks within seconds. This system could for example be used to probe a specimen above and below an absorption edge of a material present in the sample, to gain additional contrasts.

4.1.2 Stress induced lens bending

While wedging of the layers of a lens can be achieved with a mask as is done here, it can also be accomplished with a stress layer, deposited onto the front or back surface of a flat lens which causes elastic deformation due to a compressive stress [95]. This raises the question whether it can also be used to change the energy of a lens, as such a stress layer should in principle allow the zone plate formula to be full-filled for a different energy. A physical bend of the lens [96] or a constant thickness offset in the layers Δd can cause the diffraction line to bend, leading to the relationship between ω and θ to deviate from a linear slope. Such a lens is difficult to characterize, as there might not be a lens tilt ω where high diffraction efficiency can be achieved for the full 2θ range, even for a lens where $E_m = E_p$. This is because it could be that $E_m > E_p$ for one part of the lens and $E_m < E_p$ for another. Added local stress could bend the lens back (or induce a bend to offset the bending from a Δd), resulting in a straight diffraction line. Such a local stress can be added by coating one side of the lens with a thin carbon layer. Such a layer could be of constant thickness to add the same amount of stress everywhere or wedged as to induce a stronger effect in one part of the lens than in another (see fig. 4.5). To test these hypotheses, a lens with a bent diffraction line and an optimal energy varying from the probe was chosen to be coated (see fig. 4.6 (a)). To un-bend the diffraction line, one end of it should remain about the same while the other is required to change. This could be achieved by coating a linear wedged layer onto one side of the lens, for example. Since a wedged layer is difficult to deposit with a FIB, a staircase with 10 steps is adopted as an approximation of the wedge. To try to unbend the diffraction line of the lens, a linear staircase as sketched in figure 4.5 (c) changing from 0 to 200 nm in 20 nm steps was coated on the front side (downstream) of the lens. The resulting energy scan is shown in figure 4.6 (c). The line does appear much straighter. To quantify the bending of the line, a parabola was fitted to it. Ideally, the quadratic coefficient should be 0, for a straight line. Through the coating, the parabolic coefficient (in arbitrary units, only relevance here is the relative change) reduced from 76.1 to 25.1. Assuming a linear relationship, an additional 50 % of the previous coating was added, resulting in a total thickness changing from 0 to 300 nm. This caused the parabolic coefficient to further reduce to 2.8, indicating indeed a linear relationship between coating thickness and bending of the line. The energy measurement is shown in 4.6 (e). Note how the line is unchanged at large 2θ values and the bend happens at small 2θ values. This is expected as the large angles, resulting from small layers at the bottom, are coated least.

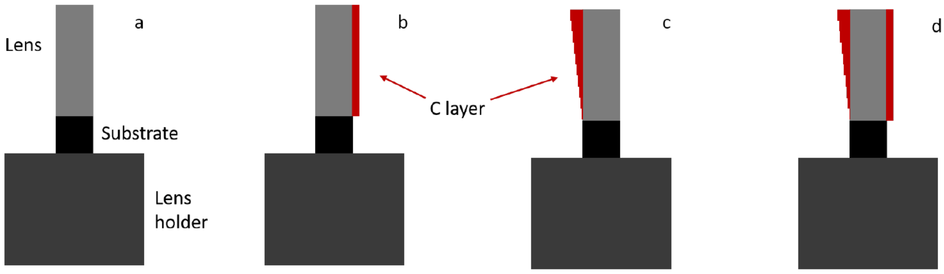

Fig. 4.5: Schematic of a carbon layer coating used to bend the lens to change the energy and curvature of the diffraction line. A lens without coating (a), a constant coating to change the energy (b), a staircase coating to change the bending of the diffraction line (c) and a combination of both (b) and (c) in (d).

The next step was to test whether a constant layer thickness can be used to change the energy of the lens. A 200 nm thick carbon layer was added to the backside of

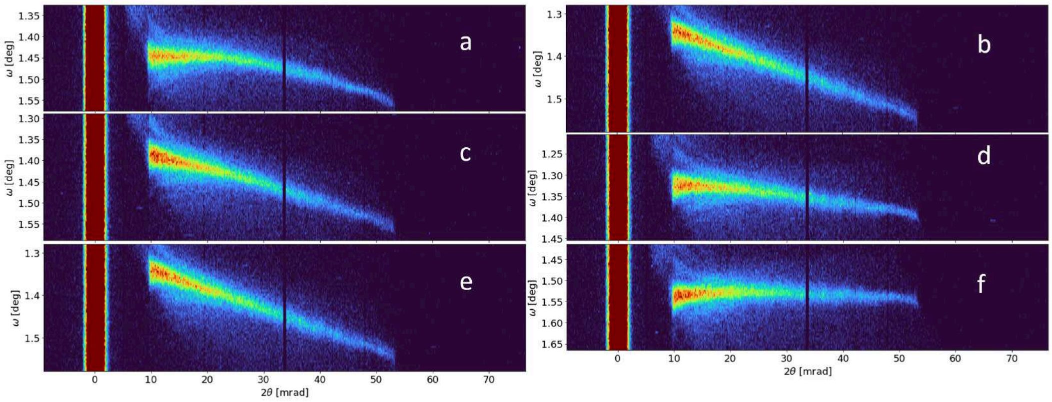

Fig. 4.6: Change of the energy scan of a lens by coating it with carbon layers. Lens without carbon layer (a). After a staircase coating on the front scaling linearly from 0 to 200 nm (c) and 0 to 300 nm (e). (b) Same as (e) for vertical comparison. After applying a constant 200 nm (d) and 300 nm (f) coating on the backside of the lens in addition to the 0 to 300 nm coating on the front side.

the lens. This caused the energy to change from 20.9 keV to 18.6 keV, as is shown in figures 4.6 (b) to (d). Assuming again a roughly linear trend, further 100 nm were deposited on the already existing 200 nm layer. The result is shown in figure 4.6 (e) and the optimal energy changed to 17.7 keV, indicating again that the change is indeed close to linear. After the change of energy, the line was slightly stronger bend again, the coefficient increased from 2.8 to 28.2. For an optimized procedure, the change of energy should be done first, targeted at matching E_m and E_p at the high angles. The rest of the angular range can then be un-bent, resulting in a straight line at the correct energy. The carbon layer does not add a measurable change to the wavefront of the lens, which was verified by wavefront scans before and after coating. Since the coatings are thin, they do not reduce the transmitted intensity significantly. Such coatings are a powerful tool to manipulate the lens diffraction behavior to the desired form or to correct for imperfections induced during the fabrication process.

4.2 Wavefront verification

Once a lens of matching energy is obtained, its wavefront can be characterized. Before going into the details about optimum wavefront characterization using the laboratory setup, a "ground-truth" has to be established. Without a verification of the retrieved wavefronts, no statements can be made regarding reconstruction quality. For this purpose, the wavefronts of two lenses were measured at the laboratory setup and then at the beamline P11 at PETRA III, for comparison. The lenses were cut from the same multilayer deposition but from opposite sides with different mask height. They are both optimized for 17.5 keV, with comparable NAs of 0.014 and 0.015 and focal length of 1.25 mm and 1.15 mm, respectively. Their individual wavefronts were measured in the laboratory setup using a set of parameters as shown in table 4.6 using the barcode sample shown in figure 2.15. Their wavefronts were retrieved using RST as described in 2.5.2 and are shown in figure 4.7 (a) and (b), respectively. They were then brought to the beamline P11 at PETRA III, Germany, and aligned to form a common focal spot. Their combined 2D wavefront was retrieved using RST and a Siemens star test sample, with the much higher flux and the high monochromaticity of the synchrotron. Further information can be found here [114]. The scan parameters are given in table 4.6 for comparison. Since the lenses are orthogonal with respect to each other, their 2D wavefront $\phi(x, y)$ can be separated into the individual 1D wavefronts of the horizontal and vertical lenses

Tab. 4.6: Scan parameters for the determination of the lens wavefronts. M is the magnification.

	No. steps	step size [nm]	D_{det} [m]	M	dwell time [s]
Lab	100	100	2	25000	30
P11	20x20	150	2.37	23700	0.1

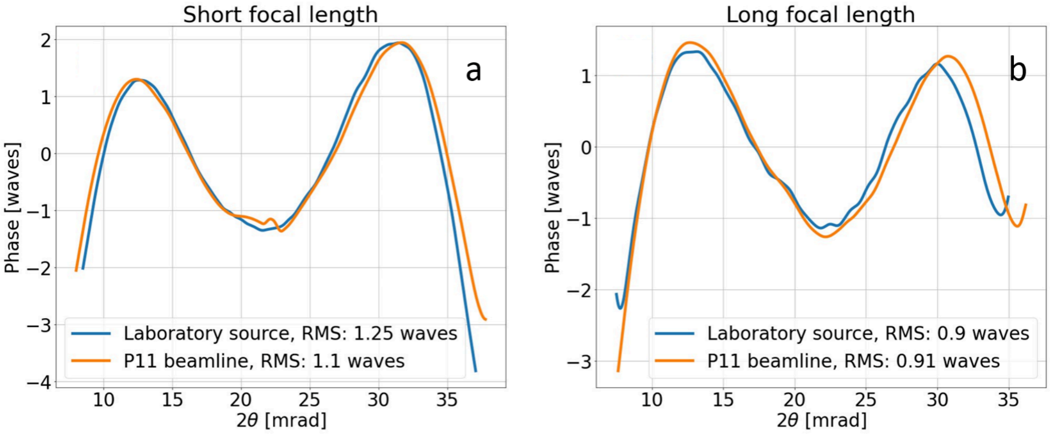

Fig. 4.7: Wavefront of the vertical focusing lens (a) and horizontal focusing lens (b) retrieved individually at the laboratory setup (blue) and decomposed from their joint 2D wavefront at the synchrotron beamline P11 at PETRA III (orange).

$$\phi(x, y) = \phi_{hor}(x) + \phi_{vert}(y). \tag{4.1}$$

Figure 4.7 shows the comparison of the wavefronts measured in 1D in the laboratory and the separated wavefronts from the 2D measurement at the synchrotron. Excellent agreement can be observed, proving the accuracy and correctness of the laboratory-based measurements. Measurement-to-measurement variance is on the same scale as the difference shown here. In addition, slight non-ideal orthogonality of the two lenses causes mixed terms which be separated into the individual wavefronts. Knowing that the laboratory measurement yields accurate results, the importance of various aspects of the lenses, samples and the measurement parameters can be explored. If the lens size or its mount affects the wavefront and what sample feature sizes are required for sufficient phase sensitivity are questions the following sections aim to answer.

4.3 Requirements on the lens

This section focuses on if and how the wavefront reconstruction of a multilayer depends on the lens's properties. This includes the size and shape to which a lens is cut. Since the lens has to be connected to a mount, the dimension and type of connection might change the behavior of the lens, through stress, for example, which is at test. This is relevant since a variation of the mounting scheme might be required depending on the experimental condition. For example, the high peak flux and photon pressure a lens might experience at an X-ray free electron laser (XFEL) requires a very strong and stable connection to the lens holder. A large contact area to the holder might also be necessary for efficient heat transfer. If such a connection induces a change in the wavefront, such would have to be determined and compensated.

4.3.1 Lens size

The size of a 1D MLL is partially predetermined by the goal of combining two lenses together to form a common 2D focal spot. For this, one lens has to be rotated by 90 degrees with respect to the other one. To make use of the full aperture of the lenses, each lens has to be at least as wide as the other is in height. The height here refers to the direction of the multilayer stack and the width to the direction parallel to the layers (and orthogonal to the beam direction). To ease alignment requirements and reduce edge effects, the lens should be at least a bit wider than its height (assuming two lenses of comparable height). Combining two MLLs of similar NA and focal length then requires two rectangular shapes which form an overlap region which is roughly squared.

While making a lens much wider than the second lenses height does not increase the usable area of the beam, it might increase its stability or allows a different mounting scheme. The lens width is not expected to influence its wavefront. To test whether this expectation is correct, three lenses of varying widths were cut from the same multilayer. Our MLLs are typically cut to a width of 100 μm. The three widths tested here were 50 μm, 100 μm and 200 μm. All three lenses were characterized at the laboratory setup and their wavefronts are shown in figure 4.8. They show no significant differences. If the difference in lens width causes a change in stress in the structure, then this has no effect on the wavefront. The lens size can hence be freely varied to match the experimental conditions and the requirements on the lens.

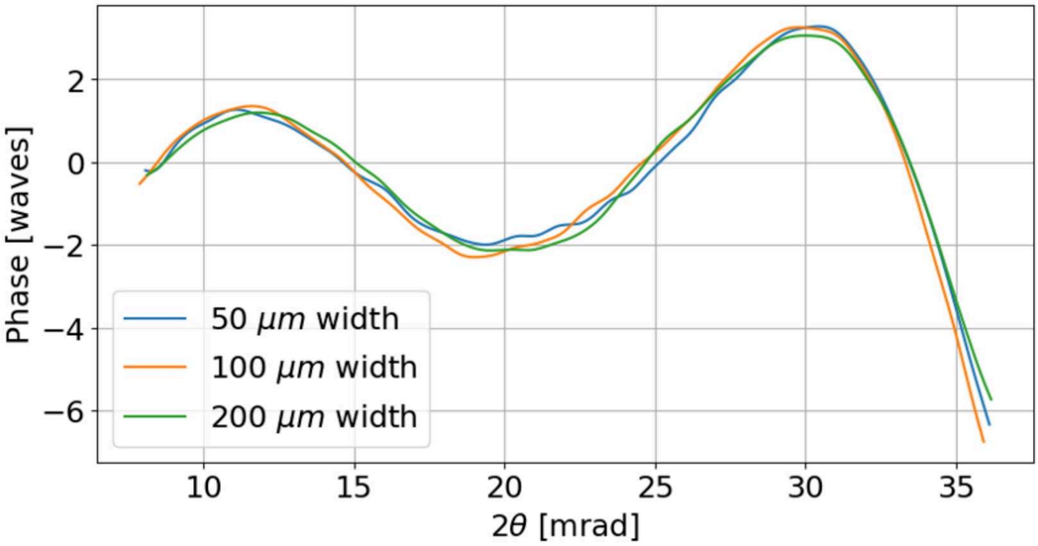

Fig. 4.8: Comparison of the wavefronts of three lenses cut from the same multilayer with a difference in width. The lens height is about 35 μm and the optical thickness is about 8 μm in all three cases.

This can be used to explore novel lens mounting schemes as will be discussed in the following section.

4.3.2 Lens support structure

Lenses so far are mounted in the "standard" configuration which is sketched in figure 4.9 (a) and can be seen in figure 2.7 in section 2.3.1. The lens has narrow supporting structures at the sides and is only connected to the substrate at the edges of those structures. For the use with laboratory setups and synchrotrons, this geometry is sufficient. XFELs however, can provide a peak brilliance several orders of magnitude higher than synchrotrons. The intense ultrashort pulses pose additional demands on the optics and their materials. FZPs have shown to degrade rapidly under intense XFEL beams due to bad heat dissipation [169]. Numerical simulations have shown that the energy deposited in MLLs exposed to XFEL pulse trains lead to a rapid increase in temperature with little heat transport due to the small connection to the substrate [73, 170]. During the commissioning of the MID beamline of the European XFEL (EuXFEL), Prasciolu et al. found that MLLs can survive in XFEL beams with few pulses per train but the low heat dissipation causes temperature gradients which bend the structure [171]. They also noted that the high photon pressure pushed the lenses significantly, causing them to tilt away from their diffraction condition. A larger supporting side structure leading to a larger contact area between the lens and the substrate as shown in figure 4.9 (b) or a new mounting design as shown in figure 4.9 (c) could help to increase the heat transport while also providing additional stability [73].

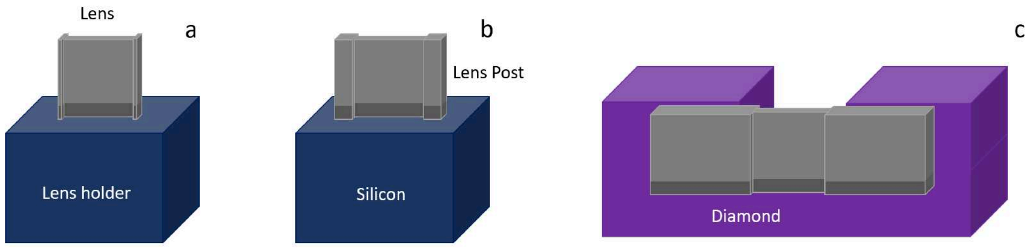

Fig. 4.9: Mounting schemes for MLLs. The standard configuration with small support structures and limited contact area between the lens and holder (a). Much larger supporting structures offering higher stability and more contact area to the holder (b). Large supporting structures with large contact area to the holder for improved heat transfer and stability (c) [73]. A cut-out of the holder behind the lens lets the focused beam pass. The lens holder is made from silicon in (a) and (b) and diamond in (c).

To test whether thicker side structures have an effect on the wavefront, two lenses cut from the same multilayer were fabricated, one in the "standard" configuration with thin supporting structure and one with bigger side posts. Their wavefronts were measured at the laboratory setup using RST. A comparison of their wavefronts is shown in figure 4.10. No significant difference is observed, the lens aberrations are therefore independent of the supporting structure size. This mounting scheme can be used to increase the stability of the lens without losing ease of access to the lens. The drawback is an increase in fabrication time, as an overall larger structure has to be fabricated.

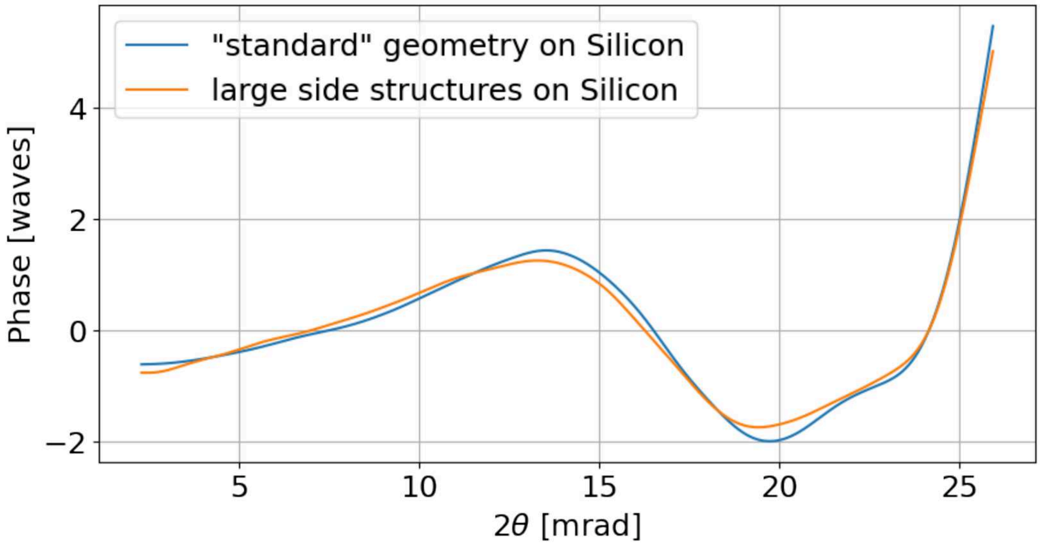

Fig. 4.10: Comparison of the wavefronts of two lenses cut from the same multilayer with a difference in support structure size, as shown in figure 4.9 (a) and (b).

While this scheme increases the stability, the lens is still vulnerable to strong photon pressures which could push it off the holder and the heat transfer is still limited by a rather small contact area. Pushing the lens against the holder as shown in figure 4.9 (c) leads to a significantly larger contact area and a more stable structure, but requires a much larger structure and a cut-out in the holder behind the lens. Since a larger fraction of the lens holder is in the beam using this geometry and a silicon holder survive the intense XFEL beam, it is replaced with diamond, which is less absorptive and offers better heat transport as well. To verify that the change of material and geometry does not significantly change the lens performance, for example through added stress, two lenses were cut from the same multilayer and mounted in the geometries shown in 4.9 (a) and 4.9 (c), respectively. Figure 4.11 shows a comparison of their wavefronts, again retrieved at the laboratory setup using RST. While the two wavefronts are not as close to each other as in the previous comparison shown in figure 4.10, the overall shape and magnitude is comparable. The slight difference is a result of the wavefront of the diamond mounted lens being a bit noisier. This is due to diffraction from the large side structures adding to the signal and slightly washing out the contrast. This is not the case at a large-scale facility where two lenses are combined, as the side structure does not overlap with the second lens and such signal can thus not contribute to the 2D pupil of the lens pair. It can hence be concluded that the lens' wavefront does not depend on the mounting scheme. While the diamond mounted lens offers improved stability and heat transport, its fabrication is lengthy as a much larger piece has to be cut from the multilayer, a cut-out has to be made into the holder and the lens has to be glued to the substrate afterwards. Lenses to be characterized can hence be prepared in the standard geometry, which can be done much faster than the other geometries, and the best lenses to be used for an experiment can be mounted in a varying geometry as required, without a loss of wavefront information.

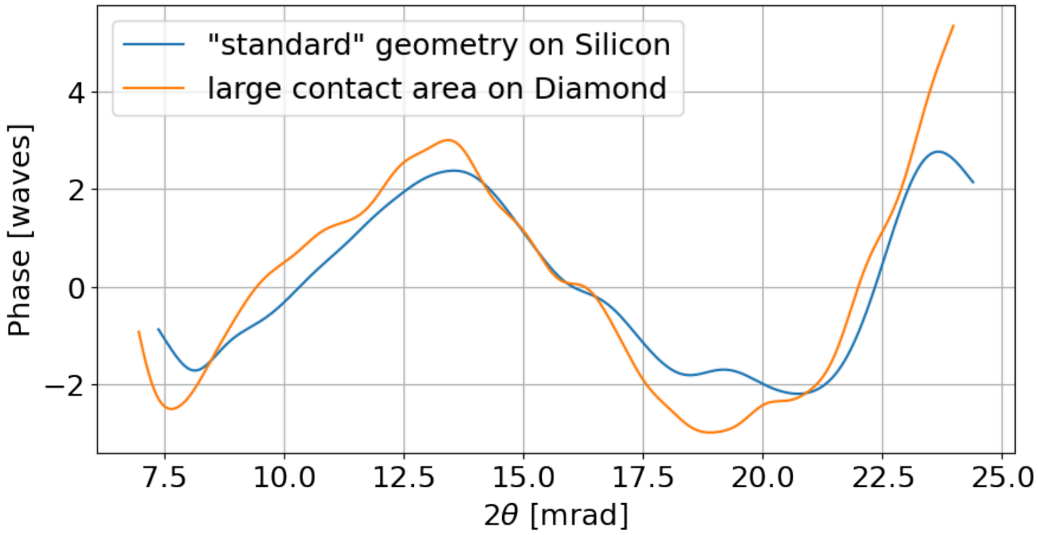

Fig. 4.11: Comparison of the wavefronts of two lenses cut from the same multilayer with a difference in support structure, as shown in figure 4.9 (a) and (c).

4.3.3 On-axis lenses

The primary focus of this thesis is on off-axis MLLs, meaning the lens does not intersect the optical axis, as sketched in figure 2.3 in chapter 2. This allows easy separation of the reflected and refracted beams by use of an order sorting blade (OSB), such that only the focused beam is incident on the sample. In an off-axis lens, the thinnest layers can be deposited first, such that roughness that builds up effects mostly the thicker layers, where its impact is less severe. In order to increase the NA, the lens can be extended to- and beyond the optical axis [172]. For example, a lens of aperture size 40 μm, fabricated off-axis by 10 μm extended to the same diffraction angle on the opposite side of the optical axis would result in an increase of NA by a factor of 2.5. Of course, this would also require the lens to gain in aperture from 40 μm to 100 μm. Such an increase in size can be difficult for off-axis lenses, as thinner and thinner periods would be required, which pose challenges on the fabrication. The on-axis lens, as is referred to here for lenses intersecting the optical axis, of above example would have the same smallest period as the 40 μm off-axis lens, while being 2.5 times larger.

Such a design nevertheless poses additional challenges. Since the periods have to increase in size up to the optical axis before decreasing again, only the thin layers at the start of the multilayer deposition show low roughness, while the build-up roughness effects the sensitive thin layers at the end, leading to an asymmetry of layer roughness between the two lens halves. For a wedged lens, a slight asymmetry of the layer tilts between the two lens halves would also be present. Since the reflected and refracted beams overlap, a combination of central beamstop and an OSB is required, to block the reflected beam, as is done with Fresnel zone plates.

The missing part in the center of a symmetric on-axis lens poses a challenge to the wavefront reconstruction. No wavefront information about the central part of the lens can be retrieved due to the lack of signal in that range. However, the relative phase between both sides is important, since both lens halves only focus to a common spot, if their separation distance is correctly following the zone plate law.

To test the performance and fabrication feasibility of an on-axis lens, a multilayer was deposited with layer thicknesses changing from thin to thick to thin. An on-axis lens optimized for 17.5 keV was prepared from it with a total multilayer height of 58.3 μm. It was characterized with the laboratory setup without a beamstop or OSB. The resulting ptychograph is shown in figure 4.12 (a). The sample features can be seen on both sides of the optical axis (set here to be at $2\theta = 0$) continuing through the center. The central part where the focused- and refracted beams overlap is masked out. The displacement map, proportional to the phase gradient, can be well reconstructed in regions outside the center as can be seen in figure 4.12 (c). Since there is no signal in the central part, the reconstruction in that range only shows noise. The trend within that range can however be well estimated from the

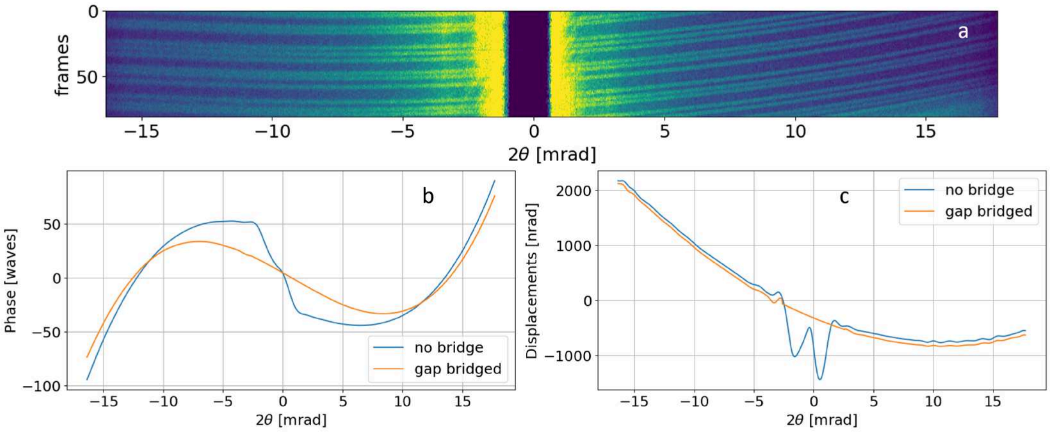

Fig. 4.12: Wavefront reconstruction of an on-axis MLL. The ptychograph (a), wavefront (b) and displacement map (c) are shown. Due to the gap in the center, no meaningful reconstruction is possible in this range. For a more accurate estimation of the wavefront, the gap can be bridged by a fit to the surrounding data prior to the wavefront calculation as shown in (c).

shape of the displacements outside the center. The trend over the full aperture of the lens follows a parabola. By fitting a second order polynomial to the data outside the center, the gap in the center can be bridged, resulting in a much smoother shape and likely a better representation of the behavior within the gap. This also leads to a better reconstruction of the wavefront, as the noisy displacement map in the center causes a bad phase reconstruction within the same range, as can be seen in figure 4.12 (b). Of course, in this example, the trend in the displacement map is smooth and bridging the gap is straightforward. If the trend is less clear and much noisier, such bridging might not be possible. Still, using RST, the relative offset or shift in the displacement map of the two lens halves could be well retrieved, if the separation distance between them would be incorrect, it would be visible there. This test shows that on-axis lenses can be fabricated in a comparable fashion to off-axis lenses and their wavefront can be reconstructed using RST. By combining two on-axis lenses, the aperture and therefore the number of photons collected by such a lens pair could be more than quadrupled, even when employing a central beamstop. To only let the beam focused by both lenses be incident on the sample, a cross-shaped beamstop has to be employed. Using only a rectangular beamstop placed in the center of the lens pair in combination with an order sorting aperture (OSA) would result in the 1D foci of the lenses also illuminating the sample, which could be interesting for multi-beam experiments. Additionally, by intentionally adding an offset between the two lens halves, a lens pair would produce four foci with a designed offset between them, which could be used for multi-beam illumination as well.

4.4 Requirements on the sample

This section aims at determining the kind of samples that are suited for wavefront reconstruction. While PXST is supposed to work with a range of prior unknown samples, they are still required to be "speckly" (= containing sufficient resolvable and traceable features) and their feature size and feature density still determine the sensitivity of the phase reconstruction. Beyond that, a sample to be routinely used in the laboratory setup should not be barely traceable but should have clear features which allows reconstruction even under non-optimal conditions, which might occur due to misalignments of the lens or sample or inefficient optics.

4.4.1 Materials and feature size

First, to be able to trace a sample, it needs to be visible in the projection holograms. This requires the sample to, at least partially, have structures made out of dense materials and/or be thick along the optical direction. Next, the phase sensitivity $\Delta\phi$ in PXST is given as [58]

$$\Delta\phi \approx \frac{2\pi}{\lambda}\frac{\sigma_{\text{eff}}^2}{zM}. \tag{4.2}$$

Here, σ_{eff} is the smallest feature (= speckle) that can still be resolved and M is the magnification of the projection, given as $M = (z_1 + z)/z_1$, where z_1 is the defocus distance of the sample and z the distance from the sample to the detector. The reconstruction precision is hence most sensitive to the feature size. A suitable sample should therefore consist of fine structures. However, the features are still required to be resolvable. If they are too fine, neighboring features be distinguished, especially in non-optimal alignment conditions. The smallest features that can be resolved depend on the source size and the lens resolution. Based on previous measurements, the smallest features that can be resolved with the laboratory setup are estimated to be around 80 nm. Since a single 1D lens produces a line focus, a sample is required to have features which vary only along one direction. Based on these initial considerations, barcode-like structures were chosen as suitable samples. Such can for example be aperiodic multilayers, which can readily be deposited using magnetron sputter deposition using the same machines used to fabricate lenses and gratings. By depositing layers of two different materials, high contrast as well as precise thickness control can be achieved. A sample of arbitrary width and optical thickness can then be cut from the multilayer stack. The resulting sample is meant to be oriented with the lines parallel to the line focus of the lens. Such barcode-like structures can also be fabricated by lithography where larger structures can be fabricated quickly but the lines are limited to larger thicknesses. Table 4.7 shows the key parameters of three samples that were prepared. S1 and S2 are multilayer based samples and S3 is made with optical lithography. SEM images of S1 and S2 as well as an optical

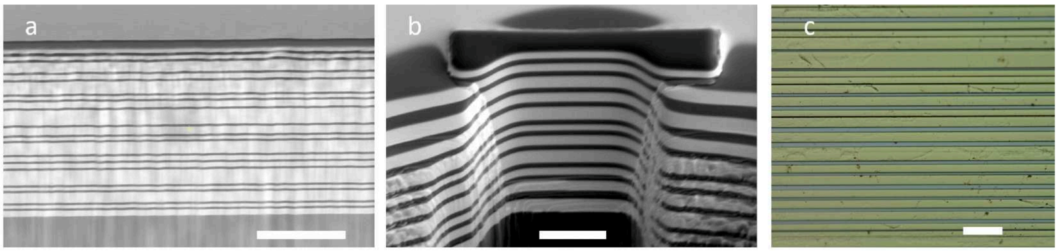

Fig. 4.13: SEM images (a) and (b) and an optical microscope image (c) of samples S1 to S3 (see table 4.7). Sample S1 contains feature sizes between 180 nm and 1000 nm (a) which are between 500 nm and 1500 nm for sample S2 (b). S1 and S2 are aperiodic multilayers. Sample S3 covers feature sizes between about 2 μm and 40 μm and is lithographically made from Gold. The scale bars are 5 μm in (a) and (b) and 50 μm in (c). SEM images (a) and (b) reproduced by courtesy of M. Prasciolu.

Tab. 4.7: List of samples and their properties. Sample S2 contain three different thicknesses next to each other.

Sample	S1	S2	S3
Smallest feature [nm]	180	500	2000
Largest feature [nm]	1000	1500	20000
Thickness [μm]	7	3, 6.5, 11	7
Material	WC/SiC	WC/SiC	Au
Fabrication	Sputtering	Sputtering	Lithography

microscope image of S3 are shown in figure 4.13. To compare their usability, all three samples were imaged with the same lens. For S2, the part with a thickness of 6.5 μm was used. Since S3 has much larger feature sizes, a step size of 100 nm and a scan range of 10 μm as used before would show only a single or no features. To cover multiple features, the step size was increased to 500 nm and the scan range to 50 μm respectively, to keep the same number of exposures while covering a larger range. The sample to detector distance was 1.4 m in all three cases with an exposure time of 30 s per frame. The resulting ptychographs are shown in figure 4.14 (a) to (c). The sample features are well resolved with high contrast in (a) and (b) but have blurry edges in the case of (c), potentially resulting from non-vertical side walls. Using RST, the wavefront of the lens was reconstructed from all three measurements. The resulting wavefronts are shown in figure 4.14 (d). The wavefront is well reconstructed in the case of sample S1 and sample S2 but the measurement did not result in an accurate reconstruction of the wavefront using sample S3. This is likely due to the larger feature sizes and blurry edges, which reduce the phase sensitivity as evident from equation 4.2. No significant difference between S1 and S2 is observed, indicating that the larger feature sizes of S2 already satisfy the required phase sensitivity for lenses with comparable NAs and aberrations as the one under investigation. For lenses with much lower aberrations, the finer structures of S1 might be required for accurate phase reconstruction.

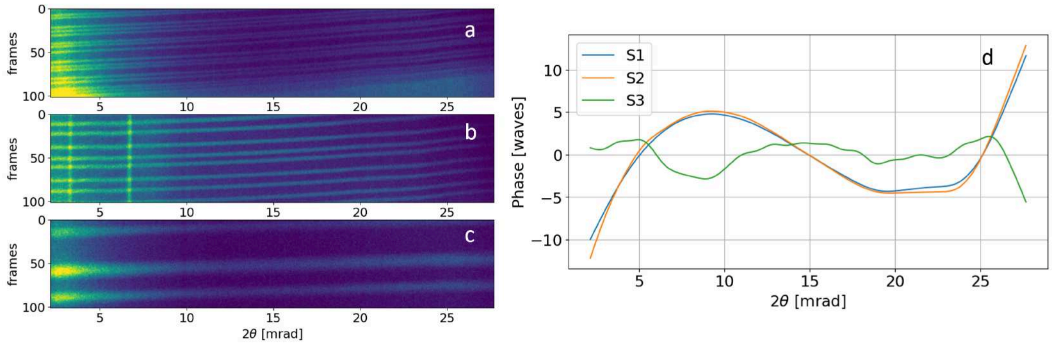

Fig. 4.14: Wavefront reconstruction of the same lens using different samples. The ptychograph using samples S1 to S3 is shown in (a) to (c), respectively. A comparison of the reconstructed wavefronts (d).

4.4.2 Optical thickness

The contrast of the sample features additionally depends on the optical thickness of the sample. Too low thickness leads to insufficient contrast. Since the beam focused by a lens is diverging in the plane of the sample, only a fraction of the rays can travel parallel to the sample features through the optical thickness of the sample. This limits the thickness of the sample, if it is too thick, such that rays traveling non-parallel to the features intersect multiple features between the front- and back surface, the contrast is washed out. To test how the sample thickness influences the wavefront reconstruction, three different thicknesses were tested for S2, 3 μm, 6.5 μm and 11 μm. For a lens spanning an angular range of 2°, the contrast is washed out on one side if the rays are parallel to the other at a thickness of about 14 μm in the case for the smallest features of S2, at a size of 500 nm. All three thicknesses were measured with the same parameters, namely a step size of 100 nm, 100 steps for a range of 10 μm and an exposure time of 30 s at a detector distance of 1 m, for comparison. The resulting ptychographs for the 3 μm, 6.5 μm and 11 μm thicknesses

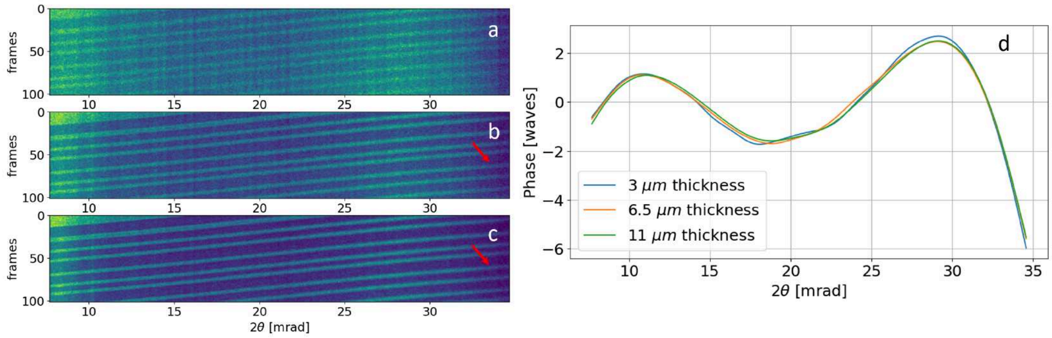

Fig. 4.15: Wavefront measurements using sample S2 with varying optical thicknesses. Ptychographs at thicknesses of 3 μm (a), 6.5 μm (b) and 11 μm (c). The red arrows indicate how the line contrast washes out at the high angles for the thicker sample. Reconstructed wavefronts from the ptychographs shown in (a) to (c) are compared in (d).

are shown in figures 4.15 (a) - (c), respectively. Thicker structures lead to higher contrast in the ptychograph, as expected. Note how the sample features start to wash out at higher 2θ values for the 11 μm thick sample compared to the 6.5 μm thick sample, as indicated by the red arrows. For a lens of higher NA, this effect would be even more pronounced and will lead to a loss of contrast as features are washed out. The thickness of 6.5 μm is therefore a good compromise between contrast and angular acceptance for lenses of NA around 0.01 to 0.02. The wavefronts reconstructions from the ptychographs shown in figures 4.15 (a) to (c) are given in figure 4.15 (d). Accurate reconstruction is achieved with all three thicknesses with no significant difference being visible. Due to the robustness of the improved RST algorithm, the lower contrast of the 3 μm thick sample or the blurry edges of the 11 μm thick sample did not hinder the reconstruction precision.

4.4.3 Misalignment

The sample is supposed to be positioned such that the layers are parallel to the line focus of the lens. This way, each fraction of the 2θ range along the width of the lens illuminates the same fraction of a sample, which is placed out of focus. A misalignment in rotation around the optical axis leads to different parts of the sample being illuminated by X-rays at the same angular position on the lens, resulting in a loss of contrast. A similar case is present, when the sample is misaligned in rotation around the axis parallel to the line focus of the lens. Since high contrast requires an optically thick sample, such misalignment leads to the front and back of the sample not overlapping properly. If the misalignment shifts the front side by the width of a sample feature, the contrast vanishes. The rotation directions are referenced here in the same way as in an airplane flying along Z with the wings spanning along X and Y scaling along the altitude. A rotation around Z is called "Roll", around X "Pitch" and around Y "Yaw". Figure 4.16 shows a schematic of how misalignment in "Roll" or "Yaw" causes a reduction of contrast in the detected signal. A coordinate system with the relevant rotations is shown as well.

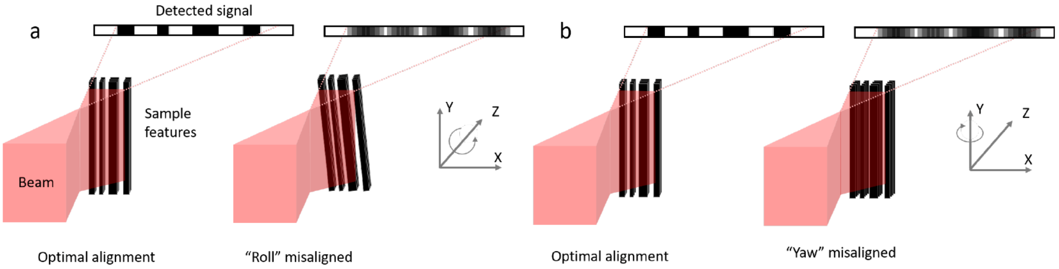

Fig. 4.16: Sample misalignment and resulting loss in contrast. A rotation around the optical axis Z (referred to as "Roll") or around the Y axis (referred to as "Yaw") leads to a loss of contrast in the magnified hologram on the detector.

To understand the impact of misalignment on the reconstructed wavefront and to determine how much misalignment can be tolerated, various misalignments in either "Roll" or "Yaw" were tested with sample S1, which has the thinnest structures and is therefore the most sensitive sample. Assuming a lens width (size along the layers and parallel to the sample features) of 50 μm, the finest features of the sample at 180 nm are expected to not be resolvable anymore at a misalignment angle of $0.18/50 \approx 0.2°$. Since larger features are present, wavefront reconstruction is still expected to be possible but at a reduced sensitivity. To test this, the sample S1 was misaligned in "Roll" by 0° to 1°and wavefront reconstruction measurements were carried out with identical parameters. For this scan series, the number of frames was 50 with a steps size of 100 nm and an exposure time of 5 s at a detector distance of 1 m. The resulting ptychographs are shown in figure 4.17. At small misalignments, the sample features can still be seen although they are blurry. As expected from the above consideration, at a misalignment of 0.2°, the smallest features start to vanish. With increasing misalignment, also bigger features can no longer be resolved. At a misalignment of 1°, no lines are visible anymore. Figure 4.18 shows the corre-

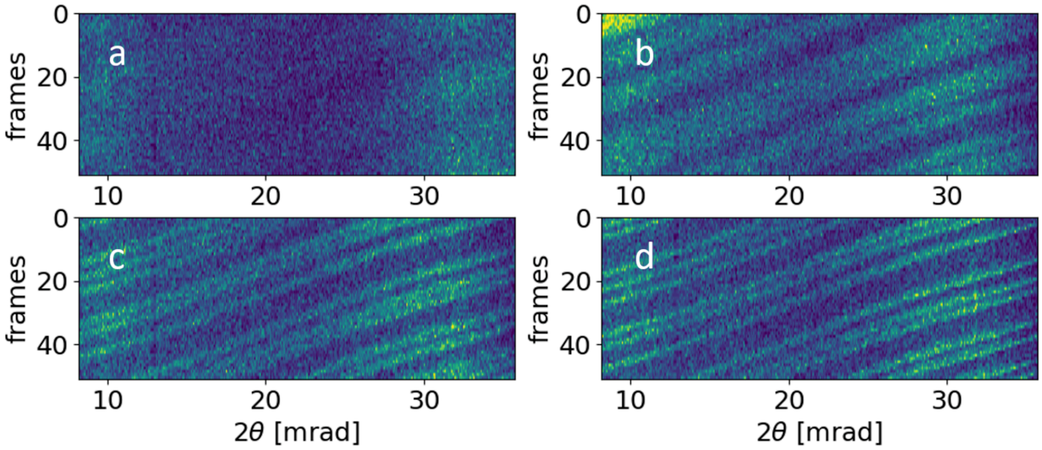

Fig. 4.17: Ptychographs at different misalignments of the sample "Roll". Misalignment of 1° (a), 0.4° (b), 0.2° (c) and no misalignment (d).

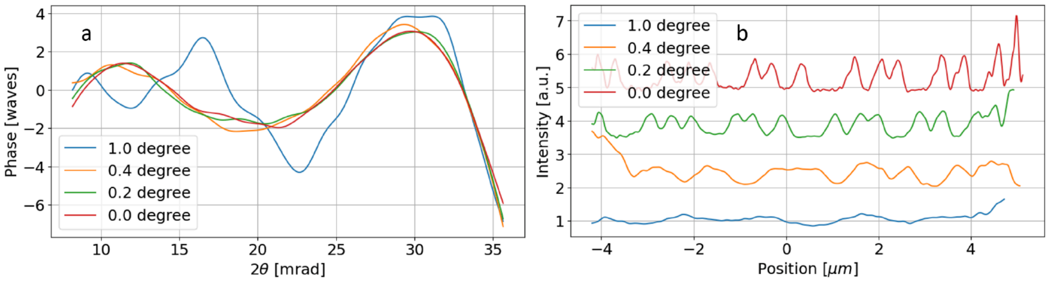

Fig. 4.18: Wavefront- and reference image reconstruction at various sample "Roll" misalignments. In (a), the wavefronts retrieved from the corresponding ptychographs shown in figure 4.17 are given. The reconstructed reference image, showing the sample features (b). They are offset along the y axis for better comparability.

sponding wavefront- (a) and reference image (b) reconstructions. A misalignment of 0.2° slightly reduces the contrast in the reference image, however, since most features can still be tracked, the wavefront reconstruction is still accurate. Some of the finest features are almost washed out, as expected. A misalignment of 0.4° leads to a reduction in phase sensitivity, as more features blur into each other. The reconstructed wavefront shape is still close to the case without misalignment, but a bit noisier due to the loss of sensitivity. In the reference image, individual features are no longer visible and only groups of lines with larger gaps in between can be distinguished. Only once the misalignment reaches values around 1° and the contrast for most features vanishes does the reconstruction fail which results in an incorrect wavefront estimate. The reference image shows barely any contrast or features at such a large misalignment.

Next, a misalignment along the "Yaw" rotation is analyzed. The alignment requirements are expected to be more relaxed in this case, as the sample thickness is smaller than the lens width. For a 7 μm thick sample like S1, the smallest features of width 180 nm are expected to vanish at a misalignment angle of $0.18/7 \approx 1.5°$. Various misalignments along "Yaw" were tested. The sample was stepped in 100 nm steps over a range of 7 μm, resulting in 70 recorded frames. The exposure time was set to 15 s and the detector was placed 1.5 m downstream of the sample. The resulting ptychographs are shown in figure 4.19 for misalignments of 3°, 2°, 0.75°and no misalignment. Almost no change in contrast is visible at a misalignment of 0.75°

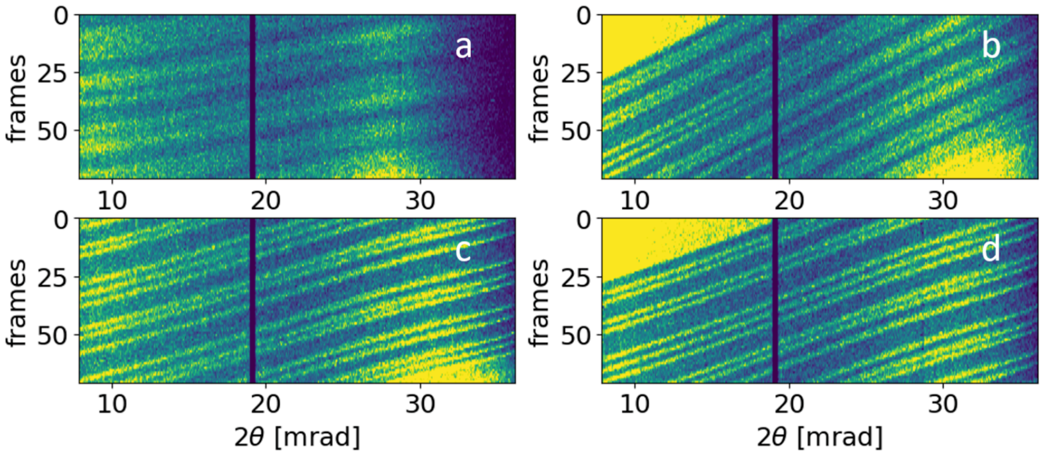

Fig. 4.19: Ptychographs at different misalignments of the sample "Yaw". Misalignment of 3° (a), 2° (b), 0.75° (c) and no misalignment (d).

and even at a misalignment of 2°, most layers can still be resolved. Only once the misalignment reaches 3°, most features can no longer be individually resolved, similar to a misalignment in "Roll" by 0.4° as shown in figure 4.17 (b). In figure 4.19 (b) it is evident that the finest features can be resolved at low 2θ values but not at large values. As discussed before, since the beam focused by the lens is divergent and thus spans a range of angles, the sample alignment can only be optimal for a fraction of the angular range. This sets an interesting limitation regarding the NA of the lens and the ratio between the feature size- and thickness t_{opt} of the sample: The maximum NA a lens can have in order to resolve all features over its full 2θ range NA_{max} is the misalignment angle at which the smallest feature contrast is expected to vanish

$$NA_{max} = \frac{\sigma_{\mathrm{eff}}}{t_{opt}}, \tag{4.3}$$

where σ_{eff} is the smallest feature of the sample. Even if the rays in the center of the angular range of the lens travel parallel to the sample layers, the contrast would vanish at either end for a lens exceeding that NA. For the example of a 7 μm thick sample with feature sizes of 180 nm, that limit would be reached for a lens spanning about 3°, with an NA of about 0.025. The lens used for above examples has an NA of 0.014, which is below this limit but close enough to lead to a reduction of contrast on one side as was seen in figure 4.15. To overcome this limitation when necessary, larger feature sizes, thinner samples or a wedged sample, potentially created by adding a stress layer as can be used to create wedged MLLs [95] could all be solutions.

From the measurements shown in figure 4.19, the wavefronts and reference images were again calculated and are given in figure 4.20 (a) and (b), respectively. Almost no loss of contrast is visible in the reference image for a misalignment of 0.75°, relaxing the alignment requirements. A misalignment of 2° leads to a reduction of contrast in the reference image by roughly a factor of 2 but individual features can still be resolved. A misalignment of 3° leads to features merging in the reference image, similarly to the case of a 0.4° misalignment in "Roll" shown in figure 4.18 (b). The wavefront reconstruction is therefore possible in all cases (see fig. 4.20 (a)), but at lower sensitivity in the case of 3°, again similar to the reconstructed wavefront shown in figure 4.18 (a) with a "Roll" misalignment of 0.4°. This result may be expected since the ratio of the lens width of 50 μm to the sample thickness of 7 μm is similar to the ratio of the misalignments where the sample features wash out $\frac{50\mu m}{7\mu m} = 7.14 \approx \frac{3^\circ}{0.4^\circ} = 7.5$.

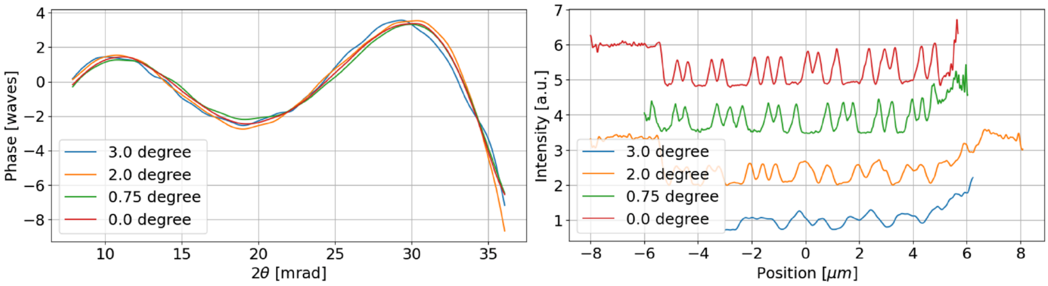

Fig. 4.20: Wavefront- and reference image reconstruction at various sample "Yaw" misalignments. In (a), the wavefronts retrieved from the corresponding ptychographs shown in figure 4.19 are shown. The reconstructed reference image, showing the sample features (b). They are offset along the y axis for better comparability.

4.5 Requirements on the measurement

In the previous two parts, the hardware requirements for the sample and lens are explored. With a given lens and sample, the measurement is conducted. However, a measurement has a lot of parameters that can be varied and must be chosen such that wavefront sensing can be achieved on reasonable timescales without compromising sensitivity. The sample and lens tests so far were carried out with a set of parameters which proved to provide accurate phase reconstruction as shown by the comparison to the wavefront retrieved at the synchrotron. The set of parameters includes the positioning of the sample and detector as well as the parameters of the measurement itself. The defocus distance d_{def} is the distance the sample is placed downstream of the lens focus and the detector distance d_{det} the distance from the sample to the detector (see fig. 2.12). The resulting magnification M is hence

$$M = \frac{d_{det} + d_{def}}{d_{def}} \approx \frac{d_{det}}{d_{def}}. \tag{4.4}$$

From the previous section note that the sensitivity can be enhanced by increasing the magnification. This can be done in two ways, placing the sample closer to focus, or placing the detector further away. In the first case, placing the sample too close to focus results in features only appearing in a single frame, as the field of view is drastically reduced, leading to no tracing of features. This can be compensated by making the steps proportionally smaller, however, this then in return requires many more steps in order to track the same number of features. The result is a timely expensive measurement. Another drawback of placing the sample too close to focus, are the wavefront aberrations. The effect of a distorted image is strongest close to the focus, which can lead to features not being recognizable between frames. The second option is placing the detector further away from the sample. This is trivially limited by the available space in the laboratory and the size of the detector. In our current laboratory setup, the distance from the sample to the detector can be anywhere from a few centimeters to up to about 3.6 m. When the detector is placed further away from the sample, the same number of photons are distributed over a larger area and thus pixels. This reduces the contrast and signal to noise (SNR) ratio. Such a reduction can be compensated by longer exposure times, which again increases the measurement duration. For high NA lenses, d_{det} is also limited by the distance at which the 2θ range of the lens covers the full range of the detector. Placing the detector further away would lead to parts of the angular range not being probed. For example, when the diffraction line of a lens of NA = 0.02 is aligned along the long side of the detector, which covers 1556 pixels of size 55 μm, the line spans over the full range of pixels at a detector distance of about 2.1 m, limiting d_{det}. A compromise between maximum phase sensitivity, SNR and measurement duration is required. It should be noted here that these limitations are only given in the current state of our laboratory setup. By exchanging the detector with a larger one or placing two adjacent to each other, a lens of given NA can be probed at a larger detector distance, for example.

The measurement parameters that can be adjusted are the defocus distance d_{def}, the detector distance d_{det} and the exposure time per frame, along with the number of steps N (and therefore recorded frames $N+1$), the size of each step δn and the total scanned range $R = N \cdot \delta n$. It is trivial that only two among R, N and δn can be chosen independently. To test the wavefront reconstruction dependence on these parameters, a set of starting parameters where chosen, from which they can be varied. This set of parameters is based on the one used in the comparison of the retrieved wavefronts from the 1D reconstructions in the lab and 2D reconstruction at the synchrotron and had previously proven to yield accurate wavefront reconstruction results as well. These values are $N = 80$ steps with a step size of $\delta n = 100$ nm resulting in a scan range $R = 80 \cdot 100$ nm $= 8$ μm. The sample is positioned at a defocus distance of $d_{def} = 100$ μm and the detector is placed 2 m downstream, resulting in a magnification of $M \approx 2000/0.1 = 20000$. The exposure time t was set to 15 s per frame. To test the wavefront reconstruction dependency on all of these parameters, a series of scans was conducted, varying one at a time. All measurements were done using the same lens, which has an NA of 0.014, a focal length of 1.2 mm and a physical height of about 35 μm.

4.5.1 Steps N, step size δn and scan range R

First, the wavefront reconstruction dependency on the scan range R, number of steps N and step size δn was explored. A few (some trivial, but important nevertheless) points set the boundary conditions for the motion parameters of the sample. First, there has to be at least one step, leading to the sample being in two different positions such that features can be traced. This is the minimum requirement but usually not sufficient, as we will see. Next, the (usable) scan range is limited by the sample size and field of view, which is based on the defocus distance. The scan range should not be much larger than the range within which a significant part of the sample is within the field of view. Otherwise, a large part of the scan does not contain features. This can lead to artifacts from the algorithm trying to track intensity fluctuations where there is no sample and unnecessarily increases the measurement duration without a gain of information. The step size has to be chosen such, that the sample moves by a distance smaller than half the field of view, otherwise features of the sample that appear in the center of a frame do not appear in at least a second one. Following up on these considerations, two sets of measurements were conducted, changing the step size δn while keeping the scan R range fixed and adjusting the number of steps N while keeping the step size δn constant. The reconstructed wavefronts are shown in figure 4.21 (a) and (b), respectively. Measurements with step sizes above 200 nm

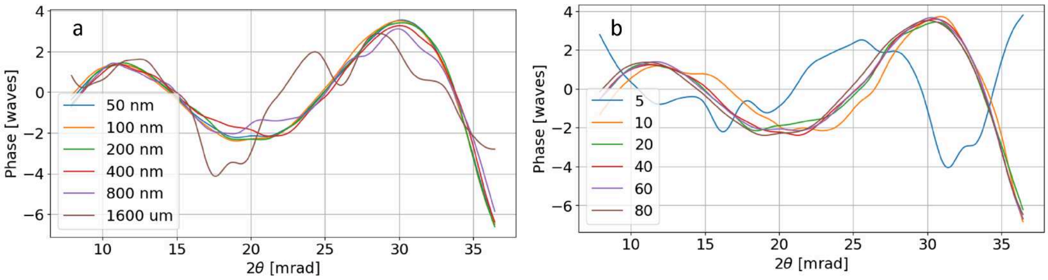

Fig. 4.21: Wavefront reconstructions based on the step size δn (a) and number of steps N (b). In (a), the scan range R is kept constant at 8 μm while in (b) the step size δn is kept constant at 100 nm.

(which is comparable to the feature size) start to lose sensitivity in the reconstruction but still manage to retrieve the correct wavefront shape. Only at step sizes above 1 μm does the reconstruction start to deviate. Note that since the scan range R is kept constant, large steps also reduce the number of steps. In (b), the step size δn is kept constant instead, changing the scan range R. With as little as 20 steps, accurate phase reconstruction could be achieved. Note that the scan range R is only 2 μm in this case, covering only a fraction of the sample. Since sufficient features can be tracked, the reconstruction is still accurate. It should be emphasized here that it is indeed not necessary to image the whole sample. The range R is sufficient if enough features can be tracked such that wavefront at each point along 2θ can be probed.

4.5.2 Defocus distance d_{def}, detector distance d_{det} and exposure time t

The following parameters can be set independently, while still affecting each other. Increasing the detector distance for instance, spreads the same number of photons over a larger number of pixels, reducing the intensity and contrast. In order to keep the same photons-per-pixel, the exposure time has to be increased. A change in defocus distance would additionally be required, if the magnification is supposed to be kept constant. They are limited by the factors mentioned in the introduction of this section. First, the exposure time was varied while the remaining parameters were kept constant. Measurements with exposure times t between 1 s and 30 s per frame were conducted. For better comparability of the contrast, their ptychographs shown in figure 4.22 are normalized by their respective whitefields, which are obtained by summing up the 1D lines along the vertical direction. Little to no difference can be seen between exposure times of 15 s and 30 s. With exposure times below 5 s, noise starts to severely reduce the contrast of the lines, at 1 s, the lines are barely visible. The wavefront reconstructions corresponding to the ptychographs shown in figure 4.22 are given in figure 4.23. Even for exposure times as low as 2 s, wavefront determination is possible due to the robustness of the improved speckle tracking

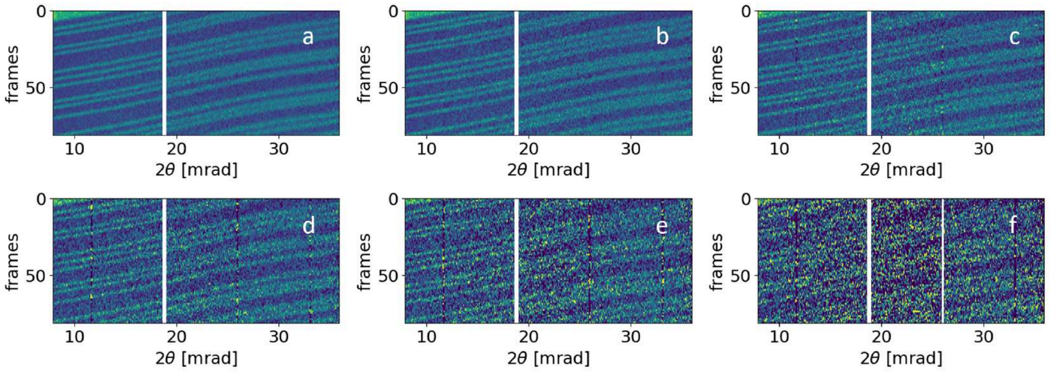

Fig. 4.22: Ptychographs at various exposure times normalized by their respective whitefields. Tested exposure times per frame are 30 s (a), 15 s (b), 8 s (c), 4 s (d), 2 s (e) and 1 s (f).

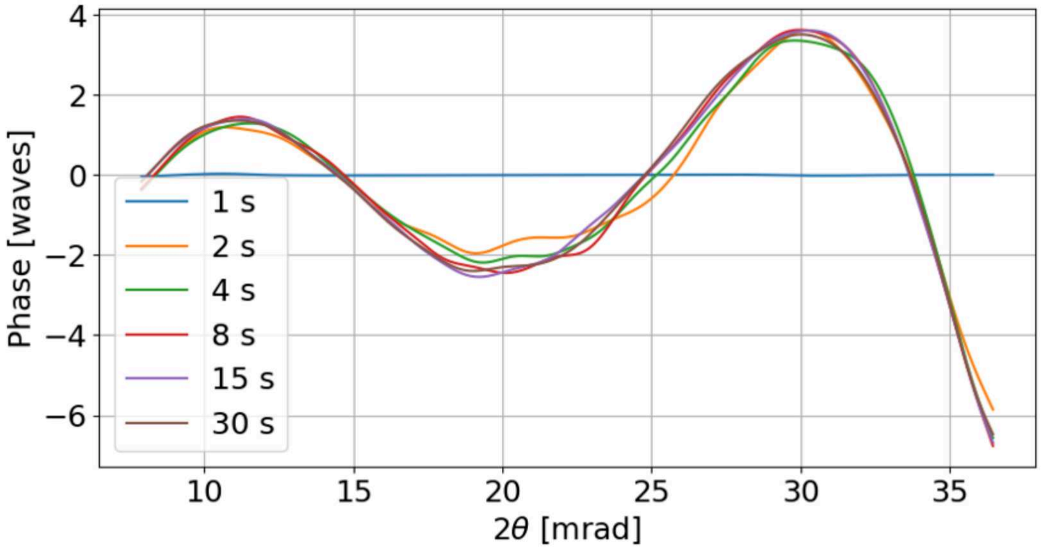

Fig. 4.23: Wavefront reconstruction based on the exposure time t. The corresponding ptychographs are shown in 4.22.

algorithm, suppressing the noisy background. Only once the features can no longer be recognized and nothing can be tracked anymore does the algorithm collapse to 0. The next point of investigation was the detector distance d_{det}. Adjusting d_{det} changes the number of pixels over which the angular range 2θ is distributed, which changes the smallest displacement that can be tracked, equal to the de-magnified pixel size. Since the same number of photons is distributed over a larger number of pixels in the case of an increased detector distance, the contrast gets reduced at a fixed exposure time (and *vice versa*). Scaling the exposure time proportionally to the detector distance allows to keep the photons-per-pixel roughly constant, which speeds up the data acquisition time at small d_{det} values and probes more accurately how the number of pixels that probe the wavefront influence the reconstruction quality. Figure 4.24 (a) shows the reconstructed wavefronts for varying detector distances with a fixed exposure time of 15 s. Smaller values of d_{det} lead to a

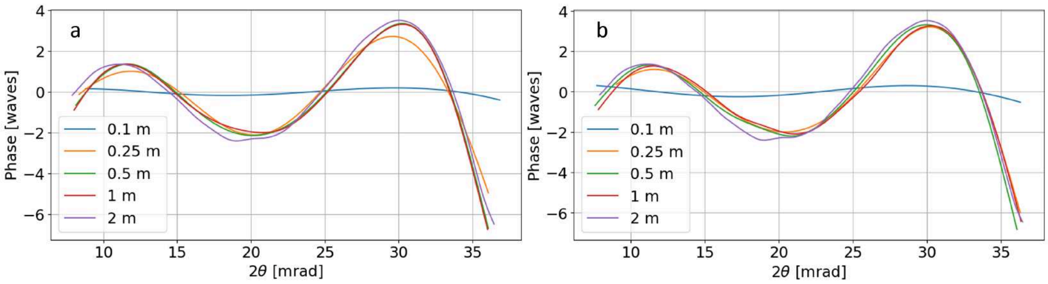

Fig. 4.24: Wavefronts reconstructed at various detector distances with a constant (15 s) exposure time (a) and an exposure time that scales proportionally with the distance (15 s at 2 m) (b).

smoother wavefront because local fluctuations be resolved. Figure 4.24 (b) shows the reconstructed wavefronts in the case where the exposure time per detector distance is kept constant, starting from 15 s at 2 m. The results are comparable, indicating that the exposure time for small d_{det} in (a) is unnecessarily long, as the contrast is sufficiently large at a constant t/d_{det} ratio. In both cases, a detector distance of 0.1 m is insufficient for an accurate reconstruction as too few pixels probe the angular range 2θ. For reference, at a detector distance of 0.1 m, the 2θ range is only covered by about 50 pixels. Both scenarios have their usages, if a measurement has to be sped up, the exposure time can be reduced together with the detector distance to not lose contrast. If the signal is weak because a lens is inefficient, for example, the contrast can be enhanced by placing the detector closer to the sample, without the need of increasing the exposure time. Note that in this example, the wavefront aberration of the tested lens is smooth and follows roughly a low-order polynomial (4-th order). In case of a rapidly changing- or noisier wavefront, large detector distances providing finer sampling along 2θ may be required.

Next, the dependence of wavefront reconstruction on the defocus distance d_{def} was explored. At values close to 0, the reconstruction is expected to collapse, as features do not appear in multiple frames anymore and can hence not be tracked and the near-field approximation collapses [58, 112]. At large defoci, the magnification reduces (assuming a constant detector distance), which leads to a reduction of phase sensitivity according to equation 4.2. In addition, the field of view increases at large defoci and might exceed the dimensions of the sample. In order to have sufficient features that can be tracked at each part of the angular range 2θ, the scan range of the sample R has to be increased by either increasing the number of steps N or the step size δn, which either increases the exposure time or reduces the sensitivity. Various defoci ranging from 0 to 1000 μm were tested. The resulting wavefronts are depicted in figure 4.25. In the case of $d_{def} = 1000$ μm, the scan range of 8 μm was insufficient to trace sufficient features in every part of the 2θ range, which caused the algorithm to collapse. To test whether a larger scan range R allows accurate wavefront reconstruction also at this defocus distance, the scan range was extended from 8 μm to 30 μm. This allowed reconstruction of the wavefront

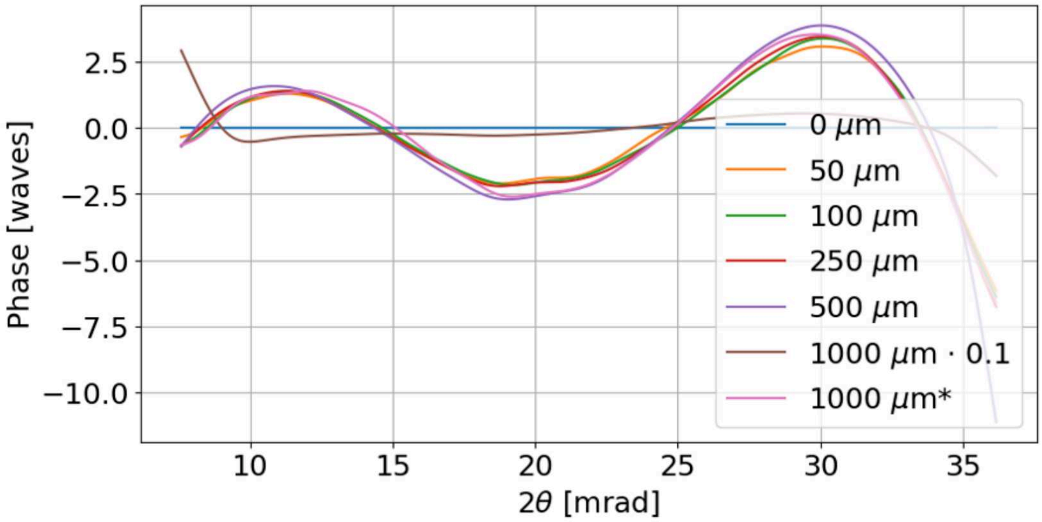

Fig. 4.25: Wavefronts reconstructed at various defocus distances. The wavefront at 1000 μm is scaled to 10 % for better comparability. In this case, the algorithm failed since insufficient features were present at the edges of the 2θ range due to the increased field of view. *Measurement range R increased from 80 μm to 300 μm to cover sufficient features at all 2θ values.

also at this defocus, but at the cost of an increased data acquisition time by a factor of 3.75. Too large defoci hence suffer from larger measurement times while also being less sensitive to phase aberrations and should be avoided. When large samples are supposed to be imaged however, large defoci might be required as the reduced field of view at small defoci would greatly increase the measurement duration. In the case where the sample was placed in focus, that is, at $d_{def} = 0$, the projection approximation collapses [173], features can no longer be tracked and the algorithm detect the wavefront aberrations anymore. The defocus should therefore be chosen such, that the magnification is high while the sample is still in the near-field regime.

4.5.3 Collimator and monochromator optics

Measurements presented thus far were carried out using the 17.5 keV X-ray beam provided by the Mo source after collimation by the collimator optics and filtering using a 50 μm thick niobium foil to suppress Kβ radiation. The collimator optic greatly increases the flux incident on the lens and thereby enables high contrast measurements at relatively short exposure times, as was shown in the previous chapters. While the filter reduces the intensity of Kβ radiation in the beam with respect to Kα radiation, the transmitted bandwidth is still large, compared to monochromated beams. A monochromator can replace the filter to increase the coherence in the beam and to reduce the bandwidth at the cost of reduced flux. Since both, collimator and monochromator are optical elements, the question arises whether they add wavefront aberrations to the beam as well. If that would be the case, their wavefronts would have to be subtracted when determining the aberrations of a lens. To test if these optics add a significant amount of wavefront aberration to the beam, measurements with- and without each optic were carried out. Since the number of photons incident on the lens is low without the use of a collimator, the exposure time had to be increased to 500 s per frame, to keep roughly the same contrast. A similar scenario is present when the monochromator replaces the filter. The reduced flux requires a longer exposure time, which was also set to 500 s. A comparison of the wavefront with- and without collimator optic, as well as with- and without monochromator are shown in figure 4.26 (a) and (b), respectively. The range of large 2θ values is missing for the monochromator measurement since the signal fades out in that range, inhibiting the reconstruction of that part of the wavefront. Neither the collimator optic, nor the monochromator significantly contribute to the wavefront aberrations. The resulting wavefront is therefore only resulting from the lens aberrations. This result also highlights that the method of ptychographic speckle tracking does indeed not require a monochromatic beam for accurate wavefront reconstruction and that using a collimator and filter can greatly speed up data acquisition time.

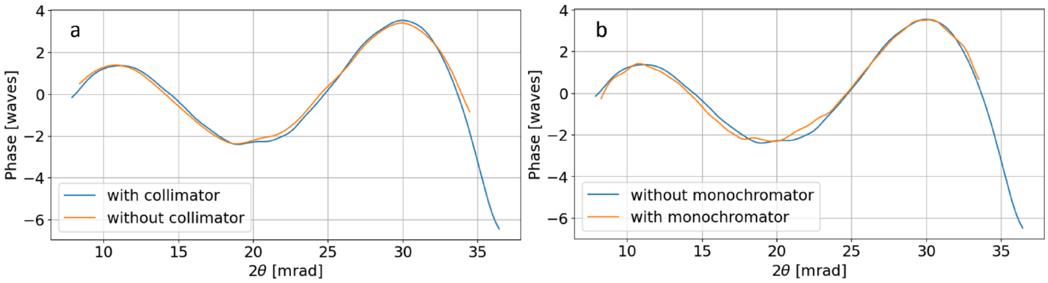

Fig. 4.26: Wavefront reconstructions with and without collimator (a) and with and without monochromator (b) in the beam. For the measurements without collimator and with monochromator, the exposure time was increased to 500 s to counteract the reduced flux. In the measurement with monochromator and the one without collimator, the signal at large 2θ values was too weak for wavefront determination in that range, hence the reduced range.

4.6 Conclusions

The laboratory setup is a powerful tool that allows not only fast but accurate and precise wavefront- and hence aberration characterization of MLLs. Due to the one-dimensional focusing nature of the lenses, they can be characterized individually and the flux from a laboratory source is sufficient for high quality measurements on short time scales. Due to the robustness of the RST algorithm, measurements with lenses and samples of varying size yielded identical results, which eases the requirements on their alignment and fabrication. Accurate phase retrieval does also not require a specific set of measurement parameters but supports a large range of e.g. magnifications or scan ranges. The wavefront of a lens can be well characterized within less than an hour after its fabrication, resulting in same-day feedback for lens manufacturing. If the results of a wavefront measurement are urgently needed, reducing the exposure time is the best way of saving time without significantly worsening the reconstruction precision. It should be noted here that for the lens studied here, the aberrations are of low order and slowly varying. In this case, the detector distance can also be reduced, as probing the wavefront at larger intervals along 2θ does not change its overall shape. If the wavefront would vary faster with respect to the diffraction angle, a reduced detector distance would not result in good reconstructions anymore even though it did in this case. It was also shown how sample misalignment causes a reduction of contrast. In the measurement parameter evaluation shown above, the sample was well aligned. To ensure reliable wavefront reconstructions even when uncertainties regarding the sample alignment are present, the measurement parameters should not be kept at the required minimum derived here. A large number of fine steps and a large detector distance and hence fine sampling of 2θ additionally allow to detect potential defects in the lens such as a phase jump or a crack.

Some limitations are a result of the setup at hand and do not apply in general to laboratory-based systems. A setup featuring a bigger detector area allows a larger detector distance at a given NA of a lens and smaller pixels allow finer sampling of the wavefront, which could be advantageous for lenses with rapidly varying wavefronts. To probe small diffraction angles with higher precision, a longer setup would be required. This would for example allow to characterize a larger fraction of the thick layers close to the direct beam of an on-axis lens, which overlap with the direct beam at small detector distances. Furthermore, an X-ray source based on a liquid jet can provide significantly higher flux than a solid anode [174]. Using such a liquid jet source, 2D wavefront reconstruction and imaging using a lens pair can be realized, as was shown before [175–177]. Since our laboratory setup already contains two hexapods and it was shown that two MLLs can be used together to form a 2D pupil in [35], a brighter source could allow 2D wavefront reconstruction and potentially imaging at reasonable timescales.

5

Phase correction

Measurements shown in this chapter are done by myself, unless stated otherwise. All images and plots shown are prepared by myself unless stated otherwise in the figure caption. Some of the results shown are published in [114] and [70] and are recreated to be shown here. Measurements done at PETRA III involved a group of people aiding in the setup and operation of the experiment.

A plane wave focused by a lens results in a parabolic wavefront profile where all points on the wavefront have the same distance to- and their gradients point at- a common spot, the focus. Any deviation from such a parabolic profile is what is referred to as wavefront aberrations, which broaden the focal spot and reduce the peak intensity. To compare- and judge the aberrations of wavefronts, this parabolic term (along with piston and tilts, which are constant and linear terms arising from an offset and tilt of the wavefront) is omitted. An ideal lens would thus result in a constant phase of 0. The measured wavefront aberrations are then the deviations from 0. The previous chapters focused on determining these deviations using a laboratory setup and a robust software- algorithm and suite. Usage of appropriate samples allows fast, precise and accurate determination of the lenses wavefront error. This chapter follows up on these measurements, discussing how the wavefront can be corrected once well characterized, to improve on the lenses focusing performance.

5.1 Deposition correction

The first method to improve on the lens's quality is to understand the major error contributors in the deposition and improve on them in the next multilayer deposition. Due to the consumption of sputter targets, the sputter rate drifts over time. In our lab, it was noted that the aberrations typically scaled with the pupil coordinate $\boldsymbol{\rho}$ to the third power [67]. Assuming the aberrations to be caused majorly by the sputter rate drift, it can be derived that a linear change in sputter rate α causes a phase term which scales with the pupil coordinate $\boldsymbol{\rho}$ to the third power [67]

$$\phi = \frac{2\pi\alpha}{3\lambda f}\boldsymbol{\rho}^3. \tag{5.1}$$

Indeed, the change of sputter rate of the magnetron systems was found to be approximately linear, as was verified by depositing many multilayers with constant parameters and observing the change in period over the deposition time. Compensating for this change can be done for subsequent depositions to reduce the aberrations caused by this effect. Figure 5.1 shows a comparison of the wavefronts of two subsequent MLL depositions. After the initial deposition, the sputter rate was calibrated based on the aberration of layer positioning. Then, a second MLL was deposited. The RMS aberration of the second deposition is lower by approximately a factor of 2. In the initial deposition, the dominant aberration scaled with the pupil coordinate ρ to the third power, resulting from a linear drift of sputter rate. After this linear drift was calibrated, the aberration of the second deposition can be seen to mainly scale with ρ to the fourth power, indicating that the linear drift was mostly compensated for and the remaining aberrations result from previously unnoticed non-linear drift terms and other imperfections in the fabrication process. This method works well to suppress large aberrations caused by such sputter rate drifts. However, since the sputter rate drift is dynamic and changes between depositions, it cannot compensate for residual aberrations.

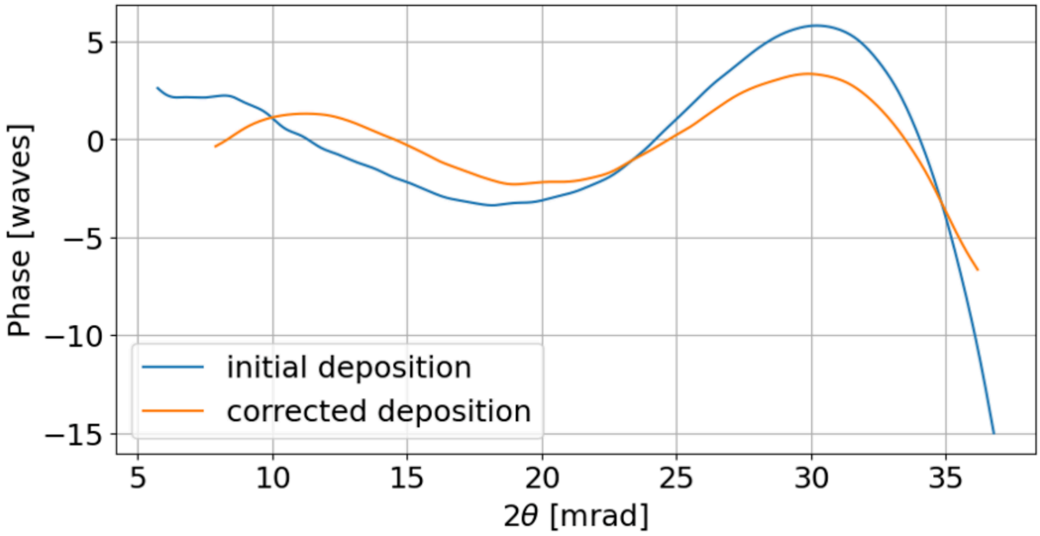

Fig. 5.1: Wavefront comparison of two lenses before and after sputter rate consumption calibration. Due to the compensation of sputter rate drift, the wavefront aberration contribution scaling with the pupil coordinate ρ to the third power is greatly reduced. The remaining aberrations dominantly scale with the pupil coordinate to the fourth power.

5.2 Refractive correctors

Utilizing the knowledge about the aberrations of a multilayer to improve on further depositions by estimating the sputter rate drift or correction a multilayer during its deposition can improve the lens quality. However, neither of these methods resulted in aberration free X-ray optics yet. To achieve diffraction limited MLLs, correction of residual aberrations is required. There are multiple possibilities on how one can reduce the aberrations of a lens, once it is fabricated and characterized. Slitting down the aperture of the lens to a fraction within which the aberrations are small is one of them. However, this greatly reduces the NA, beam area on the lens and hence flux through focus and worsens the resolution the lens can achieve. This could make the lens not suited anymore for the experiment they were designed for. Another and more practical approach is to induce a correction to the wavefront via refraction. The lens itself could be utilized as such a refractive corrector by shaping its thickness according to the aberration profile [178], but at the cost of reduced diffraction homogeneity and efficiency. A more common method is to add an additional element to the beam, which adds a phase term to the wavefront opposite of the lens's aberrations, as to cancel them out. Such can be achieved by a material of homogeneous composition, shaped to the right profile as to induce the desired phase shift via refraction [64–68, 179]. Given a phase profile $\phi(\boldsymbol{\rho})$, the shape of the correcting element $t(\boldsymbol{\rho})$ must follow [70]

$$t(\boldsymbol{\rho}) = -\frac{\lambda}{2\pi\delta}\phi(\boldsymbol{\rho}), \tag{5.2}$$

where δ is the refractive index decrement of the corrector material. For small aberrations, this can be accomplished by a thin, so-called phase plate. A schematic of a refractive corrector is given in figure 5.2. The correcting element can be placed either upstream or downstream of the lens, if its thickness is small compared to the focal length. If placed in the focused beam, its shape has to be adjusted according to the distance from the lens and the reduced size of the beam.

Such correctors have seen great success in correcting aberrations of various X-ray optics including CRLs [64, 66, 180], KB mirrors [179, 181] and MLLs [68]. A thin

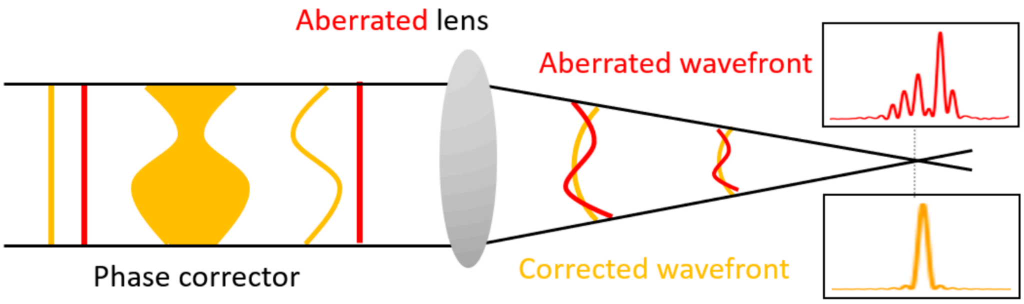

Fig. 5.2: Schematic of a refractive phase corrector. The phase corrector induces a phase term to the wavefront opposite of the aberration of the lens. The sum of the phase terms of both elements then adds to zero, resulting in an aberration free focus. The inlets show the intensity distribution in the focal plane for the aberrated (red) and corrected (yellow) wavefronts.

element (or two, one for each direction) formed to the right shape is placed in the beam together with the optics after they have been characterized. Such elements can be fabricated by cutting the shape into a material via ablation or by additive techniques such as 3D printing, for example [182]. They can be fabricated with shapes changing along 1D or 2D, depending on the optics they should correct. For circular CRLs for example, they are typically circular as well [64, 66], while structures changing along one direction are employed to correct individual KB mirrors [181] or planar lenses [180]. The material is hereby of great importance. A material with a high refractive power, that is, large δ, can induce a large phase shift even with a thin element. However, most materials with large δ values as for example W, are also strongly absorbing, reducing the usable flux and potentially heating up the corrector. It is therefore critical, to compare the δ/β ratio of materials, that is, the refraction per absorption, do determine the most suited candidates. Materials with a larger ratio induce a given phase shift at a lower loss of intensity. By such a metric, polymer, which is often used in 3D printing, is a much more suited candidate than W. Other options include aluminum and diamond. A material with low refractive index decrement δ but large δ/β value has the disadvantage that it, while not absorbing much, it requires a longer (thicker) structure along the beam propagation. This leads to large aspect ratios and potentially unstable structures. Large structures usually also do not fit between the optics and the sample and have to be placed upstream of the optics. On the upside, structures of materials with small δ ease the requirements on fabrication precision since a slight error in the structure thickness or a small error of its shape does not significantly change the correction.

5.2.1 Compound corrector

Thin corrective phase plates are great, as they can be manufactured fast, easy and cheap, allow straightforward modifications or design changes and can be placed in the beam with a simple translational stage. Their limitation is in the amount of aberrations they can correct. For X-rays δ is small for all materials ($10^{-5} - 10^{-6}$ for hard X-rays) and a thin phase plate can only induce a limited amount of phase onto the beam. For aberrations on the scale of a few waves, the required optical thickness of a corrector can be several hundred μm. For a lens of several tens of μm in height, the required structure would have to have a large aspect ratio which is unstable. It would also have steep surfaces that are difficult to fabricate, some of which may be below the critical angle of reflection. Large aspect ratios additionally require precise angular alignment, as small rotations of the structure around any axis can significantly worsen the correction.

Lenses with high NA tend to suffer from larger aberrations as their fabrication is more challenging. The typical NA of CRLs and other optics corrected with thin phase plates is on the scale of 10^{-3}, while the MLLs subject of this thesis have NAs of

10^{-2} and above. They therefore experience larger aberrations, especially since the aberrations tend to scale with a polynomial of third order or higher. When large aberrations are present, a single phase plate is not sufficient. Since larger aberrations deteriorate the focus performance stronger than small aberrations, correcting them becomes of even higher importance.

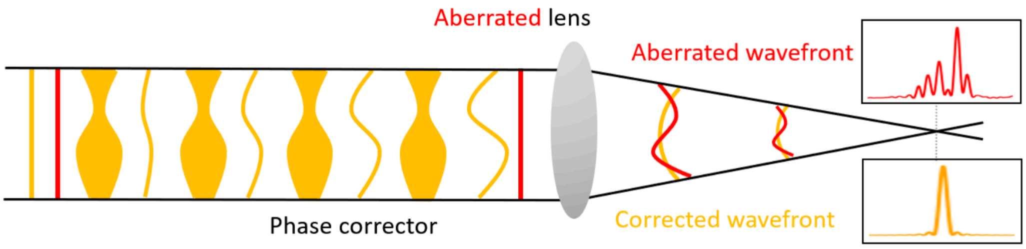

Fig. 5.3: Schematic of a compound corrector. An array of correcting elements each add a small amount of correction to the beam which add up to the required aberration compensation. Colors and inlets as in figure 5.2.

A solution to the large aspect ratio requirement is to split the correction onto N elements, each correcting 1/N of the aberrations. Equation 5.2 then modifies to

$$t(\boldsymbol{\rho}) = -\frac{\lambda}{2\pi\delta N}\phi(\boldsymbol{\rho}). \tag{5.3}$$

Each individual structure can then be treated as a thin phase plate with reasonable aspect ratio and structural stability. Placing them in a row leads to their phase contributions adding up to the desired correction. Due to their similarity to CRLs, they are referred to as compound refractive correctors (CRCs) [67]. A schematic of a CRC can be seen in figure 5.3. They have to be well aligned with respect to each other, in order to function as desired. This can for example be achieved by 3D printing them in a row onto a common substrate or carving them into the same piece. Such a joint base structure ensures their relative alignment when placed in the beam. For a lens pair, the wavefront correction is required to vary along both directions along the 2D pupil. 3D printing allows to fabricate (almost) arbitrary shapes and has proven to be a great option for additive phase corrector manufacturing [66, 68]. In addition to 3D printing being fast, cheap and allowing the uncomplicated implementation of modifications, printing a row of phase correctors onto a joint substrate eases their relative alignment as no assembling of individual structures is required post fabrication. Due to these reasons, 3D printing was chosen for the fabrication of such CRCs.

5.2.2 Nanoscale 3D printing

3D printing is a technique that saw strong development in the past few decades. The ability to fabricate almost arbitrary structures fast, cheap and with high precision greatly enhances the development of various experimental setups and techniques. Proof-of-concept ideas can be tested with ease without the need for extensive time and money investment. These 3D printing techniques found their way into the μm and nm world, allowing the direct fabrication of optics for various wavelength using two photon polymerization (2PP) [183, 184]. 2PP is a technique in which a liquid resist solidifies when two photons are absorbed at the same time. This requires a high local intensity, which can be achieved by focusing a laser into the resist, for example. Only in the vicinity close to the focal spot is the intensity high enough to induce the 2PP processes, resulting in high printing precision and small printable feature size. Using 2PP, refractive optics such as single lenses [185, 186] or compound systems [187, 188] such as compound refractive lenses [189, 190] can be printed with previously unprecedented precision. The high degree of control even allows to print optics directly onto the end of fibers, for example [191, 192]. Such 3D printed refractive lenses have found success also in combination with other optics such that FZP as to realize achromatic [193] and apochromatic [194] focusing in the X-ray regime. Aside from refractive optics, 2PP can be used to fabricate diffractive lenses [195] and even metalenses [192, 196] for wavelength around the visible spectrum.

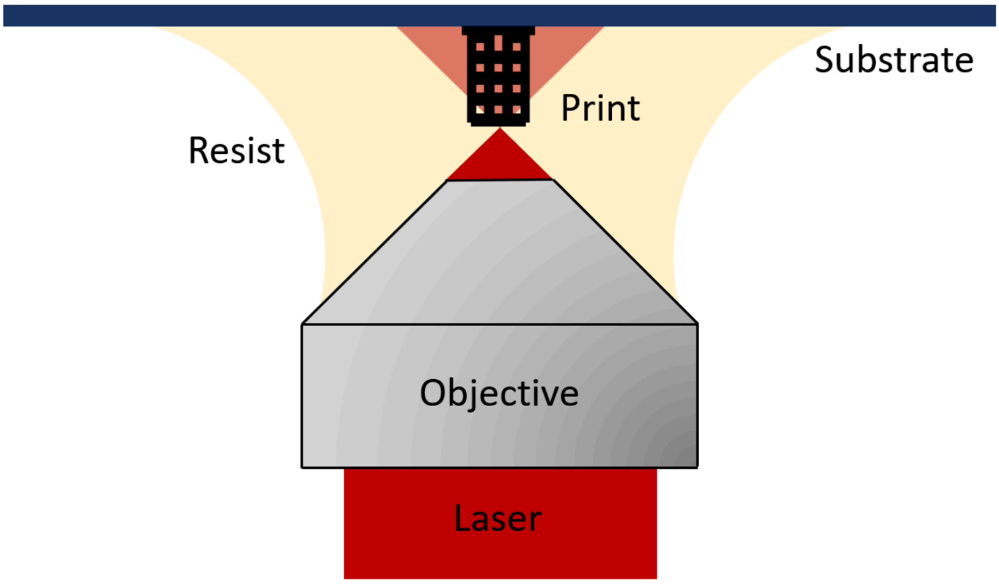

Fig. 5.4: Schematic of 2PP using the dip-in laser lithography (DiLL) method. A laser is focused into a resist placed on a substrate by an objective lens immersed within the resist. Only within the local vicinity of the laser focus does two-photon-polymerization occur, allowing to print structures by scanning the focus through the resist.

Nanoscribe professional GT is a 3D printer which utilizes 2PP to print structure with a precision on the scale of a few hundred nm. Here, an objective lens focusing an infrared laser is dipped into a liquid resist and focuses on the substrate on which the resist is placed. This configuration is called dip in laser lithography (DiLL). A schematic can be seen in figure 5.4. Other configurations such as the resist being placed on the other side of the substrate and the objective being immersed in oil instead are also possible. In order for the printer to determine the interface between the resist and substrate, the difference in refractive index is required to be sufficiently large (with the required difference depending on the objective lens) [197]. This dictates what resists can be used in combination with which substrates. The laser focus then traces out the structure layer by layer, solidifying the designed structure. By varying the laser power and the scan speed, the thickness of the printed voxels, lines and layers can be adjusted. All of the printing parameters can be set in the associated software provided by Nanoscribe called DeScribe. To print, a drop of resist is placed onto a substrate. The objective lens is positioned close to the upside-down hanging substrate such that it is immersed within the resist. The print is done upside-down and starts with the layers attached to the substrate (bottom layers of the printed structure). After a print is finished, the remaining resist has to be washed away and the print has to be developed. Only after this development stage is the structure hard and stable. To develop the structure, it is immersed in PGMEA (propylene glycol methyl ether acetate). The development duration should be at least 30 minutes. If the structure is porous or contains small channels, it is advisable to develop the structure longer, to ensure that the developer reaches every part of the print. After the development stage, the remaining PGMEA has to be washed away. This is achieved by immersing the print in IPA (isopropanol or 2-Propanol) for a few

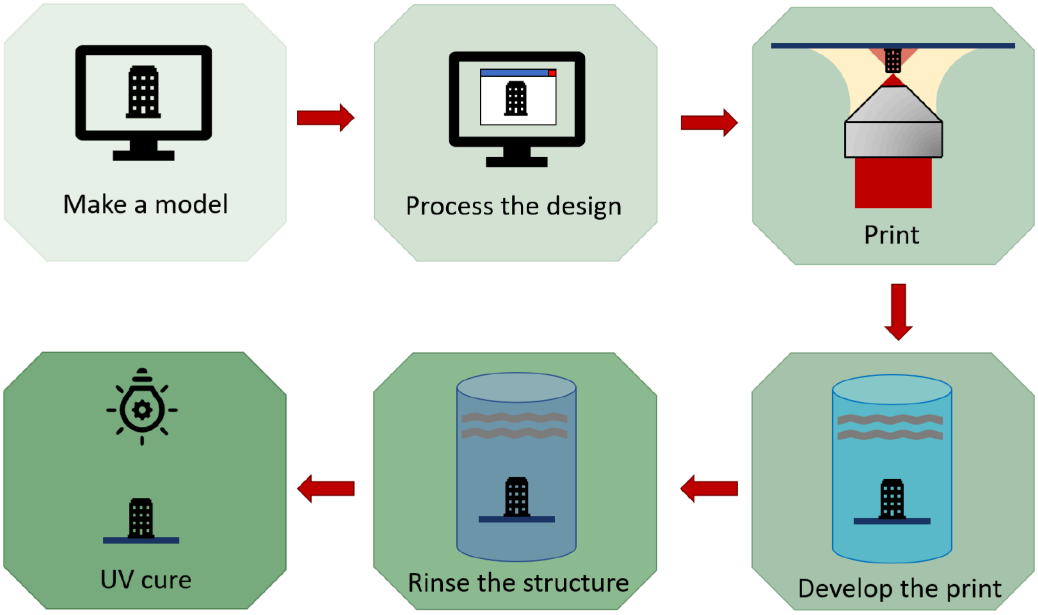

Fig. 5.5: Workflow of 3D printing a structure using 2PP and the DiLL configuration. The model to be printed is processed in the DeScribe software provided by Nanoscribe where the print parameters can be selected. It is then printed using a suited resist, substrate and objective lens. After developing the print in a bath, remaining developer liquid is washed away using IPA. To harden the structure, optional UV curing can be employed.

minutes. The structure can then be blow dried using a nitrogen gun. At this stage, the structure is ready. In order to further harden the structure, an additional step of UV curing for 30 minutes can be done afterwards. The workflow is summarized in figure 5.5. To speed up the printing process for large structures, it is possible to only print the shell of the structure with a supporting scaffold inside instead and bulk harden the trapped resist inside using UV curing after the development. In this case, the UV curing is a mandatory step.

5.2.3 Printing parameters and materials

Determining the optimum printing parameters is crucial to the print quality and speed. Both over- and underexposure of the resist leads to a reduction of print quality. If the intensity is severely too low, polymerization does not take place. At too high intensities, the structure might get bloated and the overexposure of already printed parts can cause explosions, damaging the structure. Additionally, a suitable resist, substrate and objective lens has to be chosen. A CRC requires high printing precision of below 1 μm to form smoothly changing surfaces, while the print duration has to stay reasonably low, such that the resist does not dry out during the print. A good compromise is offered by the 25× objective available from Nanoscribe. It offers a printing precision on the scale of 400 nm. The resist to be optimally used with this objective is called IP-S and using ITO (indium tin oxide) coated glass as a substrate yields the required difference in refractive index decrement, according to the manual [197]. A 63× objective can in principle offer higher resolution, which however is not required to correct for slowly varying wavefronts. IP-S is printed in the DiLL configuration described earlier. The print is developed in PGMEA for 30 minutes before being immersed in IPA for 5 minutes to wash remaining resist and developer away. Afterwards, the structure is UV cured for 30 minutes to make it more resilient against high intensity X-ray beams.

In order to optimize the print quality and speed, various printing parameters can be chosen. The two most defining parameters for the print are the laser power P and the scan speed S. The laser power changes the voxel size within which the polymerization can take place. The scan speed changes how long each point is exposed and, important as well, the time a print takes. This leads to a deposited dose D in the material that scales approximately as [198]

$$D \approx \frac{P^2}{S}. \tag{5.4}$$

A print with a certain parameter pair of laser power and scan speed might hence be accelerated by increasing the scan speed and adjusting the laser power accordingly. To determine optimal parameters, a test structure was printed with 25 different combinations of power and speed. Figure 5.6 (a) shows an optical microscope image

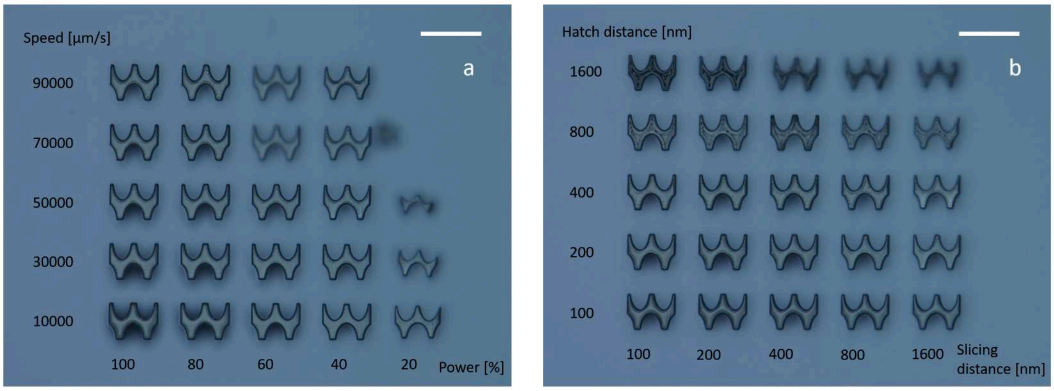

Fig. 5.6: Optical microscope images of tests of various print parameter combinations. Varying laser power and scan speed at a constant slicing and hatching distance of 400 nm (a). Varying slicing and hatching distances at a constant laser power of 60 % and a scan speed of 50000 μm/s (b).

of the prints with the laser power varying between 20 % and 100 % and the scan speed varying from 10000 μm/s to 90000 μm/s in 25 different combinations. At low doses (high speed and low power), the structures are not printed well or not at all. Some are deformed or too short, as can be seen by them not being in focus in the picture. At very high doses, the structures start to become bloated.

The distance between two layers and between two print lines within the same layer also influence the deposited dose and printing speed of the print. They are called slicing- and hatching distance, respectively. If the laser power is high, the printing voxels are large and the distance between two lines or layers can be increased. However, to form a smooth structure, printing overlapping lines is required. To ensure no risk of overexposing already printed structures, the dose then has to be reduced. The tests of laser power and speed shown above were done using a slicing and hatching distance of 0.4 μm. To explore the influence of these parameters on the print quality, a series of structures with various combinations of slicing- and hatching distances were printed as well, at a constant laser power of 60 % and a scan speed of 50000 μm/s. The resulting structures can be seen in figure 5.6 (b). Large hatching distances lead to individual lines being visible instead of a smooth layer and, in combination with large slicing distances, bad structures. As one might expect, the fastest print does not lead to the best result. One more parameter set which influences the printed shape and quality that can be chosen is the contour count and the contour distance. Instead of printing each layer from one side to the other, a contour of the shape can be printed first, with subsequent filling of the layer within this contour. This can help to smoothen the structure shape at the edges and adding stability during the printing process. The contour count sets the number of printed contour lines which make up the contour and the contour distance is the distance between those lines. Together with the previous four parameters, this results in a six-dimensional parameter space to explore. Various combinations were tested to determine the optimum parameter combination for a shape designed to

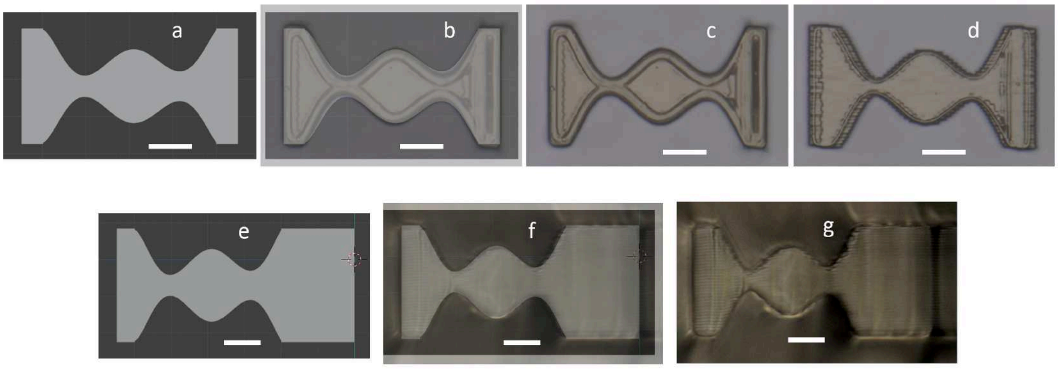

Fig. 5.7: Comparison of the model and print for a structure varying along the horizontal and vertical direction. (a) And (e) show the model along the horizontal and vertical direction, respectively. (c) And (g) show optical microscope images of the respective prints using the optimal print parameters given in table 5.1. Overlays of the design and print are shown in (b) and (f). (d) Shows an example print along the horizontal direction without contour lines with reduced surface smoothness. The scale bars are 10 μm.

correct 1/20 of the aberrations of a lens with shape varying along the print height and along the direction parallel to the substrate surface. In these combinations, the scan speed was varied between 10000 and 100000 μm/s, the power between 20 and 100 %, the slicing-, hatching- and contour distance between 100 nm and 1000 nm and the contour count between 1 and 10. The print which matched the design the most is shown in figure 5.7. Both, the model and print as well as an overlay of both are shown for the vertical and horizontal direction. The optimum print parameters are given in table 5.1. A large contour helps to ensure smooth surfaces and a low dose (high scan speed and medium laser power) combined with a slicing distance of 400 nm enables a precise printing shape also in the vertical direction. The high scan speed additionally results in a fast print. Figure 5.7 (d) shows an example print without a contour print which shows rough front and back surfaces. It it not surprising that the hatching- and contour distance of the optimum print parameters are identical, as the contour distance is essentially hatching the contour. It might be more surprising that the optimal slicing- and hatching distances are identical, considering that the theoretical resolution of the objective is 595 nm laterally and 3313 nm axially and therefore worse in the direction along the structure height [199, 200]. However, considering that the same printing precision along

Tab. 5.1: Optimum printing parameters used to fabricate the shapes shown in figure 5.7.

Laser power [%]	50 %
Scan speed [μm/s]	100000
Slicing distance [nm]	400
Hatching distance [nm]	400
Contour count	5
Contour distance [nm]	400

both directions is required and with the low dose small voxels can be printed, it is a natural consequence of the requirements.

Using the above parameters, printing a single row containing 20 elements changing along the vertical direction and 20 changing along the horizontal direction takes about 40 minutes. To further reduce the print time, the shell and scaffold method can be adopted. There, as the name suggests, only the shell of the structure is printed with a scaffold inside for stability, instead of bulk printing the full structure. To test this, the same structure was printed using this method. After developing the structure with the liquid developer, the encapsulated resist was developed by UV curing. This speeds up the printing process since most of the volume does not have to be polymerized by the laser. The print time reduced by about a factor of 2 to roughly 20 minutes. After the UV curing, it was noticed however that the scaffold surfaces were still visible. This could lead to unwanted refractions or reflections of said surfaces or interfaces, which is why this method was found to be not suited for this application. Furthermore, for prints that do not require UV curing, the time gained in the reduced print duration might not compensate the duration of the additional UV curing step required using the scaffold method. In the mentioned example, the scaffold method plus 30 minutes of curing would take 50 minutes while the solid print without UV curing would only take 40 minutes. When printing large- or many structures where the UV curing duration is small compared to the print duration, the scaffold method can still offer a significantly decrease of fabrication time.

5.2.4 Design considerations

After optimal print parameters were found, there were a few things that have to be taken into account for optimal functionality of a printed CRC. First, the corrector should not have high frequency structural changes. These vary from measurement to measurement and would cause small misplacements of the corrector to locally induce an incorrect amount of wavefront to the beam. To rid the wavefront of local fluctuations, a high order polynomial can be fitted to the phase. This rids the phase of local high frequency variations while still following its overall shape. The next thing is the position of the corrector with respect to the lenses. In principle, it can either be placed upstream (before) or downstream (after) the lenses. To properly correct the lens, the wavefront has to be propagated from the lenses to the plane in which the corrector is placed. When placed downstream, the focusing of the beam has to be considered as well. Placing it downstream of the lenses is only suited for thin correctors and lenses with long focal length. Since high NA MLLs have short focal length which the length of a compound corrector can even exceed, it is required to be placed upstream of the lenses.

When a plane wave passes the corrector placed upstream of the lenses, the wavefront

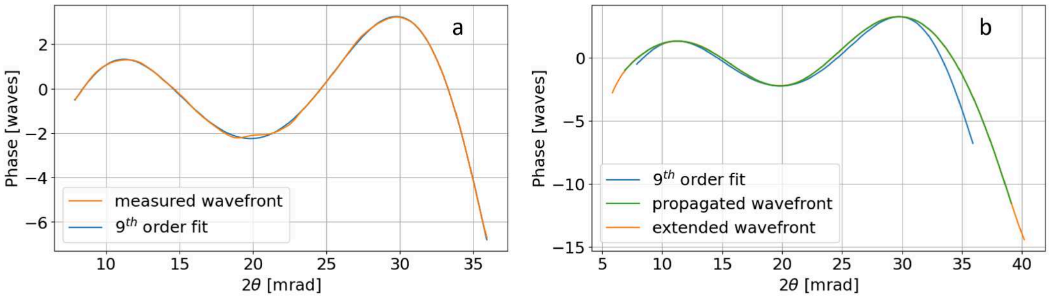

Fig. 5.8: Smoothing and back-propagation of a wavefront. The measured wavefront is smoothed by a 9^{th} order polynomial fit (a). This smoothed wavefront is then back-propagated to the position where the detector is supposed to be placed and extended at both ends to remove edge effects (b).

gradient downstream of the corrector and upstream of the lenses is non-zero, which leads to a change of phase and intensity distribution if left to propagate. A corrector placed upstream of the lenses should therefore be placed as close as possible to the lenses to minimize this effect. However, due to geometric limitations of the technical setup, it is not possible to place the corrector arbitrarily close to the lenses. To compensate for the propagation effect, the corrector shape has to be adjusted. To ensure that the phase induced by the corrector matches the design at the lens plane, the aberration of the lens is back-propagated to the plane of the corrector. An example of the smoothing and propagation of the wavefront of a lens can be seen in figure 5.8 (a) and (b), respectively. To get rid of potential edge effects, the propagated phase can be extended by a few μm on each side. This shape is then chosen as $\phi(\boldsymbol{\rho})$ based on which the corrector shape is designed according to equation 5.3.

Since each correcting element has a back- and front surface, they can be shaped with a mirrored profile. Then, 1/2N of the correction is applied when the rays enter the shape and again when they leave. Such a mirrored structure would have a thickness of 0 in the thinnest position. To ensure structural stability, a constant offset can be added to each element in the center between the two surfaces. This slightly increases the absorption. If the structure edges are required to be pointy, with angles below 90 degrees, the precision and stability at the sides can be improved by adding a constant block to the sides. For a structure correcting along the direction normal to the substrate, placing an offset between substrate and corrector helps to ensure that no signal is cut off by the substrate and that no reflections of the surface interfere with the signal. An example design along both directions, horizontal and vertical can be seen in figure 5.9 (a). They have a constant thickness offset of 6 μm as well as additional 5 μm thick structures at the sides for the horizontal- and at the top for the vertical structure, respectively. The offset at the bottom of the vertical structure is increased to 15 μm. For the case of an MLL pair, each structure would correct 1/20 of the aberration of one lens. For a full correction, 20 of the shown pairs would be required. After initial tests, it became clear that the angular alignment of an array of

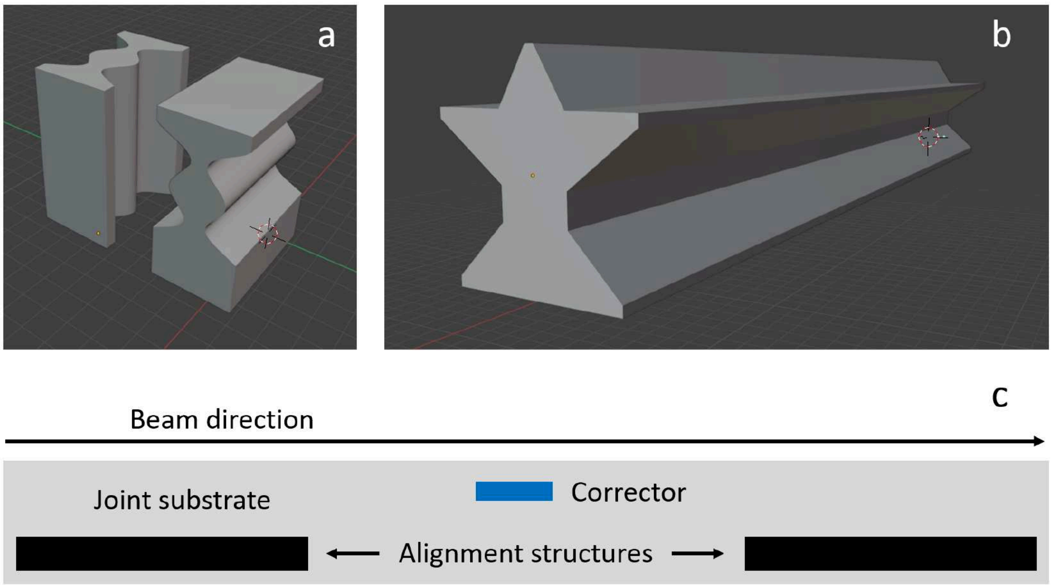

Fig. 5.9: Example design of a pair of correctors for the vertical and horizontal direction (a). Alignment structure to aid the angular alignment of the corrector (b). Positioning of the corrector and alignment structures (c). Overlapping the two alignment structures in the beam ensures the rotational alignment of the corrector.

correcting elements is not trivial. Small misalignments can cause large deviations in the induced wavefront. To aid with the alignment, two elongated star-like structures can be printed onto the same substrate as the phase correctors with the long side parallel to the beam direction. By placing them far apart from each other along the beam propagation direction, the rotational alignment of the CRC can be achieved by overlapping the shadows of the two structures in the beam like aiming a gun with rear- and front sight. A model of the alignment structure is shown in figure 5.9 (b) and the relative position of two such structures together with a CRC in shown in figure 5.9 (c). A star like shape was chosen since its pointy features allow precise overlap in all directions and the wide base ensures stability. The optical thickness (along the beam) was set as 1.5 mm. This is sufficient material to be visible with ease in the X-ray beam without being too long to the point where the front and back of the structure would not be overlapping anymore. The distance between the two should be significantly larger than their length, they were therefore placed around 10 mm apart.

5.2.5 1D phase correction

To test the feasibility of a CRC consisting of many individual elements, a 1D corrector for a single MLL, consisting of 20 individual elements was printed. Distributing the correction over 20 elements leads to aspect ratios of the structure of about $1:2$, resulting in stable structures and smooth surfaces. Since the laboratory setup yields sufficient flux to characterize a single lens, a 1D corrector can be tested in this environment.

The wavefront of a single MLL was first measured in the laboratory setup (as explained earlier). The lens has an NA of 0.014 with a focal length of 1.2 mm and a multilayer height of 35 μm. The lens wavefront is shown in figure 5.10 (a). Taking into account the considerations above, a mirrored shape was designed where each surface is supposed to correct 1/40 of the aberrations with a constant offset of 5 μm in the center. This adds 100 μm of optical thickness to the structure. A gap of about 8 μm is left between individual elements for the undeveloped resist to escape. The propagation distance between the CRC and the lens was designed to be 20 mm. The model uses a slicing distance of 400 nm, a hatching distance of 400 nm and a contour count of 5. The resulting polymer structure with an assumed composition of $\mathrm{C_{14}H_{18}O_7}$ (the main component in IP-S) of density $1.2\,\mathrm{g\,cm^{-3}}$ is calculated to have a refractive index decrement of $\delta = 8.62 \times 10^{-7}$ at $17.5\,\mathrm{keV}$ [201]. To test whether the refractive index decrement assumption matches reality, rows with 18 to 22 elements were printed, for the design of 20 elements. An image of the design is shown in figure 5.10 (b). They were printed using IP-S as a resist with the 25 × objective mentioned above. ITO coated glass with dimensions of 25 mm × 25 mm × 0.7 mm was used as the substrate. After printing, the structure was developed in PGMEA for 30 minutes before being immersed in IPA for 5 minutes and finally UV cured for 30 minutes. To ensure the alignment of the structures with respect to each other, the print remained on the substrate. The substrate with the CRC rows and alignment structures was placed on a hexapod in the laboratory setup. Using the alignment structures, the CRC with 20 elements was positioned in the X-ray beam upstream of the lens and the wavefront measurement was repeated. Figure 5.10 (a) shows the wavefront comparison before and after correction. The aberrations are largely compensated and the root-mean-square (RMS) value of the wavefront being reduced by more than 80 % from 1.25 waves to 0.19 waves. Afterwards, the CRCs with 18, 19, 21 and 22 elements were tested as well. The remaining aberrations were worse in all cases, indicating that the assumption about the refractive index decrement δ was indeed correct. For this lens, the theoretical diffraction limited PSF full width

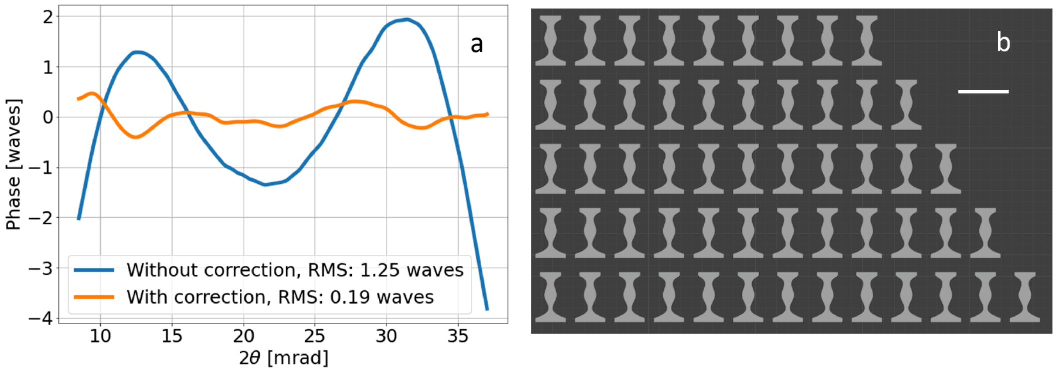

Fig. 5.10: Correction of a single MLL. Wavefront before and after correction (a). CRC rows with 18 to 22 elements (not fully shown) (b). The scale bar is 50 μm.

half maximum (FWHM) is 2.1 nm. Due to the aberrations of the lens, the actual resolution of the lens is worse. Without correction, the FWHM was 4.7 nm which improved to 2.6 nm after the corrector was added to the beam, much closer to the optimum.

The concept of a CRC thus proved to be feasible and can be utilized to greatly reduce the residual aberrations of an MLL. Since two lenses are required to form a small focal spot, this concept had to be extended to correct two orthogonally placed MLLs. Since the flux of the laboratory setup is insufficient for 2D phase retrieval, this was tested at a synchrotron facility instead.

5.2.6 2D phase correction

After the successful test of a CRC for a single lens in the laboratory setup, the next step was the extension to two lenses for 2D imaging. A corrector for two lenses has to vary in shape along both directions, with each shape following the aberrations of one lens. Both lenses can be pre-characterized individually in the laboratory setup and a phase corrector for both can be fabricated before the start of an experiment. The two lenses to be corrected were cut from the same multilayer as the lens shown to be corrected in chapter 5.2.5. Their wavefronts were therefore similar to the one shown in figure 5.10 and their NAs were 0.014 and 0.015, respectively. Since the MLLs are placed orthogonal with respect to each other, the required 2D profile of the corrector $t(x, y)$ can then be build from the individual 1D profiles $t_h(x)$ and $t_v(y)$ as

$$t(x, y) = t_h(x) + t_v(y), \tag{5.5}$$

with h denoting the horizontal and v the vertical focusing directions, respectively. Figure 5.11 (a) shows the model of such a 2D shape designed to correct two orthogonally placed MLLs, without additional side structures for better visibility. Note that the substrate is below the structures, such that one surface is changing along the direction normal to the substrates surface and one along the direction parallel to the substrates surface. Such a structure was then printed with additional sidewall structures, similar to the 1D case. Figures 5.11 (b) and (c) show optical microscope images of the print as seen from the top and side, respectively. The focal plane of the microscope is in the center of the structure. While the shape along the horizontal direction as seen from the top follows the design, the vertical as seen from the side does not. Instead, it is misshaped, resulting in a flat central part and pointy indentations. This is likely due to a proximity effect resulting from the shape of the structure. To solve this issue, the 2D corrector was instead designed to consist of two rows of 1D elements, each correcting only one lens. Since the lenses are orthogonal with respect to each other, such a corrector does not lead to cross terms. With this approach, 20 elements with shape varying along the horizontal

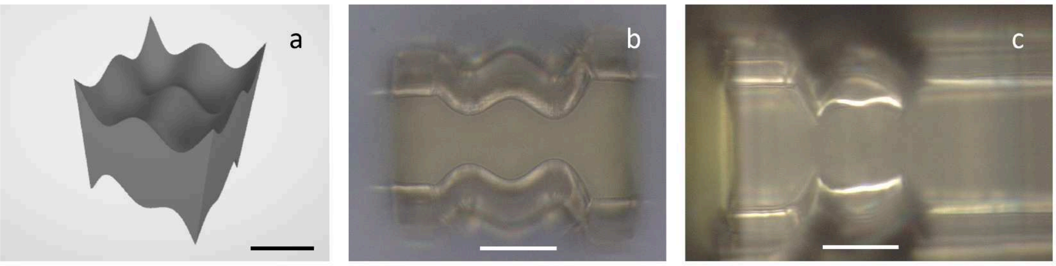

Fig. 5.11: Design and print of a 2D corrector. 3D model of the corrector without supporting side walls (a). Microscope images of a printed 2D corrector with support structures (b), (c). Top view focused to the center of the print (b). Side view of the same structure, again focused on the center of the structure (c). The shape along the horizontal direction (b) follows the design while the shape along the vertical does not (c). The scale bars are 20 μm.

direction are supposed to correct the horizontally focusing lens and 20 elements with shape varying along the vertical direction are designed to correct the vertically focusing lens. A pair of 1D correcting elements is shown in figure 5.12 (a). 20 such pairs are then required to form the 2D CRC. With the same parameters from table 5.1 which resulted in good shapes along both directions, the CRC was printed onto an ITO coated glass substrate using IP-S. This time, the substrate was cut to a size of 20 mm × 10 mm × 0.7 mm prior to printing, to allow the positioning of the corrector in close proximity of the lenses, with an estimated distance between the CRC and the lenses of 20 mm. An SEM image of a pair of correcting elements along both directions is given in figure 5.12 (b). Using this approach, the shape of the print did follow the design in both direction well, as expected. Here, multiple rows were printed again to allow a slight increase or decrease (up to $\pm 10\%$) of the induced wavefront, in case the 2D wavefront reconstructed at the synchrotron is slightly bigger or smaller than what was estimated from the measurement at the laboratory setup. Two alignment structures were printed alongside the CRCs with a distance of about 9.5 mm in between them along the beam propagation direction. An optical microscope image of one alignment structure and a few rows of the correcting elements is shown in figure 5.12 (c). The lens pair together with the

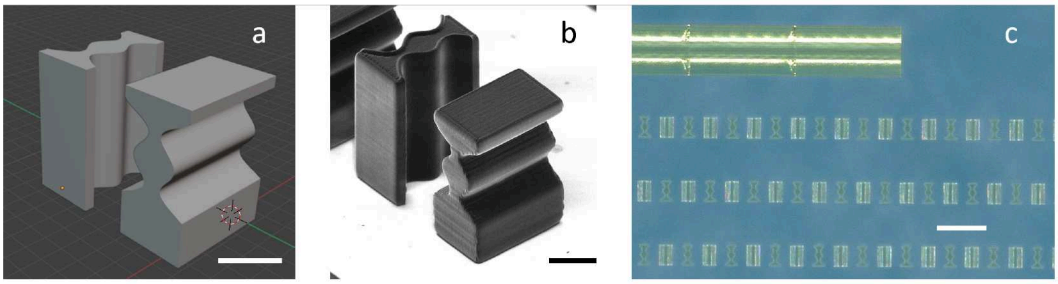

Fig. 5.12: Model of a pair of 1D correctors, designed to each correct 1/20 of the aberrations of one lens (a). SEM image of the print (b). Optical microscope image showing multiple rows of correctors as well as an alignment structure as seen from the top (c). The scale bars are 20 μm in (a) and (b) and 100 μm in (c). SEM image (b) reproduced by courtesy of M. Prasciolu.

corrector was brought to the P11 beamline at PETRA III, Germany. The lenses were aligned in the X-ray beam at 17.5 keV and their 2D wavefront was reconstructed through RST using a gold Siemens star sample. For this, the sample was placed around 85 μm out of focus and stepped in 0.2 μm steps on a grid with 6 × 6 points. At each position, a frame was recorded with an exposure time of 1.5 s, resulting in a total scan time of around 1 minute. A schematic of the setup is shown in figure 5.13. Afterwards, the corrector was aligned in the beam aided by the alignment structures and placed 20 mm upstream of the lenses. The wavefront of the combined system was retrieved by repeating the same measurement with the Siemens star sample. The 2D wavefronts before and after the addition of the corrector can be seen in figure 5.14 (a) and (b), respectively. Terms such as piston tilt and defocus are omitted. A great reduction of the residual aberrations can be observed. The RMS

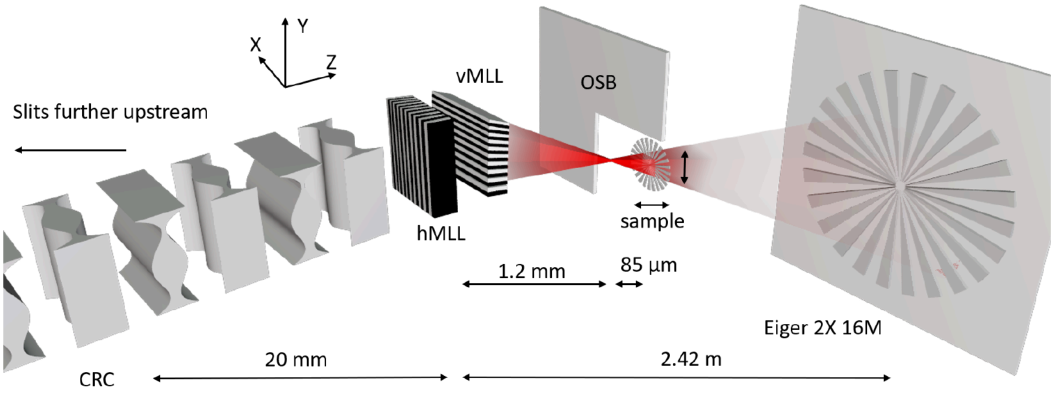

Fig. 5.13: Schematic of the experimental setup used for 2D phase correction. The lens pair produced a diverging beam in which a Siemens star sample was positioned. Magnified holograms were recorded on an Eiger 2X 16M pixel array detector. The CRC was placed upstream of the lens pair. An OSB placed between lenses and sample blocks unwanted diffraction orders and a slit pair upstream of the setup (not shown) reduces the beam in size equal to the overlap aperture of the lens pair.

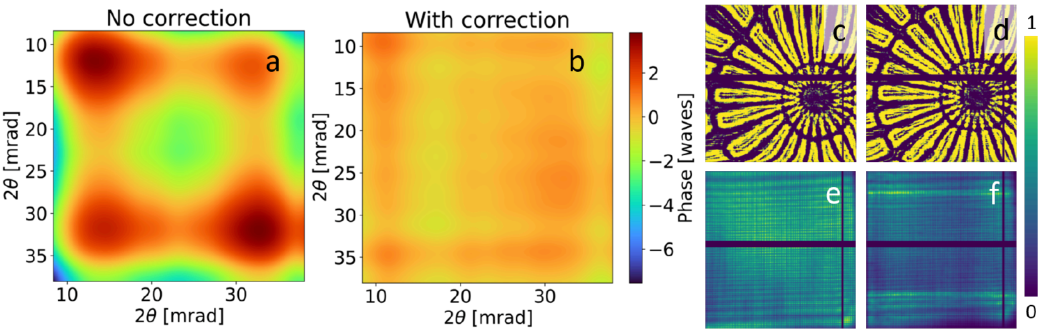

Fig. 5.14: 2D wavefront before (a) and after (b) wavefront correction. Terms such as piston, tilt and defocus are omitted. A single whitefield corrected image of the Siemens star sample without (c) and with the corrector in the beam. The corresponding whitefields are shown in (e) and (f), respectively.

error of the wavefront was reduced from 1.67 to 0.40 waves. A single whitefield corrected image of the Siemens star before and after inserting the corrector into the beam can be seen in (c) and (d), respectively. Distortions are visibly reduced with the corrector present. The corresponding whitefields can be seen in (e) and (f), respectively. Since the corrector shape leads to slight redistribution of intensity, the whitefield is slightly less homogeneous than without, showing regions of increased count density. Since the complex wavefront E at the lens plane can fully describe the beam distribution downstream of the lens, the beam caustics and the PSF in the focal plane can be calculated from it. The complex wavefront E is given by the whitefield A and phase ϕ as

$$E = \sqrt{A}e^{i\phi}. \tag{5.6}$$

Figure 5.15 shows the beam caustics cut through the Y-Z plane (a) and X-Z plane (c) around the focal plane for the uncorrected lens pair. The caustics after aberration correction are given in (b) and (d), respectively. Before correction, typical spherical aberration is observed, where many rays intersect the central axis in different planes along Z and the brightest spot is shifted along Z. This is a result of the aberration scaling dominantly with the pupil coordinate to the fourth power. After the CRC was inserted into the beam, a bigger fraction of the rays crosses the optical axis in a common focal plane, leading to a more defined focal spot and higher intensity.

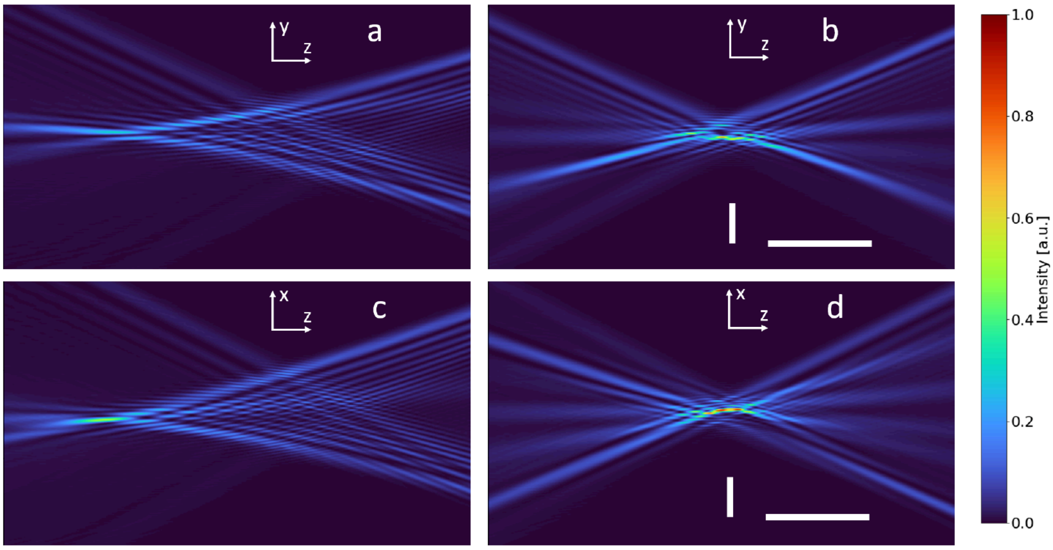

Fig. 5.15: Beam caustics around the focal plane. Without (a) and with (b) correction in the y-z plane as well as without (c) and with (d) correction in the x-z plane. The scale bars are 5 μm along z and 50 nm along x and y.

By cutting through the X-Y plane at the Z-position of highest intensity, the PSF in the focal plane can be visualized. Figure 5.16 (a) and (b) show the PSF without and with correction present, respectively. The intensity scale is normalized to an ideal, aberration free lens pair. The maximum therefore depicts the Strehl ratio, which is 1 for an ideal lens. Optics with values above 0.8 are considered diffraction limited.

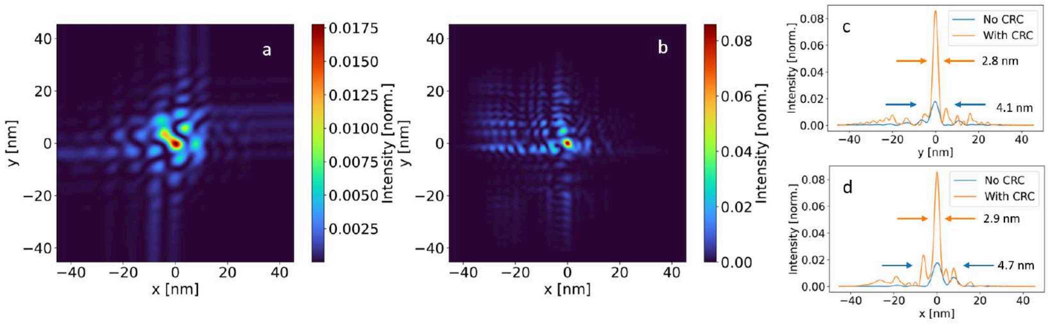

Fig. 5.16: PSF without (a) and with corrector (b) present. Vertical and horizontal 1D line cuts through focus are given in (c) and (d), respectively. The intensity is normalized to an ideal lens pair. The FWHM as determined from Gaussian fits are given in (c) and (d).

The strong side feature in the uncorrected case is a result of non-ideal orthogonality of the two lenses, leading to 45° astigmatism. The PSF with the corrector present shows a much smaller focal spot with higher peak intensity. The FWHM decreased from 4.7 nm × 4.1 nm to 2.9 nm × 2.8 nm, while the Strehl ratio increased from 0.018 to 0.086. 1D cuts along the horizontal and vertical directions are shown in figure 5.16 (c) and (d). The peak intensity increased by a factor of about 4.8.

To understand what types of aberrations are present and have been corrected in this case, wavefronts are often decomposed into Zernike polynomials [202, 203]. The even Zernike polynomials (even over the azimuthal angle ϕ)) are defined as

$$Z_n^m(\rho, \phi) = R_n^m(\rho)\cos(m\phi) \tag{5.7}$$

and the odd polynomials as

$$Z_n^{-m}(\rho, \phi) = R_n^m(\rho)\sin(m\phi). \tag{5.8}$$

Here, n and m are positive integers with $n \geq m \geq 0$, ρ is the radial distance with $1 \geq \rho \geq 0$ and R_n^m are the so-called radial polynomials which can be found in literature [203]. They form an orthonormal basis in which individual terms can be matched to specific aberrations like defocus (Z_2^0), coma (Z_3^1 and Z_3^{-1}) and astigmatism (Z_2^{-2} and Z_2^2). They are however, defined on a round aperture. Through a Gram-Schmidt orthogonalization, Zernike-like polynomials can be derived for the rectangular aperture as well [204, 205]. Figure 5.17 shows the first 15 (until n = 4) Zernike-like polynomials defined over the rectangular aperture. Terms which are not separable are only possible with non-orthogonal alignment of the lenses, their presence hence indicates a relative alignment error between them. To understand which aberration terms were predominantly present in the wavefront of the MLL pair and which aberrations the corrector was able to reduce, the 2D wavefronts shown in figures 5.14 (a) and (b) were decomposed into rectangular Zernike-like polynomials. The first 21 terms which have meaningful amplitudes are shown in figure 5.18. The

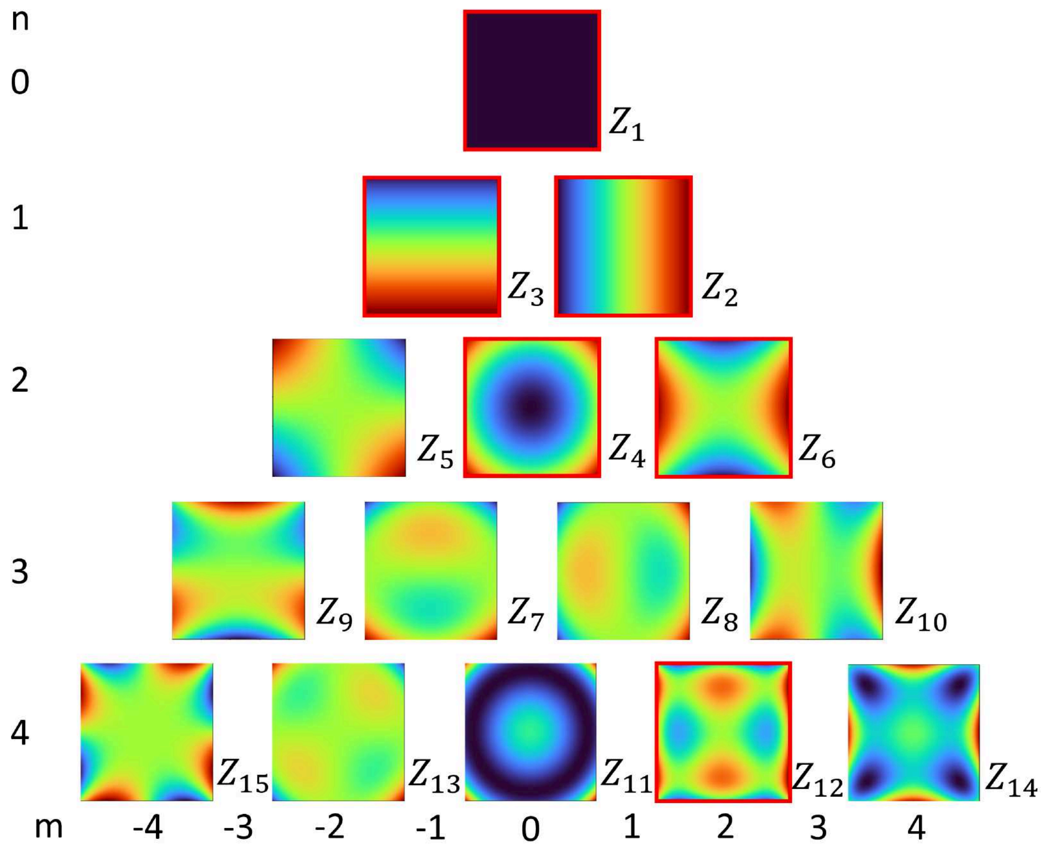

Fig. 5.17: The first 15 Zernike-like polynomials on a rectangular aperture arranged by their n and m numbers with the corresponding Zernike numbers following Noll's sequential indices. Terms separable into horizontal- and vertical components are marked with a red border.

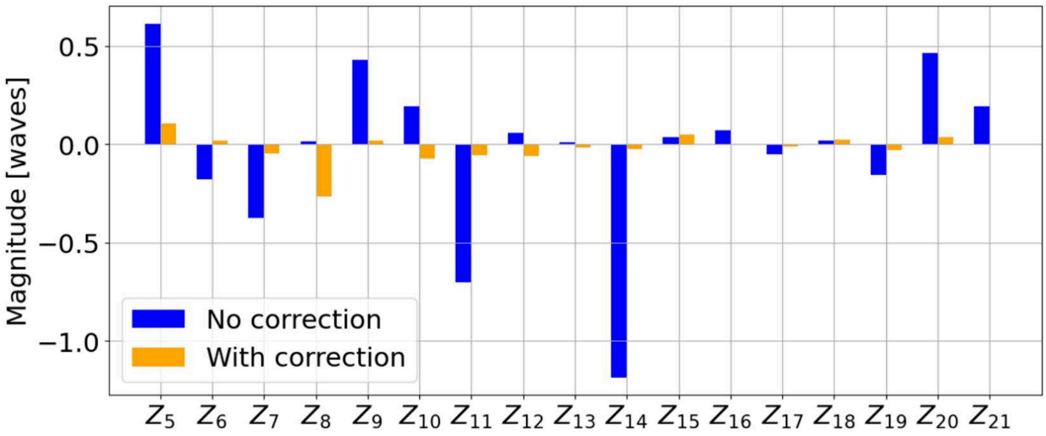

Fig. 5.18: Decomposition of the 2D wavefronts shown in figure 5.14 (a) and (b) into rectangular Zernike-like polynomials Z_k following Noll's sequential indices k.

magnitudes of most terms are greatly reduced, most notable spherical aberration Z_{11} and tetrafoil aberration Z_{14} which are the terms that are responsible for the four most notable peaks of the wavefront shown in figure 5.14 (a). These are a result of the dominant aberration of the lenses which scale with the pupil coordinate to the fourth power. Vertical coma Z_7 is reduced but horizontal coma Z_8 is increased, which could be due to a scaling error of the print along one direction or arise from the difference in print resolution along the horizontal- and vertical directions. The term characteristic for 45° astigmatism, Z_5, is reduced as well. This is surprising since this term results from orthogonal misalignment of the lens pair and the corrector was designed assuming orthogonal lenses. Therefore, it was not designed to correct for any mix-terms like Z_5. The reduction of this term indicates that the corrector was likely slightly misaligned around the optical axis as well, partly offsetting the misalignment of the lenses.

5.2.7 Future improvements

The 3D printed phase correctors have shown great success in reducing the remaining aberrations of high NA MLLs. To further improve on their design and performance, a few challenges should be addressed. Combining both directions into a single element would slightly reduce absorption, as the number of constant offsets would be halved. For such a structure to print with satisfactory precision and surface smoothness, further investigation of printing parameters is required. Depending on the shape of the wavefront that is to be corrected, for example a shape that is overall more convex than the concave shape shown in figure 5.11, it may print fine with the given parameters. Alternatively, the number of elements could be increased, leading to structures of lower depth at the cost of increased absorption. Since the print resolution is worse in Z (along the height of the structure) than in X and Y, the shape changing along the vertical direction is less precise than the horizontal one. To avoid the print being non-isotropic for the two lens correction directions, the structure has to be printed such that the optical axis is normal to- and not parallel to the substrate surface. In order to print multiple elements in vertical row, a supporting structure as was used in [193] and [194] is required. This geometry does not allow overhanging structures, requiring twice the elements or steeper structure surfaces. Additionally, large aspect ratio structures become unstable when placed in the beam due to the lack of support from the substrate. Once aberrations are low enough, the phase might be correctable with a single element again. Such can be printed along either direction. For the aberrations present here, structures consisting of only one element were printed as well, to test their feasibility. Figures 5.19 (a) and (b) show optical microscope images of a phase corrector for the vertically and horizontally focusing lenses, respectively. To utilize the enhanced printing precision in X and Y, the structures where printed with the optical axis normal to the substrate. Since large aspect ratios ($\sim 60:1$) are present and the structures are pointy, additional support structures where added at the sides. The central part is without additional support. This leaves the corrector vulnerable to even slight bending, which in turn significantly worsens its performance. The pointy edges of the structure required

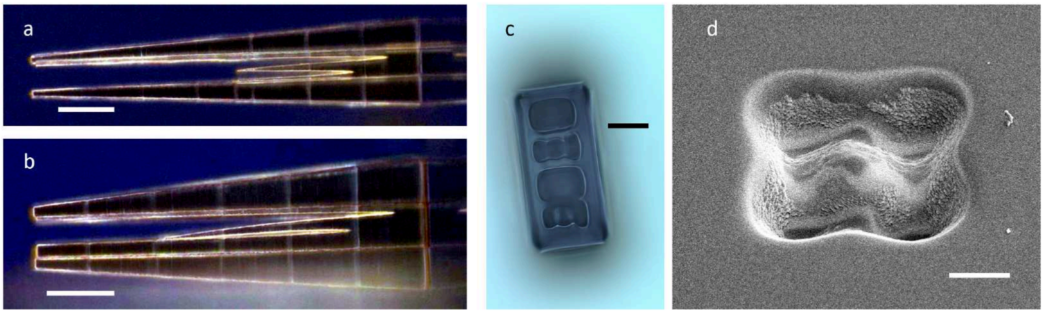

Fig. 5.19: Single element phase corrector for the vertical (a) and horizontal (b) focusing lens. The substrate is on the right side. A fused silica print of two pairs of phase correcting elements on a pedestal (c). A 2D phase corrector FIB milled into diamond. The scale bars are 100 μm in (a) and (b), 50 μm in (c) and 10 μm in (d). SEM image (d) reproduced by courtesy of M. Prasciolu.

due to the shape of aberrations is difficult to print with high quality and could lead to surfaces being below the critical angle of reflection. If the correction for both MLLs would be combined in a single such element, the required aspect ratio would increase further and strong proximity effects might take place. Still, for lenses with significantly smaller aberrations, such a structure could be an improvement. Once the wavefront with correction present was characterized, one can aim at further reducing the remaining aberrations. This could for example be done by modifying the corrector design to include a correction for the leftover wavefront and printing a new and improved CRC to replace the initial one. The additional phase term could either be distributed over all elements again or, if sufficiently small, be printed as an additional single element in front of- or behind the CRC. The difficulty in this approach lies in the accurate positioning of the new corrector in the same position where the previous one was. Slight misalignments below 1 μm could lead to no improvement or even worsening of the correction. To add the additional required phase term to the beam without the need for such realignment, the remaining aberrations could be corrected for by a single thin phase plate, added into the beam with an additional stage. This would allow to keep the alignment of the CRC while improving on the overall correction. In the example shown, the intensity re-distribution induced by the phase corrector is small, but noticeable. For a more homogeneous illumination field or for the correction of lenses with larger aberrations, wavefront engineering approaches must be employed [206, 207].

The corrector is still treated as a thin lens, though its extension along the optical axis is quite large. While wavefront propagation is accounted for between the corrector and lenses, it is neglected between individual elements. The change of shape required between two neighboring elements is below the print precision, which is why it can be neglected here but might become relevant at longer distances. Since the structure is made from polymer, it can deteriorate in the X-ray beam if exposed over long durations. While a replacement can be manufactured quickly with low efforts, re-alignment takes time. Multiple correctors can be printed onto the same substrate, which allows the exchange of them by a simple translation. However, fine tuning the position still takes time and effort. A suitable long-term solution could require a different material. Nanoscribe now offers the possibility to print fused silica, which result in much more resilient structures [208]. A fused silica corrector was printed with the 10× objective from Nanoscribe using the GP-Silica resist and silicon as a substrate. The test print is shown in figure 5.19 (c). Printed were two pairs of correctors onto a pedestal. Such a pedestal is necessary since the structures contract during sintering, which is an additional development step required to turn the printed structure into fused silica [209]. While the overall shape is recognizable, the structure is too bulgy. With improved printing parameters and designs, this method could still lead to stable correcting elements which could be part of a permanent installation at a beamline offering aberration corrected nano-focusing optics. Bauer et al. developed a new resin called POSS (polyhedral oligomeric silsesquioxane) which allows to print fused silica at higher resolutions [210] which could be an excellent candidate for improved phase corrector structures. Another promising material with comparable δ/β ratio to polymer is diamond. Since δ is larger in diamond than in polymer, the optical thickness of the structure can be reduced. Diamond CRLs are already in use for X-ray focusing by refraction [211–213]. A phase corrector could be cut from diamond by FIB milling, for example. When milling a structure from diamond, a single 2D corrector for both lenses can be fabricated that does not suffers from proximity effects. An example of the 2D correcting shape shown in figure 5.11 (a) cut into diamond with a FIB is shown in figure 5.19 (d). The overall shape matches the design well, though additional polishing is required to form a smooth surface. Such structures could be utilized at XFELs, where the structures have to withstand high peak intensities.

6

Imaging with multilayer Laue lenses

This chapter present some results from different imaging modalities that utilize MLLs and were obtained at large scale facilities such as synchrotrons and XFELs. The experiments were carried out by a collaborative effort of a team with many people who proposed and planed these experiments. My own contributions are in aligning lenses and samples as well as setting up and conducting the measurements. Part of the data analysis was recreated by myself. Results shown which were obtained by colleagues are marked accordingly in the figure caption. Parts of the results shown in this chapter are published in [214] and [215] and recreated to be shown here.

The previous chapters focused on the development, characterization and correction of high NA MLLs. Using a laboratory setup in combination with a robust algorithm, allows fast and precise wavefront reconstruction of MLLs fabricated in-house. This chapter follows up on high-quality, well characterized and aberration-corrected MLLs of high NA and exemplary shows different applications of such lenses in X-ray imaging. Many imaging techniques such as projection holography or near field ptychography are enhanced by the high NA of the MLLs that allow to focus X-rays to nanometer spots. High NA MLLs also opened up completely new methods such a convergent beam crystallography.

6.1 General setup

In the following I will describe a portable and compact MLL based X-ray microscope. Even though some components vary from experiment to experiment, the heart of the setup is almost always identical. It will be described here in general terms with necessary adjustments being mentioned in the individual sections. With this setup we want to shape and focus an X-ray beam using MLLs and provide the ability to place various samples in- and close to the lenses focus, to allow the exploration of a range of imaging schemes. A schematic of the setup is shown in figure 6.1. In the center of the setup are the two MLLs that form the lens pair for 2D focusing. They are placed on a set of hexapods, which allows alignment in six degrees of freedom with one being placed upside down, the same way as they are positioned in the laboratory setup described in chapter 2.5. A third hexapod holding the phase

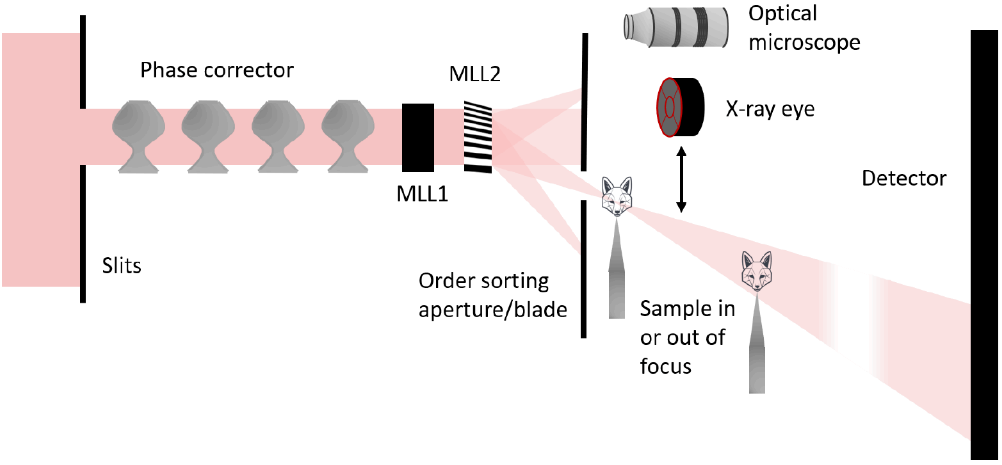

Fig. 6.1: Schematic of the general setup. An incoming beam is shaped to the size of the lenses by a pair of slits. A CRC upstream of the lens pair induces the required phase correction. The lens pair focuses the beam. MLL1 is focusing along the horizontal direction and has a slightly longer focal length than MLL2, which focuses along the vertical direction. Unwanted diffraction orders are blocked by an OSB or OSA. Samples can be positioned in- or out of focus and are imaged onto a detector far downstream. An optical microscope and X-ray eye are utilized for positioning and pre-alignment of optics and samples and can be positioned in the beam as required.

corrector is placed upstream of the two which hold the lenses. To shape the beam to the size of the lenses, a pair of slits is placed upstream of the optics. Collimation of the beam or pre-focusing, as well as monochromatization of the rays is done by stationary beamline optics which are different for each beamline and experiment. To block the fraction of the beam transmitted but not reflected by the lenses and other focusing orders, an order sorting aperture (OSA) is placed between the lenses and the focus. This can be a square pinhole or an L-shaped beamstop, the second one is referred to as an order sorting blade (OSB). This OSA or OSB has to be placed at a distance from the lenses where the focused and unfocused beams separate. The distance from the thickest lens layers to the optical axis, the NA as well as the focal length determine this distance and the resulting working distance, which is the distance from the OSA or OSB to the focus. This working distance limits the extent a sample can have while still allowing its positioning in the focus. Samples can be positioned on a designated stage downstream of the OSA which allows translational and rotational movement for alignment and measurements. Various detectors are positioned after or around the sample. Depending on the experimental goals and conditions, these can include different types of detectors but the common setup includes at least two types, an X-ray eye and a photon counting pixel detector, as are present in the laboratory setup as well. The X-ray eye is used for pre-alignment of lenses and samples and the photon counting detector for wavefront characterization measurements and further data acquisition. An optical microscope aligned along the beam axis is used to pre-align optics and samples and can be used as a reference to place different samples at identical positions with respect to the X-ray beam. Other detectors might include additional photon counting detectors at various angles and distances, an X-ray fluorescence detector or a transmission intensity detector like a diode, for example.

6.1.1 Component alignment

Positioning all components of the setup at their design positions is not a trivial task and their alignment is of great importance for the achievable results. A misplacement of one lens with respect to the other, can add aberrations to the wavefront which worsen the focus, for example. The first step is to align the lens pair. They are positioned in the beam at a distance from each other along the optical axis approximately equal to their difference in focal length using the optical microscope. The X-ray eye is then utilized to overlap them in the X-ray beam and tilt them to their diffraction angle. This can be observed as the lens turning opaque, as most of the transmitted beam is shifted from the refracted- to the reflected beam. The phase corrector can be pre-aligned using the X-ray eye as well, by overlapping the shadows of the alignment structures to ensure the angular alignment and subsequently overlapping the CRC shadow with the overlap region of the lens pair. Exchanging the X-ray eye to the photon counting pixel detector downstream of the lenses allows to observe the diverging diffraction orders of the lenses. Most of the signal can be found in four different signals, since both lens can either reflect or refract the beam, creating four different scenarios as sketched in figures 6.2 (a) and (b). The first one is when the beam is refracted by both lenses, in this case no focusing takes takes place. It is referred to as the (0,0) order. Next are the two beams which are reflected only by

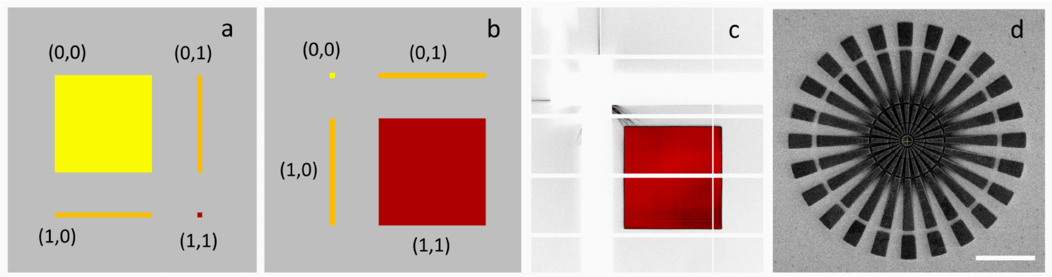

Fig. 6.2: Sketch of the diffraction orders expected from an MLL pair in the focal plane (a) and on a detector far downstream (b). The fraction of the beam reflected by both lenses is referred to as (1,1) and by none as (0,0). Note that the size of the (0,0) beam is identical in (a) and (b). The parts only reflected by either the horizontally- or vertically focusing lens are (0,1) and (1,0), respectively. A detector frame showing the 2D lens pupil (1,1) (c). The other orders are blocked by an L-shaped beamstop (visible as a white shadow). An SEM image of a typical Siemens star used for lens alignment (d). The scale bar is 5 μm and the innermost spoke width 50 nm. Siemens star SEM image (d) reproduced by courtesy of M. Prasciolu.

one lens but not the other. The divergent 1D foci result in a line on the detector. Since one lens is focusing along the horizontal- and one along the vertical direction, two lines, one along each direction are present on the detector. These are referred to as the (0,1) and (1,0) orders, respectively. Photons which are reflected and hence focused by both lenses are in the (1,1) order. This beam appears on the detector as a magnified rectangle, mimicking the lenses overlap area and is the beam that is used for imaging. To ensure the orthogonality of the lenses, both 1D lines are aligned along the detector pixel rows and columns. Fine tuning of the lens tilts to maximize the counts in the (1,1) order and ensure homogeneous illumination is done afterwards. Slits can be used to reduce the beam size to the overlap area of the lens pair. To block the (0,0), (0,1) and (1,0) orders, an L-shaped beamstop can be positioned in front of the detector as is shown in figure 6.2 (c). They can also be blocked by the OSA or OSB between the lens and sample, to ensure that only the focused beam is incident on the sample. To ensure optimal lens alignment and accurately determine the position of the focal plane, the wavefront of the lens pair has to be determined. The wavefront reconstruction is done using RST and a test sample, usually a gold Siemens star as the one shown in figure 6.2 (d). Such a sample offers high contrast, is well characterized as a reference and its features are of various sizes and shapes. The Siemens star is positioned downstream of the focus and the wavefront is retrieved using RST by stepping the sample along a 2D grid. From the wavefront aberration, the defoci along the horizontal- and vertical directions and the orthogonality of the lenses can be determined. Astigmatism along 0°- 90° indicates that the lenses do not focus to the same plane and their distance along the optical axis has to be adjusted. This can also be seen as the Siemens star being elliptical instead of round, due to a difference in magnification along the vertical- and horizontal direction. While the depth of focus (DOF) given by

$$DOF = \pm\frac{\lambda}{2(\mathrm{NA})^2} \tag{6.1}$$

is small for high NA lenses, equal to 700 nm at an energy of 17.5 keV for a lens of NA 0.01 for example, the effective depth along the beam direction at which high intensity is present is much larger when wavefront aberrations are present. This can be seen in figures 5.15 (a) and (c) and it eases the alignment precision requirement for aberrated lenses. Astigmatism along 45° is a result of non-ideal orthogonality and requires a rotation of one of the two lenses around the optical axis. Since RST determines the defocus distance, the sample can be moved into the focal plane. The position of the focus can be recorded on the optical microscope which allows to place other samples directly into the focus by placing them in the same position relative to the optical microscope, acting as a reference point.

6.2 Projection holography

PXST retrieves the phase of an optic through an iterative update of the displacement map and an estimate of a reference image of the sample, by tracing feature between overlapping projection holograms as explained in chapter 2.4.1. After convergence, a high-quality and potentially high-resolution aberration free image of the (prior unknown) sample is obtained. Therefore, phase retrieval and imaging via projection holography is done within the same measurement. By placing the sample a distance d_{def} downstream of focus, high magnifications $M = (d_{det} + d_{def})/d_{def} \approx d_{det}/d_{def}$ can be obtained, where d_{det} is the distance from the sample to the detector. M is typically in the range from a few thousands to a few tens of thousands. A detector with a pixel size of 75 μm such as an Eiger detector, would have an effective pixel size of 5 nm at a magnification of 15000 for example. High-resolution projection holograms can therefore be recorded of large (tens of μm) samples using the PXST and RST algorithms. Figure 6.3 shows a few examples of images obtained using projection holography in combination with the RST algorithm at the P11 beamline at PETRA III. On the left is a 500 nm thick Siemens star test pattern made from gold as the one shown in figure 6.2 (d), the center shows a diatom from the Antarctic sea and the right a nanoporous gold structure with pore sizes down to about 10 nm, which varies linearly in optical thickness from about 1 μm (left) to 13 μm (right). The Siemens star was imaged at a defocus distance of around 1000 μm, resulting in a magnification of 2500 at a detector distance of 2.5 m. It was scanned on a 21 × 21 points grid of step size 2 μm with an exposure time of 0.5 s. The diatom was placed at a defocus distance of about 490 μm while the detector was placed 2.37 m downstream, resulting in a magnification of about 4800. It was scanned on a grid of 21 × 21 points with a step size of 6.5 μm along the vertical- and 5.5 μm along the horizontal direction, with an exposure time of 1 s per frame. For the

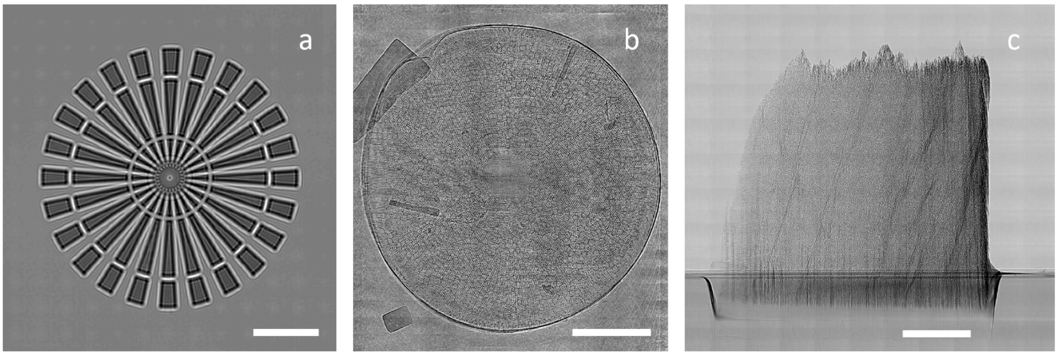

Fig. 6.3: A few examples of sample reference images reconstructed from projection holograms using RST. A Siemens star like the one shown in figure 6.2 (d) is shown in (a). A diatom from the Antarctic sea (b). A nanoporous gold structure with shape similar to the Elbphilharmonie in Hamburg (c). The scale bars are 5 μm in (a) and 20 μm in (b) and (c). Diatom provided by C. Hamm (AWI) and nanoporous gold provided by S. Shi (Hereon) and shaped by M. Prasciolu (DESY).

nanoporous gold, a defocus of 800 μm resulted in a magnification of about 3000. It was scanned with 11 × 11 points with a step size of 10 μm in each direction and an exposure time of 5 s per image. The color scale ranges from (white to black) 0.5 to 1.5 in 6.3 (a), from 0.98 to 1.02 in (b) and 0.3 to 1.3 in (c). The robustness of the improved algorithm allows dynamical whitefield correction, which adapts the background for changing illumination intensities. This is especially useful for longer measurements, where a fluctuation in intensity is often inevitable (see fig. 2.11 in chap. 2.4.2 for an image of the diatom without such background correction). Since the sample is usually scanned in a grid pattern, periodic artifacts may be present in the reconstructed image. These can be reduced by use of the improved algorithm as well but some remain, as can be seen in the background of the nanoporous gold structure. To further reduce such artifacts, the sample could be scanned on a non-regular grid, such as a spiral pattern. The magnification can be increased by placing the sample closer to focus, however, at too small d_{def} values, sample features may be heavily distorted due to the lens aberrations and the near field approximation does no longer hold. Defocus distances down to 50-100 μm are possible, as was concluded from chapter 4.5. At small defoci, the field of view is reduced, resulting in a smaller fraction of the sample being imaged or requiring more scan points to cover the same sample area. This imaging technique greatly benefits from high NA optics, where the highly divergent beam can lead to high magnifications and a overall large fields of view.

6.3 Scanning transmission X-ray microscopy

Scanning transmission X-ray microscopy (STXM) is a technique were a sample is placed in focus and stepped along the plane normal to the beam [216–218]. At each position, the total transmitted intensity is recorded. The resolution is limited by the size of the beam and the step size should therefore be comparable to the focal spot size for highest resolution. This method benefits strongly from high NA, aberration corrected MLLs, as they allow focusing to small spots, in the range of a few nanometer in size. These small spots allow fine sampling of a specimen. Figure 6.4 shows a few examples of images obtained via STXM imaging at the P11 beamline at PETRA III. In each example, the total transmitted intensity as recorded on a photon counting pixel array detector downstream of the sample is summed up at each scan point. The figures therefore represent absorption maps of the sample, where more absorptive parts (may it be higher density or thicker structures) lead to fewer transmitted photons. (a) and (b) show the Siemens star from figure 6.2 (d) at different sampling intervals covering 100 × 100 pixels. The pixel size in (a) is 25 nm and 10 nm in (b). The exposure times were 10 ms and 50 ms, respectively. The innermost spoke width of 50 nm are clearly resolved. (c) shows a barcode-like

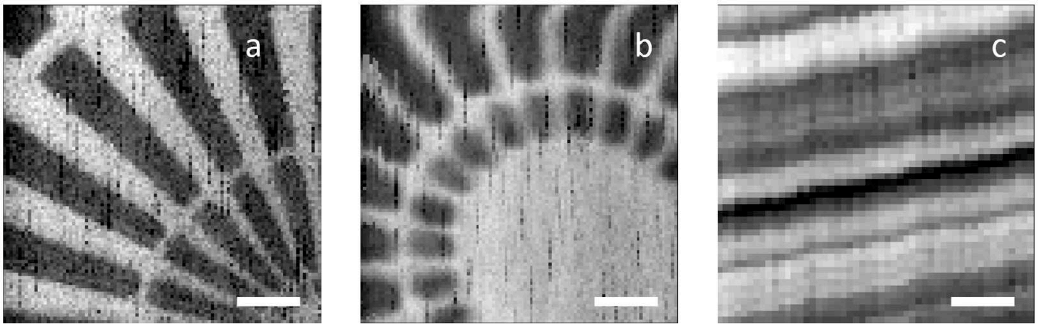

Fig. 6.4: Examples of images obtained from STXM measurements. The upper left part of the Siemens star shown in figure 6.2 (d), close to the center (a). The central features of the same Siemens star (b). A barcode-like multilayer with layers ranging in thickness between 1 nm and 40 nm (c). The scale bars are 500 nm, 200 nm and 50 nm, in (a), (b) and (c), respectively.

multilayer with nm sized layers, ranging from 1 nm to 40 nm. The image shows 50 × 50 pixels with a pixel size of 5 nm which were recorded with an exposure time of 100 ms. Layers with thicknesses down to one to two pixels, corresponding to thicknesses of 5 to 10 nm can be resolved. The color scales range from 1.9×10^6 to 2.5×10^6 counts (a), 5.4×10^6 to 7.3×10^6 counts (b) and 1.1×10^6 to 1.6×10^6 counts (c). A disadvantage of this technique is that samples which absorb only lightly result in low contrasts on a large background. The resolution additionally depends critically on how well a sample is placed in focus. The DOF of an ideal lens as given in equation 6.1 is around 360 nm for a lens with an NA of 0.014 operated at an energy of 17.5 keV ($\lambda \approx 0.071$ nm). A sample placed outside of this range experiences a larger beam which results in a reduction of resolution. Here, the aberrations of the lenses can be advantageous as mentioned before. The DOF of an aberrated lens can be much larger that the value given above, as can again be seen from the beam caustics in figure 5.15 (a) and (c) in chapter 5.2.6.

6.4 Near field ptychography

Ptychography is a technique where the structure of a sample is computed from a set of diffraction patterns obtained from scattering a beam of the sample [219, 220], while the probing beam is stepped along the sample with overlap between frames. The overlap sets constraints on the reconstruction which allows to solve the phase problem. For its realization, samples are often placed in the focused beam and far-field diffraction patterns are recorded. Near field ptychography on the contrary, as the name suggests, is a near field technique where overlapping magnified projection images are recorded instead of far field diffraction patterns [221, 222]. This allows the recording of real-space images of a sample where the overlap between frames again sets constraints to fully characterize the beam and sample. The attentive reader might notice that the experimental realization of this method is identical to projection holography: A sample is placed downstream of the focus in the highly divergent beam and stepped in the plane orthogonal to the beam with step sizes smaller than the field of view while magnified projection holograms are recorded on a detector. This was realized at the P11 beamline at PETRA III, Germany, where various samples were imaged onto an Eiger detector with pixel size of 75 μm. Figure 6.5 shows the reconstructed phases of various samples using near field ptychography. A description of the reconstruction method can be found at [215]. The nanoporous gold structure reconstruction was obtained using 21 $\times$ 3 (vertical$\times$horizontal) scan points of size 0.1 μm and 0.25 μm along the vertical- and horizontal direction, respectively. At each position, a frame was recorded with an exposure time of 5 s. For the Siemens star, 21 $\times$ 21 sample positions were recorded with a step size of 0.3 μm in both directions and an exposure time of 1 s per frame. The decorated particles in (c) were imaged by scanning the sample on a 11 $\times$ 11 points grid with 0.5 μm step size and 50 frames with exposure times of 0.1 s were recorded at each position and later averaged. A random deviation of the step size by up to 25 % was employed to reduce grid artifacts. The nanoporous gold structure was imaged at a magnification of about 32470, resulting in a pixel size of 2.3 nm, the Siemens star with a magnification of around 11850 resulting in a pixel size of 6.3 nm and the decorated particles had a magnification of 16300, which resulted in a pixel size of 4.6 nm. High resolution down to below 10 nm is achieved [215]. With this technique the 20 nm pores in (a) are well resolved and the innermost

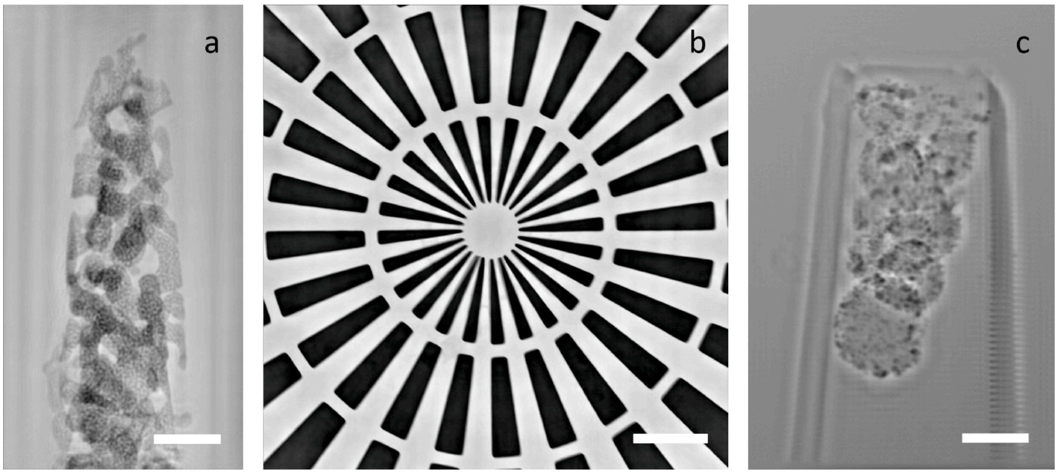

Fig. 6.5: Near field ptychographic reconstructions of the phase of various samples. A hierarchically nanoporous gold structure with smallest pore sizes around 20 nm (a). A gold Siemens star test pattern (b). In (c), iron particles decorated with gold nano particles inside a glass capillary can be seen. The color scales range from 0.0 (white) to 0.6 rad (black) (a), 0.0 to 0.7 rad (b) and 0.3 to 0.5 rad (c). The scale bars are 0.5 μm (a), 1 μm (b) and 0.5 μm (c), respectively. Nanoporous gold provided by S. Shi (Hereon) and shaped by M. Prasciolu (DESY), decorated particles provided by A. Weimer (UHH) and A. Feld (UHH). Analysis done and data provided by W. Zhang.

spokes of the Siemens star with width of 50 nm are crisp sharp. While the principle in projection holography and near field ptychography is similar, the requirements on the measurement parameters differ. For example, near field ptychography requires a larger overlap between adjacent frames of more than 90 % (compared to $\sim 50+$ % for speckle tracking) and is more prone to grid artifacts, as can be seen in figure 6.5 (c) on the right side of the glass capillary, even with random deviations in the step size. A spiral scan pattern instead of a grid would hence benefit this technique a lot. A great advantage of near field ptychography is that the achievable resolution is only limited by the NA of the optic. High NA MLLs as are discussed here are therefore excellent for such a technique, especially since this technique does not rely on aberration free optics. Lenses trading a higher NA for larger aberrations can therefore be a great choice for near field ptychography.

6.5 Convergent beam crystallography

Crystallography is a well-established technique which aims to characterize the structure of crystals and crystallized proteins through diffraction of coherent light from the periodic structures. The structure of proteins for example define their functionality, hence their reconstruction helps to understand the fundamental building blocks of life. In coherent diffractive imaging (CDI), a collimated beam is diffracted off a sample and the position of Bragg peaks is recorded on a detector. By collecting many such patterns from various sides of the sample either by rotation or by probing many identical samples at various orientations, the structure is reconstructed in Fourier- and then real space. Bragg peaks appear everywhere where the Bragg condition is satisfied for any given crystal plane. In convergent beam crystallography (CBC), a highly convergent (divergent) beam is incident on the sample instead. Since this beam spans a large range of angles, the Bragg condition is satisfied at far more positions inside the structure. For a plane previously in Bragg condition for a given ray, there is now a range of angles satisfying it, leading to streaks instead of peaks. Additionally, planes which were previously not at Bragg angles might be excited now thanks to the large range of angles present in a convergent beam along both directions. This highlights the importance of high NA MLLs for this technique, where a high NA leads to a large range of angles. This method results in a richer diffraction pattern and a higher information density per frame. As an example, an approximate 150 μm diameter zeolite crystal was placed in the divergent beam created by an MLL pair with NAs of 0.014 and 0.015 at the beamline P11 at PETRA III, at a defocus distance of around 5.5 mm, where its size roughly filled the field of view. A frame recorded on an Eiger 16M detector is shown in figure 6.6 (a). It contains a rich diffraction pattern of a multitude of diffraction streaks, arranged in circles. (b) shows a zoom in of the area marked with the red rectangle in (a). From a full rotation

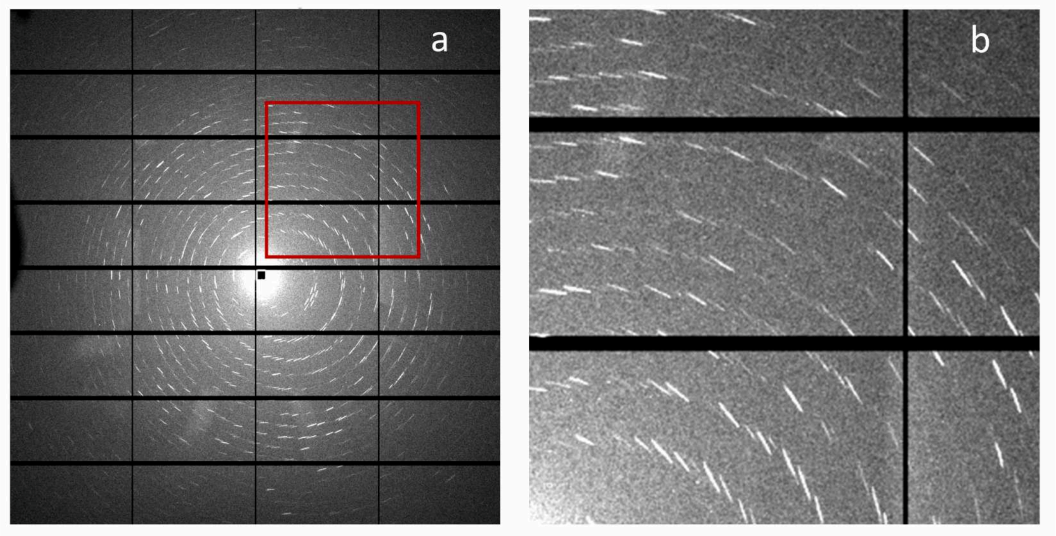

Fig. 6.6: Convergent beam crystallography done on a zeolite crystal. A rich diffraction pattern showing lots of streaks along circular arrangements (a). Enlargement of the area in (a) marked with the red box (b). The color scale ranges from 0 (black) to 5 (white).

dataset (180°), the three-dimensional structure of the crystal can be reconstructed. This technique greatly enhances the amount of information that can be gained from a single exposure of the sample which could speed up the data acquisition time and is made possible by the high NA of the MLLs.

6.6 Compton scattering imaging

Many X-ray imaging methods including some mentioned thus far as for example STXM utilize the absorption of X-rays in matter to generate contrast. Since absorbed photons deposit energy in the material and X-rays have sufficient energy to ionize, samples are damaged while being imaged. This limits the resolution at which a sample can be probed before degradation. This is of special relevance for biological specimen, where a sample might be destroyed before it can be imaged at the desired resolution. While sample preparation such as cryogenic cooling can increase the resilience, they do not allow to image samples *in vivo* and methods like (cryogenic) electron microscopy can only probe the surface. Since absorption reduces with λ^2 as the photon energy increases, the deposited dose can be reduced by operating at high photon energies. High energy X-rays can penetrate deeply into- and through matter which allows to investigate extended samples. However, the high penetration power and low absorption leads to vanishing absorption contrasts in imaging techniques such as STXM. At high photon energies, Compton scattering becomes the dominant process of light-matter interactions for low Z materials. Compton scattering is the inelastic scattering of photons from charged particles, typically electrons. An incident photon of wavelength λ inelastically scattered from an electron at an angle θ loses a fraction of its energy and thus changes its wavelength to λ' following

$$\lambda' - \lambda = \frac{h}{m_e c}(1 - \cos(\theta)), \tag{6.2}$$

where h is the Planck constant, m_e the electron rest mass and c the speed of light. For Carbon, the highest Compton scattering cross section is at around 60 keV, for example. An image can then be formed by collecting Compton scattered photons in a method referred to as scanning Compton X-ray microscopy (SCXM) [223]. In SCXM, a sample is placed in the focal plane and stepped through the beam, similar as in STXM. Instead of collecting the transmitted beam intensity behind the sample, off-axis scattered photons are detected. SCXM is therefore a dark-field imaging technique, which allows to collect high-resolution images of biological samples at much lower doses than other techniques at comparable resolutions [214]. It is a dark-field technique since scattering only occurs when a sample is present (note that air is also a sample and therefore adds to the scattering background). It should be noted here that since Compton scattering is element insensitive (as can be seen from eq. 6.2), the obtained dark-field images are quantitative maps of the electron density. Due to Compton scattering being inelastic, no scattering is present in the forward direction. Instead, the biggest yield per solid angle is above and below the optical axis (for horizontally polarized light) [214, 223]. The experimental setup shown in figure 6.7 is hence adapted such that two additional detectors placed above and below the optical axis capture the scattered X-rays, while the downstream detector functions as an I_0 beam monitor, tracking fluctuations in the beam intensity as the absorption of the samples is negligible. As the scattered light does not carry additional spatial information, all scattered photons at a given sample position can be summed up, in similar fashion to STXM. To reduce background and scattering

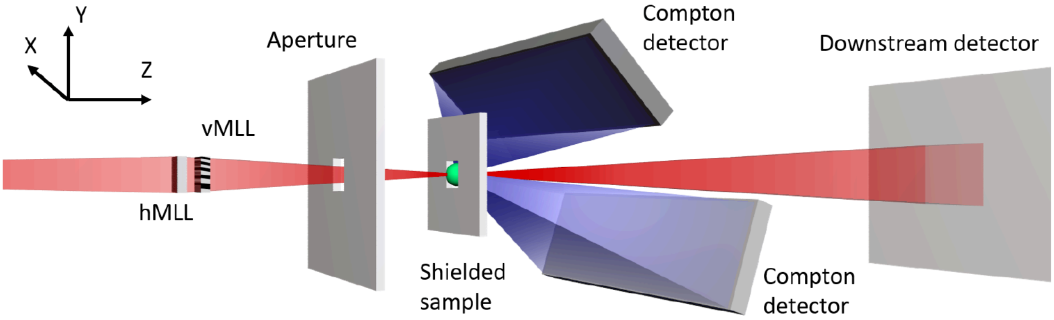

Fig. 6.7: Schematic of the setup used for Compton imaging. The high energy X-ray beam is focused onto a sample by a pair of MLLs (vMLL focuses vertically and hMLL horizontally). An aperture between lenses and sample and a shield around the sample block stray light. The Compton scattered photons are collected by two dark-field detectors, positioned above and below the optical axis. The transmitted signal is recorded on a downstream detector.

from sources other than the sample, lead cones were placed on the detectors with openings at the tip and angled pointing at the interaction region. This setup was

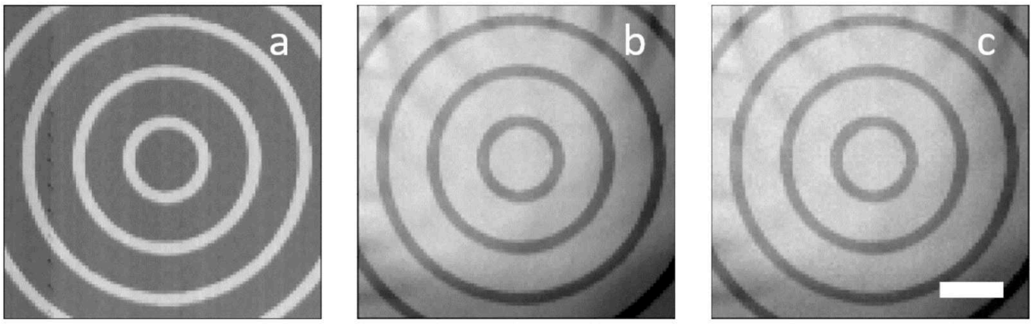

Fig. 6.8: SCXM images of the downstream (a), upper (b) and lower (c) detector of a bulls eye sample. In the parts with the structure present, photons are scattered and absorbed, the transmitted- and scattered images are therefore complementary. Ghost images can be seen in (b) and (c) which are a result of parasitic diffraction orders scattering off the sample. The scale bar is 10 μm.

prepared at the P07 beamline at PETRA III at 60 keV. For an initial test, a 13 μm thick gold bulls-eye sample was placed in the focus of the beam and stepped around a 2D grid. Figure 6.8 shows the SCXM image (photons recorded at each sample position) on all three detectors of a bulls-eye obtained by scanning it with 100×100 steps of 0.5 μm with an exposure time of 20 ms per frame and summing up all pixels on the detectors at each position. The color scales range from 1.1×10^7 (black) to 1.3×10^7 (white) counts (a), 5×10^4 to 1×10^5 counts (b) and 8×10^3 to 2.2×10^5 (c). Since absorption in this sample is non-negligible, a complementary image of the scattering map (b),(c) can be seen in the transmission (a). Due to the experimental geometry, the lower Compton detector was further away from the sample and hence collected a smaller solid angle range, resulting in a weaker scattering signal. To maximize the contrast and normalize the electron density maps by beam fluctuations, the signal from the two Compton detectors can be summed up and divided by the signal from the downstream detector. A few examples of this Compton scattered signal normalized by the transmission signal obtained from biological samples are shown in figure 6.9. The samples shown include a diatom shell (a), pine pollen (b) and hair on a mosquito wing (c). The color scales go from low (black) to high (white) signal and the scan parameters can be found in table 6.1. The achievable resolution was about 72 nm [214]. It should be noted here that

Tab. 6.1: Measurement parameters of the SCXM images presented in figure 6.9.

Sample	Image	Steps	Step size [nm]	Dwell time [ms]
Diatom	(a)	200×200	50	50
Pollen	(b)	800×800	50	50
Hairs	(c)	200×200	100	50

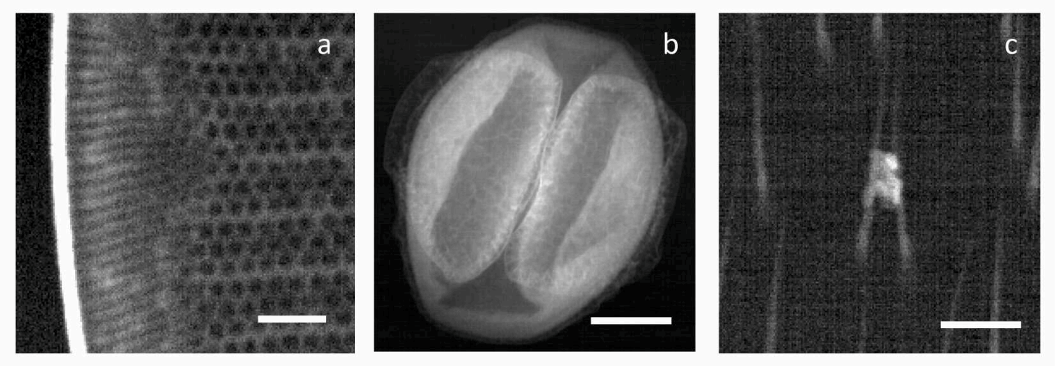

Fig. 6.9: Examples of dark-field images of biological samples obtained by Compton imaging. Shown are part of a diatom (a), a pine pollen grain (b) and hairs on a mosquito wing (c). The color scales range from low scattering (black) to high scattering (white). The scale bars correspond to 2 μm (a), 10 μm (b) and 5 μm (c). The measurement parameters can be found in table 6.1. Diatom provided by C. Hamm (AWI).

the resolution is not limited by the lenses, which could focus the beam to below 10 nm, but instead by the source size of the synchrotron. Since PETRA III is a third-generation synchrotron, it does not provide a diffraction-limited source size at such high energies. Therefore, Compton scattering imaging would greatly benefit from fourth generation synchrotrons such as PETRA IV. Not only could smaller sampling be realized, the increased flux would also speed up data acquisition by several orders of magnitude. This potentially allows imaging at resolutions approaching 10 nm and below in 3D without exceeding the tolerable doses. Fast data acquisition may also allow to track changes over time, such as the movement of particles inside the cell. Further information on the dose the samples experience using this technique and how it compares to other imaging techniques can be found at [214].

6.7 Focusing XFEL X-ray beams with MLLs

Results shown thus far are from measurements done at either laboratory setups or synchrotrons. There, lenses and samples are illuminated at a rather constant rate. XFELs produce ultrashort X-ray pulses, with peak intensities orders of magnitude higher than what can be achieved at synchrotrons. Both, the high peak power as well as the ultrashort time scale opened up new opportunities and possibilities for research in the fields of biology, chemistry, physics and material science [224–226]. Effects such as non-linear Compton scattering [227, 228] require intensities on a sample which can only be achieved by focusing the bright XFEL pulses to sub-μm spots. MLLs are excellent candidates for the extreme focusing of XFEL pulses, as their small foci lead to high local intensities. The very same intensity that enables new experiments poses challenges to the optics. A non-negligibly fraction of the incoming beam is absorbed by the lens, heating it up [73, 170]. This is especially true for the operating X-ray energies at XFELs, which are typically lower than what is used at the synchrotron for the experiments presented here. Due to the high repetition rate offered by XFELs today, the lens has little time to distribute the heat away and cool down. Z. Rek et al. showed that a pulse train can heat up an MLL mounted in the "standard" configuration (defined in fig. 4.9 in chapter 4.3 with an example shown in fig. 6.10 (a)) to well above 1000 K [73]. The lens being composed of a dense material like WC further increases the absorption and thus energy deposition in the lens. By replacing WC with a lower Z material, the absorption of the material can be decreased [72]. Another advantage of a lower Z material is that the optimum thickness at which the highest diffraction efficiency is achieved shifts to larger values. A lens made from a lower Z material cut to its optimum thickness hence has a larger volume within which the energy is deposited and the heat can be distributed. The second factor limiting the heat distribution is the connection between the lens and the lens holder. In the "standard" configuration, the lens is only connected to the holder at two points. This greatly inhibits heat transport. To allow heat to dissipate faster, a larger contact area is required. Since trains of intense X-ray pulses carry significant momentum which add high stress to the connection points between the lens and holder, a larger contact area also prevents the lens from being pushed off the mount. The large contact area lens mount discussed in chapter 4.3 offers an improved design for such conditions, aiding both, the heat dissipation and the stability against photon pressure. An example of a lens fabricated in this configuration is shown in figure 6.10 (b). The lens extends to both sides of the area used for focusing and is glued to the back of the substrate. A channel is cut from the substrate in order to not block the beam. Since the lens is glued to the side of the holder facing the incoming beam, the pressure pushes the lens against the mount, reducing the risk of the lens losing connection to the substrate. By crossing two such lenses in the X-ray beam of the EuXFEL and placing a sample downstream of focus, projection holograms can be obtained, in similar fashion as is done at the

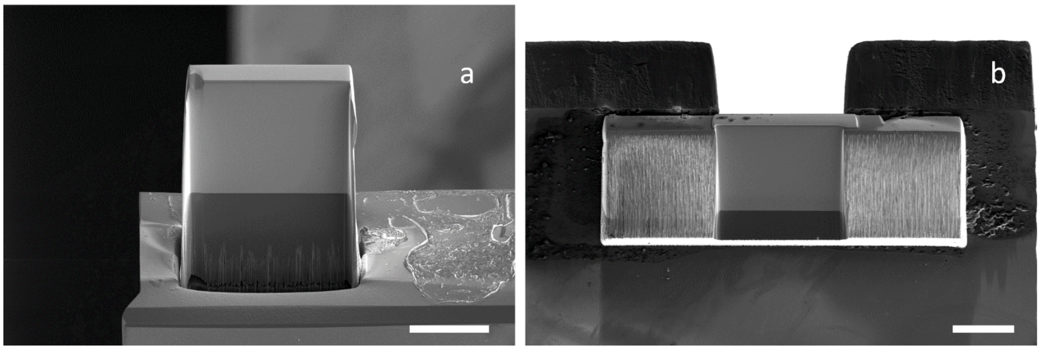

Fig. 6.10: Comparison of the "standard" lens configuration (a) and the large contact area design (b) which were introduced in figure 4.9 in chapter 4.3. The larger contact area increases the heat transport and stabilizes the lens against the photon pressure. Both lenses are mounted on 100 μm thick diamond substrates. The scale bars are 50 μm. Reproduced by courtesy of M. Prasciolu and J. C. Wong.

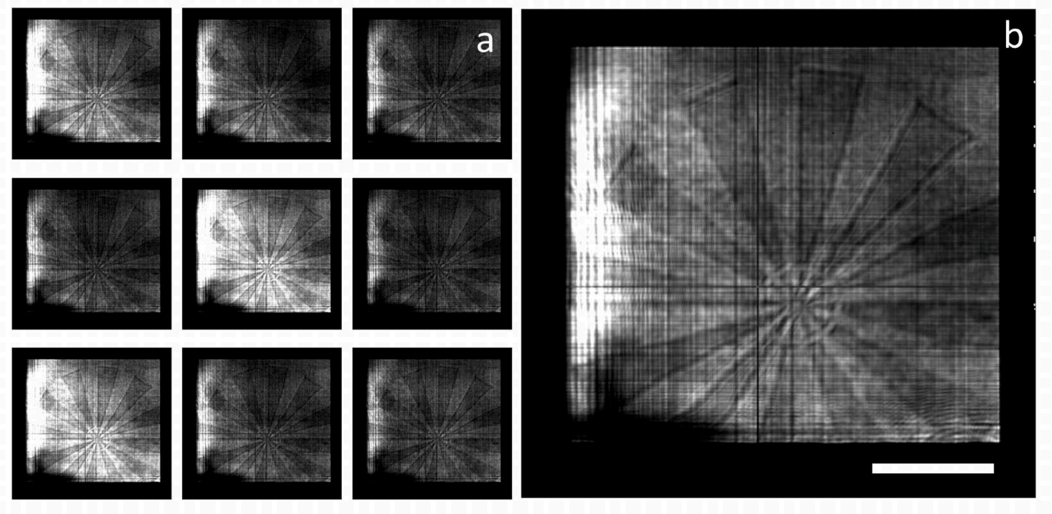

Fig. 6.11: MLLs used at the EuXFEL to image a Siemens star sample. Due to the intensity fluctuations of the beam, the illumination varies from shot to shot. A few images of single shots (a). A clearer image can be obtained by taking many individual shots. The average of 100 shots (b). The color scale ranges from 100 to 2000 counts. The scale bar is 5 μm.

synchrotron. At the XFEL however, the intensity fluctuates from shot to shot. This is shown in figure 6.11 (a), where a few images of individual shots are given. By averaging many individual images, a clearer picture can be acquired, as is shown in (b), where 100 frames were averaged.

7

Summary and outlook

With the advent of fourth generation synchrotrons, there is a growing need for high quality X-ray optics that can fully exploit the available beam qualities. Systems based on multi-bend achromats can provide diffraction limited- and symmetric source sizes in the hard X-ray regime at- and below wavelengths of 1 Å. High quality and efficient X-ray optics are required to focus such beams to spot sizes approaching 1 nm. Multilayer Laue lenses (MLLs) have emerged in the last two decades as a new type of X-ray optic that can in principle focus hard X-rays with high efficiency (> 60 %) to 1 nm spots. However, the manufacturing precision requirements of optics for such extreme focusing are challenging. This is no different for MLLs, where misplaced layers cause wavefront aberrations that decrease the focusing performance and result in a broadening of the focal spot. To improve the quality and performance of high numerical aperture (NA) MLLs for extreme focusing, rapid lens characterization and subsequent correction of aberrations is required. To accelerate the development cycle of MLLs, laboratory-based wavefront characterization can be used, which is made possible by commercially available X-ray sources with sufficient flux and new and improved phase retrieval methods that allow phase reconstruction in noisy and incoherent environments.

To determine the optimum working conditions for multilayer optics, periodic multilayer gratings made from W/SiC and WC/SiC were investigated. This allows to probe the diffraction efficiency and the optimum optical thickness of a volume diffractive structure at individual bilayer periods. It was found that high quality multilayer structures with individual layer thicknesses in the single digit nanometer range can be produced with high accuracy using magnetron sputter deposition, achieving diffraction efficiencies as high as 60 % at a photon energy of 17.5 keV. While a drift in sputter rate during deposition can cause large phase aberrations in MLLs, it only leads to a small change of the period in the grating structures, which was found to not significantly affect the diffraction performance. Instead, it was found that the main limitation is the layer intermixing, causing a reduction in the highest possible diffraction efficiency and requiring optically thicker structures. As the depth of this effect - found to be about 0.4 nm - is roughly constant, it has a greater effect on thinner periods. As a result, the ideal shape of an MLL is a trapezoid (with concave sidewalls), that is optically thinner at the thicker periods and optically thicker at the thinner periods. For lenses whose thinnest layers are close to the substrate, the

shape is already a trapezoid because the sidewalls of the structure are not perfectly vertical, which is a result of the focused ion beam fabrication. The depth of layer mixing also limits the aperture size of MLLs. At a distance from the optical axis where the required multilayer period decreases to 0.8 nm, the diffraction efficiency is expected to decrease to 0. Increasing the aperture of the lens beyond this limit would not increase the NA of the lens.
In contrast to other X-ray optics, the efficiency of multilayer optics increases with increasing photon energy. The absorption within the optic decreases with λ^2 far from absorption edges, but the optimal multilayer thickness required for the highest diffraction efficiency increases only approximately linearly with photon energy, resulting in an overall higher efficiency at high energies. This was demonstrated by preparing periodic multilayer gratings for an X-ray energy of 60 keV, with which diffraction efficiencies of up to 80 % could be achieved. High photon energies are attractive for imaging of biological samples as the reduced absorption reduces the radiation damage to such samples.

Using the knowledge gained from periodic gratings, MLLs of ideal optical thickness were produced. To improve their fabrication in terms of layer placements, their wavefronts were characterized using a laboratory X-ray setup and a robust and improved phase retrieval algorithm. The improved algorithm, available as an open access Python module called pyrost, was developed in our group to handle outliers in the measured data and yield accurate results even when the signal-to-noise ratio is low by incorporating machine learning techniques. This algorithm was used to investigate the conditions under which circumstances a precise and accurate phase retrieval of MLLs in a laboratory setup is possible and which requirements the lenses themselves and the probing samples have to fulfill. It was shown that the pyrost algorithm holds its promise regarding its robustness and that the wavefront reconstruction results are largely independent of the data acquisition conditions, as long as the sample and lens are aligned with respect to each other. The wavefront characterization of MLLs previously took > 10 h which has now been reduced to a few minutes without compromising accuracy.

The wavefront of a lens can be related to the layer displacements in the multilayer structure, allowing to implement a correction for subsequent depositions. It has been noted previously that the sputter rate changes approximately linearly with time, resulting in a phase aberration that scales with the pupil coordinate to the third power. By estimating the expected sputter rate drift from the characterization of a previous multilayer, aberrations can be reduced through the implementation of a correction factor into the next deposition. Although this allows the production of lenses with lower aberrations, its precision is limited as the sputter rate change is not exactly linear and varies between depositions. Nevertheless, due to the very high NA of our MLLs, significant aberrations remain that need to be corrected externally.

Since thin refractive phase correctors are not sufficient to correct aberrations of the order of magnitude that the high NA MLLs experience, the concept of a compound refractive corrector was realized. The idea of using the additive refractive correction from many individual elements had previously been proposed but not realized to correct high NA MLL pairs used for high-resolution imaging. In this work, 3D printing of polymer refractive correctors was successfully implemented. Using an array of 20 corrector pairs, the aberrations of first a single MLL and later a lens pair were reduced by more than 75 %, increasing the peak intensity by a factor of 4.8. This resulted in a reduction of the point spread function full width half maximum from 4.7 nm × 4.1 nm to 2.9 nm × 2.8 nm, which is a new record and close to the diffraction limited spot size of 2.1 nm × 2.1 nm.

With well-characterized and aberration-corrected MLLs, several imaging schemes have been realized at synchrotrons. For projection imaging at high magnifications, a resolution well below 10 nm has been achieved, which is only possible due to the high NA of the MLLs. The X-ray beam focused by the high NA optics covers a wide angular range, allowing the exploration of a new imaging technique, convergent beam crystallography, which uses the diffraction of a convergent - instead of a collimated - beam to produce rich diffraction patterns that can map the microscopic structure of the crystal. At 60 keV, high quality dark-field images of various biological samples have been obtained at much lower doses compared to coherent scattering techniques with resolutions up to 70 nm, which were limited by the size of the source rather than the lenses. With an improved mount, MLLs were also able to focus XFEL beams.

The next natural step should be to extend high-resolution imaging to three dimensions. Both projection imaging and scanning Compton X-ray microscopy can be combined with tomography to form high-resolution 3D reconstructions. Especially the latter will benefit from fourth generation synchrotrons, which allow the focusing capabilities already offered by MLLs at high energies to be fully exploited. With a diffraction-limited source, the lenses that enabled a resolution of 70 nm at 60 keV could already provide resolutions below 10 nm. A future upgrade of PETRA III to PETRA IV could provide three orders of magnitude higher brilliance at high energies, which would significantly reduce the time needed to acquire complete three-dimensional datasets.

While polymer phase correctors cannot withstand the intensity of an XFEL, phase correctors made from 3D printed glass or cut from diamond could be employed to further improve the lens performance at both XFELs and synchrotrons. The compound design can be improved by considering the propagation between individual structures and designing each shape individually, similar to adiabatically focusing lenses. It is possible to improve the phase corrector by adding any residual aberrations to its design and fabricating a new one during the experiment. However, the relative position to the lenses might be misaligned after exchanging the structure, which could ultimately lead to a deterioration of the wavefront instead of an improvement. Instead, a better approach would be to add a single thin phase plate to the beam in addition to the already positioned compound corrector, which can correct any residual aberrations. Such a combination of optics has the potential to achieve diffraction limited imaging approaching 1 nm in the future.

Improvements to the deposition system, such as a more precise active feedback system, could also reduce aberrations to the point where a compound approach for a phase corrector becomes obsolete. With the reduction of residual aberrations, the precision requirements for accurate phase retrieval increases, demanding continuous improvements of existing algorithms. Low aberrations through precise deposition control allow the NA of multilayer optics to be increased by extending them to the optical axis and beyond, more than doubling the NA without the need to produce thinner layers, something which is currently limited by layer intermixing. Depositing a multilayer on a wire to produce a volume zone plate further simplifies the optics alignment. However, such a structure is even more challenging to fabricate for high resolutions.

To further improve the laboratory-based wavefront characterization techniques, brighter sources are promising. Liquid jet based setups or new table-top systems such as plasma wakefield acceleration based free electron lasers could provide sufficient flux to enable 2D wavefront characterization of a lens pair using a laboratory setup. This could potentially allow to bring some imaging techniques using MLLs like projection imaging from synchrotrons to laboratory setups, reducing the need for beamtime access. With improvements in the manufacturing and characterization of high quality high NA MLLs and the advent of fourth generation synchrotrons, MLLs are expected to have a bright future in the realm of high resolution X-ray microscopy.

Appendix

8

A List of abbreviations

Table 8.1 shows an alphabetically sorted list of the abbreviations used in this thesis.

Tab. 8.1: List of abbreviations used in this thesis.

Abbreviation	Meaning
2PP	Two photon polymerization
AFL	Adiabatically focusing lens
BLMG	Blazed lamellar multilayer grating
CBC	Convergent beam crystallography
CDI	Coherent diffractive imaging
CRC	Compound refractive corrector
CRL	Compound refractive lens
DiLL	Dip-in laser lithography
DOF	Depth of focus
DTD	Dynamical theory of diffraction
EBL	Electron beam lithography
EUV	Extreme ultraviolet
EuXFEL	European X-ray free electron laser
FIB	Focused ion beam
FWHM	Full width half maximum
FZP	Fresnel zone plate
IPA	Isopropanol
ITO	Indium tin oxide
KB	Kirkpatrick–Baez
LMG	Lamellar multilayer grating
MBG	Multilayer coated blazed grating
MLL	Multilayer Laue lens
NA	Numerical aperture
OPD	Optical path difference
OSA	Order sorting aperture
OSB	Order sorting blade
PFIB	Plasma focused ion beam
PGMEA	Propylene glycol methyl ether acetate
PSF	Point spread function
PXST	Ptychographic X-ray speckle tracking
RMS	Root mean square
R-PXST	Robust ptychographic X-ray speckle tracking
RST	Robust speckle tracking
SCXM	Scanning Compton X-ray microscopy
SEM	Scanning electron microscopy
SMG	Sliced multilayer grating
SNR	Signal to noisy ratio
STXM	Scanning transmission X-ray microscopy
VPHG	Volume phase holographic grating
XFEL	X-ray free electron laser
XRD	X-ray diffraction
XRF	X-ray fluorescence
XST	X-ray speckle tracking

Bibliography

[1] P. F. Tavares, S. C. Leemann, M. Sjöström, and Å. Andersson, „The max iv storage ring project,“ *Journal of synchrotron radiation*, vol. 21, no. 5, pp. 862–877, 2014 (cit. on p. 1).

[2] P. Raimondi, „Esrf-ebs: The extremely brilliant source project,“ *Synchrotron Radiation News*, vol. 29, no. 6, pp. 8–15, 2016 (cit. on p. 1).

[3] L. Liu, N. Milas, A. Mukai, *et al.*, „A new 5ba low emittance lattice for sirius,“ *Proc. IPAC'13*, pp. 1874–1876, 2013 (cit. on p. 1).

[4] *Aps upgrade introduction*, `https://www.aps.anl.gov/`, APSUpgrade (cit. on p. 1).

[5] A. White, K. Goldberg, S. Kevan, *et al.*, „A new light for berkeley lab—the advanced light source upgrade,“ *Synchrotron Radiation News*, vol. 32, no. 1, pp. 32–36, 2019 (cit. on p. 1).

[6] Y. Jiao and G. Xu, „PEPX-type lattice design and optimization for the high energy photon source,“ *Chin. Phys. C*, vol. 39, no. 6, p. 067 004, Jun. 2015 (cit. on p. 1).

[7] C. G. Schroer, I. Agapov, W. Brefeld, *et al.*, „PETRA IV: the ultralow-emittance source project at DESY,“ *Journal of Synchrotron Radiation*, vol. 25, no. 5, pp. 1277–1290, Sep. 2018 (cit. on p. 1).

[8] T. Watanabe and H. Tanaka, „Spring-8 upgrade project: Accelerator redesigned and restarted,“ *Synchrotron Radiation News*, vol. 36, no. 1, pp. 3–6, 2023 (cit. on p. 1).

[9] G. E. Ice, J. D. Budai, and J. W. Pang, „The race to x-ray microbeam and nanobeam science,“ *Science*, vol. 334, no. 6060, pp. 1234–1239, 2011 (cit. on p. 1).

[10] T. Tomie, „X-ray lens,“ 2 526, 409, 1994 (cit. on p. 1).

[11] A. Snigirev, V. Kohn, I. Snigireva, and B. Lengeler, „A compound refractive lens for focusing high-energy x-rays,“ *Nature*, vol. 384, no. 6604, pp. 49–51, 1996 (cit. on p. 1).

[12] S. Bajt and C. G. Schroer, „Sub-micrometer focusing and high-resolution imaging with refractive lenses and multilayer laue optics,“ *Synchrotron Light Sources and Free-Electron Lasers: Accelerator Physics, Instrumentation and Science Applications*, pp. 1161–1188, 2020 (cit. on p. 1).

[13] J. Patommel, S. Klare, R. Hoppe, *et al.*, „Focusing hard x rays beyond the critical angle of total reflection by adiabatically focusing lenses,“ *Applied Physics Letters*, vol. 110, no. 10, p. 101 103, Mar. 2017 (cit. on p. 1).

[14] P. Kirkpatrick and A. V. Baez, „Formation of optical images by x-rays,“ *JOSA*, vol. 38, no. 9, pp. 766–774, 1948 (cit. on p. 1).

[15] K. Yamauchi, H. Mimura, S. Matsuyama, *et al.*, „Focusing mirror for coherent hard x-rays,“ *Synchrotron light sources and free-electron lasers: accelerator physics, instrumentation and science applications*, pp. 1093–1122, 2020 (cit. on p. 1).

[16] Y. Suzuki, „Resolution limit of refractive lens and fresnel lens in x-ray region,“ *Japanese Journal of Applied Physics*, vol. 43, no. 10R, p. 7311, Oct. 2004 (cit. on p. 2).

[17] H. Mimura, S. Handa, T. Kimura, *et al.*, „Breaking the 10 nm barrier in hard-x-ray focusing,“ *Nature Physics*, vol. 6, no. 2, pp. 122–125, 2010 (cit. on p. 2).

[18] K. Yamauchi, H. Mimura, T. Kimura, *et al.*, „Single-nanometer focusing of hard x-rays by kirkpatrick-baez mirrors,“ *Journal of Physics: Condensed Matter*, vol. 23, no. 39, p. 394 206, Sep. 2011 (cit. on p. 2).

[19] J. Yamada, S. Matsuyama, I. Inoue, *et al.*, „Extreme focusing of hard x-ray free-electron laser pulses enables 7 nm focus width and 1022 w cm-2 intensity,“ *Nature Photonics*, vol. 18, no. 7, pp. 685–690, 2024 (cit. on p. 2).

[20] W. Chao, J. Kim, S. Rekawa, P. Fischer, and E. H. Anderson, „Demonstration of 12 nm resolution fresnel zone plate lens based soft x-ray microscopy,“ *Optics Express*, vol. 17, no. 20, pp. 17 669–17 677, 2009 (cit. on p. 2).

[21] I. Mohacsi, I. Vartiainen, B. Rösner, *et al.*, „Interlaced zone plate optics for hard x-ray imaging in the 10 nm range,“ *Scientific Reports*, vol. 7, no. 1, p. 43 624, 2017 (cit. on p. 2).

[22] J. Maser, G. B. Stephenson, S. Vogt, *et al.*, „Multilayer laue lenses as high-resolution x-ray optics,“ in *Design and microfabrication of novel X-ray optics II*, SPIE, vol. 5539, 2004, pp. 185–194 (cit. on p. 2).

[23] H. Kang, J. Maser, G. Stephenson, *et al.*, „Nanometer linear focusing of hard x rays by a multilayer laue lens,“ *Physical Review Letters*, vol. 96, no. 12, p. 127 401, 2006 (cit. on pp. 2, 14).

[24] H. C. Kang, G. B. Stephenson, C. Liu, *et al.*, „Sectioning of multilayers to make a multilayer laue lens,“ *Review of scientific instruments*, vol. 78, no. 4, 2007 (cit. on p. 2).

[25] H. Yan, V. Rose, D. Shu, *et al.*, „Two dimensional hard x-ray nanofocusing with crossed multilayer laue lenses,“ *Opt. Express*, vol. 19, no. 16, pp. 15 069–15 076, Aug. 2011 (cit. on p. 2).

[26] H. Yan, R. Conley, N. Bouet, and Y. S. Chu, „Hard x-ray nanofocusing by multilayer laue lenses,“ *Journal of Physics D: Applied Physics*, vol. 47, no. 26, p. 263 001, 2014 (cit. on pp. 2, 11).

[27] A. J. Morgan, M. Prasciolu, A. Andrejczuk, *et al.*, „High numerical aperture multilayer laue lenses,“ en, *Sci. Rep.*, vol. 5, no. 1, p. 9892, Jun. 2015 (cit. on pp. 2, 15).

[28] S. Bajt, M. Prasciolu, H. Fleckenstein, *et al.*, „X-ray focusing with efficient high-NA multilayer laue lenses,“ en, *Light Sci. Appl.*, vol. 7, no. 3, p. 17 162, Mar. 2018 (cit. on p. 2).

[29] K. T. Murray, A. F. Pedersen, I. Mohacsi, *et al.*, „Multilayer laue lenses at high x-ray energies: Performance and applications," en, *Opt. Express*, vol. 27, no. 5, pp. 7120–7138, Mar. 2019 (cit. on pp. 2, 14, 18).

[30] R. Conley, C. Liu, J. Qian, *et al.*, „Wedged multilayer laue lens," *Review of Scientific Instruments*, vol. 79, no. 5, 2008 (cit. on pp. 2, 14).

[31] H. Yan, H. C. Kang, R. Conley, *et al.*, „Multilayer laue lens: A path toward one nanometer x-ray focusing," *X-Ray Optics and Instrumentation*, vol. 2010, no. 1, p. 401 854, 2010 (cit. on p. 2).

[32] H. N. Chapman and S. Bajt, „A ray-trace analysis of x-ray multilayer laue lenses for nanometer focusing," *Journal of Optics*, vol. 22, no. 11, p. 115 610, 2020 (cit. on pp. 2, 3, 17).

[33] M. Prasciolu, A. Leontowich, J. Krzywinski, *et al.*, „Fabrication of wedged multilayer laue lenses," *Optical Materials Express*, vol. 5, no. 4, pp. 748–755, 2015 (cit. on pp. 2, 14, 15).

[34] R. Conley, N. Bouet, Y. S. Chu, *et al.*, „Multilayer laue lens: A brief history and current status," *Synchrotron Radiation News*, vol. 29, no. 4, pp. 16–20, 2016 (cit. on pp. 2, 12).

[35] H. N. Chapman, M. Prasciolu, K. T. Murray, J. L. Dresselhaus, and S. Bajt, „Analysis of x-ray multilayer laue lenses made by masked deposition," *Optics express*, vol. 29, no. 3, pp. 3097–3113, 2021 (cit. on pp. 2, 14, 15, 27, 53, 78).

[36] T. Liese, V. Radisch, and H.-U. Krebs, „Fabrication of multilayer laue lenses by a combination of pulsed laser deposition and focused ion beam," *Review of scientific instruments*, vol. 81, no. 7, 2010 (cit. on p. 2).

[37] U. Bonse and M. Hart, „An x-ray interferometer," *Applied Physics Letters*, vol. 6, no. 8, pp. 155–156, 1965 (cit. on p. 3).

[38] S. Wilkins, T. E. Gureyev, D. Gao, A. Pogany, and A. Stevenson, „Phase-contrast imaging using polychromatic hard x-rays," *Nature*, vol. 384, no. 6607, pp. 335–338, 1996 (cit. on p. 3).

[39] R. G. Lane and M. Tallon, „Wave-front reconstruction using a shack–hartmann sensor," *Applied optics*, vol. 31, no. 32, pp. 6902–6908, 1992 (cit. on p. 3).

[40] B. C. Platt and R. Shack, *History and principles of shack-hartmann wavefront sensing*, 2001 (cit. on p. 3).

[41] T. Weitkamp, B. Nöhammer, A. Diaz, C. David, and E. Ziegler, „X-ray wavefront analysis and optics characterization with a grating interferometer," *Appl. Phys. Lett.*, vol. 86, no. 5, p. 054 101, 2005 (cit. on p. 3).

[42] M. Idir, P. Mercere, M. H. Modi, *et al.*, „X-ray active mirror coupled with a hartmann wavefront sensor," *Nucl. Instrum. Meth. Phys. Res. A*, vol. 616, no. 2-3, pp. 162–171, 2010 (cit. on p. 3).

[43] S. Berujon, H. Wang, S. Alcock, and K. Sawhney, „At-wavelength metrology of hard x-ray mirror using near field speckle," *Optics express*, vol. 22, no. 6, pp. 6438–6446, 2014 (cit. on p. 3).

[44] H. Wang, J. Sutter, and K. Sawhney, „Advanced in situ metrology for x-ray beam shaping with super precision,“ *Optics Express*, vol. 23, no. 2, pp. 1605–1614, 2015 (cit. on p. 3).

[45] Y. Kayser, C. David, U. Flechsig, *et al.*, „X-ray grating interferometer for in situ and at-wavelength wavefront metrology,“ *J. Synchr. Rad.*, vol. 24, no. 1, pp. 150–162, 2017 (cit. on p. 3).

[46] J. Hagemann, A.-L. Robisch, M. Osterhoff, and T. Salditt, „Probe reconstruction for holographic x-ray imaging,“ *J. Synchr. Rad.*, vol. 24, no. 2, pp. 498–505, 2017 (cit. on p. 3).

[47] S. Matsuyama, T. Inoue, J. Yamada, *et al.*, „Nanofocusing of x-ray free-electron laser using wavefront-corrected multilayer focusing mirrors,“ *Sci. Rep.*, vol. 8, no. 1, p. 17 440, 2018 (cit. on p. 3).

[48] J. Yamada, T. Inoue, N. Nakamura, *et al.*, „X-ray single-grating interferometry for wavefront measurement and correction of hard x-ray nanofocusing mirrors,“ *Sensors*, vol. 20, no. 24, p. 7356, 2020 (cit. on p. 3).

[49] A. Mikhaylov, S. Reich, M. Zakharova, *et al.*, „Shack–hartmann wavefront sensors based on 2d refractive lens arrays and super-resolution multi-contrast x-ray imaging,“ *Journal of synchrotron radiation*, vol. 27, no. 3, pp. 788–795, 2020 (cit. on p. 3).

[50] G. Zan, D. J. Vine, W. Yun, *et al.*, „Quantitative analysis of a micro array anode structured target for hard x-ray grating interferometry,“ *Physics in Medicine & Biology*, vol. 65, no. 3, p. 035 008, 2020 (cit. on p. 3).

[51] J. Vila-Comamala, L. Romano, K. Jefimovs, *et al.*, „High sensitivity x-ray phase contrast imaging by laboratory grating-based interferometry at high talbot order geometry,“ *Optics Express*, vol. 29, no. 2, pp. 2049–2064, 2021 (cit. on p. 3).

[52] S. Zhao, Y. Yang, Y. Shen, *et al.*, „Optics metrology and at-wavelength wavefront characterization by a microfocus x-ray grating interferometer,“ *Opt. Express*, vol. 29, no. 14, pp. 22 704–22 713, 2021 (cit. on p. 3).

[53] Y. Kim, D. Oh, S. Huh, *et al.*, „Deep learning-based statistical noise reduction for multidimensional spectral data,“ en, *Rev. Sci. Instrum.*, vol. 92, no. 7, p. 073 901, Jul. 2021 (cit. on p. 3).

[54] Z. Shi, K. Jefimovs, L. Romano, J. Vila-Comamala, and M. Stampanoni, „Laboratory x-ray interferometry imaging with a fan-shaped source grating,“ *Optics Letters*, vol. 46, no. 15, pp. 3693–3696, 2021 (cit. on p. 3).

[55] S. Berujon, H. Wang, and K. Sawhney, „X-ray multimodal imaging using a random-phase object,“ *Physical Review A—Atomic, Molecular, and Optical Physics*, vol. 86, no. 6, p. 063 813, 2012 (cit. on p. 4).

[56] K. S. Morgan, D. M. Paganin, and K. K. W. Siu, „X-ray phase imaging with a paper analyzer,“ *Applied Physics Letters*, vol. 100, no. 12, p. 124 102, Mar. 2012 (cit. on p. 4).

[57] S. Berujon, E. Ziegler, and P. Cloetens, „X-ray pulse wavefront metrology using speckle tracking,“ *J. Synchr. Rad.*, vol. 22, no. 4, pp. 886–894, 2015 (cit. on p. 4).

[58] A. J. Morgan, H. M. Quiney, S. Bajt, and H. N. Chapman, „Ptychographic X-ray speckle tracking,“ *Journal of Applied Crystallography*, vol. 53, no. 3, pp. 760–780, Jun. 2020 (cit. on pp. 4, 20, 64, 75).

[59] A. J. Morgan, K. T. Murray, M. Prasciolu, *et al.*, „Ptychographic X-ray speckle tracking with multi-layer Laue lens systems,“ *Journal of Applied Crystallography*, vol. 53, no. 4, pp. 927–936, Aug. 2020 (cit. on pp. 4, 20).

[60] A. J. Morgan, K. T. Murray, H. M. Quiney, S. Bajt, and H. N. Chapman, „*speckle-tracking*: a software suite for ptychographic X-ray speckle tracking,“ *Journal of Applied Crystallography*, vol. 53, no. 6, pp. 1603–1612, Dec. 2020 (cit. on pp. 4, 20).

[61] R. James, „The dynamical theory of x-ray diffraction,“ in ser. Solid State Physics, F. Seitz and D. Turnbull, Eds., vol. 15, Academic Press, 1963, pp. 53–220 (cit. on p. 4).

[62] H. C. Kang, G. B. Stephenson, C. Liu, *et al.*, „High-efficiency diffractive x-ray optics from sectioned multilayers,“ *Applied Physics Letters*, vol. 86, no. 15, p. 151 109, Apr. 2005 (cit. on p. 5).

[63] K. Sawhney, D. Laundy, V. Dhamgaye, and I. Pape, „Compensation of X-ray mirror shape-errors using refractive optics,“ *Applied Physics Letters*, vol. 109, no. 5, p. 051 904, Aug. 2016 (cit. on p. 5).

[64] F. Seiboth, A. Schropp, M. Scholz, *et al.*, „Perfect x-ray focusing via fitting corrective glasses to aberrated optics,“ en, *Nat. Commun.*, vol. 8, no. 1, p. 14 623, Mar. 2017 (cit. on pp. 5, 81, 82).

[65] D. Laundy, V. Dhamgaye, T. Moxham, and K. Sawhney, „Adaptable refractive correctors for x-ray optics,“ *Optica*, vol. 6, no. 12, pp. 1484–1490, Dec. 2019 (cit. on pp. 5, 81).

[66] V. Dhamgaye, D. Laundy, S. Baldock, T. Moxham, and K. Sawhney, „Correction of the X-ray wavefront from compound refractive lenses using 3D printed refractive structures,“ *Journal of Synchrotron Radiation*, vol. 27, no. 6, pp. 1518–1527, Nov. 2020 (cit. on pp. 5, 81–83).

[67] K. T. Murray, „Wavefront aberrations of high numerical aperture x-ray optics,“ Ph.D. dissertation, Universität Hamburg, 2021 (cit. on pp. 5, 17, 26, 79, 81, 83).

[68] F. Seiboth, A. Kubec, A. Schropp, *et al.*, „Rapid aberration correction for diffractive x-ray optics by additive manufacturing,“ *Opt. Express*, vol. 30, no. 18, pp. 31 519–31 529, Aug. 2022 (cit. on pp. 5, 81, 83).

[69] B. Ji, S. Yue, L. Zhou, M. Li, and G. Chang, „Novel figuring method for a multilayer laue lens,“ *Opt. Express*, vol. 30, no. 26, pp. 46 838–46 848, Dec. 2022 (cit. on p. 5).

[70] J. L. Dresselhaus, M. Zakharova, N. Ivanov, *et al.*, „X-ray focusing below 3 nm with aberration-corrected multilayer laue lenses,“ *Opt. Express*, vol. 32, no. 9, pp. 16 004–16 015, Apr. 2024 (cit. on pp. 5, 79, 81).

[71] S. Bajt, H. N. Chapman, A. Aquila, and E. Gullikson, „High-efficiency x-ray gratings with asymmetric-cut multilayers,“ *JOSA A*, vol. 29, no. 3, pp. 216–230, 2012 (cit. on pp. 8, 9, 31, 32, 36).

[72] M. Zakharova, Z. Rek, B. Šarler, and S. Bajt, „On the thermal stability of multilayer optics for use with high x-ray intensities,“ *Opt. Mater. Express*, vol. 14, no. 8, pp. 1933–1948, Aug. 2024 (cit. on pp. 9, 44, 116).

[73] Z. Rek, H. N. Chapman, B. Šarler, and S. Bajt, „Numerical simulation of heat load for multilayer laue lens under exposure to xfel pulse trains,“ *Photonics*, vol. 9, no. 5, 2022 (cit. on pp. 9, 32, 59, 60, 115, 116).

[74] A. Authier, *Dynamical theory of X-ray diffraction*. Oxford University Press on Demand, 2004, vol. 11 (cit. on p. 9).

[75] K. Li, M. Wojcik, and C. Jacobsen, „Multislice does it all—calculating the performance of nanofocusing x-ray optics,“ *Opt. Express*, vol. 25, no. 3, pp. 1831–1846, Feb. 2017 (cit. on pp. 10, 13).

[76] E. J. Jaeschke, S. Khan, J. R. Schneider, and J. B. Hastings, *Synchrotron light sources and free-electron lasers: accelerator physics, instrumentation and science applications*. Springer, 2016 (cit. on p. 11).

[77] D. Attwood, *Soft x-rays and extreme ultraviolet radiation: principles and applications*. Cambridge University Press: Cambridge, 2000 (cit. on p. 11).

[78] W. Chao, J. Kim, S. Rekawa, P. Fischer, and E. H. Anderson, „Demonstration of 12 nm resolution fresnel zone plate lens based soft x-ray microscopy,“ *Opt. Express*, vol. 17, no. 20, pp. 17 669–17 677, Sep. 2009 (cit. on p. 11).

[79] M. Mayer, C. Grévent, A. Szeghalmi, *et al.*, „Multilayer fresnel zone plate for soft x-ray microscopy resolves sub-39nm structures,“ *Ultramicroscopy*, vol. 111, no. 12, pp. 1706–1711, 2011 (cit. on p. 11).

[80] Y. S. Chu, J. M. Yi, F. De Carlo, *et al.*, „Hard-x-ray microscopy with Fresnel zone plates reaches 40nm Rayleigh resolution,“ *Applied Physics Letters*, vol. 92, no. 10, p. 103 119, Mar. 2008 (cit. on p. 11).

[81] S. Flenner, A. Kubec, C. David, *et al.*, „Hard x-ray nano-holotomography with a fresnel zone plate,“ *Opt. Express*, vol. 28, no. 25, pp. 37 514–37 525, Dec. 2020 (cit. on p. 11).

[82] A. G. Michette, *Optical Systems for Soft X Rays*. Plenum Press: New York, 1986 (cit. on p. 11).

[83] T. Fujita, H. Nishihara, and J. Koyama, „Fabrication of micro lenses using electron-beam lithography,“ *Opt. Lett.*, vol. 6, no. 12, pp. 613–615, Dec. 1981 (cit. on p. 11).

[84] K. Keskinbora, C. Grévent, U. Eigenthaler, M. Weigand, and G. Schütz, „Rapid prototyping of fresnel zone plates via direct ga+ ion beam lithography for high-resolution x-ray imaging,“ *ACS Nano*, vol. 7, no. 11, pp. 9788–9797, 2013, PMID: 24151983 (cit. on p. 11).

[85] F. Marschall, J. Vila-Comamala, V. Guzenko, and C. David, „Systematic efficiency study of line-doubled zone plates,“ *Microelectronic Engineering*, vol. 177, pp. 25–29, 2017, Advances in Micro- and Nano-Patterning (cit. on p. 11).

[86] K. Jefimovs, J. Vila-Comamala, T. Pilvi, *et al.*, „Zone-doubling technique to produce ultrahigh-resolution x-ray optics,“ en, *Phys. Rev. Lett.*, vol. 99, no. 26, p. 264 801, Dec. 2007 (cit. on p. 11).

[87] J. Vila-Comamala, A. Diaz, M. Guizar-Sicairos, *et al.*, „Characterization of high-resolution diffractive x-ray optics by ptychographic coherent diffractive imaging,“ *Opt. Express*, vol. 19, no. 22, pp. 21 333–21 344, Oct. 2011 (cit. on p. 11).

[88] I. Mohacsi, I. Vartiainen, B. Rösner, *et al.*, „Interlaced zone plate optics for hard x-ray imaging in the 10 nm range,“ en, *Sci. Rep.*, vol. 7, no. 1, Mar. 2017 (cit. on p. 11).

[89] C. Chang and A. Sakdinawat, „Ultra-high aspect ratio high-resolution nanofabrication for hard x-ray diffractive optics,“ en, *Nat. Commun.*, vol. 5, no. 1, p. 4243, Jun. 2014 (cit. on p. 11).

[90] Y. Suzuki, A. Takeuchi, H. Takano, and H. Takenaka, „Performance test of fresnel zone plate with 50 nm outermost zone width in hard x-ray region,“ *Japanese Journal of Applied Physics*, vol. 44, no. 4R, p. 1994, Apr. 2005 (cit. on p. 11).

[91] Y. T. Chen, T. N. Lo, C. W. Chiu, *et al.*, „Fabrication of high-aspect-ratio fresnel zone plates by e-beam lithography and electroplating,“ *Journal of Synchrotron Radiation*, vol. 15, no. 2, pp. 170–175, Mar. 2008 (cit. on p. 11).

[92] H. C. Kang, H. Yan, R. P. Winarski, *et al.*, „Focusing of hard x-rays to 16 nanometers with a multilayer Laue lens,“ *Applied Physics Letters*, vol. 92, no. 22, p. 221 114, Jun. 2008 (cit. on p. 14).

[93] A. T. Macrander, A. Kubec, R. Conley, *et al.*, „Efficiency of a multilayer-Laue-lens with a 102 μm aperture,“ *Applied Physics Letters*, vol. 107, no. 8, p. 081 904, Aug. 2015 (cit. on p. 14).

[94] X. Huang, R. Conley, N. Bouet, *et al.*, „Achieving hard x-ray nanofocusing using a wedged multilayer laue lens,“ *Opt. Express*, vol. 23, no. 10, pp. 12 496–12 507, May 2015 (cit. on p. 14).

[95] S. Niese, P. Krüger, A. Kubec, *et al.*, „Fabrication of customizable wedged multilayer laue lenses by adding a stress layer,“ *Thin Solid Films*, vol. 571, pp. 321–324, 2014, Multilayers 2013 (cit. on pp. 14, 54, 70).

[96] N. Bouet, A. T. Macrander, J. Maser, *et al.*, „Large aperture and wedged multilayer laue lens for x-ray nanofocusing,“ en, *J. Nanosci. Nanotechnol.*, vol. 19, no. 1, pp. 575–584, Jan. 2019 (cit. on pp. 14, 54).

[97] S. Bajt, M. Prasciolu, H. Fleckenstein, *et al.*, „X-ray focusing with efficient high-NA multilayer laue lenses,“ en, *Light Sci. Appl.*, vol. 7, no. 3, p. 17 162, Mar. 2018 (cit. on p. 14).

[98] L. Zhou, S. Yue, M. Li, P. Liu, and G. Chang, „A compound multilayer laue lens with multiple tilting angles,“ *Nuclear Instruments and Methods in Physics Research Section A: Accelerators, Spectrometers, Detectors and Associated Equipment*, vol. 806, pp. 87–91, 2016 (cit. on p. 14).

[99] B. Ji, S. Yue, Q. Hou, *et al.*, „A linear gradient multilayer laue lens,“ *Optics Communications*, vol. 552, p. 130 031, 2024 (cit. on p. 14).

[100] A. Andrejczuk, J. Krzywinski, and S. Bajt, „Influence of imperfections in a wedged multilayer laue lens for the focusing of x-rays investigated by beam propagation method,“ *Nuclear Instruments and Methods in Physics Research Section B: Beam Interactions with Materials and Atoms*, vol. 364, pp. 60–64, 2015, 12th International School and Symposium on Synchrotron Radiation in Natural Science (cit. on p. 17).

[101] H. Yan, H. Kang, J. Maser, *et al.*, „Characterization of a multilayer laue lens with imperfections," *Nuclear Instruments and Methods in Physics Research Section A: Accelerators, Spectrometers, Detectors and Associated Equipment*, vol. 582, no. 1, pp. 126–128, 2007 (cit. on p. 17).

[102] L. Hu, G. Chang, P. Liu, and L. Zhou, „Focusing performance of a multilayer laue lens with layer placement error described by dynamical diffraction theory," *Journal of Synchrotron Radiation*, vol. 22, no. 4, pp. 936–945, 2015 (cit. on p. 17).

[103] K. Strehl, „Aplanatische und fehlerhafte abbildung im fernrohr," *Zeitschrift für Instrumentenkunde*, vol. 15, no. 7, pp. 362–370, 1895 (cit. on p. 18).

[104] K. Strehl, „Über luftschlieren und zonenfehler," *Zeitschrift für Instrumentenkunde*, vol. 22, pp. 213–217, 1902 (cit. on p. 18).

[105] R. Burge, M. Fiddy, A. Greenaway, and G. Ross, „The phase problem," *Proceedings of the Royal Society of London. A. Mathematical and Physical Sciences*, vol. 350, no. 1661, pp. 191–212, 1976 (cit. on p. 18).

[106] R. W. Harrison, „Phase problem in crystallography," *JOSA a*, vol. 10, no. 5, pp. 1046–1055, 1993 (cit. on p. 18).

[107] G. Taylor, „The phase problem," *Acta Crystallographica Section D: Biological Crystallography*, vol. 59, no. 11, pp. 1881–1890, 2003 (cit. on p. 18).

[108] Y. Shechtman, Y. C. Eldar, O. Cohen, *et al.*, „Phase retrieval with application to optical imaging: A contemporary overview," *IEEE signal processing magazine*, vol. 32, no. 3, pp. 87–109, 2015 (cit. on p. 18).

[109] P. Hariharan, *Basics of interferometry*. Elsevier, 2010 (cit. on p. 19).

[110] J. Hartmann, *Objektivuntersuchungen*. Springer, 1904 (cit. on p. 19).

[111] R. V. Shack, „Production and use of a lenticular hartmann screen," in *Spring Meeting of Optical Society of America, 1971*, vol. 656, 1971 (cit. on p. 19).

[112] N. Ivanov, J. L. Dresselhaus, J. Carnis, *et al.*, „Robust ptychographic x-ray speckle tracking with multilayer laue lenses," *Opt. Express*, vol. 30, no. 14, pp. 25 450–25 473, Jul. 2022 (cit. on pp. 22, 23, 75).

[113] N. Ivanov, *X-ray imaging with high numerical aperture X-ray optics*. Universität Hamburg (Germany), 2023 (cit. on p. 23).

[114] J. L. Dresselhaus, H. Fleckenstein, M. Domaracky̌, *et al.*, „Precise wavefront characterization of x-ray optical elements using a laboratory source," *Review of Scientific Instruments*, vol. 93, no. 7, 2022 (cit. on pp. 23, 26, 52, 57, 79).

[115] *Lambda x-ray detectors*, `https://x-spectrum.de/products/lambda/`, X-Spectrum (cit. on p. 25).

[116] M. Domaracky, `https://gitlab.desy.de/cfel-sc-public/kamzik3`, Kamzik3 (cit. on p. 26).

[117] C. David, B. Nöhammer, H. Solak, and E. Ziegler, „Differential x-ray phase contrast imaging using a shearing interferometer," *Applied physics letters*, vol. 81, no. 17, pp. 3287–3289, 2002 (cit. on p. 31).

[118] A. Momose, S. Kawamoto, I. Koyama, *et al.*, „Demonstration of x-ray talbot interferometry," *Japanese journal of applied physics*, vol. 42, no. 7B, p. L866, 2003 (cit. on pp. 31, 32).

[119] F. Pfeiffer, T. Weitkamp, O. Bunk, and C. David, „Phase retrieval and differential phase-contrast imaging with low-brilliance x-ray sources," *Nature physics*, vol. 2, no. 4, pp. 258–261, 2006 (cit. on p. 31).

[120] A. Momose, W. Yashiro, Y. Takeda, Y. Suzuki, and T. Hattori, „Phase tomography by x-ray talbot interferometry for biological imaging," *Japanese journal of applied physics*, vol. 45, no. 6R, p. 5254, 2006 (cit. on pp. 31, 32).

[121] F. Pfeiffer, M. Bech, O. Bunk, *et al.*, „Hard-x-ray dark-field imaging using a grating interferometer," *Nature materials*, vol. 7, no. 2, pp. 134–137, 2008 (cit. on p. 31).

[122] E. Treacy, „Optical pulse compression with diffraction gratings," *IEEE Journal of quantum Electronics*, vol. 5, no. 9, pp. 454–458, 1969 (cit. on p. 31).

[123] V. Chauhan, P. Bowlan, J. Cohen, and R. Trebino, „Single-diffraction-grating and grism pulse compressors," *JOSA B*, vol. 27, no. 4, pp. 619–624, 2010 (cit. on p. 31).

[124] X. Shen, S. Du, W. Liang, *et al.*, „Two-step pulse compressor based on asymmetric four-grating compressor for femtosecond petawatt lasers," *Applied Physics B*, vol. 128, no. 8, p. 159, 2022 (cit. on p. 31).

[125] D. Dravins, „High-dispersion astronomical spectroscopy with holographic and ruled diffraction gratings," *Applied Optics*, vol. 17, no. 3, pp. 404–414, 1978 (cit. on p. 31).

[126] J. Marsh, D. Mar, and D. Jaffe, „Production and evaluation of silicon immersion gratings for infrared astronomy," *Applied Optics*, vol. 46, no. 17, pp. 3400–3416, 2007 (cit. on p. 31).

[127] Y. Zhang, W. Li, W. Duan, Z. Huang, and H. Yang, „Echelle grating spectroscopic technology for high-resolution and broadband spectral measurement," *Applied Sciences*, vol. 12, no. 21, p. 11 042, 2022 (cit. on p. 31).

[128] E. G. Loewen and E. Popov, *Diffraction gratings and applications*. CRC Press, 2018 (cit. on p. 31).

[129] J. Gao, P. Chen, L. Wu, B. Yu, and L. Qian, „A review on fabrication of blazed gratings," *Journal of Physics D: Applied Physics*, vol. 54, no. 31, p. 313 001, 2021 (cit. on p. 31).

[130] E. Palmer, M. Hutley, A. Franks, J. Verrill, and B. Gale, „Diffraction gratings (manufacture)," *Reports on Progress in Physics*, vol. 38, no. 8, p. 975, 1975 (cit. on p. 31).

[131] M. Neviere and W. R. Hunter, „Analysis of the changes in efficiency across the ruled area of a concave diffraction grating," *Applied Optics*, vol. 19, no. 12, pp. 2059–2065, 1980 (cit. on p. 31).

[132] M. C. Hettrick, „Varied line-space gratings: Past, present and future," in *Diffraction Phenomena in Optical Engineering Applications*, SPIE, vol. 560, 1986, pp. 96–108 (cit. on p. 31).

[133] Y. Takeuchi, Y. Yoneyama, T. Ishida, and T. Kawai, „6-axis control ultraprecision microgrooving on sculptured surfaces with non-rotational cutting tool," *CIRP annals*, vol. 58, no. 1, pp. 53–56, 2009 (cit. on p. 31).

[134] P. Mouroulis, D. W. Wilson, P. D. Maker, and R. E. Muller, „Convex grating types for concentric imaging spectrometers,“ *Applied Optics*, vol. 37, no. 31, pp. 7200–7208, 1998 (cit. on p. 31).

[135] M. Okano, H. Kikuta, Y. Hirai, K. Yamamoto, and T. Yotsuya, „Optimization of diffraction grating profiles in fabrication by electron-beam lithography,“ *Applied optics*, vol. 43, no. 27, pp. 5137–5142, 2004 (cit. on p. 31).

[136] H. Ju, P. Zhang, J. Liang, S. Wang, and Y. Wu, „Blazed silicon gratings fabricated by deflecting crystal orientation (111) silicon wafer,“ *Journal of Micro/Nanolithography, MEMS and MOEMS*, vol. 4, no. 1, pp. 019 701–019 701, 2005 (cit. on p. 31).

[137] J. Frühauf and S. Krönert, „Wet etching of silicon gratings with triangular profiles,“ *Microsystem Technologies*, vol. 11, pp. 1287–1291, 2005 (cit. on p. 31).

[138] C. Shen, X. Tan, Q. Jiao, *et al.*, „Convex blazed grating of high diffraction efficiency fabricated by swing ion-beam etching method,“ *Optics Express*, vol. 26, no. 19, pp. 25 381–25 398, 2018 (cit. on p. 31).

[139] J. Seely, M. Kowalski, R. Cruddace, *et al.*, „Multilayer-coated laminar grating with 16% normal-incidence efficiency in the 150-Å wavelength region,“ *Applied optics*, vol. 36, no. 31, pp. 8206–8213, 1997 (cit. on p. 31).

[140] C. T. DeRoo, J. Termini, F. Grisé, *et al.*, „Limiting spectral resolution of a reflection grating made via electron-beam lithography,“ *The Astrophysical Journal*, vol. 904, no. 2, p. 142, 2020 (cit. on p. 31).

[141] S. Wen, Q. Huang, A. Sokolov, *et al.*, „High efficiency multilayer coated laminar gratings with high line density for tender x-ray region,“ *Optics & Laser Technology*, vol. 168, p. 109 979, 2024 (cit. on p. 31).

[142] W. R. Hunter, M. P. Kowalski, J. C. Rife, and R. G. Cruddace, „Investigation of the properties of an ion-etched plane laminar holographic grating,“ *Applied Optics*, vol. 40, no. 34, pp. 6157–6165, 2001 (cit. on p. 31).

[143] L. Romano, J. Vila-Comamala, K. Jefimovs, and M. Stampanoni, „High-aspect-ratio grating microfabrication by platinum-assisted chemical etching and gold electroplating,“ *Advanced Engineering Materials*, vol. 22, no. 10, p. 2 000 258, 2020 (cit. on p. 31).

[144] S. C. Barden, J. A. Arns, and W. S. Colburn, „Volume-phase holographic gratings and their potential for astronomical applications,“ in *Optical Astronomical Instrumentation*, SPIE, vol. 3355, 1998, pp. 866–876 (cit. on p. 31).

[145] S. C. Barden, J. A. Arns, W. S. Colburn, and J. B. Williams, „Volume-phase holographic gratings and the efficiency of three simple volume-phase holographic gratings,“ *Publications of the Astronomical Society of the Pacific*, vol. 112, no. 772, p. 809, 2000 (cit. on p. 31).

[146] I. K. Baldry, J. Bland-Hawthorn, and J. Robertson, „Volume phase holographic gratings: Polarization properties and diffraction efficiency,“ *Publications of the Astronomical Society of the Pacific*, vol. 116, no. 819, p. 403, 2004 (cit. on p. 31).

[147] S. Werner, P. Guttmann, F. Siewert, *et al.*, „Spectromicroscopy of nanoscale materials in the tender x-ray regime enabled by a high efficient multilayer-based grating monochromator,“ *Small Methods*, vol. 7, no. 1, p. 2 201 382, 2023 (cit. on p. 31).

[148] X. Yang, I. V. Kozhevnikov, Q. Huang, and Z. Wang, „Unified analytical theory of single-order soft x-ray multilayer gratings,“ *JOSA B*, vol. 32, no. 4, pp. 506–522, 2015 (cit. on p. 31).

[149] J. C. Rife, W. R. Hunter, T. W. Barbee, and R. G. Cruddace, „Multilayer-coated blazed grating performance in the soft x-ray region,“ *Applied optics*, vol. 28, no. 15, pp. 2984–2986, 1989 (cit. on p. 31).

[150] J. Rife, T. Barbee Jr, W. Hunter, and R. Cruddace, „Performance of a tungsten/carbon multilayer-coated, blazed grating from 150 to 1700 ev,“ *Physica Scripta*, vol. 41, no. 4, p. 418, 1990 (cit. on p. 31).

[151] D. Voronov, E. Anderson, R. Cambie, *et al.*, „A 10,000 groove/mm multilayer coated grating for euv spectroscopy,“ *Optics Express*, vol. 19, no. 7, pp. 6320–6325, 2011 (cit. on p. 31).

[152] D. Voronov, E. Gullikson, F. Salmassi, T. Warwick, and H. Padmore, „Enhancement of diffraction efficiency via higher-order operation of a multilayer blazed grating,“ *Optics letters*, vol. 39, no. 11, pp. 3157–3160, 2014 (cit. on p. 31).

[153] A. V. Vinogradov, „Gratings and zone plates based on sliced multilayer structures,“ in *X-Ray and Extreme Ultraviolet Optics*, SPIE, vol. 2515, 1995, pp. 22–36 (cit. on p. 31).

[154] R. Fechtchenko, A. Vinogradov, and D. Voronov, „Optical properties of sliced multilayer gratings,“ *Optics communications*, vol. 210, no. 3-6, pp. 179–186, 2002 (cit. on p. 31).

[155] D. L. Voronov, R. Cambie, R. M. Feshchenko, *et al.*, „Development of an ultrahigh-resolution diffraction grating for soft x-rays,“ in *Advances in X-Ray/EUV Optics and Components II*, SPIE, vol. 6705, 2007, pp. 102–113 (cit. on p. 31).

[156] D. L. Voronov, R. Cambie, E. M. Gullikson, *et al.*, „Fabrication and characterization of a new high density sc/si multilayer sliced grating,“ in *Advances in X-Ray/EUV Optics and Components III*, SPIE, vol. 7077, 2008, pp. 53–64 (cit. on p. 31).

[157] R. van der Meer, I. Kozhevnikov, B. Krishnan, *et al.*, „Single-order operation of lamellar multilayer gratings in the soft x-ray spectral range,“ *AIP advances*, vol. 3, no. 1, 2013 (cit. on p. 31).

[158] Q. Huang, J. Feng, T. Li, *et al.*, „Narrowband lamellar multilayer grating with low contrast mosi2/si materials for the soft x-ray region,“ *Journal of Physics D: Applied Physics*, vol. 52, no. 19, p. 195 303, 2019 (cit. on p. 31).

[159] M. Prasciolu, A. Haase, F. Scholze, H. N. Chapman, and S. Bajt, „Extended asymmetric-cut multilayer x-ray gratings,“ *Opt. Express*, vol. 23, no. 12, pp. 15 195–15 204, Jun. 2015 (cit. on p. 31).

[160] *Microprep™ pro*, `https://microprep.pro/microprep-pro`, 3D-Micromac (cit. on p. 33).

[161] M. Panalytical, `https://www.malvernpanalytical.com/en/products/category/x-ray-diffractometers`, Panalytical (cit. on p. 36).

[162] D. G. Stearns, „X-ray scattering from interfacial roughness in multilayer structures,“ *Journal of Applied Physics*, vol. 71, no. 9, pp. 4286–4298, May 1992. eprint: `https://pubs.aip.org/aip/jap/article-pdf/71/9/4286/18650344/4286\_1\_online.pdf` (cit. on p. 41).

[163] D. L. Windt, R. Hull, and W. K. Waskiewicz, „Interface imperfections in metal/Si multilayers,“ *Journal of Applied Physics*, vol. 71, no. 6, pp. 2675–2678, Mar. 1992. eprint: `https://pubs.aip.org/aip/jap/article-pdf/71/6/2675/18649644/2675\_1\_online.pdf` (cit. on p. 41).

[164] H. Yan, „X-ray dynamical diffraction from multilayer laue lenses with rough interfaces,“ *Physical Review B—Condensed Matter and Materials Physics*, vol. 79, no. 16, p. 165 410, 2009 (cit. on pp. 41, 42).

[165] R. Kelley, K. Song, B. Van Leer, D. Wall, and L. Kwakman, „Xe+ fib milling and measurement of amorphous silicon damage,“ *Microscopy and Microanalysis*, vol. 19, no. S2, pp. 862–863, 2013 (cit. on p. 43).

[166] L. Zehnder, „Ein neuer interferenzrefraktor,“ *Zeitschrift für Instrumentenkunde*, vol. 11, pp. 275–285, 1891 (cit. on p. 45).

[167] L. Mach, „Ueber einen interferenzrefraktor,“ *Zeitschrift für Instrumentenkunde*, vol. 12, no. 3, p. 89, 1892 (cit. on p. 45).

[168] H. N. Chapman, S. Bajt, and M. Prasciolu, „Method for producing a multilayer laue lens,“ EP3996112B1, 2024 (cit. on p. 53).

[169] C. David, S. Gorelick, S. Rutishauser, *et al.*, „Nanofocusing of hard x-ray free electron laser pulses using diamond based fresnel zone plates,“ *Scientific Reports*, vol. 1, 2011 (cit. on p. 59).

[170] Z. Rek, H. N. Chapman, S. Bajt, and B. Šarler, „Numerical simulations of temperature loads on multilayer laue lenses,“ in *Journal of Physics: Conference Series*, IOP Publishing, vol. 2766, 2024, p. 012 034 (cit. on pp. 59, 115).

[171] M. Prasciolu, K. T. Murray, N. Ivanov, *et al.*, „On the use of multilayer laue lenses with x-ray free electron lasers,“ vol. 11886, 2021 (cit. on p. 59).

[172] H. N. Chapman, C. Li, S. Bajt, *et al.*, *Convergent-beam attosecond x-ray crystallography*, 2024. arXiv: `2409.11127 [physics.optics]` (cit. on p. 62).

[173] D. Paganin, *Coherent X-ray optics*. Oxford University Press, USA, 2006 (cit. on p. 76).

[174] *The metal-jet technology*, `https://www.excillum.com/products/metaljet/`, excillum (cit. on p. 78).

[175] I. Zanette, T. Zhou, A. Burvall, *et al.*, „Speckle-based x-ray phase-contrast and dark-field imaging with a laboratory source,“ *Physical review letters*, vol. 112, no. 25, p. 253 903, 2014 (cit. on p. 78).

[176] T. Zhou, I. Zanette, M.-C. Zdora, *et al.*, „Speckle-based x-ray phase-contrast imaging with a laboratory source and the scanning technique,“ *Optics letters*, vol. 40, no. 12, pp. 2822–2825, 2015 (cit. on p. 78).

[177] M.-C. Zdora, P. Thibault, and I. Zanette, „State of the art and recent advances in x-ray speckle-based phase-contrast imaging,“ *Developments in X-Ray Tomography XIII*, vol. 11840, pp. 116–122, 2021 (cit. on p. 78).

[178] B. Ji, S. Yue, L. Zhou, M. Li, and G. Chang, „Novel figuring method for a multilayer laue lens,“ *Optics Express*, vol. 30, no. 26, pp. 46 838–46 848, 2022 (cit. on p. 81).

[179] K. Sawhney, D. Laundy, V. Dhamgaye, and I. Pape, „Compensation of x-ray mirror shape-errors using refractive optics,“ *Appl. Phys. Lett.*, vol. 109, no. 5, p. 051 904, 2016 (cit. on p. 81).

[180] F. Seiboth, A. Schropp, M. Lyubomirskiy, *et al.*, „On-chip aberration correction for planar nanofocusing x-ray lenses by focused ion-beam milling,“ *Applied Physics Letters*, vol. 122, no. 24, 2023 (cit. on pp. 81, 82).

[181] D. Laundy, V. Dhamgaye, T. Moxham, and K. Sawhney, „Adaptable refractive correctors for x-ray optics,“ *Optica*, vol. 6, no. 12, pp. 1484–1490, 2019 (cit. on pp. 81, 82).

[182] F. Seiboth, D. Bruckner, M. Kahnt, *et al.*, „Hard x-ray wavefront correction via refractive phase plates made by additive and subtractive fabrication techniques,“ *Journal of Synchrotron Radiation*, vol. 27, pp. 1121–1130, 2020 (cit. on p. 82).

[183] F. Niesler and M. Hermatschweiler, „Two-photon polymerization—a versatile microfabrication tool: From maskless lithography to 3D printing,“ *Laser Tech. J.*, vol. 12, no. 3, pp. 44–47, 2015 (cit. on p. 84).

[184] H. Wang, C.-F. Pan, C. Li, *et al.*, „Two-photon polymerization lithography for imaging optics,“ *International Journal of Extreme Manufacturing*, vol. 6, no. 4, p. 042 002, Apr. 2024 (cit. on p. 84).

[185] S. Ristok, S. Thiele, A. Toulouse, A. M. Herkommer, and H. Giessen, „Stitching-free 3d printing of millimeter-sized highly transparent spherical and aspherical optical components,“ *Opt. Mater. Express*, vol. 10, no. 10, pp. 2370–2378, Oct. 2020 (cit. on p. 84).

[186] V. Aslani, A. Toulouse, M. Schmid, *et al.*, „3d printing of colored micro-optics,“ *Opt. Mater. Express*, vol. 13, no. 5, pp. 1372–1384, May 2023 (cit. on p. 84).

[187] T. Gissibl, S. Thiele, A. Herkommer, and H. Giessen, „Two-photon direct laser writing of ultracompact multi-lens objectives,“ *Nature photonics*, vol. 10, no. 8, pp. 554–560, 2016 (cit. on p. 84).

[188] S. Thiele, K. Arzenbacher, T. Gissibl, H. Giessen, and A. M. Herkommer, „3d-printed eagle eye: Compound microlens system for foveated imaging,“ *Science Advances*, vol. 3, no. 2, e1602655, 2017 (cit. on p. 84).

[189] A. K. Petrov, V. O. Bessonov, K. A. Abrashitova, *et al.*, „Polymer x-ray refractive nanolenses fabricated by additive technology,“ *Opt. Express*, vol. 25, no. 13, pp. 14 173–14 181, Jun. 2017 (cit. on p. 84).

[190] M. Mirzaeimoghri, A. Morales Martinez, A. Panna, *et al.*, „Nano-printed miniature compound refractive lens for desktop hard x-ray microscopy,“ *PloS one*, vol. 13, no. 8, e0203319, 2018 (cit. on p. 84).

[191] T. Gissibl, S. Thiele, A. Herkommer, and H. Giessen, „Sub-micrometre accurate free-form optics by three-dimensional printing on single-mode fibres,“ *Nature Communications*, vol. 7, no. 1, p. 11 763, 2016 (cit. on p. 84).

[192] W. Hadibrata, H. Wei, S. Krishnaswamy, and K. Aydin, „Inverse design and 3d printing of a metalens on an optical fiber tip for direct laser lithography,“ *Nano letters*, vol. 21, no. 6, pp. 2422–2428, 2021 (cit. on p. 84).

[193] A. Kubec, M.-C. Zdora, U. T. Sanli, *et al.*, „An achromatic x-ray lens,“ *Nature Communications*, vol. 13, no. 1, p. 1305, 2022 (cit. on pp. 84, 99).

[194] U. T. Sanli, G. Rodgers, M.-C. Zdora, *et al.*, „Apochromatic x-ray focusing,“ *Light: Science & Applications*, vol. 12, no. 1, p. 107, 2023 (cit. on pp. 84, 99).

[195] D. Wu, L.-G. Niu, Q.-D. Chen, R. Wang, and H.-B. Sun, „High efficiency multilevel phase-type fractal zone plates,“ *Opt. Lett.*, vol. 33, no. 24, pp. 2913–2915, Dec. 2008 (cit. on p. 84).

[196] M. Plidschun, H. Ren, J. Kim, *et al.*, „Ultrahigh numerical aperture meta-fibre for flexible optical trapping,“ *Light: Science & Applications*, vol. 10, no. 1, p. 57, 2021 (cit. on p. 84).

[197] N. GmbH., *Photonic professional (gt) user manual*, Nanoscribe GmbH, 2015 (cit. on pp. 85, 86).

[198] Nanoguide, *Adjusting the dose*, `https://support.nanoscribe.com/hc/en-gb/articles/360001159713-Adjusting-the-Dose` (cit. on p. 86).

[199] J. Fischer and M. Wegener, „Three-dimensional optical laser lithography beyond the diffraction limit,“ *Laser & Photonics Reviews*, vol. 7, no. 1, pp. 22–44, 2013 (cit. on p. 88).

[200] Nanoguide, *25x objective*, `https://support.nanoscribe.com/hc/en-gb/articles/360002482713-25x-Objective` (cit. on p. 88).

[201] W. T. Elam, B. D. Ravel, and J. Sieber, „A new atomic database for x-ray spectroscopic calculations,“ *Radiation Physics and Chemistry*, vol. 63, no. 2, pp. 121–128, 2002 (cit. on p. 92).

[202] Z. von F, „Beugungstheorie des schneidenver-fahrens und seiner verbesserten form, der phasenkontrastmethode,“ *physica*, vol. 1, no. 7-12, pp. 689–704, 1934 (cit. on p. 97).

[203] M. Born and E. Wolf, *Principles of optics: electromagnetic theory of propagation, interference and diffraction of light*. Elsevier, 2013 (cit. on p. 97).

[204] W. Swantner and W. W. Chow, „Gram–Schmidt orthonormalization of Zernike polynomials for general aperture shapes,“ *Appl. Opt.*, vol. 33, no. 10, pp. 1832–1837, 1994 (cit. on p. 97).

[205] E. Muslimov, E. Hugot, W. Jahn, *et al.*, „Combining freeform optics and curved detectors for wide field imaging: A polynomial approach over squared aperture,“ *Opt. Express*, vol. 25, no. 13, pp. 14 598–14 610, 2017 (cit. on p. 97).

[206] M. D. Levenson, „Wavefront engineering for photolithography,“ *Phys. Today*, vol. 46, no. 7, pp. 28–36, 1993 (cit. on p. 100).

[207] C. G. Schroer, F. Seiboth, A. Schropp, *et al.*, „Hard x-ray wavefront engineering for aberration correction and beam shaping,“ in *Advances in X-Ray/EUV Optics and Components XVII*, SPIE, vol. 12240, 2022, pp. 163–170 (cit. on p. 100).

[208] F. Kotz, P. Risch, K. Arnold, *et al.*, „Fabrication of arbitrary three-dimensional suspended hollow microstructures in transparent fused silica glass,“ *Nature Communications*, vol. 10, no. 1, 2019 (cit. on p. 101).

[209] F. Kotz, A. S. Quick, P. Risch, *et al.*, „Two-photon polymerization of nanocomposites for the fabrication of transparent fused silica glass microstructures,“ *Advanced Materials*, vol. 33, no. 9, p. 2 006 341, 2021 (cit. on p. 101).

[210] J. Bauer, C. Crook, and T. Baldacchini, „A sinterless, low-temperature route to 3d print nanoscale optical-grade glass,“ *Science*, vol. 380, no. 6648, pp. 960–966, 2023 (cit. on p. 101).

[211] S. Terentyev, V. Blank, S. Polyakov, *et al.*, „Parabolic single-crystal diamond lenses for coherent x-ray imaging,“ *Applied Physics Letters*, vol. 107, no. 11, p. 111 108, Sep. 2015 (cit. on p. 101).

[212] S. Antipov, S. Baryshev, J. Butler, *et al.*, „Single-crystal diamond refractive lens for focusing x-rays in two dimensions,“ *Journal of synchrotron radiation*, vol. 23, no. 1, pp. 163–168, 2016 (cit. on p. 101).

[213] M. P. Irina Snigireva and A. Snigirev, „Diamond x-ray refractive optics,“ *Synchrotron Radiation News*, vol. 34, no. 6, pp. 12–20, 2021 (cit. on p. 101).

[214] T. Li, J. L. Dresselhaus, N. Ivanov, *et al.*, „Dose-efficient scanning compton x-ray microscopy,“ *Light: Science and Applications*, vol. 12, no. 1, 2023 (cit. on pp. 103, 113–115).

[215] W. Zhang, J. L. Dresselhaus, H. Fleckenstein, *et al.*, „Fast and efficient hard x-ray projection imaging below 10 nm resolution,“ *Opt. Express*, vol. 32, no. 17, pp. 30 879–30 897, Aug. 2024 (cit. on pp. 103, 110).

[216] H. H. Pattee, „The scanning x-ray microscope,“ *J. Opt. Soc. Am.*, vol. 43, no. 1, pp. 61–62, Jan. 1953 (cit. on p. 108).

[217] P. Horowitz and J. A. Howell, „A scanning x-ray microscope using synchrotron radiation,“ *Science*, vol. 178, no. 4061, pp. 608–611, 1972 (cit. on p. 108).

[218] C. Jacobsen, S. Williams, E. Anderson, *et al.*, „Diffraction-limited imaging in a scanning transmission x-ray microscope,“ *Optics Communications*, vol. 86, no. 3-4, pp. 351–364, 1991 (cit. on p. 108).

[219] F. Pfeiffer, „X-ray ptychography,“ *Nature Photonics*, vol. 12, no. 1, pp. 9–17, 2018 (cit. on p. 109).

[220] J. Rodenburg and A. Maiden, „Ptychography,“ *Springer Handbook of Microscopy*, pp. 819–904, 2019 (cit. on p. 109).

[221] M. Stockmar, P. Cloetens, I. Zanette, *et al.*, „Near-field ptychography: Phase retrieval for inline holography using a structured illumination,“ *Scientific reports*, vol. 3, no. 1, p. 1927, 2013 (cit. on p. 109).

[222] M. Stockmar, I. Zanette, M. Dierolf, *et al.*, „X-ray near-field ptychography for optically thick specimens,“ *Physical Review Applied*, vol. 3, no. 1, p. 014 005, 2015 (cit. on p. 109).

[223] P. Villanueva-Perez, S. Bajt, and H. Chapman, „Dose efficient compton x-ray microscopy,“ *Optica*, vol. 5, no. 4, pp. 450–457, 2018 (cit. on p. 113).

[224] C. Pellegrini, „X-ray free-electron lasers: From dreams to reality,“ *Physica Scripta*, vol. 2016, no. T169, p. 014 004, 2017 (cit. on p. 115).

[225] U. Bergman, V. K. Yachandra, and J. Yano, *X-ray free electron lasers: applications in materials, chemistry and biology*. Royal Society of Chemistry, 2017, vol. 18 (cit. on p. 115).

[226] S. Boutet and M. Yabashi, „X-ray free electron lasers and their applications,“ *X-Ray Free Electron Lasers: A Revolution in Structural Biology*, pp. 1–21, 2018 (cit. on p. 115).

[227] D. D. Meyerhofer, „High-intensity-laser-electron scattering,“ *IEEE journal of quantum electronics*, vol. 33, no. 11, pp. 1935–1941, 1997 (cit. on p. 115).

[228] A. Di Piazza, C. Müller, K. Z. Hatsagortsyan, and C. H. Keitel, „Extremely high-intensity laser interactions with fundamental quantum systems,“ *Rev. Mod. Phys.*, vol. 84, pp. 1177–1228, 3 Aug. 2012 (cit. on p. 115).

List of Figures

List of Tables

Colophon

This thesis was typeset with LaTeX 2_ε. It uses the *Clean Thesis* style developed by Ricardo Langner. The design of the *Clean Thesis* style is inspired by user guide documents from Apple Inc.

Download the *Clean Thesis* style at `http://cleanthesis.der-ric.de/`.

Eidesstattliche Versicherung

Hiermit versichere ich an Eides statt, die vorliegende Dissertationsschrift selbst verfasst und keine anderen als die angegebenen Hilfsmittel und Quellen benutzt zu haben.

Sofern im Zuge der Erstellung der vorliegenden Dissertationsschrift generative Künstliche Intelligenz (gKI) basierte elektronische Hilfsmittel verwendet wurden, versichere ich, dass meine eigene Leistung im Vordergrund stand und dass eine vollständige Dokumentation aller verwendeten Hilfsmittel gemäß der Guten wissenschaftlichen Praxis vorliegt. Ich trage die Verantwortung für eventuell durch die gKI generierte fehlerhafte oder verzerrte Inhalte, fehlerhafte Referenzen, Verstöße gegen das Datenschutz- und Urheberrecht oder Plagiate.

Hamburg, September 27, 2024

Jan Lukas Dresselhaus